

Numerical Investigation of Intershaft Hydraulic Seals in a Gas Turbine Engine

Achinie Warusevitane

B.Eng., M.Sc.

Thesis submitted to The University of Nottingham

for the degree of Doctor of Philosophy

November 2023

To my parents for their unwavering support and constant words of encouragement!

Abstract

Civil aero-engines contain two or three shafts that are supported by bearings. Seals are required both between pairs of rotating shafts and between static elements and shafts. Seals located between two co/contra rotating shafts are known as intershaft seals and are typically either hydraulic or oil backed. This thesis focuses on research relevant to improved design capability for intershaft hydraulic seals.

A hydraulic seal is formed by a seal fin on the inner shaft immersed in an annulus of oil on the outer shaft where the oil in the annulus is centrifuged outwards by the radial pressure gradient. Once formed a hydraulic seal does not allow air to flow across the seal and any pressure difference across the seal creates different oil levels either side of the fin. Despite their reliable operation with zero leakage, the application of hydraulic seals is restricted due to the lack of knowledge of their operation and performance, existing design approaches with high safety factors and temperature limitations. Research and development of the next generation of hydraulic seals needs to focus on addressing these issues so that the seal design can be fully optimised and seals can be utilized in hotter zones in future engines. Understanding of the detailed fluid dynamic behaviour during hydraulic seal operation is relatively limited with very little published data. The difficulty lies in the existence of numerous flow patterns in the two-phase flow in an application such as this which also involves highly rotational turbulent flow with transient effects, making computational modelling of these elements extremely

challenging. There is an acknowledged need for improved knowledge of performance and operational capability of hydraulic seals and this provides context for this work. Computational Fluid Dynamics (CFD) provides a means to bridge this gap identified in design capability. The few existing studies on hydraulic seals have used Volume-of-Fluid (VoF) based CFD techniques to model the flow within the seal and provide a fundamental view of the application of interest in this work. The design insights provided by these studies into the application of hydraulic seals were limited due to the limitations associated with the size of the meshes employed. However, the focus of this work is to develop a modelling methodology that is reliable and accurate to refine the understanding of flow physics of intershaft hydraulic seals.

Prior experimental and analytical investigations into fully and partially wetted rotating disks have been used in this thesis to aid understanding of the performance and flow characteristics of hydraulic seals as there are many geometric and operational similarities. These fundamental experimental investigations in the literature provide validation data that allows us to establish a CFD modelling methodology. To develop a reliable modelling methodology, the first part of the work in this thesis compares the flow characteristics of a fully wetted rotating disk against experimental results available in literature including the radial and tangential velocity components. This thesis subsequently investigates the flow characteristics of a partially wetted disk by examining the effect on the angular velocity of the fluid core with varying engagement and spacing ratios for two flow regimes.

The maximum pressure capacity of a hydraulic seal is one of the key features of a hydraulic seal which signifies the maximum operating pressure the seal can sustain before a stream of air forces its way through it. Therefore, it is highly desirable to develop the capability to accurately predict the maximum operating pressure of hydraulic seals to inhibit any airflow through the seal and thereby avoiding possible blow-out of the seal. From an engine perspective this is important as maintaining seal functionality ensures an efficient sealing system which prevents the oil from leaving the bearing chamber. In the limited published research relating to hydraulic seals, there exists a few design approaches based on analytical derivations. The limitations and assumptions used in these analytical approximation methods have not been fully explored.

An approach to evaluate the maximum pressure capacity of a hydraulic seal is subsequently introduced in this work. Building on previously published studies, this work presents results of a numerical study into the performance of a simplified 2D hydraulic seal geometry. Modelling the seal without an oil feed into the trough, the second part of the thesis reports a numerical CFD methodology based on an axisymmetric VoF method carried out on ANSYS-Fluent. Results are presented for a range of shaft speeds of 2000-8000 rpm for the high speed shaft and 1000-4000 rpm for the low speed shaft and varying axial fin positions within the trough. Analysis of the performance of hydraulic seals, as conducted in this work, is not new, but the adapted finer resolution and the methodology followed to determine the maximum possible pressure a seal can sustain is novel. Through this approach, a criteria for a

broken seal is developed in this research. As a part of this study, a parametric investigation was carried out to examine the effect of the seal geometry and shaft rotational speeds on the maximum pressure capability of the seal. The work also identified different flow regimes and patterns that exist in a hydraulic seal. The CFD data shows that the seal can withstand higher pressure at higher shaft speed with the characteristic following the expected linear relationship between differential pressure and shaft speed squared. The seal could withstand a higher differential pressure if the fin was closer to the housing on the high pressure side with this being attributed to the secondary air flow in the cavity. In this study, the available analytical correlation methods are collated and a comprehensive analysis of the reliability of these methods is provided. The average core velocity values obtained using different analytical approaches are compared and it is found that one where core angular velocity is proportional to the area averaged rotational velocities of the housing and fin was the best match to CFD data.

Building on the 2D modelling work, a full 3D model of the hydraulic seal is created including a jet-delivered continuous through-flow oil feed added to the seal on the Low Pressure (LP) side to examine the oil behaviour in the seal. The numerical simulations are based on a model representative of a hydraulic seal configuration investigated in an experimental study at the University of Nottingham. The CFD study shows the oil flow breaking up into droplets/ligaments followed by the oil film formed around the circumference of the trough using a Volume-of-Fluid method when an operational differential pressure is maintained across the seal. A quantitative evaluation of the

disturbance created on the surface by the jet, demonstrates that the greatest disturbance is caused at the point of impact and the oil film thickness is only impacted by a negligible variation of +/- 0.1mm downstream. The CFD prediction of the behaviour of oil in the trough is in agreement with experiments and the high quality CFD images of the jet impact behaviour compare reasonably well with experimental results. The CFD analysis on the jet penetration shows that the oil targeted into the trough mixes with the existing bulk oil reservoir in the seal and does not spray straight off the jet supply.

The thesis also includes an investigation into thermal effects including oil-related heat transfer in the modelled hydraulic seal. An approach has been developed and applied to characterize the heat transfer within a hydraulic seal. The results show that most of the cooler oil from the jet mixes with the oil column in the LP cavity leading to a temperature difference not too significant in the oil volumes in the two chambers. The temperature of the oil column in the HP chamber is only approximately 3 K higher than that of the oil volume in the LP chamber. A considerable amount of heat is removed from the trough walls. Comparison of the computed oil exit temperature from the CFD results obtained at the exit of the modelled domain shows fair agreement with the experimental measurements of the temperature obtained for the oil in the sump of the hydraulic seal arrangement.

This current work presents the development and application of a useful modelling approach applicable to intershaft hydraulic seals. The established methodology will facilitate improved future seal designs supporting future more efficient aeroengine designs. Of particular note is the 3D modelling study that allows 3D effects in the seal

to be quantified for the first time. A novel consistent approach was developed to define seal capacity in terms of leakage rate. A detailed understanding of the effect of geometry and other parameters on the maximum pressure capacity of the seal is added to knowledge. The thermal investigation of the flow within a hydraulic seal also represents the first CFD study on hydraulic seals introducing thermal effects.

Acknowledgements

This research was carried out at the Mechanical and Aerospace Systems Research Group (MAS) formerly known as Gas Turbine Transmissions Research Centre (G2TRC) within the Rolls-Royce University Technology Centre at the University of Nottingham. The first part of this PhD project was funded through Rolls-Royce and the second part of the research was funded through a University of Nottingham doctoral studentship.

Some of the work in this thesis was carried out as a part of the CORNERSTONE research programme. I thank Rolls-Royce plc and the EPSRC for the support under the Prosperity Partnership Grant \Cornerstone: Mechanical Engineering Science to Enable Aero Propulsion Futures, Grant Ref: EP/R004951/1. I'm deeply grateful for the generous financial support I received from the Researcher Academy at the University of Nottingham, the Student Advisory Committee within American Society of Mechanical Engineers (ASME) organization and especially, my research group. This allowed me the opportunity to attend the Turbo Expo 2022 conference in Rotterdam, the Netherlands and Turbo Expo 2023 in Boston, USA. The support I received was beyond just funding – it opened doors to invaluable experiences, broadening my horizons and allowing me to connect with peers from around the world.

First and foremost, I would like to express my deepest gratitude to my research supervisors, Prof. Kathy Johnson and Dr. Stephen Ambrose, for their invaluable

guidance, support, patience and mentoring throughout this journey. Their immense knowledge and passion for research have been a constant inspiration to me over the years. This thesis would not have been possible without their countless hours of insight, feedback, and encouragement. Feedback and suggestions received from Dr. Richard Jefferson-Loveday, my internal examiner during my first and second year review have also been very helpful in this work. Prof. Carol Eastwick has been very inspirational and supportive throughout my PhD journey.

I am very grateful for an incredible group of researchers at MAS who are extremely skilled and have been nothing but supportive. I have definitely benefitted from the experience and technical expertise of Dr. Sandeep Mouvnal, Dr. Kuldeep Singh, Dr. Loizos Christodoulou, Dr. Rajab Omar, Dr. Neville Rebelo, Dr. Dafne Gaviria Arcila, Dr. Arun Prabhakar, Dr. Martin Berthold, Dr. Colin Foord and Mike Walsh. They have generously provided their time and knowledge to enhance my work. Their insightful questions and perspective pushed me to dig deeper and have greatly strengthened my research skills and this final work.

To the past and present members of the MAS research group - your friendship and support along the way helped make the tough days bearable and the triumphs all the more sweet. I will cherish the fond memories of helpful discussions, late nights working side by side, and celebrations marking each milestone with my colleagues that have become lifelong friends, especially with Dr. Yuen-Ling Kong and Dr. Sunil Chadha through what started as conversations about work. I must also acknowledge the support

I have received from Thomas Gresham and William Lavie that allowed me to work from home during my thesis write-up period.

In addition, I must acknowledge my technical buyers at Rolls-Royce plc for enabling such fruitful collaborative projects and very thorough feedback provided on my publications. The UTC partnership doctoral conferences dramatically expanded the scope and impact of my graduate studies.

Finally, my completion of this degree could not have been accomplished without the unconditional love and patience of my family. To my parents who instilled me with curiosity and grit in the pursuit of knowledge and advancement. And especially my sister, Ruchinie, for being a steady pillar of support through all the ups and downs of my life. To my close friends Deepak Asokan, Jeniffer Vanlangenberg, thank you for all of your support, buoying me through setbacks and always lending a patient ear or motivation. To my best friend Simon, this would not have been easy without your constant support, thank you for always believing in me. This journey would not have been possible without all of you.

I thank the Almighty for making this journey a possibility.

Table of Contents

Abstract ..... **i**
Acknowledgements ..... **vii**
Table of Contents ..... **x**
List of Figures ..... **xiv**
List of Tables ..... **xxiii**
Nomenclature ..... **xxiv**
1 Introduction **1**
1.1 Background 1
1.2 Sealing in gas turbine engines 5
1.2.1 Internal air system 7
1.2.2 Sealing in the transmission system 9
1.2.3 Intershaft hydraulic seals 16
1.3 The challenge 24
1.4 Aim & Objectives 27
1.5 Thesis content and structure 30
1.6 List of Publications 34
2 Literature Review **36**
2.1 Flow dynamics of rotor-stator cavities 37
2.1.1 Boundary layers in rotating disk systems 40
2.1.2 Characterization of flow in rotor-stator cavities - The original dispute 42
2.1.3 Enclosed rotor-stator disk systems 48
2.2 Jet flow dynamics 63
2.2.1 Jet application in a hydraulic seal 63
2.2.2 Overview of liquid jet break-up 64
2.2.3 Jet break-up phenomenon 65
2.2.4 Primary jet break-up 69
2.2.5 Secondary break-up 80

2.3 Oil film break-up and the impact of droplets generated....89
2.3.1 Splashing....89
2.3.2 Edge separation....92
2.3.3 The impact of droplets on liquid films....94
2.4 Interface dynamics and behaviour....95
2.5 Non-isothermal flows....103
2.5.1 Heat transfer within flows in rotating disk systems....105
2.5.2 Oil related heat transfer....110
2.6 Flow within hydraulic seals....115
2.7 Summary....117
3 Development of the Numerical Framework....119
3.1 Introduction....119
3.2 Geometry generation....120
3.3 Numerical Grid....121
3.4 Numerical Modelling....122
3.4.1 Fundamental concepts of flow equations....122
3.4.2 Turbulence Modelling....126
3.4.3 Multiphase Flows....149
3.4.4 Discretization....155
3.4.5 Boundary conditions....165
3.5 Overview of the adopted modelling approach....166
3.5.1 Turbulence modelling....166
3.5.2 Multiphase modelling....172
3.5.3 Discretisation....174
3.6 Summary....175
4 Investigations into fully and partially wetted disk geometries with relevance to intershaft hydraulic seals....176
4.1 Investigation into a fully wetted disk rotating in a stationary housing....179
4.1.1 Numerical model formulation....182
4.2 Flow characteristics of fully wetted disks....190

4.3 Investigations into a partially wetted disk rotating in a stationary casing ..198
4.3.1 Nonflow regime 200
4.3.2 Through-flow regime 225
4.4 Summary 236
5 2D Modelling of Intershaft Hydraulic Seals: Numerical Investigation into Operation of Hydraulic Seals 239
5.1 Derivation of maximum pressure capacity of hydraulic seals 242
5.2 Overview of Analytical oil angular velocity prediction methods 244
5.3 Numerical modelling approach 247
5.3.1 Mesh 250
5.4 Numerical results of parametric study 253
5.4.1 Defining Maximum Pressure 254
5.4.2 Maximum seal pressure 257
5.4.3 Determination of average angular velocity 260
5.4.4 Core angular velocity 260
5.4.5 Effect of shaft speed and axial position of fin 262
5.4.6 Analysis of Extreme Fin Positions 268
5.4.7 Tangential velocity distribution between housing and fin 269
5.4.8 Comparison of Numerical Results and Analytical Predictions 271
5.4.9 Engine condition 277
5.5 Validation of numerical results 280
5.6 Summary 285
6 3D Modelling of Intershaft Hydraulic Seals with an Oil Feed 287
6.1 Experimental set-up and procedure 289
6.2 Numerical modelling approach 292
6.3 Mesh 295
6.4 Investigation into the impact of jet on the pool of oil in through 300
6.4.1 Jet behaviour 302
6.4.2 Flow field Analysis 314
6.4.3 Comparison against experimental results 316

6.5 Thermal effects: oil related heat transfer.....319
6.5.1 Numerical model formulation.....319
6.5.2 Numerical study and Validation.....322
6.6 Summary.....332
7 Conclusions and Future work.....334
7.1 Conclusions.....334
7.2 Contribution to knowledge.....341
7.3 Future work.....342
References.....344

List of Figures

Figure 1-1: The effect of the key components and different stages on the pressure and temperature profiles along the engine. 3

Figure 1-2: Major aero-engine sealing locations 6

Figure 1-3: Schematic of a section of the internal air system 9

Figure 1-4: The mechanical arrangement of a typical three-shaft gas turbine engine. 10

Figure 1-5: Basic full flow type recirculatory oil system of an aero-engine 11

Figure 1-6: A cut away view of a Rolls-Royce Trent engine with marked locations of the bearing chambers. 12

Figure 1-7: Locations of the eight bearings in a Rolls-Royce Trent 1000 engine 13

Figure 1-8: Bearing chamber labyrinth seals 15

Figure 1-9: Aero-engine seal types 18

Figure 1-10: Hydraulic seal arrangement in a bearing chamber. 20

Figure 2-1: Flow phenomena associated with intershaft hydraulic seals 37

Figure 2-2: Typical rotor-stator disk system 39

Figure 2-3: Velocity profiles demonstrating characteristics of the flow in a rotor-stator cavity 44

Figure 2-4: The experimental configuration used in the experiment by Dijkstra & van Heijst 47

Figure 2-5: Typical flow characteristics of Batchelor flow model 49

Figure 2-6: Regions of flow for an enclosed rotor-stator disk space identified by Daily and Nece 50

Figure 2-7: The test apparatus used by Sirivat.....55

Figure 2-8: Flow structure visualised from above the stator in the experiment by Séverac et al.....61

Figure 2-9: Simple illustration of a jet exiting a nozzle.....65

Figure 2-10: Diagram illustrating the break-up regimes for a jet exiting a nozzle.....70

Figure 2-11: Primary breakup regimes 71

Figure 2-12: Jet stability curve illustrating break-up regimes 74

Figure 2-13: The secondary break-up morphology illustrating the regimes.....83

Figure 2-14: Illustration of the splashing mechanism.....90

Figure 2-15: Film separation phenomenon following a sharp edge. 93

Figure 2-16: Deformation of droplets in a shear-driven flow.....95

Figure 2-17: (a) Free surface construction in VoF; (b) Simple line interface construction (SLIC); (c) Piecewise linear interface construction (PLIC) 101

Figure 3-1: The effect of Reynolds number on the flow 128

Figure 3-2: Energy cascade diagram.....130

Figure 3-3: Hierarchical structure of turbulence modelling 130

Figure 3-4: Energy spectrum of turbulence 133

Figure 3-5: Typical velocity profile for a turbulent boundary layer 145

Figure 3-6: Near wall treatment depending on mesh type 148

Figure 3-7: Vertex-centred control volume 156

Figure 3-8: Types of CFD solvers 164

Figure 4-1: The experimental set-up used by Daily and Nece 181

Figure 4-2: Typical tangential velocity profiles 182

Figure 4-3: Geometry investigated in the CFD study modelling a fully wetted rotating disk 184

Figure 4-4: Comparison of meshes tested along a line at r/a = 0.765 in the fully wetted disk CFD investigation 187

Figure 4-5: Comparison of average swirl velocity data between meshes used 187

Figure 4-6: Truncated view of Mesh 2 – 0.25 mm element sized mesh 188

Figure 4-7: Axial profile of tangential velocity at r/a = 0.983 when $Re\Omega$ = 4.4 x 10^6 for s/a = 0.0255 189

Figure 4-8: Axial profile of tangential velocity at $Re\Omega$ = 4.4 x 10^6 for s/a = 0.0255 and r/a = 0.765 191

Figure 4-9: Radial velocity profile axially obtained at $Re\Omega$ = 4.4 x 10^6 for s/a = 0.0255 and r/a = 0.765 195

Figure 4-10: In-plane non-dimensionalised velocity vectors coloured by velocity for the secondary flow at $Re\Omega$ = 4.4 x 10^6 and s/a = 0.0255 196

Figure 4-11: Schematic of the experimental apparatus used in the study by Ketola and McGrew 199

Figure 4-12: Geometry investigated in the CFD study modelling a partially wetted rotating disk 201

Figure 4-13: Boundary conditions modelled in the CFD model for the partially wetted disk case 203

Figure 4-14: Comparison of meshes investigated monitoring the profiles of tangential velocity along a line through the liquid r/a = 0.862 207

Figure 4-15: Solution for the case with X = 0.374 208

Figure 4-16: Contours of water volume fraction for the non-flow case 210

Figure 4-17: Normalised in-plane velocity vectors for the non-flow case around the interface 211

Figure 4-18: Streamlines in the axial gap between the stationary and rotating disks for the non-flow case around the interface 212

Figure 4-19 : Streamline patterns plotted for the water phase in the axial gap between the stationary and rotating disks 214

Figure 4-20: The axial profiles of non-dimensionalised tangential velocity 216

Figure 4-21: The axial profiles of non-dimensionalised radial velocity plotted at various engagement ratios 218

Figure 4-22: The axial profiles of non-dimensionalised tangential velocity 219

Figure 4-23: The axial profiles of non-dimensionalised radial velocity 221

Figure 4-24: Normalized pressure data for s/a = 0.1 and engagement ratios 223

Figure 4-25: Effect of engagement ratio on velocity ratio for non-flow regime 224

Figure 4-26: Geometry used in the CFD study with model boundary conditions 227

Figure 4-27: Effect of engagement ratio on velocity ratio for flow cases 229

Figure 4-28: Contours of volume fraction of water for the CFD case with $Q = 1.945$ x 10^{-4} m^3/s and $X = 0.312$ 231

Figure 4-29: Contours of static pressure in the cavity between the stationary and rotating disks for the CFD case with $Q = 1.945$ x 10^{-4} m^3/s and $X = 0.312$.....232

Figure 4-30: The axial profiles of non-dimensionalised tangential velocity 233

Figure 4-31: The axial profiles of non-dimensionalised radial velocity.....235

Figure 5-1: Nomenclature for maximum pressure derivation of a hydraulic seal 242

Figure 5-2: Mesh used in the CFD study with the model boundary conditions 248

Figure 5-3: Locations of lines used to obtain tangential velocity profiles, analyze the flow domain and nomenclature used to define area 251

Figure 5-4: Comparison of tangential velocity profiles along line 1 252

Figure 5-5: Comparison of average core tangential velocity data between meshes investigated.....253

Figure 5-6: Comparison of oil volume fraction contours for numerically calculated pressures of the hydraulic seal when ΩH = 6000 rpm and ΩF = 3000 rpm 255

Figure 5-7: Oil volume fraction contours for numerically calculated pressures of the hydraulic seal at ΔP_{max} = 2.29 bar when ΩH = 6000 rpm and ΩF = 3000 rpm 255

Figure 5-8: Comparison of oil volume fraction contours for numerically calculated pressures of a failed hydraulic seal when ΩH = 6000 rpm and ΩF = 3000 rpm 256

Figure 5-9: Air leakage data of the seal when ΩH = 6000 rpm and ΩF = 3000 rpm 258

Figure 5-10: Air leakage data of the seal when ΩH = 4000 rpm and ΩF = 2000 rpm 259

Figure 5-11: Average oil angular velocities computed along line 1, line 2 and line 3 at axial fin positions of (a) 0.25; (b) 0.5; and (c) 0.75.....261

Figure 5-12: Maximum pressure capacity of the seal at three different fin positions263

Figure 5-13: Effect of shaft rotational speeds on the maximum pressure capacity of the seal 264

Figure 5-14: Contours of oil volume fraction at ΩH = 6000 rpm and ΩF = 3000 rpm for an operating seal pressure of 2.07 bar.....265

Figure 5-15: Truncated view of normalised in-plane velocity vectors at ΩH = 6000 rpm and ΩF = 3000 rpm for an operating seal pressure of 2.07 bar 267

Figure 5-16: Effect of axial displacement of fin on sealing capacity when ΩH = 8000 rpm.....269

Figure 5-17: Tangential velocity profile along line 1 and line 2 in the LP chamber at maximum pressure capacity when ΩH = 6000 rpm and ΩF = 3000 rpm...270

Figure 5-18: Comparison of analytically estimated seal capacity against numerically computed seal capacity 273

Figure 5-19: Geometrical domain considered for the approximation of bulk Ωoil through area based factor methods 274

Figure 5-20: Comparison of oil volume fraction contours for numerically calculated pressures of the hydraulic seal between 4 to 4.2 bar 278

Figure 5-21: Air leakage data of the seal for the engine condition case when ΩH = 10000 rpm and ΩF = 1780 rpm 279

Figure 5-22: Maximum pressure capacity results of the seal for all shaft speeds considered in the main study 280

Figure 5-23: Comparison of numerically computed seal capacity against experimental data, literature and analytically computed seal capacity at s/wH = 0.5.....281

Figure 5-24: Normalised in-plane velocity vectors at ΩH = 6000 rpm and ΩF = 3000 rpm for an operating seal pressure of 3.34 bar at s/wH = 0.05. 283

Figure 6-1: Oil-based inter-shaft seal main components 289

Figure 6-2: Comparison of meshes investigated for the single phase model in this study 296

Figure 6-3: Isometric view of poly-hexcore mesh used in the CFD study. 297

Figure 6-4: Cross-sectional xy view of the mesh used in the CFD study with the model boundary conditions.....298

Figure 6-5: Region of local refinement around the nozzle and oil path 299

Figure 6-6: Contours of oil volume fraction at ΩH = 4000 rpm and ΩF = 2000 rpm for a seal with an oil feed rate of 1.62 l/min and an operating pressure of 0.2 bar when fin is positioned at s/wH = 0.5 301

Figure 6-7: CFD images of jet behaviour before the jet impinges on the oil pool captured during the study at various time intervals.. 303

Figure 6-8: CFD images of jet behaviour after impingement illustrating the impact on the oil pool at various time intervals.....304

Figure 6-9: Comparison of jet behaviour illustrating two orthogonal views of the oil jet images captured during the experiment 305

Figure 6-10: Oil jet instability likely caused by a start-up feature captured around 0.294 s illustrated on a cross- sectional view of the nozzle 306

Figure 6-11: Angular locations investigated to obtain tangential velocity profiles plotted on contours of iso-surface of oil volume fraction, $\alpha i, VF = 0.5$ 307

Figure 6-12: Tangential velocity profiles along angular co-ordinate iso-clips at intersection between oil column and angular locations 308

Figure 6-13: Angular locations of the trough relative to nozzle placement for measurement of oil pool thickness.....309

Figure 6-14: The impact of jet on surface of oil volume in the trough plotted on contours of iso-surface of oil volume fraction, $\alpha i, VF = 0.5$ 310

Figure 6-15: Contours of iso-surface of oil volume fraction, $\alpha i, VF = 0.5$ 311

Figure 6-16: Comparison of oil distribution showing point of jet impact on the trough and variation of oil height around the trough 312

Figure 6-17: Pathlines coloured by the x-co-ordinate in the streamwise direction plotted from the oil inlet in the fully developed solution.....313

Figure 6-18: Normalised in-plane velocity vectors of the flow field highlighting regions of recirculation zones plotted in midplane slice at $\theta 2.$ 315

Figure 6-19: The view visible through the viewing tube in the experiments 316

Figure 6-20: Oil Shedding from the edge of the trough 318

Figure 6-21: Front view of the hydraulic seal with contours of oil volume fraction displaying oil shedding behaviour 319

Figure 6-22: Illustration of oil feed penetration at ΩH = 10000 rpm and ΩF = 1780 rpm for oil feed rate of 1.1 l/min and an operating pressure of 0.2 bar with fin positioned at s/wH = 0.5. 325

Figure 6-23: Normalised in-plane velocity vectors within the oil reservoir when there is an oil feed with a rate of 1.1 l/min and an operating pressure 0.2 bar 326

Figure 6-24: Contours of static temperature across the seal for an oil feed rate of 1.1 l/min and an operating pressure of 0.2 bar.....327

Figure 6-25: Comparison of temperature profiles for experimental/numerical tests when shaft rotational speeds = 10000rpm, 1780rpm; seal operational pressure = 2 bar; oil feed rate = 1.1 l/min 328

Figure 6-26: The locations of temperature measurements in experimental arrangement and CFD study 329

Figure 6-27: Radial temperature variation of the ejected oil film from the spill over point to the CFD outlet boundary 331

List of Tables

Table 2-1: Jet break-up characterization based on liquid and ambient properties.....73

Table 2-2: Modes of secondary break-up varying with transitional We for Newtonian drops when Oh < 0.1.....85

Table 2-3: Depiction of droplet impact surface classified by relative film thickness .91

Table 4-1: The Main geometric parameters of fully wetted disk CFD case.....183

Table 4-2: Size of meshes investigated for mesh sensitivity study 186

Table 4-3: The principal geometric parameters used in partially wetted disk study .201

Table 4-4: Principal modelling features of the CFD model of the partially wetted disk case.....204

Table 4-5: Mesh sizing of the CFD case modelling partially wetted disk.....206

Table 4-6: Principal modelling features of the CFD model of the partially wetted disk case.....228

Table 5-1: Properties of oil used in the seal.....247

Table 5-2: Size of meshes investigated for mesh sensitivity study 251

Table 6-1: Recorded test conditions in the experiment used for CFD validation.....291

Table 6-2: Properties of oil used in the seal used in the CFD study and experimental investigation.....293

Table 6-3: Sizes of meshes investigated for mesh sensitivity study.....295

Nomenclature

a	Radius of the rotating disk (m)
a_1	Radius of the shaft (m)
a_i	Linearized coefficient for ϕ
a_j	Linearized coefficient for ϕ_j
A	Surface area (m^2)
A_{cell}	Total cell area (m^2)
A_f	Vector representing the area of f (m^2)
A_F	Area of fin (m^2)
A_H	Area of housing (m^2)
A_{liq}	Area of the liquid phase (m^2)
b	Thickness of rotating disk (m)
$B_{thermal}$	Thermal Rossby number
c	Radial clearance between rotating disk and end stationary wall (m)
C_μ	Default model constant used in the k-epsilon model = 0.09
$C_{1\epsilon}$	Default model constant used in the k-epsilon model = 1.44
$C_{2\epsilon}$	Default model constant used in the k-epsilon model = 1.92
C_D	Discharge coefficient
C_m	Moment coefficient
C_p	specific heat at constant pressure (J/kgK)

C_P	Pressure coefficient
C_v	Specific heat at constant volume (J/kgK)
C_w	Flowrate coefficient
d	Diameter (m)
d_0	Droplet diameter (m)
d_{cro}	Cross stream diameter (m)
d_j	Jet diameter (m)
$\bar{d}$	Average diameter (m)
D_h	Hydraulic diameter = $\frac{4A}{\varphi}$ (m)
D_ω	Damped cross-diffusion derivative term in the SST $k-\omega$ model
${D_\omega}^+$	Positive part of the cross-diffusion derivative term in the SST $k-\omega$ model
E	Internal energy (J)
$E(\kappa)$	Energy spectrum function (m^3/s^2)
Ek	Ekman number
F_1	Blending function 1 in the SST $k-\omega$ model
F_2	Blending function 2 in the SST $k-\omega$ model
Fr	Froude number
g	Gas quantities
$g(\kappa l)$	Undetermined function used to compute spectral energy
g_i	The gravity component in the ith direction (m/s^2)
G	Aspect ratio of the rotor-stator cavity

G_b	Production of turbulence kinetic energy due to buoyancy in the $k-\varepsilon$ model
G_k	Production of turbulence kinetic energy due to mean velocity gradients in the $k-\varepsilon$ model
$\overline{G_k}$	generation of turbulence kinetic energy due to mean velocity gradients in the SST $k-\omega$ model
G_ω	Production of ω in the $k-\omega$ model
h^*	Non-dimensional oil pool depth
h_{ext}	External heat transfer coefficient (W/m^2K)
h_{of}	Oil film thickness (m)
h_T	Convective heat transfer coefficient (W/m^2K)
H^*	Relative oil film thickness
i	Each value from the population
k	Kinetic energy of eddies (J/kg)
k_f	Thermal conductivity $(W/m\,K)$
K	Velocity ratio
K_m	Individual control volume
l	Length of a large eddy (m)
l_B	Break-up length (m)
l_0	Integral length scale
L	Characteristic length (m)
M	Non-overlapping control volumes
M_{net}	Net mass exchange between the phases present (kg)

Ma	Mach number
Ma_t	Turbulent Mach number
n	Previous time-step (s)
$\vec{n}$	Unit vector perpendicular to the boundary
n_s	Spread parameter
$n+1$	Current time step (s)
N	Number of faces in the control volume geometry
Nu_r	Local Nusselt number
$\overline{Nu_r}$	Mean Nusselt number
$\overline{Nu_{r,d}}$	Mean Nusselt number of free disk
Oh	Ohnesorge number
p	Static pressure (Pa)
p_a	Wall static pressure at the disk tip radius (Pa)
p_{inlet}	Static pressure at the inlet (Pa)
p_{outlet}	Static pressure at the outlet (Pa)
p_r	Wall static pressure at local disk radius r (Pa)
ΔP	Pressure capacity of a hydraulic seal (Pa)
ΔP_{max}	Maximum pressure capacity (Pa)
$\Delta P_{max_{BL}}$	Maximum pressure capacity of the baseline case (Pa)
Pr	Prandtl number
Pr_F	Fluid Prandtl number

Pr_{turb}	Turbulent Prandtl number = $Pr_{turb} = \frac{\varepsilon_M}{\varepsilon_H}$
$\dot{q}$	Heat flux (W/m^2)
$\dot{q}_w$	Heat flux to/from the wall (W/m^2)
Q	Volumetric Flowrate (m^3/s)
r	Local radius of the disk (m) / radial co-ordinate
r_d	Vector displacement between the centroids of upstream cell and the face f
r_j	Jet radius (m)
Δr	radii difference between the outer and inner radius of the cavity (m)
R	Radial location of the interface (m)
R_A	Radius of the housing protruding from the parallel edge (m)
R_{A_1}	Liquid level in the HP chamber of a hydraulic seal (m)
R_B	Radius to the spill-over point (m)
R_{B_1}	Liquid level in the LP chamber of a hydraulic seal (m)
R_c	Oil film curvature
R_F	Radius of the fin (m)
R_H	Radius of the housing (m)
R_i	Inner radius of a cavity (m)
R_I	Radius of the shaft in a hydraulic seal (m)
R_k	Default model constant used in the $k-\omega$ model
R_m	Curvature parameter used to specify a cavity $= \frac{R_i + R_o}{R_o - R_i}$
R_o	Outer radius of a cavity (m)

$R_{overspill}$	Radius at the overspill point (m)
R_w	Specific gas constant (J/kgK)
R_β	Default model constant used in the $k-\omega$ model
R_ω	Default model constant used in the $k-\omega$ model
Re	Reynolds number
Re_A	Air flow Reynolds number
Re_{OF}	Oil film flow Reynolds number
Re_h	Reynolds number based on the height of the cavity
Re_Ω	Circumferential Reynolds number
Re_δ	Local Reynolds number based on the local radius of the disk
$Re_{\delta,c}$	Critical transition Reynolds number based on the local radius of the disk
Ra	Rayleigh number
Ro	Rossby number
s	Axial clearance between rotating disk/housing and end stationary wall/fin (m)
S_{CV}	Control volume surface
S_h	Source term for heat generation
S_{ji}	Mean strain rate tensor
S_k	User defined term used in the $k-\varepsilon$ model
S_ε	Strain magnitude
S_{α_i}	Source term in Equation (3-59)
S_ϵ	User defined term used in the $k-\varepsilon$ model
S_ϕ	Source term defined in the FVM model equations

S_ω	User defined term used in the $k-\ \omega$ model
t_L	Large eddy turn over time (s)
t_η	Kolmogorov time scale (s)
Δt	Time step (s)
T	Temperature (K)
T_a	Temperature of the ambient environment (K)
T_{ext}	External heat sink temperature (K)
T_f	Temperature of the fluid (K)
T_F	Temperature of the film flow (K)
${T_F}^+$	Non-dimensional temperature of the oil film
T_0	Initiation time (s)
T_{tot}	Total break-up time (s)
T_w	Wall temperature (K)
T_1	Temperature of the rotor in stator-rotor cavity (K)
T_2	Temperature of the stator in stator-rotor cavity (K)
Ta	Taylor number
u	Velocity in *x* direction (m/s)
u^*	Non-dimensional friction velocity
u^+	Velocity normalised by Reynolds number
U	Velocity magnitude (m/s)
U'	Fluctuating velocity component (m/s)
$\overline{U}$	Mean flow velocity (m/s)

U_j	Jet velocity (m/s)
U_m	Value of velocity stored in each control volume K_m (m/s)
U_r	Radial velocity (m/s)
U_x	Axial velocity (m/s)
U_φ	Tangential velocity (m/s)
U_τ	Shear velocity (m/s)
v	Velocity in y direction (m/s)
V	Volume (m^3)
$\dot{V}_F$	Volume flow rate through the face (m^3/s)
w	Velocity in z direction (m/s)
w_H	Housing width (m)
We	Weber number
We_c	Critical Weber number
We_g	Gas Weber number
We_L	Liquid Weber number
x	x co-ordinate
$\bar{x}$	Mean deviation
Δx	The distance between mesh elements (m)
X	Engagement ratio
X_A	Thickness of the housing base in the LP chamber (m)
X_B	Thickness of the housing base in the HP chamber (m)
X_F	Fin thickness (m)

X_T	Thickness of the housing protruding outwards at radius R_A (m)
y	Distance from the wall/ y co-ordinate
y^+	Distance from the wall normalised by Reynolds number
Y_d	Cumulative Mass Fraction
Y_k	Dissipation of turbulence kinetic energy k, due to turbulence
Y_M	Term accounting for compressibility effect
Y_ω	Dissipation of ω due to turbulence
z	Distance normal to the rotating disk/housing (m)
$\overline{\rho u'_i u'_i}$	Reynolds stress tensor

Greek Symbols

α	Flow angle (°)
α^*	Damping function related to turbulent viscosity at low Re numbers
α^*_∞	Default model constant used in the $k-\omega$ model = 1
α_0	Default model constant used in the $k-\omega$ model = 1/9
α_∞	Default model constant used in the $k-\omega$ model = 0.52
α_{axial}	Axial wavenumber
α_g	Volume fraction of gas phase
α_i	Volume fraction at the given time-step
$\alpha_{i,VF}$	Volume fraction
$\alpha_{i,F}$	Face value of the volume fraction of ith phase

$\alpha_i^{(n+1)}$	Volume fraction at the current time-step
α_l	Volume fraction of liquid phase
β_{fluid}	Angular velocity of fluid core
$\beta_{thermal}$	Fluid thermal expansion coefficient
β^*_∞	Default model constant used in the $k-\omega$ model = 0.09
β_i	Default model constant used in the $k-\omega$ model = 0.072
Γ	Effective diffusivity
λ	Wavelength
λ_{max}	Wavelength of the most unstable wave
σ	Standard deviation
σ_L	Surface tension (N/m)
σ_k	Default model constant used in the $k-\varepsilon$ model = 1.0
σ_ϵ	Default model constant used in the $k-\varepsilon$ model = 1.3
σ_ω	Turbulent Prandtl number for k; constant used in the $k-\omega$ model
ε	Dissipation rate (m^2/s^3)
ϵ	Rate of supply of energy
ϵ_H	Eddy diffusivity for heat
ϵ_M	Eddy diffusivity for momentum
η	Kolmogorov length scale (m)
$\theta_1, \theta_2\ and\ \theta_3$	Angular positions along the oil film (°)
ζ	Radius ratio

ζ^*	Default model constant used in the $k-\omega$ model = 1.5
κ	Wavenumber
κ_c	Karman constant
κ_{if}	Interface curvature
μ	Dynamic viscosity (Pa/s)
μ_t	Turbulent viscosity (Pa/s)
υ	Kinematic viscosity (m^2/s)
υ_F	Fluid kinematic viscosity (m^2/s)
υ_t	Turbulent kinematic viscosity (m^2/s)
ρ	Density (kg/m^3)
ρ_g	Density of gas phase (kg/m^3)
ρ_l	Density of liquid phase (kg/m^3)
ρ_ϵ	Rate of destruction of ε
τ	Shear stress (Pa)
φ	Circumference of the chamber (m)
ϕ	Quantity integrated over a control volume V
ϕ_f	Convective value of ϕ flowing through the face f
Ψ	Numerical domain
Ω	Rotation rate of the first disk (rad/s)
Ω_F	Fin rotational speed (rad/s)
Ω_H	Housing rotational speed (rad/s)
Ω_{oil}	Angular velocity of the oil core in the seal (rad/s)

Ω_1	Angular velocity of the rotating plane (rad/s)
ω	Specific rate of dissipation
γ_1	Angular velocity of the fluid as $z \to \infty$ (rad/s)
γ_2	Rotation rate of first disk (rad/s)
δ	Boundary layer thickness (m)

Abbreviations

2D	Two-Dimensional
3D	Three-Dimensional
AC	Alternating Current
AMG	Algebraic Multigrid
ASM	Algebraic Stress Model
3DTBL	Three-Dimensional Turbulent Boundary Layers
BEK	Bödewadt-Ekman- Kármán
CAD	Computer Aided Design
CFD	Computational Flow Dynamics
CFL	Courant-Friedrichs-Lewy
CSF	Continuous-Surface-Force
DC	Direct Current
DDB	Droplet Deformation and Breakup
DNS	Direct Numerical Simulation

FBH	Front Bearing Housing
FDM	Finite Difference Method
FEM	Finite Element Method
FSM	Fractional-Step Method
FVM	Finite Volume Method
HP	High Pressure
hp	Horsepower
HPC	High Performance Computing
IGB	Internal Gear Box
IP	Intermediate Pressure
ITS	Institute for Thermal Flow Machines
K-H	Kelvin-Helmholtz
KIT	Karlsruhe Institute of Technology
LDV	Laser Doppler velocimetry
LES	Large Eddy Simulation
LP	Low Pressure
LS	Level Set
MPS	Moving Particle Semi-implicit
NASA	National Aeronautics and Space Administration
NITA	Non-Iterative Time Advancement
NS	Navier-Stokes
PISO	Pressure-Implicit with Splitting of Operators

PSD	Power Spectrum Density
PDA	Phase-Doppler Anemometry
PSD	Power Spectrum Density
p-v	Pressure-velocity
RANS	Reynolds-averaged Navier-Stokes
RMSE	Root Mean Square Error
RSM	Reynolds Stress Model
R-T	Rayleigh-Taylor
SFC	Specific Fuel Consumption
SIMPLE	Semi-Implicit Method for Pressure-Linked Equations
SIMPLEC	Semi-Implicit Method for Pressure-Linked Equations-Consistent
SLIC	Simple Line Interface Construction
SST	Shear-Stress Transport
STF	Shaft Test Facility
TBH	Tail Bearing Housing
VoF	Volume-of-Fluid

CHAPTER 1

1 Introduction

1.1 Background

Extensive research, innovative designs and fabrication approaches have led to significant progress in aero-engine performance over the years but at the cost of increased complexity and there remains narrower margins for improvement in conventional turbomachines than previously. In the recent years, focus has widened from overall aircraft performance gains to include requirements of the passenger for security, safety, comfort, reliability, affordability due to the ever increasing demands of the traveling public and this has led the airlines to operate on narrower profit margins [1]. In such a climate, research leading to moderate improvements in efficiency, specific fuel consumption (SFC) and emissions make these goals highly viable.

However, the groundwork laid out for engine design, customer gains and research objectives in the 1970's by NASA, still remain valid in today's aerospace industry [2]. One of the elements identified in the NASA report is that of engine sealing and the work presented in this PhD thesis is a study on aero-engine intershaft hydraulic seals. Looking at more recent aviation regulations, Flightpath 2050: Europe's Vision for

Aviation published by the European Commission, covers the key assets and research challenges involved in air transport addressing quality, affordability, safety and environment related aspects and acknowledges the key challenges associated with the propulsion system [3]. This involves advanced design approaches, modelling and simulation validation, concurrent engineering, probability and risk analysis, noise reduction, emission reduction, and improved aircraft-engine integration. Also highlighted in this vision is the importance of operating at increased temperatures and pressures in the engine core in order to reach peak efficiencies throughout the flight. The engine design process, which was conventionally regarded as a combination of integrated component tasks, is now considered a multi-disciplinary approach which requires the aero-engine industry to optimize existing design approaches and explore advanced sub systems design technologies.

Many component and discipline interactions combined with inherited conflicts encountered along the engine design process, such as improved cycle efficiencies, led to manufacturing complexity, increased costs and weight restrictions creating a challenging engineering task. Overall engine performance is dictated by a combination of engine efficiency, reliability and safety design criteria which are function critical and as explained above, it depends heavily on the interaction of highly advanced subsystems. This becomes evident in Figure 1-1, which illustrates the variation in temperature and pressure profiles of a typical aero-engine due to the function of each principal component. This gives an indication as to how the temperatures and pressures are affected during each engine phase and what type of advances in individual

components and sub systems could be made by aero-engine designers to withstand these harsh temperatures for service lives of 20,000-hrs or more.

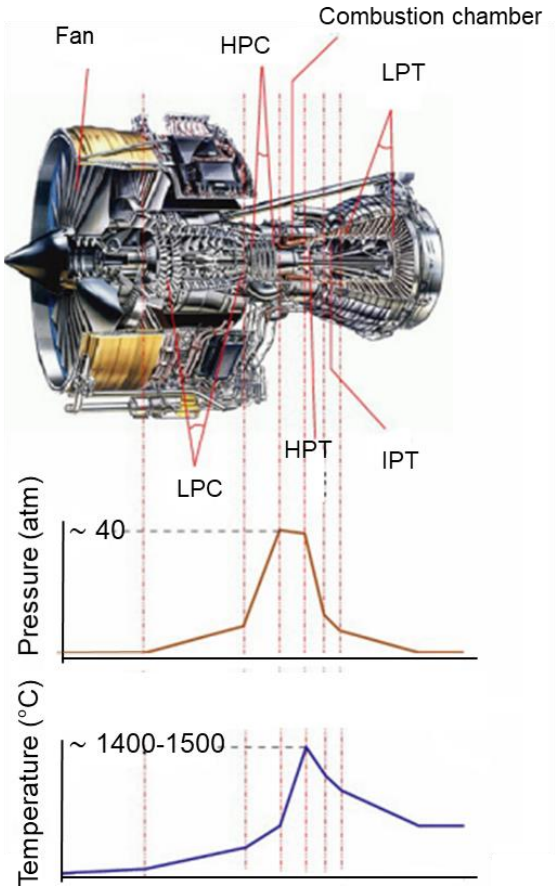


Figure 1-1: The effect of the key components and different stages on the pressure and temperature profiles along the engine. The image shows the intermediate pressure compressor (IPC), high pressure compressor (HPC), high pressure turbine (HPT), intermediate pressure turbine (IPT), and low pressure turbine (LPT) in a Rolls-Royce Trent 800 engine [4]

Additionally, ever more stringent noise and emission regulations have necessitated the need to identify and address future aero-engine requirements. To address these goals intended for high performance engines, significant improvements in each of the single

component segments are required. Previously, improved individual component performance could lead to increased profit margins. Conversely, without addressing matters related to each component, the concerns with the global engine industry at present could easily convert into decreased profit margins despite individual component gains.

With global and regional airlines becoming increasingly cost conscious, the industry needs to identify and develop engineering solutions to tackle engine performance related issues [2]. Continuous improvement is standard practice in the aerospace sector and it is identified that increased compressor pressure ratios, cycle temperatures and shaft speeds improve engine efficiency and reduce the engine weight as signified by cycle studies [1]. Such improvements depend heavily on the transmission system demanding more efficient and effective air and oil systems as transmission components have to endure higher temperatures and mechanical loads at decreased dimensions. This has resulted in investigating gains achievable in the transmission system absolutely imperative. As a result, advancing the existing sealing technology in the transmission system has been viewed as a vital supporting component technology. This is because it offers promising potential to meet requirements for SFC, thrust-to-weight ratio, operating costs, durability, emissions and environmental targets. The work presented in this thesis describes in detail a study investigating aero-engine intershaft seals.

This introductory chapter summarises the journey towards achieving sealing objectives established in the 1970's and introduces the focal point of research of this thesis.

1.2 Sealing in gas turbine engines

Sealing technologies are subjected to constant development and improvement. The progress is continuous. From a research point of view, labyrinth seals are presented as an expiring technology. On one hand, attempts are being made to find suitable efficient alternatives with better operational characteristics. On the other hand, novel studies are conducted to investigate the flow in advanced compliant seals and to develop improved designs which would result in more robust sealing technologies and lower fuel burn. It is a relentless battle between obsolete technologies, their shortcomings and ever growing requirements of the policy makers, engine manufacturers, airlines and customers. In view of the recent fuel crisis leading to fuel price fluctuations and rapid depletion of fossil fuel resources on Earth, efforts made to deliver insights into important physical mechanisms with the aim of improving the state of the art will play a pivotal role in addressing the growing demand for advanced sealing technologies.

Aero-engine seals currently being used can be categorised into six technologies – Face, Labyrinth, Brush, Film Riding, Outer Air/Blade tip and Intershaft. Each has its own range of applications depending on the environment it is being used in, factoring in conditions such as pressure ratios, operating temperatures and surface speed. Corresponding to the usage and environment, materials are chosen which include single elements such as carbon alone, or even alloys such as nickel or cobalt superalloys [4].

A key portion of the efficiency in aero-engines is generated through bypass fans and inline combustors. A modification in sealing parameters can lead to a change in the

dynamics of the entire engine which may very well not be desirable [5]. Therefore, considerations such as differences in thermal and mechanical characteristics and pressure gradients should be carefully reviewed by engine designers. Interface materials and coatings used in dominant types of seals in aero-engines, both static and dynamic, such as labyrinth, brush, face and mechanical seals ensure safe operation. Major sealing locations in an aero-engine identified by Bill and Ludwig [6] are schematically presented in Figure 1-2. They include shroud seals in the fan and compressor, compressor inter-stage and discharge seals known as labyrinth seals, combustor static seals, balance piston seals, turbine shroud seals and turbine rim cavity seals [6].

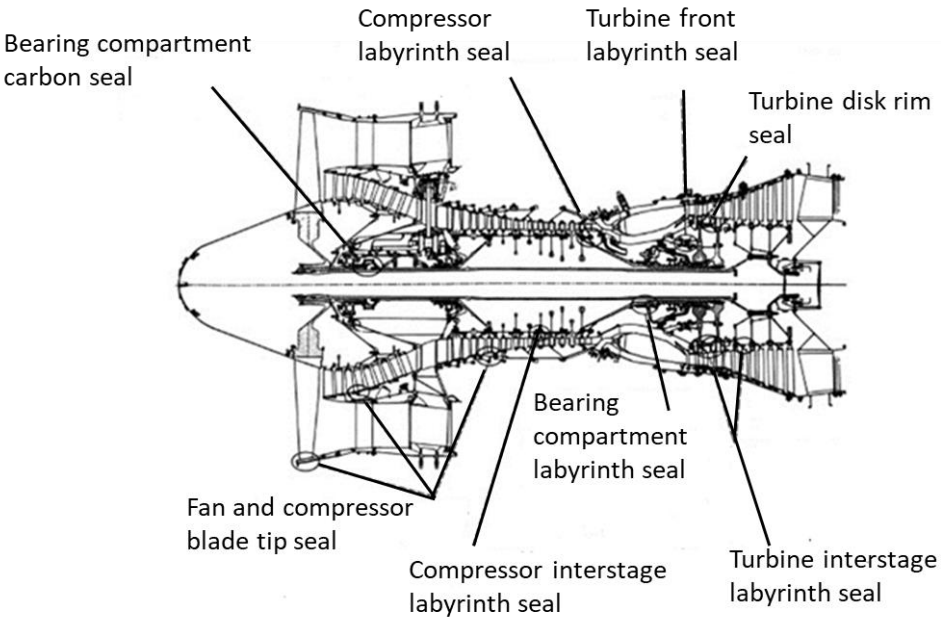


Figure 1-2: Major aero-engine sealing locations [6]

Typically, labyrinth, brush, leaf or carbon seals are used in the bearing compartments to prevent any leakage of oil out of the chambers. These all operate with a positive pressure and the compressor-bled air represents a parasitic loss for the engine. Labyrinth seals used in the compressor stages provide bearing thrust balance on the rear compressor hub, thereby reducing the pressure outside the bearing compartment. The air bled from one of the compression stages to create a positive pressure gradient across the labyrinth seal used in the early turbine stages is also used for cooling of blades and disks. Turbine rim seals limit ingress of the hot gas path flow into the disk cavities which house the rotating turbine disks, and regulate disk cavity purge flows as well as blade and disk cooling fluid flows. Labyrinth seals are also used as compressor interstage and discharge seals to prevent gas recirculation around the stator. Shroud seals are used in fan and compressor to control clearance which helps maintain compressor efficiency and provide protection against tolerance distortion.

1.2.1 Internal air system

The gas turbine is an internal combustion engine that uses air as the working fluid. The airflows that do not directly contribute to the generation of thrust is defined as the internal air system. The internal air system is an integral subsystem in modern gas turbines which performs several key functions to ensure a safe and efficient operation of the engine. The internal air system is responsible for the cooling of internal and accessory units, controlling the axial pressure loading on the bearings, isolating the oil system while preventing hot gas ingestion into the turbine disc cavities from the main

annulus, maintaining appropriate turbine blade tip clearances, delivery of air for ice protection and bearing chamber sealing.

In bearing chamber seals, oil is prevented from leaving the chamber by a positive pressure gradient across the seals. Due to the close correlation between the engine performance and interface clearances, reduced leakage achieved through efficient sealing is extremely desirable. This is one of the main functions of the internal air system and drives the research towards effective methods of controlling interface clearances. The range of application extends to maintaining a coolant flow supply, managing internal air flows and helping preserve the rotordynamic stability. Controlling clearances depends significantly on the types of seals used. In many cases, seals and their interfaces are sacrificial, enduring abrasion, friction, erosion, oxidation, foreign object damage and deposits in areas of high stress, temperatures, mechanical, aerodynamic and impact loadings [7]. Effective clearance control leads to a reduction in SFC and improved service life, but must account for large changes in thermal and centrifugal forces [5]. One of the other applications most relevant to the work presented in this thesis is the supply of airflow for bearing chamber sealing. This is discussed in detail in subsequent sections.

As the airflow passes through the compressor, its pressure and temperature are raised, increasing the amount of work done on the air. Therefore, the sealing air is bled from an early compressor stage, proportionate with each function it serves to reduce the parasitic loss to the engine. These functions may use up to 20% of the total engine core mass airflow [8]. A truncated segment of the internal air system focused in a section of

the high-pressure/intermediate pressure (HP-IP) region of a three shaft engine is highlighted in Figure 1-3. The regions shown in white represent the later stages of the HP compressor, combustor, HP turbine and IP turbine. The region with air delivered from the HP compressor is denoted by red. Areas where there is oil present are indicated by green.

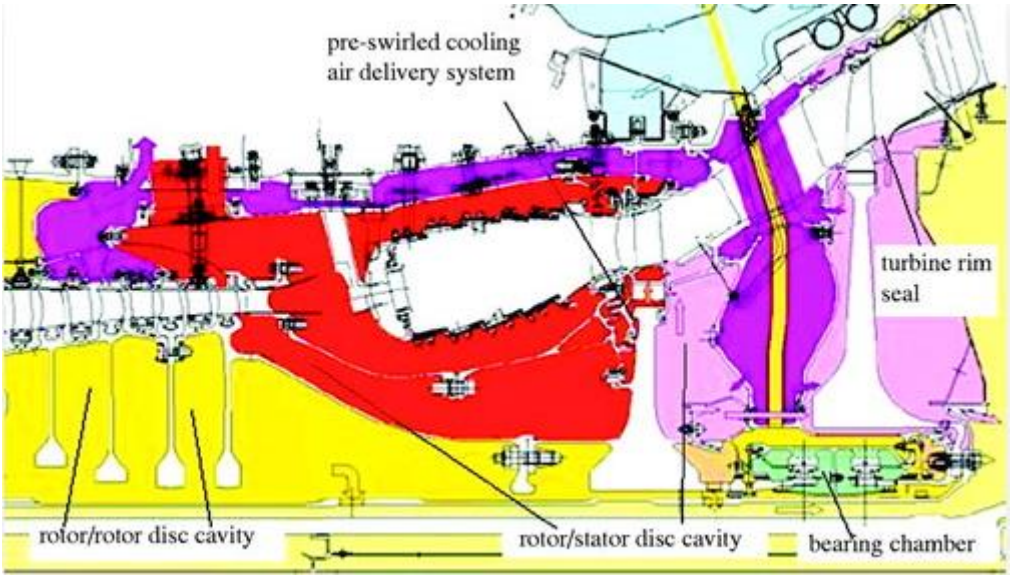


Figure 1-3: Schematic of a section of the internal air system, showing the HP and IP sections for a three shaft engine [8]

1.2.2 Sealing in the transmission system

Obviously the gas path in an aero-engine is extremely important as it is here that thrust is generated. However, an efficient and effective transmission system is also central to aero-engine operation. Aero-engines operate with either two- or three-shafts with large

civil engines usually being 3-shaft (high pressure, HP; intermediate pressure, IP; and low pressure, LP).

A schematic of the main components of a typical three shaft engine is presented in Figure 1-4. The aircraft transmission subsystem consists of shafts and gearboxes and is responsible for transmitting mechanical power and supporting the rotating components within the engine. Therefore, the transmission system is required to have high reliability during the entire product life cycle. These shafts are supported by bearings transmitting the loads to static elements. Current bearing technology is such that bearings require oil and the oil system is responsible for lubrication and cooling of the gears, bearings and splines in the transmission system.

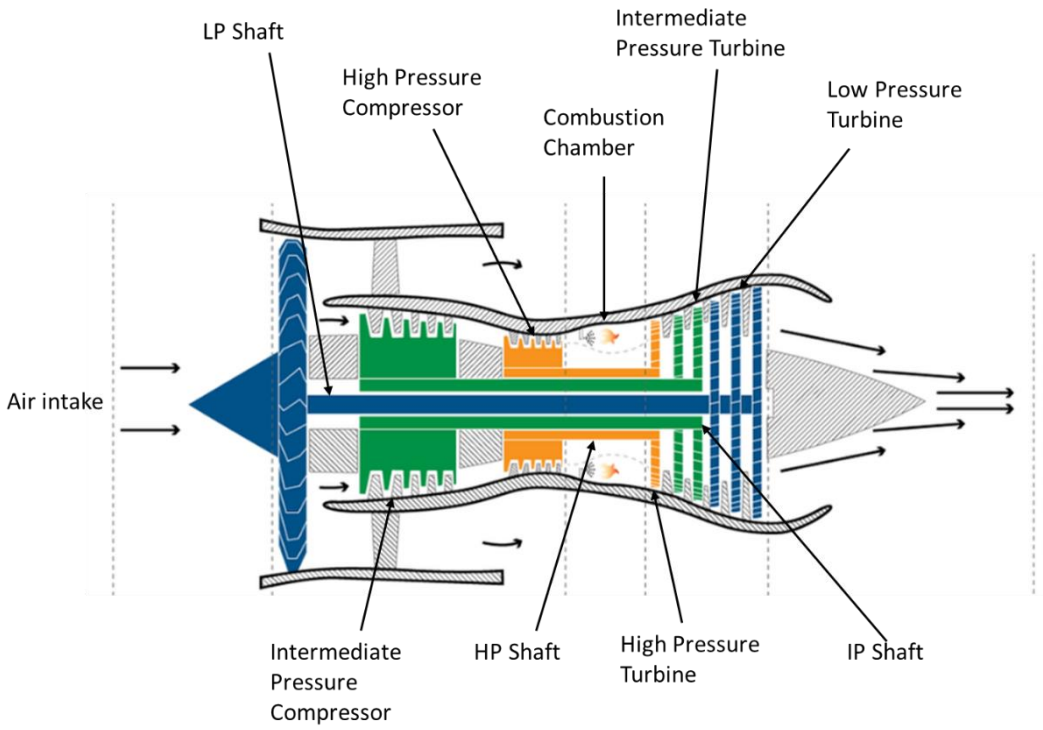


Figure 1-4: The mechanical arrangement of a typical three-shaft gas turbine engine. Image from [9]

In a gas turbine engine, a self-contained recirculatory oil system is used. The oil is distributed from the colder tank to the moving parts in the transmission system, static parts in the engine core and is then pumped back to the oil tank. A full flow type oil system for a 3-shaft civil aero-engine is schematically presented in Figure 1-5 which shows the basic components that comprise an engine oil system.

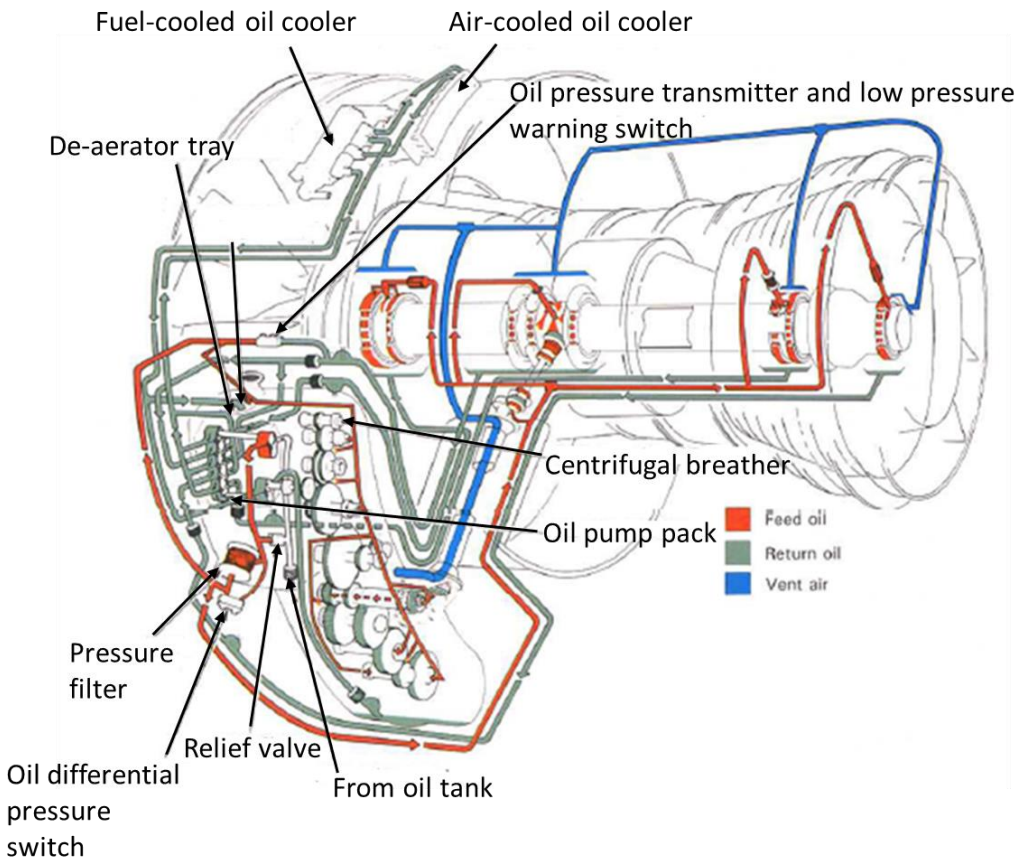


Figure 1-5: Basic full flow type recirculatory oil system of an aero-engine [10]

The oil that is used gets scavenged out is filtered and cooled for further re-use. As explained previously, the engine efficiency can be improved with higher operational temperatures. Hence, the pressure and temperature conditions of the oil are critical for

the engine operation. As the oil system plays a crucial role in heat management, it is important that the system is designed carefully so that failures such as oil fire, oil decomposition and coking can be prevented by avoiding unnecessary working of the oil. This can be done by inhibiting longer oil residing times during its recirculatory flow around the engine.

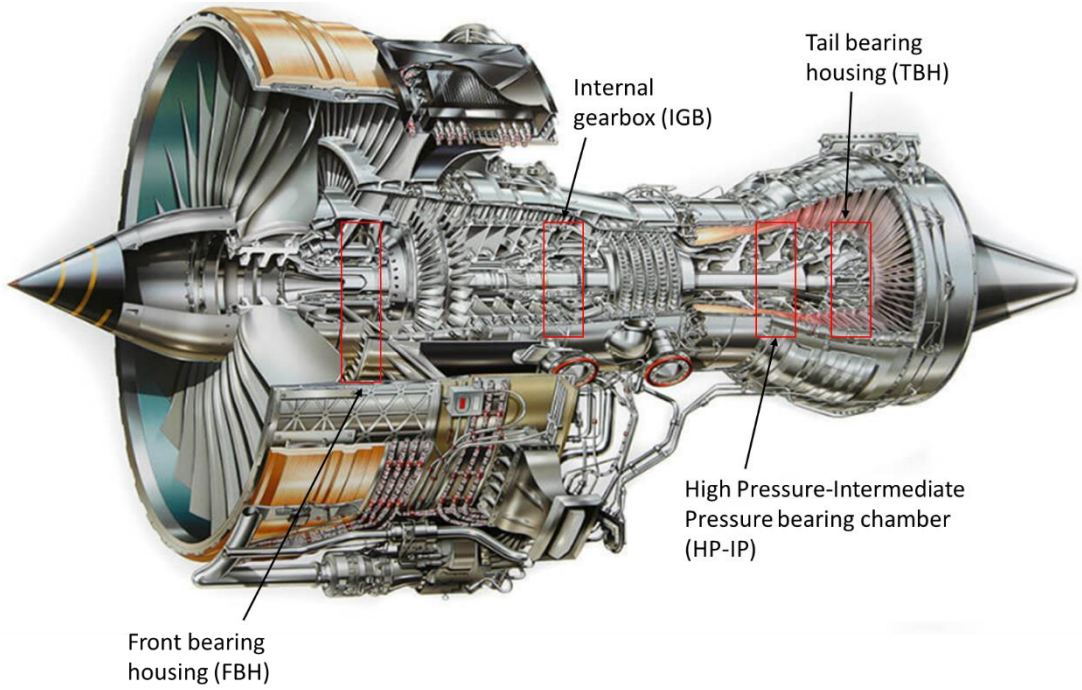


Figure 1-6: A cut away view of a Rolls-Royce Trent engine with marked locations of the bearing chambers. Image from [4]

It is also essential to ensure that the oil is prevented from entering into the gas path while effective lubrication and cooling of the bearings is maintained. The bearings are housed in bearing chambers, cylindrical enclosures that are typically sealed with airblown seals such as labyrinth seals creating a highly rotating complex two-phase

environment [11]. A modern three shaft engine may typically be supported by eight bearings with four bearing chambers as shown in Figure 1-6.

Figure 1-6 shows the front bearing housing (FBH); the internal gearbox (IGB); the high pressure-intermediate pressure (HP-IP) bearing chamber and the tail bearing housing (TBH). Of these the most demanding and the hottest are the chambers in the middle of the engine, particularly the HP-IP as it is closest to the combustion chamber. A more detailed view of the locations of the bearings in a civil three-shaft aero-engine is illustrated in Figure 1-7.

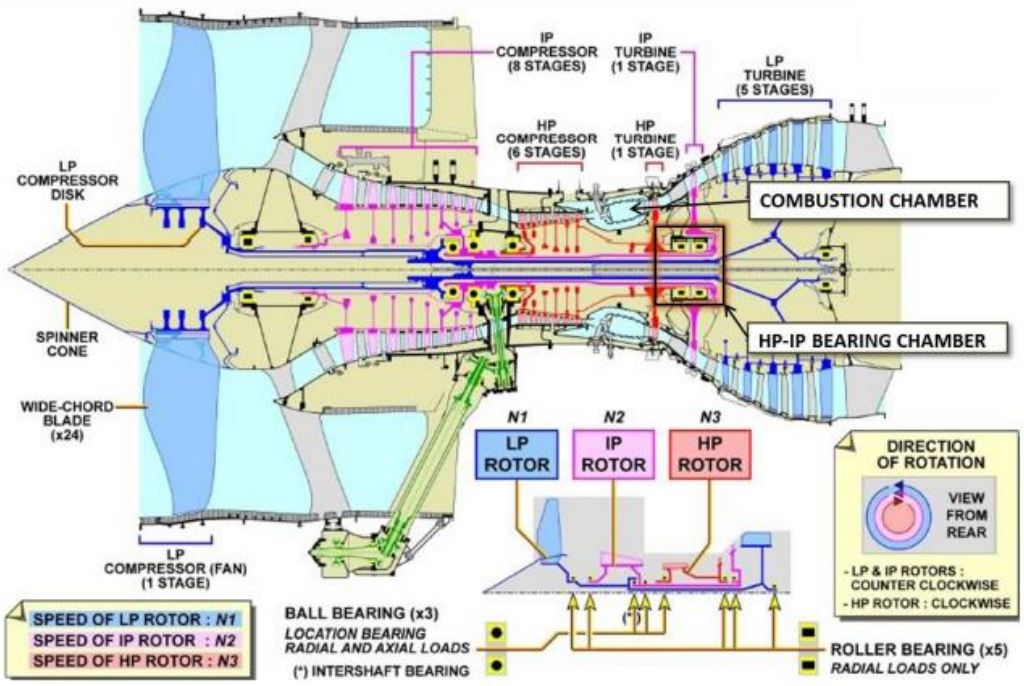


Figure 1-7: Locations of the eight bearings in a Rolls-Royce Trent 1000 engine [12]

Oil is prevented from leaving the chambers that surround the bearings by creating a positive pressure gradient across the seals provided which are known as air-blown seals.

Pressurized air taken from the compressor bleeds is supplied to labyrinth seals to seal the bearing chambers from hot surroundings.

Labyrinths are the most extensively and frequently used gas seals in aero-engines. Labyrinth seals are used to seal air and hot gas in the main gas path as well as to seal oil/air mixtures in bearing chambers by restricting the gas leakage into the bearing compartments [11].

Labyrinth seals are non-contact dynamic seals and in bearing chambers these seals are used in locations between static and rotating elements as illustrated in Figure 1-8. The air leaking through the seal precludes the oil from leaking out. In engines where the gas and oil temperatures are relatively low, a single labyrinth seal can be used to seal the oil/air mixtures. The positive pressure across the seal allows the entry of a relatively high air flow into the chambers, a feature of most clearance seals. The radial clearance between the fin and the static casing directly affects the leakage flow in a labyrinth structure and higher leakage flows affect the performance of the engine and results in an efficiency loss. Moreover, the seal clearance tends to increase over time due to radial and axial excursions on the rotating and stationary elements of the seals caused by large thermal gradients also leading to a significant power loss [13, 14].

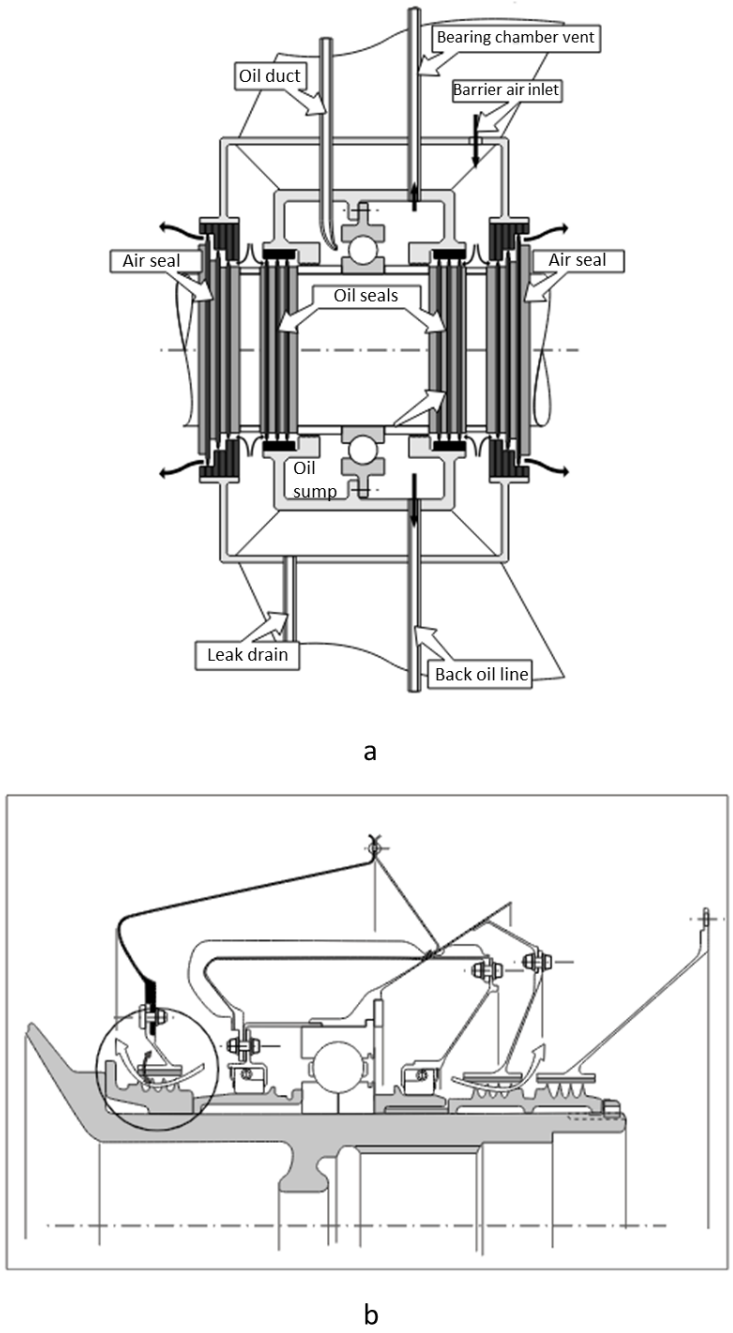


Figure 1-8: Bearing chamber labyrinth seals (a) schematic representation of a bearing chamber configuration with a multitude of seals (b) sectional view of the labyrinth seals used in a bearing chamber [15]

At low pressures, this reduction in efficiency due to seal leakage is not as prominent as at high pressures where the high leakage flows become substantial with a performance penalty. Apart from ensuring that adverse pressure gradients across the seal are avoided at all times to prevent high oil losses, another key drawback of labyrinth seals is that the associated higher leakages also necessitate equivalent larger ducting requirements that causes easier passage of airborne water and dirt into the bearing compartment which can have an undesirable effect on the operational life of the bearings within [16].

Better leakage properties, reduction in secondary coolant and parasitic flows, maintenance, component longevity are some of the elements related to sealing technology that are of utmost importance to engine performance. There remains a need for improved and detailed knowledge of flow phenomena and sealing technology, especially in bearing chambers.

1.2.3 Intershaft hydraulic seals

Within some bearing chambers there are locations where sealing is required between two rotating shafts. Intershaft seals are essential elements within bearing chambers, providing a seal between two differentially rotating shafts. They typically consist of one or more fins mounted on one shaft interacting with an oil reservoir formed by an oil feed into a trough on the other. There are different technological and performance challenges associated with these than with the air-blown seals. An intershaft seal can be used in the following instances:

- In an annular space between two co-axial shafts that co-rotate relative to each other, maintaining an axial fluid pressure differential across the seal.

- In an annular space between two co-axial shafts that counter-rotate relative to each other, such as gas turbine engine drive shafts, maintaining an axial air pressure differential across the seal.

- In shafts in a bearing chamber, typically maintaining a pressure between an air/oil mixture and air on either side.

At present intershaft seals in civil aero-engines are usually oil backed intershaft seals or hydraulic seals. An oil backed seal is similar to a labyrinth seal except that in place of an abradable element, the fins dip into an oil trough. The trough is empty when the engine is not in operation but fills, creating the seal at start up. A hydraulic seal consists of a single fin dipping into a trough as illustrated in Figure 1-9, where other seal types are also shown. Again, the trough is empty when the engine is not running but it fills and creates a seal during engine operation. While an oil backed seal can support airflow through, a hydraulic seal does not and can therefore withstand a differential pressure.

Hydraulic seals act as zero flow air seals that can support a larger pressure difference across the seal when used in rotating applications subjected to centrifugal forces. There has been some research conducted into formation, operation under steady conditions and breakdown of oil-backed and hydraulic seals. However, with scant published research available in the public domain, there is an acknowledged need for improved knowledge and this provides context for this PhD research.

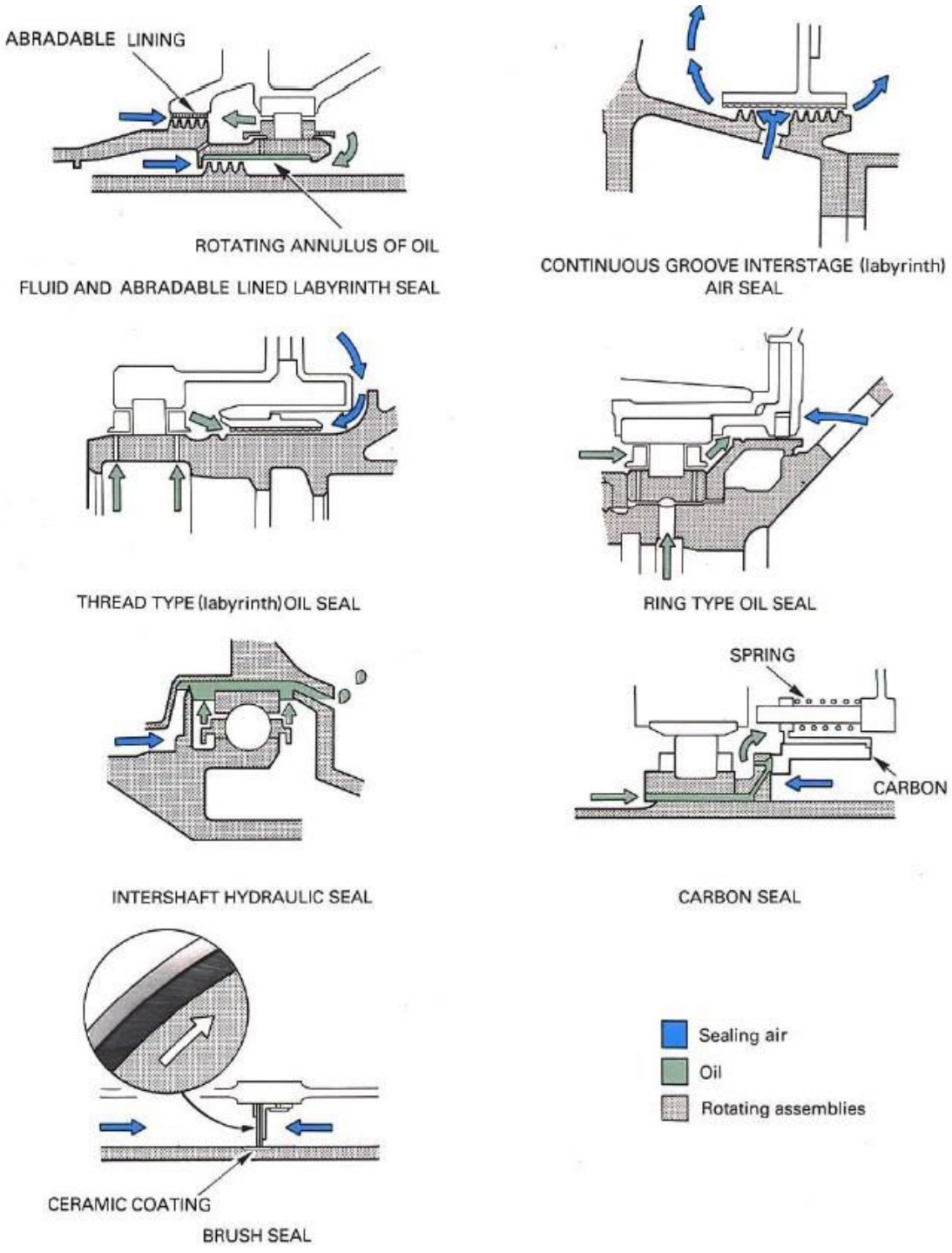


Figure 1-9: Aero-engine seal types [10]

Hydraulic seals are used where a sealing fluid exists; typically within bearing chambers or gearboxes. In bearing chambers, a hydraulic seal is located between co-rotating shafts and it can maintain a differential pressure between the air/oil mixture on either side. The seal is formed between a trough (also sometimes referred to as the housing) on the outer shaft and a fin on the inner shaft; the fin is submerged in an annulus of fluid as illustrated in Figure 1-10. The seal is empty when the engine is not in operation and the seal formation time will depend on the oil feed rate, shaft speed and engine operating conditions.

During engine operation, rotation is imparted to the fluid in the trough as it is centrifuged outwards by the outer shaft. As the fluid is subjected to centripetal forces due to the angular velocity of the rotating shafts, a radial pressure gradient across the inter-shaft cavity is created. This pressure difference imposed across the seal is maintained by a difference in height of the fluid in the two columns. This acts as an obstruction to air flow thus forming a zero flow seal. In contrast to oil backed seals, which can support an airflow through, large differential pressures can be accommodated by hydraulic seals: the differential air pressure either side of the seal is balanced by the differential radial pressure of the fluid on either side of the fin [7]. While the key motive behind the application of this type of seal is to provide a path for oil feed or scavenge route using a rotating pressure bulk head, they can also be used as debris traps. Although the latter poses the risk of blockage, these seals allow variable and/or interrupted oil flow through [17].

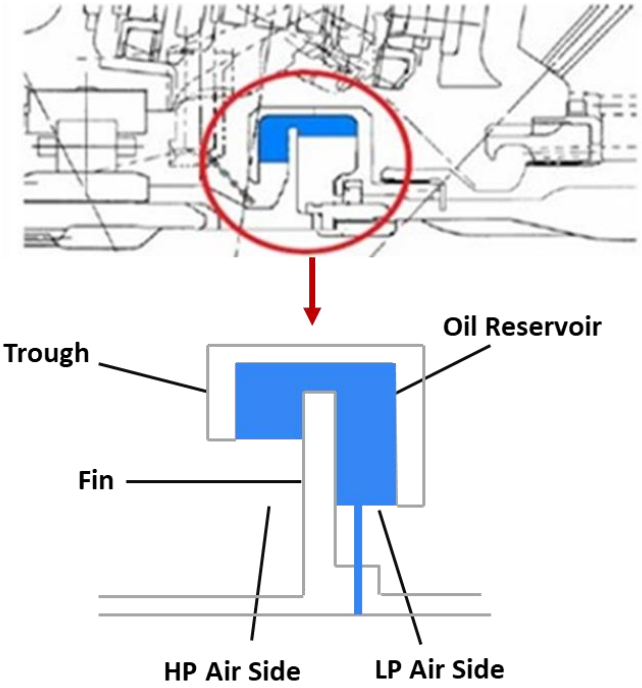


Figure 1-10: Hydraulic seal arrangement in a bearing chamber. Upper image from [7], lower schematic illustrating the main components

Hydraulic seals are also utilized in high pressure pumps, where the housing does not rotate, and thereby allowing vanes to be installed on the disk with the intent of increasing the circumferential velocity of the fluid, thus increased centrifugal forces. The seal diameter can be reduced due to its potential to seal larger pressure differences [18]. When used as an intershaft seal in a bearing chamber, where the outer wall is connected to high pressure, adequate swirl is provided by smooth walls due to the rotation of outer wall of the seal [19].

Although in principle hydraulic seals could be used between contra-rotating shafts, no examples can be found in literature to support this. According to Denecke et al. [19],

the application of hydraulic seals is restricted to co-rotating shafts. A reason for this could be that the velocity gradient through the oil in the trough would pass through zero and therefore gravity could locally become important whereas in the co-rotating situation centrifugal effects dominate. It is worth noting that most of successful testing experience with hydraulic seals involve co-rotating environments. It has been shown with results from previous limited testing on contra-rotating seals that their maximum pressure capacity is lower than that of co-rotating seals for the same trough angular velocities.

Hydraulic seals are well-known for their excellent sealing properties and are able to provide complete sealing with zero leakage over their operational range, these seals are relatively robust and insensitive to shaft swirl and misalignment. Proper sizing and design ensure efficient functionality of the seal at all positive and negative pressure differences preventing any gas leakage. They also have high tolerance to vibration and are subjected to low power loss [19]. However, one of the disadvantages is that if the applied pressure difference exceeds a critical value, the seal will fail completely. One of the significant attributes of a hydraulic seal is its maximum pressure capacity: this is the pressure difference the seal can sustain before air forces its way through the seal. The pressure difference imposed across the seal and the maximum or “blow-out” pressure vary significantly around an engine’s operating envelope.

In a hydraulic seal oil is supplied using a direct or indirect feed to initiate and maintain seal formation when the engine is in operation. A continuous oil supply should be sustained to remove the excessive heat generated through shearing associated with the

velocity gradients and minimize the potential for oil degradation [20]. Hendricks et al. [1] explain that seal failures are governed by axial and radial thermal expansions when the power consumption is maximum. Hence, a hydraulic seal should be carefully designed so that the oil feed into the seal is increased when used in a high temperature environment to minimize the potential for oil degradation and coking that can be caused by high wall temperatures [21]. It is also important to ensure oil in the recirculation zones remains below the critical temperature as the temperature of the fluid is increased as the power consumed by the seal is dissipated [19]. In a patented design, Bock [22] introduced a baffle to define a flow path to reduce the residence time within the seal in order to eliminate the above mentioned issues. The purpose of this design was to restrict the oil temperature from exceeding the maximum allowed so that the seal could be used in hotter regions of the engine.

Currently, labyrinth seals are extensively used to seal bearing chambers at locations between static and rotating elements [11]. However, as explained in Section 1.2.2, the seal clearance gradually enlarges over the operational time due to wear of the abradable lining caused by radial and axial deviations of the elements resulting in degraded sealing performance. On the contrary, the superior sealing characteristics of hydraulic seals restricts the entry of air flow into the cavities while sustaining large pressure differentials. Efficient sealing provided by hydraulic seals inhibit oil leakages into the internal parts of the engine. Failure to maintain an effective sealing system can potentially result in unrecovered oil loss from the bearing chamber. Depending on the architecture this could lead to a deterioration in cabin air quality or fire in the engine

core [23]. Therefore, hydraulic seals offer several attractive advantages over conventional seals for intershaft applications. Substituting labyrinth seals with alternate seal types also enables implementation of novel lubrication approaches that can eliminate vent lines removing the associated weight and expense penalties [19].

One of the main goals of this work is to investigate the flow phenomenon and dynamic effects within intershaft hydraulic seals and to propose improvements in the current modelling approaches. This project builds on previous work done on hydraulic seals and further develops existing design practices. Computational Fluid Dynamics (CFD) provides the means for addressing this goal. The investigations reported in this thesis develop CFD models of the fluid flow to capture the behaviour of transient and thermal effects in the cavity between two co-rotating shafts.

1.2.3.1 Principle of operation

The 3 primary components of a hydraulic seal are; a trough, a fin and an oil reservoir as illustrated in Figure 1-10. The Equilibrium of the opposing pressure and centrifugal force imposed on the volume of oil maintains the seal during engine operation. In this case, a difference in fluid height is created across a central body (fin) by the fluid of known density (oil) and the oil level that is outboard on the side of the seal is subjected to a lower pressure. The pressure difference caused by the difference in oil height known as the ‘pressure head’ is sustained in a similar manner as in a simple U-tube manometer [17].

1.2.3.2 Pressure Differential

The basic principle of the hydraulic seal operation can be thought of as a mechanism where gravitation is replaced by centrifugal force. The mathematical expression used to determine the maximum pressure capacity of a hydraulic seal stems from the fundamental equation for the steady state radial momentum equilibrium on an infinitesimal fluid as discussed in detail in Chapter 5. At very high rotational speeds of the housing and the fin, force of gravity can be neglected. However, gravity should be taken into account when the rotational speeds are low, hence the equation used to compute the maximum pressure capacity of a hydraulic seal will not be valid at all rotational speeds.

1.3 The challenge

Advancement of technologies related to the transmission and oil systems has trailed behind compared to the progress in the main gas flow path components such as compressors, combustors and turbines. It has been recognised that many of the critical issues associated with the development of a new engine followed by its introduction into service phase are due to main line transmission components. To address these demands, many initiatives have been taken in the recent past. Some of the approaches implemented focused on particular research areas of value [24]. Since then, a great deal of emphasis has been placed on the flow modelling of a bearing chamber and CFD predictions of the flow field across an air/oil seal. One such application is intershaft hydraulic seals.

Computational modelling of these elements is challenging as it involves highly rotational multiphase flow with complex geometry and transient effects. The capability to build a full model of a hydraulic seal is highly desirable but this presents a number of challenges due to the flow phenomena involved. With a multiphase flow model, it is difficult to model the fluid interaction and behaviour especially in different scenarios of a seal such as formation, steady state operation, blow-out and oil ejection. It is extremely appealing to develop one model to represent all the different scenarios with interchanging mass, momentum and heat transfer. However, this requires a comprehensive understanding of the two-phase flow effects in hydraulic seals which has not been completely achieved yet. At the start of the engine operation, cooler oil is injected into the seal to fill the seal. As a flow of oil comes through forming the seal, it reaches steady state conditions once the trough becomes full. At this point the oil exists in two columns withstanding a pressure difference. Once the trough becomes completely filled, the oil starts to splash back and shed off the edge of the trough as ligaments before eventually breaking up into droplets. This is because when a cooler oil feed is injected into a pool of hot oil in the trough, the impingement of cooler oil flow on the surface of the oil pool results in a transfer of momentum depending on the method and direction of injection. The fate of these oil droplets that either (i) splash back during the jet fill process or (ii) ejected from the non-fill side of the seal also involves complex flow physics due to their disposition and interaction with air outside the seal assembly. These droplets can be extremely small and ideally a CFD model should be capable of capturing these droplets.

Bubbles of gas/air that progress across the seal as the operating pressure increases and their interaction with the oil volume is potentially another element that must be taken into account in a hydraulic seal model. The oil/gas interface moves radially as the pressure increases and its behaviour cannot be pre-determined. The deformation of the interface is dictated by the rotational speeds of the shafts, the geometrical features of the seal and the properties of the oil. The various forms of existence of these fluids interchange mass and momentum and sometimes heat. For example, an impingement of a cooler droplet into a pool of hotter liquid will add mass by mixing and transfer of momentum into the pool which may result into a splash. Additionally, the impact of the jet impingement on the pool of oil in the seal is also an important phenomenon which dictates the performance of the seal. Therefore, the development of a universal model is challenging due to all these complex flow phenomena and interaction of phases associated with a hydraulic seal. Computational Fluid Dynamics (CFD) is an important research design tool used to investigate a number of flow phenomena that are not yet fully understood with hydraulic seals being one of them. CFD allows us to develop models to capture the behaviour of mass, momentum and heat transfer aspects in a hydraulic seal and this is extremely crucial in understanding the underlying flow physics and making informed design decisions.

There is limited published research relating to hydraulic seals, and the accuracy and reliability of the existing design approaches based on analytical derivations has not been fully explored. Most of the studies related to hydraulic seals have been carried out through experiments and numerical simulations, although much of the experimental

data has not been made available to the public. The numerical studies related to hydraulic seals have been mostly limited to two-dimensional and isothermal models. An experimental study conducted at the University of Nottingham investigating the performance of hydraulic seals established that a seal takes approximately 20 -50 s to form [25]. Despite having access to very powerful High Performance Computing (HPC) facilities, the detailed computational calculations of the formation and operation scenarios of a hydraulic seal simulating a minimum of physical flow time of 20 s is not currently viable.

Developing a reliable methodology to predict the maximum pressure capacity of hydraulic seals is still underway. A number of key studies have been conducted in the recent past to develop the CFD capability/methodology to deliver a robust modelling approach. Some of the important published work in this regard are numerical investigations by Young and Chew [26], Denecke et al. [19], and Mathews et al. [27].

1.4 Aim & Objectives

As discussed above, there is strong motive to improve understanding of the existing intershaft sealing technology. The work proposed is to develop CFD two-phase modelling capability for aero-engine intershaft seals and validate against available experimental data. The validated methodology can then be used to extend knowledge beyond existing data and should lead to vastly improved understanding of the way seals form, perform and breakdown. Such valuable capability will ultimately result in developing a deeper understanding of the interfacial flow physics in intershaft seals.

The primary motivation of this project is to develop and apply an approach that is both computationally efficient as well as highly accurate adding to knowledge and capability in the field of aero-engine intershaft sealing. This is carried out by investigating the flow, pressure and heat transfer characteristics of hydraulic seals with the aid of RANS numerical models. These characteristics are relatively undocumented in previous literature. This research aim is pursued by the following objectives which have been carried out as part of the CORNERSTONE project:

1. Conduct literature review to establish State of the Art for oil backed and hydraulic intershaft seals and identify areas of existing literature.

2. Develop steady state two-dimensional concentric models of a hydraulic seal and establish controlling parameters, comparing to experimental data where available.

3. Extend methodology for modelling transient scenarios and apply to situations such as seal filling, fin incursion, blow-out and other operational scenarios to add to knowledge and understanding.

4. Extend investigation to three-dimensional models investigating seal filling and turbulent effects.

5. Develop a thermal model for a hydraulic intershaft seal and investigate oil related heat transfer within the seal comparing to experimental data where available.

The primary objectives of this work have resulted in novel computational modelling approaches and tools that have not been previously implemented in numerical investigations of intershaft hydraulic seals. This work expands limited existing knowledge on the complex two-phase flow behaviours exhibited in the confined cavities between two co-rotating shafts. The outcomes of this research provide validation data and insights into the intricate flow dynamics within hydraulic seals. The novel contributions and knowledge additions delivered in this work over prior analyses on this topic include:

- In this work, a reliable methodology to model the flow within a hydraulic seal is developed through a parametric study investigating the effect of geometry, rotational shaft speeds, extreme configurations and engine condition. A consistent tool to predict the maximum operating pressure of hydraulic seals is introduced for the first time. A comprehensive analysis on the available analytical correlations that are used to predict the seal capacity and their validity is presented.

- Also presented in this work is a CFD modelling approach for a full 3D model of a hydraulic seal. This is the first numerical investigation which considers the 3D effects of the flow as well as an oil feed into a hydraulic seal. The study includes a detailed discussion on the effect of the jet on the oil in the trough. This study provides valuable insights into flow field within the seal and presents both quantitative and qualitative evaluation of the jet impact behaviour.

- Investigation on thermal effects including oil-related heat transfer in hydraulic seals presented in this thesis is also the first CFD study to characterize the performance of a hydraulic seal considering the heat generated and dissipated. A modelling framework to include effects of viscous heating generated within a seal is developed in this study which yields results of more realistic flow behaviour that have not been documented in prior investigations.

1.5 Thesis content and structure

This work comprises a numerical study of a chosen hydraulic seal geometry, expanding upon the groundwork of the previous studies and prior work. This project aims to collate the prior established analytical approximations related to oil angular velocity estimations, which would be valuable in the development of a robust modelling capability of hydraulic seals. This thesis is divided into three main parts based on the flow phenomena of interest. With scant experimental and numerical data on hydraulic seals available, the first part of the thesis focuses on investigating operational and geometrical characteristics of rotating disks in enclosed cavities. A published fundamental experimental study into a disk rotating in a cavity provides a geometry and validation data for a preliminary, single phase CFD study. This fully-wetted configuration was a precursor to CFD tests investigating partially wetted configurations, closer to hydraulic seals which formed the basis for the next stage of investigations.

The second part of the thesis aims to formulate a two-dimensional (2D) model to examine the performance of a hydraulic seal without an oil feed. Building on the previous research into hydraulic seals and learnings from the numerical studies of the rotating disks, the thesis looks at developing a reliable numerical modelling strategy based on a parametric study which accounts for the key geometrical features of a hydraulic seals assembly. Hydraulic seals are mostly utilized in parts of the engine that are not easily accessible and require a high integrity seal to withstand substantial pressure differences. Therefore, this section attempts to review the established analytical approximations to propose improvements to the existing numerical models and to develop novel modelling approaches to predict the maximum operating pressure of a hydraulic seal.

The final part of the thesis then extends the numerical investigation to develop a three-dimensional (3D) model of a hydraulic seal with an oil feed. Of particular interest is the effect of the jet on the behaviour of the oil in the trough and the influence of 3D effects on the maximum pressure capacity of the seal, comparing with the data obtained from the 2D studies in the previous part. This is combined with a qualitative comparison obtained from an experimental program investigating a hydraulic seal with jet fill at the University of Nottingham. This section also investigates the viscous heating and oil related heat transfer within hydraulic seals.

This thesis consists of seven chapters, as summarised here.

Chapter 1 gives an introduction to sealing in aero-engines, with an emphasis on sealing in the transmission system. This chapter also includes a discussion on the background of intershaft hydraulic seals and the principle of operation. To provide context for the work undertaken the identified research gaps are highlighted along with the aims and objectives for the research undertaken. The chapter also includes the structure of the thesis and the contribution to knowledge of the work presented.

Chapter 2 presents a review of identified prior scholarship relevant to hydraulic seals. This chapter is devoted to the discussion of different flow phenomena experienced in a hydraulic seal which is the primary application of this work. The purpose of this chapter is to systematize a survey of literature on these flow phenomena which lays the foundation to the subsequent chapters enabling the development of a robust modelling methodology for the application of hydraulic seals.

Chapter 3 highlights the CFD methodology used in the thesis. A description of the geometry, numerical grid, numerical models and post-processing details are included in this chapter. The basis for experimental and CFD studies into hydraulic seals is research into fully and partially wetted disks.

Chapter 4 provides a detailed analysis of fundamental experiments in literature upon which the computational modelling approach of a hydraulic seal was developed, presenting the basis for experimental and CFD studies into hydraulic seals is research into fully and partially wetted disks. This chapter includes existing analytical approaches and compares CFD modelling data obtained during the PhD research with

data for a fully wetted rotating disk against experimental results available in literature. Analysis of flow field characteristics are discussed. The chapter then goes on to investigate partially wetted disks – a geometry a step closer to the full hydraulic seal geometry. CFD data is presented and analysed examining the effect on the angular velocity of the fluid core with varying engagement and spacing ratios for two flow regimes.

Chapter 5 develops a 2D model of a hydraulic intershaft seal and delivers a numerical assessment of maximum pressure capacity of the seal with no oil feed. A comparison between the analytical oil speed correlation methods and numerical results is presented. This chapter also lists the findings of the parametric study based on CFD work conducted to investigate the influence of various parameters on the maximum pressure capability of the seal, including fin location within the trough.

Chapter 6 presents the analysis and discussion of the numerical investigation of a hydraulic seal with an oil feed. The focus is on the oil in the trough and therefore does not focus on droplet generation through jet splashing. The results of an experimental investigation of a hydraulic seal with jet fill varying jet angle and jet flowrate conducted within complementary experimental program (COAST) is presented. The results of the CFD study modelling this seal are compared to experimental data. This work investigates the fate of oil that either splashes back from the seal during the jet fill process or is ejected from the seal on the non-fill side. Of particular interest is the effect of the jet on the behaviour of the oil in the trough. This chapter also includes a qualitative comparison with results from an experimental program investigating a

hydraulic seal with jet fill at the University of Nottingham. This chapter also contains results from a CFD investigation into thermal effects including oil-related heat transfer and comparison to experimental data.

Chapter 7 presents a summary of the conclusions drawn from each chapter and highlights the novelty of the work presented. This chapter also includes recommendations for future work.

1.6 List of Publications

Some of the work included in of this thesis is published in the following papers:

Published

A. Warusevitane, K. Johnson, S. Ambrose, M. Walsh, and C. Young, "Numerical Investigation Into Fully and Partially Wetted Disk Geometries With Relevance to Intershaft Hydraulic Seals," in *Turbo Expo: Power for Land, Sea, and Air, 2020*, vol. 84058, p. V001T01A025: American Society of Mechanical Engineers.

A. Warusevitane, K. Johnson, and S. Ambrose, "Numerical Investigation Into Maximum Pressure Capability of Intershaft Hydraulic Seals," in *Turbo Expo: Power for Land, Sea, and Air*, 2022, vol. 86113, p. V10CT32A025: American Society of Mechanical Engineers.

A. Warusevitane, K. Johnson, R. Omar, and S. Ambrose, 3D modelling of a hydraulic seal with an oil feed, focussing on the effect of the jet on the behaviour of oil in the trough: paper presented at Turbo Expo 2023.

In preparation

A. Warusevitane, K. Johnson, and S. Ambrose, Numerical Investigation Into Maximum Pressure Capability of Intershaft Hydraulic Seals with Validation: Intention to submit to ASME Journal of Turbomachinery.

CHAPTER 2

2 Literature Review

The work undertaken is concerned with the two-phase flow of liquid and air in an aero-engine application. As discussed in Section 1.3, the liquid phase in a hydraulic seal exists as (i) a pool of oil obstructing an air flow through while sustaining large pressure differentials during operation, (ii) droplets which splash back from the seal during formation and (iii) droplets and ligaments that may eject from the seal on the non-fill side. This chapter compiles a review of literature on flow phenomena experienced in hydraulic seals such as flow induced by rotating disks in a cavity, rimming flows, oil related heat transfer, jet impingement and break-up dynamics, droplet generation and finally multiphase modelling of hydraulic seals which is the principal research focus leading to the approaches proposed in this thesis. The phenomena associated with a hydraulic seal is illustrated in Figure 2-1.

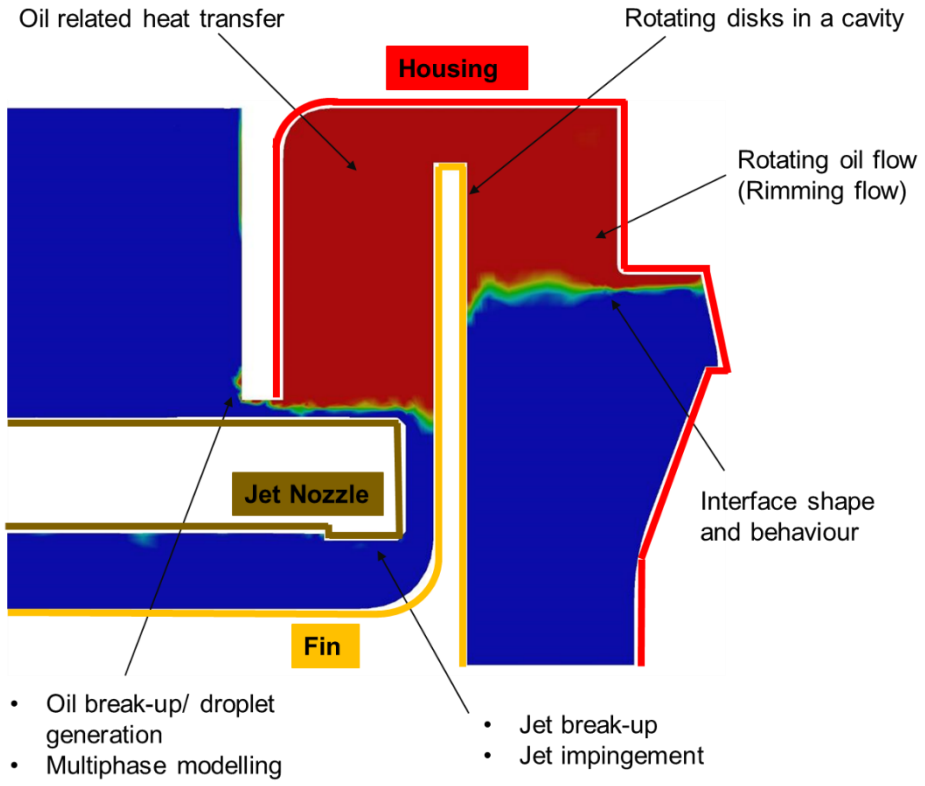


Figure 2-1: Flow phenomena associated with intershaft hydraulic seals

2.1 Flow dynamics of rotor-stator cavities

Intershaft hydraulic seals are essential elements within bearing chambers, providing a zero flow air seal across an inter-shaft cavity between two differentially rotating shafts. Therefore, to appreciate the flow characteristics in a hydraulic seal and to develop a numerical model capable of producing an accurate representation of the flow field, it is important to understand the flow physics of a configuration comparable to hydraulic seals. With a paucity of literature on hydraulic seals, there is a lot to be learned from investigating configurations similar to the seals. To this purpose, a survey into the

literature for relevant research work on rotor-stator cavities is presented in this section. There exists abundant literature on rotor-stator cavities due to the popularity of the topic that has grown with its role in numerous industrial applications. This section intends to present a review on previous key studies that have contributed to knowledge, with a focus on experimental and numerical results which shed light on the physics and dynamics of the flow in different conditions.

When a disk rotates adjacent to a disk that is stationary, it forms a cavity known as a rotor-stator cavity. The flow characteristics in the cavity are majorly influenced by the proximity of the disks, flow conditions around the periphery, and the flow rate of the supply of flow into the cavity. The flow within a rotor-stator disk cavity system is a research area of considerable prominence due to its wide range of engineering applications and has been studied for over a century. The rotor-stator cavity as illustrated in Figure 2-2 is a distinct configuration of a rotating disk system. Several geometrical and non-dimensional parameters are associated with a rotor-stator cavity. The parameters used to identify a rotor-stator cavity are the aspect ratio G, disk or rotational Reynolds number Re_Ω based on the outer radius of the rotating disk and the flow rate coefficient C_W. These parameters can be numerically presented as follows:

$$G = \frac{s}{a} \tag{2-1}$$

$$Re_{\Omega} = \frac{\Omega a^2}{\upsilon} \tag{2-2}$$

$$C_W = \frac{Q}{\upsilon a} \tag{2-3}$$

where s is the axial clearance between the rotating and stationary disk, Ω is angular velocity of the rotating disk, a is radius of the rotating disk, υ is the kinematic viscosity of the fluid, Q is the volumetric flowrate.

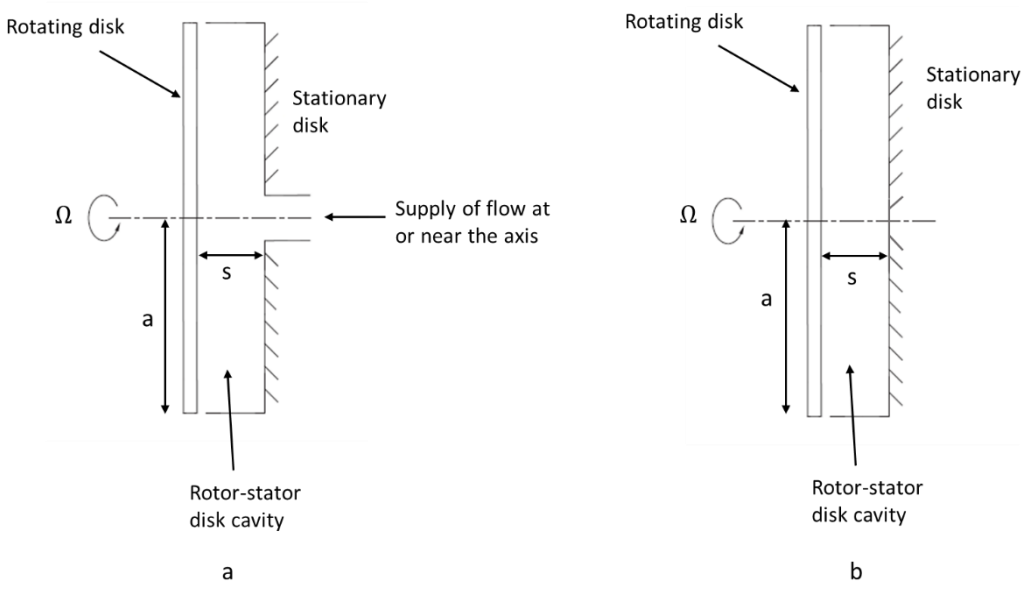


Figure 2-2: Typical rotor-stator disk system (a) open cavity with through-flow; (b) enclosed cavity with no through-flow

Different Reynolds number definitions are used to characterize the flow in rotor-stator cavities, with the appropriate choice depending on the specific context and geometry of

the problem. The Reynolds number based on the cavity height is defined as $Re_h = (\Omega h^2)/\vartheta$, where h is the height of the cavity. The local Reynolds number based on the local radius of the disk is calculated as $Re_\delta = r/\delta$ where r is the local radial value and $\delta = \sqrt{\vartheta/\Omega}$ is the characteristic length scale. For finite cavities, an alternate definitions exists where the Reynolds number is $Re_\Omega = (\Omega r^2)/\vartheta$.

In configurations where there are two rotating disks, with rotational speeds Ω and γ_2, the parameter γ_2/Ω has been used to classify two disk geometries into three distinct categories: the rotor-stator group where $\gamma_2/\Omega = 0$; co-rotating disks where $\gamma_2/\Omega > 0$; and counter-rotating disks where $\gamma_2/\Omega < 0$. Here, Ω and γ_2 are the rotation rates of the first and second disks respectively. Predominantly, the collective term 'rotor disk system' is used to distinguish all three groups.

2.1.1 Boundary layers in rotating disk systems

Some of the earliest work which attracted attention to this application are theoretical and experimental studies on boundary layers of single rotating disks by Ekman [28], von Kármán [29] and Bödewadt [30]. Three boundary layer types usually develop on a rotating disk that are collectively known as the BEK boundary layer family. In such a configuration, the characterisation of the flow is done using the Rossby number (Ro), which is the ratio of the inertial force to Coriolis force. This yields an infinite number of elements to the BEK family; the arrangement, Ro = −1, 0, 1 represents a von Kármán, an Ekman and a Bödewadt layer. A rather common instance of BEK boundary layers

is rotor-stator disk cavity. Here, the characteristics of the boundary layers on the rotating and stationary disks are different to that of a typical BEK boundary layer due to the radial boundaries imposed by the finite radius of the rotating and stationary disks. Much of the popularity of rotating disk boundary layers stems from von Kármán's [29] similarity solution for laminar flow over a single infinite disk rotating in a quiescent fluid. The derivation of this analytical solution for the three-dimensional boundary layer serves as a means of validation to many numerical investigations carried out years later, even today. The similarity theory by von Kármán involves three independent profiles for the stream-wise, cross-wise and wall-normal velocity components. The boundary layer developed on a rotating disk has evolved into a reference model for three-dimensional boundary layer investigations. This is due to the relatively simple geometry, the absence of pressure gradients in the stream-wise direction (direction of mean flow), and the ability to predict the laminar flow instabilities as a result of the inflectional point in the cross-wise velocity profile which is also a feature of three-dimensional boundary layers, such as those developed on swept-back wings.

Similarly, the boundary layers developed on the rotating and stationary disks in a rotor-stator cavity are very similar to the Ekman and Bödewadt boundary layers of the BEK family. Therefore, some of the characteristics of the BEK type boundary layers can also be seen on the rotor and stator elements. However, due to the finite length of rotating and stationary disks in the cavity, the flow characteristics of a classic BEK boundary layer along the radial boundaries are altered. In such instances, the behaviour and characteristics of a BEK boundary layer and a boundary layer developed on the rotor-

stator element differ. In a rotor-stator cavity, the boundary layer developed on the stator is named the Bödewadt layer and the boundary layer on the rotor is more commonly referred to as the Ekman layer. Here, the flow induced due to rotation is treated as one unified flow rather than considering separate Ekman and Bödewadt boundary layers.

2.1.2 Characterization of flow in rotor-stator cavities - The original dispute

From a fundamental perspective, research has been mainly focused on infinite geometries due to the ability to obtain exact similarity solutions of Navier-Stokes equations for the basic axisymmetric stationary flows. Prior to the advent of large amounts of experimental data and analytical solutions, following von Kármán's similarity solution theory, Batchelor [31] considered one and two-parameter problems [1] to propose a more generalised approach to achieve exact solutions for steady axisymmetric viscous rotating flows. In this study, single disks of infinite length, a member of the one-parameter family was defined with a solution space of $\gamma_1/\Omega_1 = (-\infty, +\infty)$, where γ_1 denotes the angular velocity of the fluid as $z \to \infty$ and Ω_1 represents the angular velocity of the rotating plane. As discussed above, von Kármán's original similarity solution is a special case developed for a single disk of an infinite length which can be characterized using $\gamma_2/\Omega = 0$.

[1] Here, the two disk family refers to a system where only one disk rotates.

To obtain a solution for the two-parameter family, Batchelor [31] investigated the flow between two differentially rotating co-axial disks where the flow was dictated by γ_2/Ω and Re_h . Re_h [2], here, is the local Reynolds number based on the height of the cavity. He noticed that at a given γ_2/Ω and relatively large Re_h, a core of fluid between the rotating and stationary disk is formed with zero radial and axial velocity gradient components and that it rotates as a solid body with an angular velocity, $\Omega K = \beta_{fluid}$, where β_{fluid} is the angular velocity of the fluid core, K is the velocity ratio, also known as the entrainment coefficient and Ω is the shaft's angular velocity. Batcher's model suggests the presence of boundary layers on both the rotating and stationary disks and that viscous effects are confined to boundary layers on each disk. This flow model implies that the boundary layer on the rotating disk is maintained with the fluid from the core pumped radially outward on the rotor due to the centrifugal effects and that the fluid returns radially inwards with an efflux from the boundary layer on the stationary disk to the core.

Two years later, Stewartson [32] proposed a different flow model suggesting that the flow in a rotor-stator cavity was comparable to that induced by a free disk in what has come to be known as the Batchelor-Stewartson controversy. He noticed that the boundary layer varies from the rotor velocity to zero as it moves away from the rotor. He conjectured that there was no core rotation and boundary layer on the stationary

[2] Local Reynolds number is used to specify the flow that undergoes transition and is different to the rotational Reynolds number used to characterize rotating viscous flows.

disk. Stewartson then presented experimental results to support his theoretical conclusions.

Velocity profiles which illustrate the distinguishable characteristics of the Batchelor and Stewartson models are presented in Figure 2-3. In this figure, the profiles of normalized components of tangential (U_φ), radial (U_r), and axial (U_x) velocity have been plotted against the normalized distance normal to the rotating disk. The axial velocity component has been scaled by a factor of 10^3 as the axial flow is negligible with respect to tangential and radial velocities.

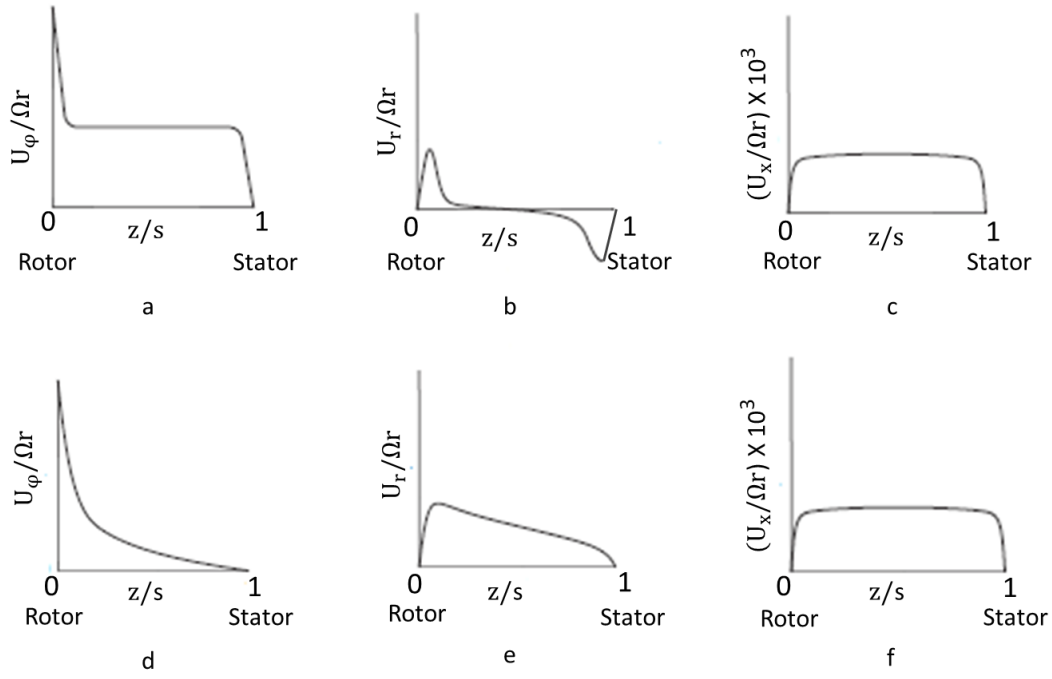


Figure 2-3: Velocity profiles demonstrating characteristics of the flow in a rotor-stator cavity: (a) to (c) illustrating characteristic velocity profiles of Batchelor flow; (d) to (f) exemplifying the flow behaviour described by Stewartson flow.

Eventually, attempting to explain the differences in flow behaviour in each model, Picha and Eckert [33] carried out an experimental study investigating the behaviour of the airflow between two co-axial disks. The rationale was that if the flow in the central core was known, then the boundary layer thickness and shear stress could be determined by applying the integrated momentum equations. The study was performed using both shrouded and unshrouded disks rotating at arbitrary angular velocities. The authors established that the core rotation was minimal and almost stationary when the disks rotated at equal and opposite angular velocities. They also noticed that a very stable core was formed at the disk centreline when the disks were co-rotating. The investigation of the flow between two unshrouded disks exhibited a forced vortex at the inner radius and a free vortex at the outer radius when rotated at identical angular velocities. The investigation also revealed that the angular velocity ratio between the core and the disk remained relatively constant over a wide range of Reynolds numbers, Re_h.

Further confirmation was furnished in subsequent studies addressing this dispute. In a numerical study investigating the similarity solutions of the Navier-Stokes equations relating to the axisymmetric flow between two infinite rotating disks, Lance and Rogers [34] observed that at higher Re_h numbers, the flow structure resembled the Batchelor flow model with a central core in solid-body rotation for all values of the angular velocity ratio between the two disks. They explained that the edge effects should be accounted for, in two configurations, that is when the two disks are co-rotating and in a rotor-stator system. The authors also found that as the Re_h is decreased, the Batchelor

flow structure with an inviscid core tends towards a purely viscous flow with merged boundary layers. In this study, the entrainment coefficient which describes the relationship between angular velocities of the rotating disk and the core, was computed to be approximately 1/3.

Mellor et al. [35] and Kreiss and Parter [36] found that different flow structures emerge due to the non-uniform and different characteristics of the boundary layer at a particular Re_h value, which confirms the validity of flow models by both Batchelor [31] and Stewartson [32]. These studies confirmed the presence of a rotating core, at certain conditions, with a tangential velocity component which was defined as a fraction of the rotor speed.

A numerical study by Dijkstra & van Heijst [37] has demonstrated that at higher Re_h, the Batchelor flow structure is applicable in flows between finite rotating and stationary disks enclosed by a cylindrical sidewall. In finite configurations, the angular velocity of the core varies with the radial distance, as opposed to the Batchelor flow experienced in infinite geometries, and hence causes the flow to deviate from the self-similar solution. This is because the boundary conditions of the similarity solution are not quite capable of the representing the finite cavities with housing walls. Therefore, Dijkstra & van Heijst [37] carried out their numerical investigation on a rotor-stator disk system in an enclosed cavity using a finite difference method to solve the Navier-Stokes equations. The experimental set-up used by the authors is presented in Figure 2-4. They explained that the observed radial outflow at the bottom of the rotor is due to the centrifugal effects and that the fluid fed in using a jet returns radially inward along the

stator. The authors computed the stream-function of the flow field within the cavity and verified that the computed velocity profiles were self-similar up to a radius ratio of 0.87 irrespective of the finite boundaries of the cavity. Finally the authors concluded that, with finite disk geometries, the flow in a rotor-stator cavity system forms into a central rotating core and it transitions to a viscous torsional Couette profile as the Re_h decreases, similar to that in infinite disk configurations.

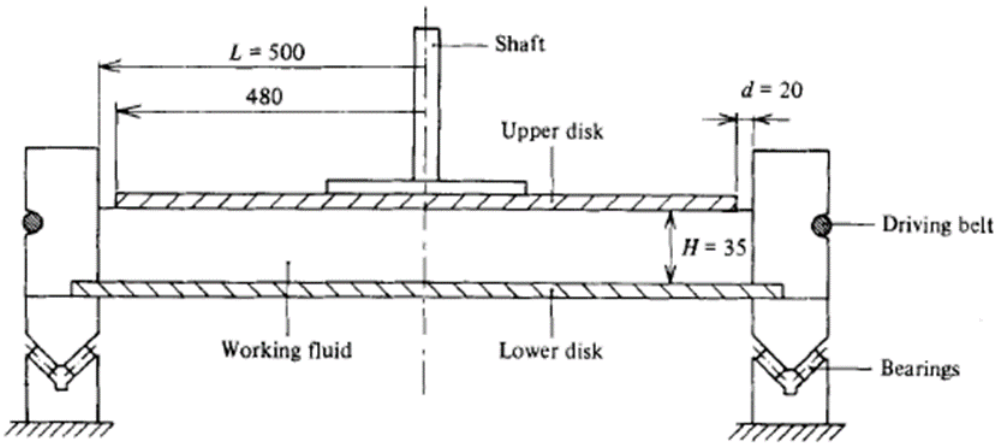


Figure 2-4: The experimental configuration used in the experiment by Dijkstra & van Heijst [37] with dimensions in mm.

Later, Poncet et al. [38] performed an experimental investigation to examine the flow characteristics in rotor-stator cavities with through-flow to compare the flow structures of Batchelor and Stewartson models. This study confirmed the findings by Gauthier et al. [39] and Dijkstra and van Heijst [37] providing further evidence on the fact that the Batchelor flow is mainly encountered in enclosed cavities, whereas the flow induced in open cavities or cavities with a superimposed centripetal or centrifugal through-flow is predominantly described by the Stewartson flow. It is now acknowledged that both

Batchelor and Stewartson solutions are admissible depending on the flow conditions. The Batchelor solution is distinguished by three distinct zones where a central rotating core is separated by two boundary layers developed on the rotating and static disks, and the Stewartson model is characterized by the absence of a rotating core and a boundary layer on the stationary disk with a tangential velocity varying towards zero outside the rotor boundary layer. However, the formed flow field is majorly influenced by the supply of the superposed flow into the cavity. In a rotor-stator cavity, an increase in superposed radial outflow will cause a decrease in the rotation of the primary flow due to the net flow of fluid supplied at the axis to the cavity. It is interesting to note that the flow that can originally be described by the Batchelor solution can shift toward the Stewartson model with minimal core rotation as the radial outflow is increased.

2.1.3 Enclosed rotor-stator disk systems

In a rotor-stator disk assembly housed in a closed cavity with no supply of fluid into the cavity, the flow structure resembles Batchelor flow characteristics. As described by the model, the flow behaviour is such that the fluid that is pumped radially outwards along the rotor then returns axially towards the stator in a boundary layer on the outer shroud. The boundary layers on the rotating and stationary disks are separated by an inviscid core of fluid that rotates at some fraction of the rotor's angular velocity. Typical streamlines of the flow field within the cavity in a rotor-stator disk system are sketched in Figure 2-5a. A distinct feature of the tangential velocity of the main flow in the cavity is that it varies axially between the rotor and stator disks. It transitions from the disk

speed in the rotor boundary layer to a constant value in the core and then reduces to zero in the stator boundary layer as illustrated in Figure 2-5b.

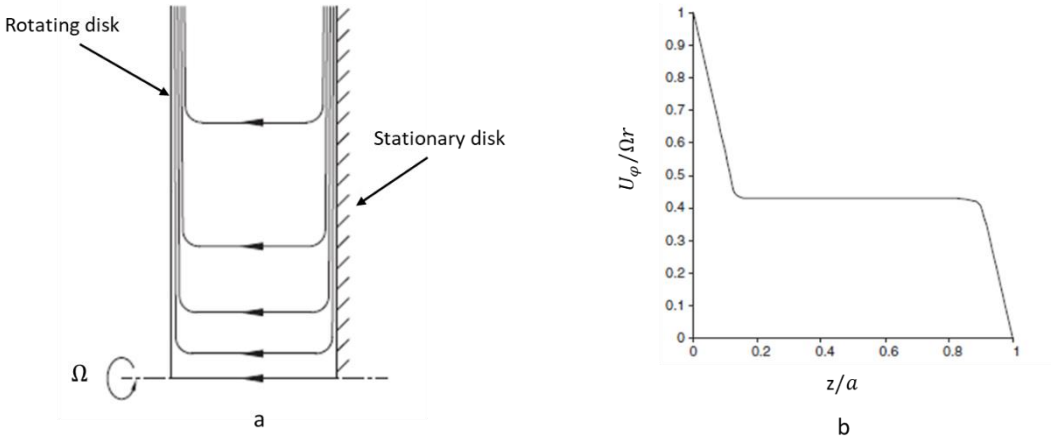


Figure 2-5: Typical flow characteristics of Batchelor flow model**:** (a) streamline pattern of the flow field confined between rotating and stationary disks as described by Batchelor flow model; (b) Tangential velocity variation within rotor-stator cavity

The characteristics of the flow that originates in a rotor-stator disk configuration do not only depend on the geometrical features of the cavity, but also on the nature of the flow, that is, whether the flow is laminar or turbulent. Daily and Nece [40] reported the existence of four flow regimes for a rotor-stator disk system in an enclosed cavity based on the aspect ratio of the cavity [3], G, and the disk Reynolds number, Re_Ω, through their theoretical and experimental studies. The identified flow regimes for cavities with longer disks where $G \ll 1$, are shown in Figure 2-6. The authors also determined the

[3] The aspect ratio of a cavity is sometimes known as the gap ratio. This is equal to s/a which is the non-dimensional axial clearance.

coefficients of moment for each of the regimes for disk Reynolds numbers ranging between 1 x $10^3 < Re_\Omega <$ 1 x 10^7 and cavity aspect ratios between $0.0127 < G < 0.217$.

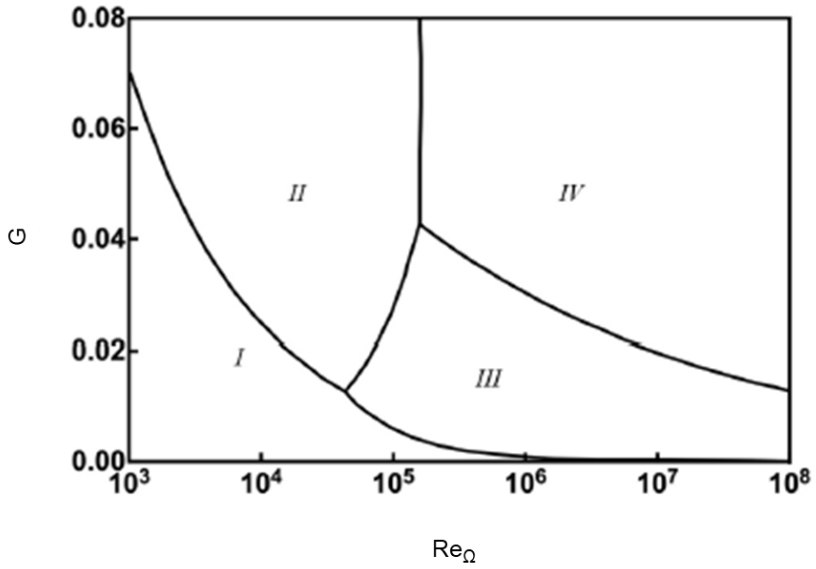


Figure 2-6: Regions of flow for an enclosed rotor-stator disk space identified by Daily and Nece [40] (I) Laminar flow and close clearance; (II) Laminar flow and large clearance; (III) Turbulent flow and close clearance; (IV) Turbulent flow and large clearance.

Daily and Nece [40] verified that the flow structure represented by regime I includes smaller clearance laminar flow of two merged boundary layers which results in a continuous variation of tangential velocity across the axial spacing between the stationary and rotating disk walls. The moment coefficient for one side of the rotating disk was defined as:

$$C_m = \frac{\pi}{GRe_\Omega} \tag{2-4}$$

Regime II is characterised by a rotating core separated by two boundary layers on the rotating and stationary disks, with a boundary layer formed by outward radial flow along the rotating disk and inward along the stationary disk. The moment coefficient for one face of the rotating disk was expressed as:

$$C_m = 1.85 G^{0.1} {Re_\Omega}^{-0.5} \tag{2-5}$$

Regime III includes close clearance turbulent flow with merged boundary layers. The relationship for the moment coefficient for this regime can be given by:

$$C_m = 0.04 G^{-0.167} {Re_\Omega}^{-0.25} \tag{2-6}$$

Regime IV denotes a turbulent flow structure in larger clearances with boundary layers on the rotating and stationary disks separated by a rotating core, again with a radial secondary flow along rotating and stationary disks. The defined moment coefficient for one side of the rotating disk which demarcates this region is given by:

$$C_m = 0.051 G^{0.1} {Re_\Omega}^{-0.2} \tag{2-7}$$

Many of the earlier experimental studies found in literature have focused on the single phase flow in rotor-stator cavities. Expanding on the essential contribution to characterize the flow within an enclosed chamber by Daily and Nece [40], Ketola and McGrew [41] presented an analytical model and experimental results characterizing the

fluid dynamics and performance of a rotating disk enclosed within a stationary housing when partially immersed in a liquid. Both non-flow and through-flow conditions were examined. The key conclusions of this study are:

- The pressure gradient in the water column can be predicted by modelling the core as rotating at a fraction of the disk speed, with the fraction dependent on geometry and flow parameters. The theory matches reasonably well with measured pressure data.

- The frictional torque acting on the disk can be determined by balancing shear stresses on the stationary and rotating surfaces. This yields expressions for torque coefficient as a function of Reynolds number, spacing ratio, and degree of wetting. Experimental values trend somewhat lower but show consistent behaviour.

- Four flow regimes are defined based on Reynolds number and spacing ratio. Analytical models are developed for each regime allowing torque, flow rate, and pressure gradients to be calculated.

- Tests confirm the strong effect of engagement ratio (wetted area) on pressure generation and frictional torque. Pressure rise degrades markedly even with low through-flow rates.

- Increasing through-flow causes an increase in frictional torque that can be estimated analytically. Correcting the data using this estimate brings measured torques in line with non-flow values.

The work presented by Ketola and McGrew [41] is of interest and very applicable to this work as this is a configuration similar to hydraulic seals. Therefore a numerical investigation is conducted to investigate the flow characteristics in enclosed cavities when the rotating disk partially submerged in liquid. The numerical approach developed and an analysis of flow characteristics are presented in Chapter 4.

In a later study, Launder et al. [42] explained that the flow can transition between the regions identified by Daily and Nece [40] and that the likely transition paths can vary between regions I →IV →III; II →I →III; and IV →III. This is due to an increase in the boundary layer thickness caused by an increase in the local disk Reynolds number. For the studies reported in this thesis, the regions of interest are III and IV, of which regime IV, exhibits the flow features of Batchelor model. Therefore, only the discussions which focus on these two regions are presented from here on.

Using a two-disk apparatus, with a rotating top disk made of Plexiglas, a part of which extending to the outer cylindrical casing and a bottom disk made of clear-anodized aluminium with an attached side wall, Sirivat [43] carried out an experimental study to examine the stability of the flow between a stationary and rotating disk by varying Re_h and G. The experimental apparatus used in this study is illustrated in Figure 2-7. The aspect ratio was varied by inserting a clear plastic sheet into the gap between the two

disks. Sirivat [43] reported the presence of three modes of instability at the investigated values of G. The instability classed as mode I, was observed as a steady-state, circular pattern for either of the G values 0.0225 and 0.0475. No other modes emerged within this range of G, as the only effect of altering the gap size would result in a change in the fundamental flow pattern, specified by $1/Ek$ [4]. As the gap was decreased leading to a reduced aspect ratio of $G = 0.014$, an entirely different mode of instability appeared which included spiral vortices with negative spiral angles that seemed to move outward. This mode of disturbance was designated as mode II. Both mode I and mode II disturbances could be observed when either one of the disks was rotating. The final mode of instability was observed at higher disk rotational speeds which featured confined almost stationary, spiral vortices. Sirivat [43] reports that these vortices have a positive spiral angle and are observed to be similar to the asymptotic instability linked with cross-flow, observed in flow experiments conducted with a single disk. Additionally, Sirivat [43] also examined the behaviours of mode I and II instabilities as the flow transitions to turbulence. It was identified that for larger values of $1/Ek$ in mode I, the turbulent flow transported inward by the sidewalls causes the transition to turbulent flow. Different to mode 1 transition, Sirivat [43] explains that the random collapses of spiral vortices, contributes to the onset of turbulence for mode II instability which occurs when $1/Ek$ has reached a value beyond 11.36.

[4] Ekman number, Ek, is used to characterize the flow as the ratio of viscous to Coriolis forces. In a cavity this is defined as $Ek = \frac{\vartheta}{\omega s^2}$ where ϑ is the kinematic viscosity, ω is the shaft rotational speed and s is the axial length of the cavity.

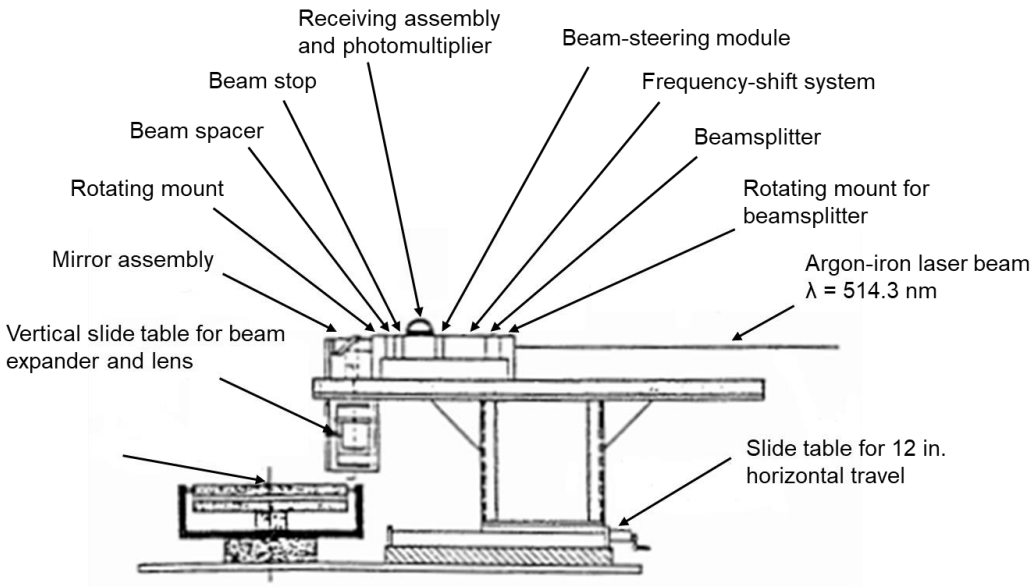


Figure 2-7: The test apparatus used by Sirivat [43]

Lingwood's theoretical [44] and experimental [45] studies fundamentally changed our understanding of process in transition to turbulence of rotating disks. Her research sparked a renewed interest in investigating the stability of rotating disk systems. While single rotating disks are known to be absolutely unstable, it is intuitive to assume that two disk systems would also exhibit absolute unstable behaviour, as this configuration contains elements of the single disk setup. Lingwood [44, 45] presented evidence which suggests that the flow over a rotating disk is initially convectively unstable and is then followed up by a convective/absolute transition. The author stated that absolute instability which is an inviscid mechanism, is different to spatial instability. These studies confirm that the parameter range in which absolute instability occurs agrees well with the experimental results of the critical Reynolds number for the onset of

laminar – turbulent transition where the mean $Re_{\delta,c}$ [5] is approximately 513 $\pm$ 3%. The inviscid analysis results of this study demonstrate that the absolute instability is not a result of Coriolis effects nor of streamline curvature effects. The work concludes that the primary agent for transition is absolute instability rather than the disturbances in the radial direction convectively. The author further suggests that this process may be applicable to transition on highly swept wings where the boundary layer is similar and the Coriolis effects are absent.

Experimental study by Gauthier et al. [39] focused on investigating the primary instability in the flow within a rotor-stator disk system enclosed by a cylindrical housing at a relatively large aspect ratio, G = 0.048, one of the aspect ratios also investigated by Sirivat [43]. The authors used two visualization methods to analyse the flow field; the first being a fluorescent lamp that is slightly larger than the disks, positioned a small distance above them and the second being a laser sheet generated by a helium-neon laser diode and a cylindrical lens. For the range of Re_h investigated, the authors found that the boundary layers separated above Reynolds numbers, Re_h > 52, using the latter technique, which also allowed them to measure the thickness of the boundary layers close to the disks. They observed that the Bödewadt layer thickness increased as the radius decreased implying a linear evolution with radius, while the Ekman layer remained with an almost constant thickness along the rotating disk. The authors observed circular waves closer to the periphery for 70 < Re_h < 140 and about 30 Type II spiral vortices as the angular velocity increases for a range of 140 < Re_h < 200. As

[5] $Re_{\delta,c}$ is used to define the critical transition Reynolds number based on the local radial value of the disk

the angular velocity is further increased, disordered patterns of vortices which appeared to be the onset of turbulence emerged at the centre beyond Re_h > 200. Gauthier et al. [39] also carried out additional experiments with a means of externally controlled forcing where the flow was disturbed by introducing periodic modulation to the rotational speed of the disk. This produced new spatiotemporal light intensity images of the propagating circular patterns. The power spectrum density (PSD) of the varying light intensity demonstrated the flow system acts as a large-band amplifier with the most amplified frequency being exactly four times the rotation rate of the disk without any externally controlled forcing. The most unstable wave number was found to be 0.5 regardless of the position and forcing frequency. This value is comparable to the wave number computed theoretically by Lingwood [46] at the onset of convective/absolute transition of circular waves in the Bödewadt layer of a single disk of infinite radius, which is 0.33. This study established that the critical Reynolds number, $Re_{\delta,c}$, was about 76, and suggested that it decreases as the aspect ratio increases.

In a numerical investigation using DNS, Serre et al. [47], examined the instabilities of the flow in a rotor-stator system. The authors investigated the effect of geometrical features such as confinement and curvature using two configurations: an annular cavity of a moderate aspect ratio, G = 0.2 and a curvature parameter [6] of R_m = 4 and 5 cavity enclosed by a shaft and shroud to study the influence of weaker curvature further away from the rotation axis and a cylindrical cavity with two aspect ratios, G = 0.2 and 0.33

[6] Curvature, R_m is a geometrical parameter used to specify a cavity. It is defined as $R_m = \frac{R_i + R_o}{R_o - R_i}$, where R_i is the inner radius and R_o is the outer radius. In a cylindrical cavity R_m = 1.

including the rotation axis to examine the impact of large curvature. They observed that the Batchelor flow transitioned to circular and spiral instabilities at sufficiently high Re, similar to the previous experimental observations by Schouveiler et al. [48, 49]. The authors claimed that these patterns that can be related to type I and type II instabilities appeared in both boundary layers. They reported that the instabilities which emerge closer to the rotating disk in the annular cavities exhibited features that are in good agreement with the instability patterns observed and measured in the Ekman layer by Faller [50]. The authors noticed that the local curvature has a profound effect on the instability modes and the threshold range for the onset of turbulence for the two configurations studied. They explained that the radial confinement in cylindrical cavities significantly influences the nature of fluid instabilities; at the lower aspect ratio, a pure Hopf bifurcation was seen while the flow transitioned to non-periodic at higher the aspect ratio value. In the annular cavity, the instability generated in the stator layer due to supercritical bifurcation, propagates through to the rotor leading to a subcritical instability in the Ekman layer. Conversely, attenuation near the shaft prevents this effect in the cylindrical cavity making it more stable compared to the annular configuration.

Another key study related to the flow within rotor-stator systems is an experimental study by Schouveiler et al. [51] investigating the instability of the flow for an enclosed rotor-stator system in detail using ultrasonic anemometry and flow visualization. The authors observed two scenarios related to transition. They noticed that when boundary layers are separated, circular and spiral waves destabilized the boundary layer on the stator and the mixing of these waves led to transition from laminar to turbulent flow.

They also observed finite spiral patterns in the laminar region when the boundary layers were merged with an increase in this phenomenon as the rotational Reynolds number was increased.

Lygren and Andersson [52] studied the turbulent flow between an infinite rotating and stationary disk by simulating an angular sector numerically using DNS with the aim of understanding the effect of turbulence due to the three-dimensionality of the flow. The simulations were performed at a local Reynolds number, Re_h of 4 x 10^5 and a small cavity aspect ratio, G of 0.02 with quasi-periodic boundary conditions imposed in the radial and tangential directions, effectively modelling the cavity as infinitely wide with no effects from the housing or sidewall. In this investigation, the mean velocity, turbulence intensity, and wall shear stress data were explored in detail and compared to experimental results of Itoh [53]. The authors added that turbulent intensities closer to the rotor were higher in the numerical study than in the experiment and this was due to the infinite length examined in the numerical study. The authors observed that the turbulent intensity and shear stresses were significantly higher near the rotor compared to the stator. They also observed that the shear stress and the mean flow gradient vectors in both rotor and stator boundary layers were more aligned than in the non-stationary three-dimensional turbulent boundary layers. This study provided a detailed analysis of the coherent structures in the three-dimensional boundary layers on the rotating and stationary disks using ensemble-averaged vortices. They found that the coherent structures found near the rotor and stator were very similar to the ones found in two-dimensional flows, and that any difference triggered was predominantly due to the

three-dimensionality of the mean flow. Further, they explained that the crossflow originating closer to the rotating disk was a result of the difference between centrifugal and pressure forces, while the crossflow closer to the stator was produced by the pressure force.

The study by Séverac et al. [54] incorporated both a numerical investigation using high order LES and experimental investigation using Laser Doppler velocimetry (LDV) measurements to investigate the flow in a rotor-stator system in an enclosed cavity with a low aspect ratio, G = 0.2. The set-up included an inner cylindrical casing attached to the rotating disk that serves as an enclosure and an outer shroud coupled with the stationary disk to simulate the finite effects that were not considered in the LES calculations by Lygren and Andersson [55, 56]. The experiments were carried out at rotational Reynolds numbers, Re_Ω, up to 1 x 10^6 and R_m = 1.8. By comparing results at three different rotational Reynolds numbers, Re_Ω, they found that the stator boundary layer transitions to turbulence at a lower Re_Ω = 1 x 10^5 while the boundary layers on the rotating disk separated with an onset of turbulence at Re_Ω = 4 x 10^5. Flow visualizations performed by Séverac et al. [54] at two Reynolds numbers, Re_Ω = 4.1 x 10^4 and Re_Ω = 1 x 10^5 from above the stator are presented in Figure 2-8. It can be seen in Figure 2-8a that at Re_Ω = 4.1 x 10^4, the flow exhibits a complex formation, yet it is still structured with large-scale spiral patterns. When the Reynolds number increases to Re_Ω = 1 x 10^5, the Bödewadt layer transitions to a clearly turbulent state, as depicted in Figure 2-8b.

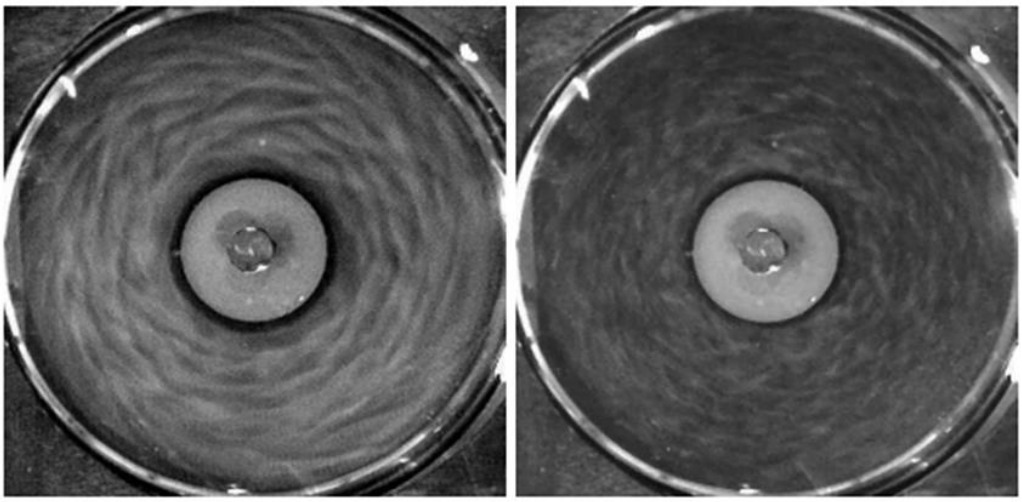


Figure 2-8: Flow structure visualised from above the stator in the experiment by Séverac et al. [54] at (a) Re_Ω = 4.1 x 10^4 and (b) Re_Ω = 1 x 10^5

Séverac et al. [54] showed that finite cavity effects were present when Re_Ω = 1 x 10^6 on boundary layers on both rotating and stationary disks. They observed around 19 spiral arms with a 16° wave angle on the rotor boundary layer in the section where 0.14 < r/a < 0.61, identifying this as a Type I instability pattern. In the fully turbulent regions, the flow structures appeared to be thinner and forming tangentially. They further added that the patterns formed on the rotating disk in the tangential direction were 'cigar shaped' while the patterns aligned on the stator in the tangential direction were 'pancake shaped'. The authors concluded that the numerical results were in excellent agreement with the LDV measurements and that the study confirmed the three-dimensional nature of both boundary layers. They explained that their study

showed a higher degree of three-dimensionality than that reported by Lygren and Andersson [52, 56] for an idealized flow between a rotor and stator.

Similar to the study by Séverac et al. [54], Makino et al. [57] studied the transitional and turbulent flow in an enclosed cavity both experimentally and numerically. Using the same geometrical parameters as Séverac et al. [54] this study investigated both cylindrical and annular cavities with an aspect ratio, G = 0.2 at rotational Reynolds numbers, Re_Ω, of 1 x 10^5 and 4 x 10^5. The authors reported that at the lower Reynolds number, the boundary layer on the rotating disk was laminar and the boundary layer on the stationary disk was turbulent. At the higher Reynolds number, a fully turbulent stator boundary layer was computed with the rotor boundary layer in the transitional state. However, this numerical study predicted fewer Type II instabilities in the rotor boundary layer, likely due to Streamline-Curvature effects described by Itoh [58]. Makino et al. [57] argued that the transition to turbulent flow resulted primarily from interactions between Type II and secondary instabilities, a mechanism explained by Faller [50].

These key studies in literature highlight that the flow between a rotating and stationary disk in an enclosed cavity can be characterised based on geometrical and operational parameters. Circular and spiral instability patterns are a common occurrence in these type of flows, with the boundary layer on the rotating disk being relatively more stable compared to the boundary layer on the stationary disk.

2.2 Jet flow dynamics

2.2.1 Jet application in a hydraulic seal

In a hydraulic seal, viscous heating is generated due to the interaction of the rotating surfaces and the oil. To mitigate the impact of viscous heating and to reduce the oil residence time, a through-flowing system with a continuous oil feed is required [59]. A through-flowing system, in this context is where oil is fed from one side of the seal allowing it to spill over at the opposite side. In aero-engine seals, this is usually achieved with a continuous jet-delivered oil feed. As a hydraulic seal is only formed at engine start-up, functional design requires that it should form promptly. The seal formation time will be determined by the rate of oil feed, rotor speeds and pressure differentials. Oil is distributed into a hydraulic seal using a direct or indirect feed when the engine is in operation. Static jets are a common application of feeding oil directly into one side of the hydraulic seal (usually the lower pressure side). These jets are mostly used when it is impractical to collect oil from an external location outboard of the hydraulic seal assembly. As jets are an integral component in a hydraulic seal system and the function of a jet is primarily to ensure reliable and efficient operation of hydraulic seals, the literature on jets and jet theory is reviewed and discussed in the following subsections.

2.2.2 Overview of liquid jet break-up

When a stream of liquid is injected into a quiescent, gaseous atmosphere at a specific velocity, a continuous jet is formed. The liquid jet that accelerates as it emerges from the nozzle exit remains intact up to a certain length, consequently resulting in ligaments due to the aerodynamic effects of the gaseous environment and instabilities on the gas-liquid interface. Subsequently, these ligaments transform into droplets due to the surface tension, σ_L, leading to the formation of a new surface area. The jet loses its velocity and dynamic pressure progressively as it moves further downstream from the nozzle exit [60]. As the distance from the nozzle exit increases, the ambient gas gradually mixes into the core of the jet. This causes the jet to transition into a mixture of air and liquid. In simple terms, this process is known as the primary break-up of a liquid jet. As the fluid exits the nozzle outlet, the jet stream formed is characterized by a circular cross-section. The resulting jet diameter, d_j, at this point is less than or equal to the physical diameter of the nozzle orifice.

Once a jet exits the nozzle and penetrates the surrounding fluid, the total momentum which was conserved is transferred to the ambient fluid. The literature provides some classifications of what constitutes a free jet. Perry et al. [61] have stated that if the cross-sectional area of the jet is less than $1/5^{th}$ of the cross-sectional area of the surrounding region, then the jet can be considered a free jet, assuming the jet fluid and surrounding fluid are the same. Additionally, a turbulent jet with a Reynolds number greater than 2000 is typically considered a free jet. A jet that emerges from the nozzle maintains its

integrity over a certain distance downstream of the nozzle before penetrating the surrounding fluid. The length of this coherent segment of the liquid stream is known as its break-up length, l_B, and is illustrated in Figure 2-9. This parameter as a function of jet exit velocity is considered as a convenient approach for characterizing the jet break-up modes [62]. If the jet has a long break-up length, it may not disintegrate completely; if the jet impacts a solid surface before any distortion occurs, it is referred to as an impinging jet.

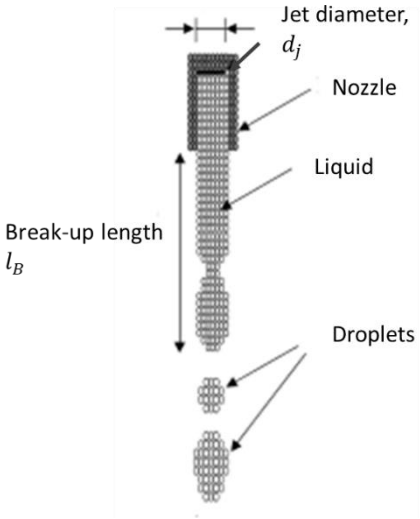


Figure 2-9: Simple illustration of a jet exiting a nozzle

2.2.3 Jet break-up phenomenon

Injection nozzles used in fuel injectors are designed to ensure successful combustion in gas turbine engines by disintegrating the fluid so that well developed atomisation can take place. However, in an application such as a hydraulic seal, a jet that does not breakup or atomise would be most desirable as the intention is to deliver all the supplied

oil into the trough. As the oil is injected into the hydraulic seal, depending on jet design, it may undergo primary and secondary breakup. The intricate nature of the jet breakup process is influenced by a number of parameters such as the geometry of the nozzle, jet velocity at the nozzle exit, turbulence of the liquid jet and the cross-flow fluid, aerodynamic forces, hydrodynamic forces and the physical and thermodynamic states of both liquid and gas. It is important to note that the initial condition of the jet as it emerges from the nozzle exit also influences the eventual jet breakup process across the different regimes.

Investigating the parameters that influence jet break-up properties mentioned above, Lee and Spencer [63] conducted a classic jet breakup study through the analysis of many photomicrographs. The authors concluded that the extent to which jet disintegration occurs, was affected by the distance the jet travels. They added that the break-up intensifies as the distance from the nozzle increases, provided that liquid viscous and surface tension forces do not overpower the disintegration forces. They also found that higher jet velocity and turbulence levels lead to more pronounced break-up while increasing liquid viscosity and surface tension results in a reduction in the rate of jet disintegration. The study also revealed that the nozzle geometry affects the jet disintegration as well, stating that the break-up rate decreases as the nozzle exit diameter increases. Their photographic study exemplifies systematic research on the effects of various parameters on jet breakup. This study provided great early insights, but building a framework for the underlying physics is key, thus, it is important to first understand the general jet breakup mechanisms involved.

The fundamental aspects of the break-up phenomenon of a liquid jet have been extensively studied experimentally and theoretically by many researchers for over a century. One of the earliest and fundamental theoretical studies on this topic is the analysis by Plateau [64] which dates back to the 19th century. Plateau [64] stated that jets break up into segments with lengths equal to 2π times the jet radius. A few years later, Rayleigh [65] looked into various modes of jet break-up focusing on low-velocity, inviscid jets of finite radius. Rayleigh [65, 66] postulated that the jet break-up length is influenced by capillary effects such as surface tension and explained that the break-up of a liquid jet is caused by hydrodynamic instabilities. Later, Schweitzer [67] highlighted that Rayleigh's analysis is not applicable to pressure-injection flows as this analysis did not examine high-velocity, turbulent liquid jets that may be affected by aerodynamic forces. These early investigations were based on Rayleigh's linear theory which predicts the most rapidly growing instability wave and the corresponding dominant length scale for jet breakup. According to the linear theory, the wave growing maximally has a wavelength approximately 9 times the original unperturbed jet radius, r_j. The experiments suggest that this instability induces pinching or break-up of the jet into drops. However, this pinching mechanism is non-linear in nature where the initial perturbation is bound to grow exponentially to amplitudes on the order of the original undisturbed jet radius for pinching and breakup to occur. Since the perturbations become so large, their behaviour can no longer be accurately modelled using linear theory. Although the linear theory provides qualitatively accurate predictions of breakup timescales, it does not perform well in predicting the jet shape and velocity characteristics at the point of breakup.

Building upon Rayleigh's research, various authors, most notably, Weber [68], and Haenlein [69] studied the effects of liquid and ambient fluid properties on jet stability and breakup characteristics. Tomotika [70] extended Rayleigh's linear stability analysis for inviscid jets investigate a stationary cylindrical strand of one viscous fluid surrounded by another, considering the interfacial surface tension effects. Qualitatively, the results are similar to inviscid jet studies, with the dominant wavelength growing to be of the order of the unperturbed, original strand radius. Tomotika [70] showed there is an optimal ratio of the jet viscosity to the ambient fluid viscosity at which the jet achieves its highest growth rate. Chandrasekhar [71] extended Rayleigh's inviscid analysis by including non-uniform jet velocities and accounting for the viscosity and density of the liquid. In his mathematical analysis, the author provided evidence supporting that increasing viscosity reduces the frequency of break-up rate and increases the droplet size. The author concluded that the disintegration of a viscous liquid jet is a product of capillary pinching and demonstrated that capillary instability leads to waves which grow linearly, scaling on the jet radius. Such studies indicated a liquid jet may disintegrate subjected to different forces under set of specific conditions and can be categorised into a variety of modes of break-up.

The break-up mechanism and the break up-length of turbulent jets were first experimentally investigated by Ricou and Spalding [72]. To understand how the break-up length is influenced in laminar jets, Tanasawa and Toyoda [73] and Grant and Middleman [62] then extended the experimental investigation to examine both laminar and turbulent jets.

2.2.4 Primary jet break-up

The study of droplet impact is crucial as it can result in great benefits in a wide and diversified range of engineering applications. The size of the droplet determines the time required for the droplet to completely vaporize its liquid component [74]. The primary breakup plays an important role as the process governs the size of droplets formed [75]. Therefore, a significant amount of research has been undertaken to understand more about the primary breakup of jets exiting nozzles and to improve the ability to accurately predict the jet dynamics and the characteristics of the resulting droplets.

The survey of literature has identified two prevalent categorization methods of jet disintegration: Ohnesorge's characterization framework and the jet stability curve. The disintegration phenomena associated with a liquid jet are classically split into four regimes as defined by Ohnesorge et al. [76]. This framework has become a subject of interest to numerous authors [77-84]. The break-up modes distinguished by this classification are Rayleigh's regime, the first wind-induced regime, the second wind-induced regime, and the atomisation regime. These droplet break-up regimes are typically graphically represented on a log-log plot of Ohnesorge number, Oh, vs Reynolds number, Re, as shown in Figure 2-10. The jet break-up mechanisms have been classified into regimes to demonstrate the geometrical characteristics of different jets as the operating conditions vary. These regimes are governed by the dominant forces exerted on the jet resulting in its disintegration, therefore, it is necessary to

distinguish these forces to analyse the break-up phenomenon in each regime. The impact of droplet size, surface tension, and density are either investigated separately or quantified through non-dimensional numbers.

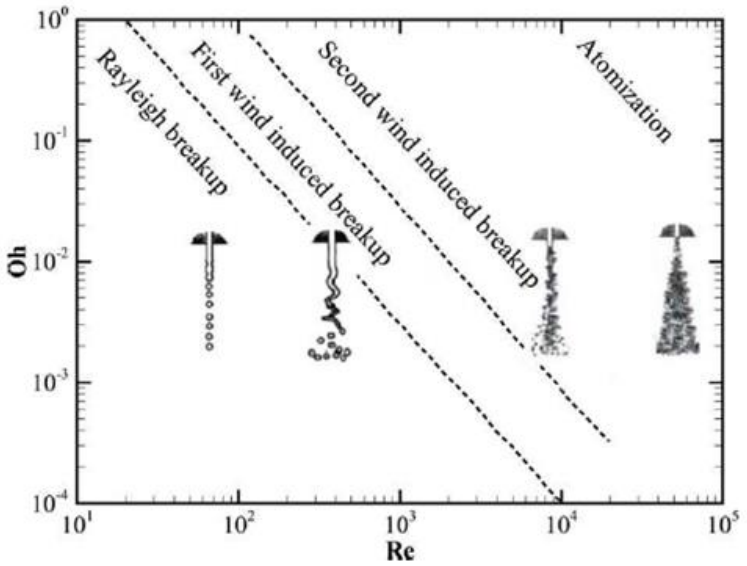


Figure 2-10: Diagram illustrating the break-up regimes for a jet exiting a nozzle [77]

In the Rayleigh break-up regime illustrated in Figure 2-11a, jet disintegration occurs much further away from the nozzle and the formed droplets have a diameter larger than that of the nozzle. Based on the findings of Rayleigh [65] and Weber [68], the general agreement is that jet break-up occurs when the wavelength of the maximally growing instability reaches the same order of scale as the jet radius, r_j. The Rayleigh break-up is characterized by the low jet velocities, insignificant surface perturbations and negligible aerodynamic forces.

First wind-induced break-up shown in Figure 2-11b, occurs at higher velocities than those of Rayleigh break-up regime. In this regime, the jet develops a wavy shape due to sinusoidal oscillations along its length, with the aerodynamic forces acting on the jet amplifying these instabilities. The amplification causes the jet to break-up a few nozzle diameters downstream with the droplet diameter in the order of jet diameter, d_j [77].

In the second wind-induced breakup regime, shown in Figure 2-11c, interactions between the liquid jet and surrounding air become very significant. Surface disturbances created by aerodynamic forces disrupt the jet much more severely than in the first wind-induced regime. The jet break-up occurs a short distance away from the nozzle exit in the second wind-induced break-up regime and the resulting droplets are smaller in size with a diameter smaller than the nozzle diameter [77].

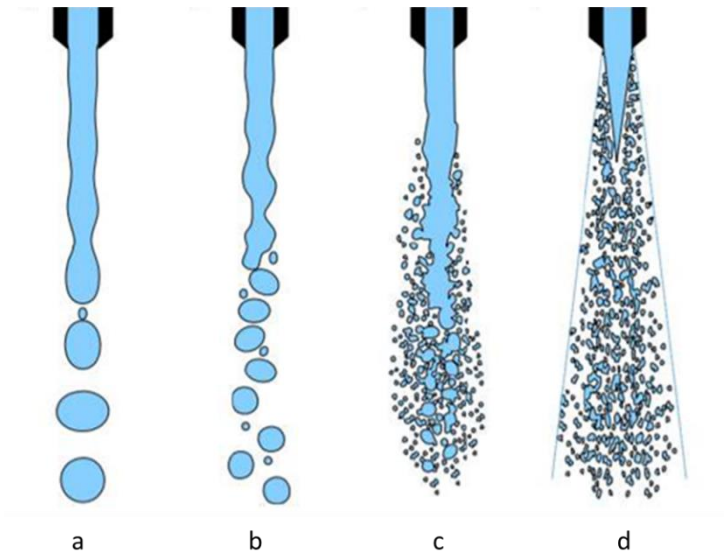


Figure 2-11: Primary breakup regimes (a) Rayleigh, (b) First wind-induced, (c) Second wind-induced (d) Atomisation [85]

The atomisation regime depicted in Figure 2-11d, is associated with very high jet velocities. This regime is characterized by the jet break-up occurring at the nozzle exit. The diameters of the droplets formed are far smaller than that of the nozzle. Tamaki et al. [86, 87] reported that cavitation is an important factor that aids in atomisation. The atomisation regime and the generation of sprays have been extensively studied by Arai et al. [81, 82, 88, 89] and Hiroyasu et al. [78-80].

Reynolds number (Re), Weber number (We), and Ohnesorge number (Oh), presented in Equations (2-8), (2-9) and (2-10) respectively, are the key parameters that play a vital role in establishing the dynamics of instability on the liquid surface resulted by droplet impact. The break-up type is determined by the Reynolds number and Ohnesorge number of the liquid exiting the nozzle. The Ohnesorge number is a function of the Weber number; the Weber number determines the ratio of fluid inertia to the fluid's surface tension. The turbulent length scales in the liquid jet are influenced by the Reynolds number.

$$Re = \frac{\rho U L}{\mu} \tag{2-8}$$

$$We = \frac{\rho U^2 L}{\sigma_L} \tag{2-9}$$

$$Oh = \frac{\sqrt{We}}{Re} = \frac{\mu}{\sqrt{\rho \sigma_L L}} \tag{2-10}$$

Where ρ is the fluid density, U is the fluid velocity, L is the characteristic length, μ is the dynamic fluid viscosity and σ_L is the surface tension of the fluid.

The classic characterization of jet breakup regimes by Ohnesorge can also be specified in terms of the liquid and ambient gas properties [85, 90-92]. These properties are represented by the liquid Weber number, We_L, which encapsulates liquid properties, and the gas Weber number, We_g, specifying the ambient gas properties. Criteria for categorizing the type of jet breakup based on the Weber number are summarized in Table 2-1.

Table 2-1: Jet break-up characterization based on liquid and ambient properties

Regime	Range
Rayleigh regime	$We_L > 8$; $We_g < 0.4$
First wind-induced regime	$0.4 < We_g < 13$
Second wind-induced regime	$13 < We_g < 40$
Atomization regime	$We_g \geq 40$

An alternative method of characterizing jet disintegration is by examining the relationship between breakup length, l_B, and the jet velocity U_j; this is known as the jet stability curve when presented graphically. The jet stability curve depicted in Figure 2-12 categorizes different break-up modes emerging due to the action of the dominant forces under a set of operating conditions, similar to the Ohnesorge's classification. The

stability curve plots l_B versus U_j and classifies five regimes: dripping flow regime, laminar region, transition region, turbulent region and the fully developed spray region.

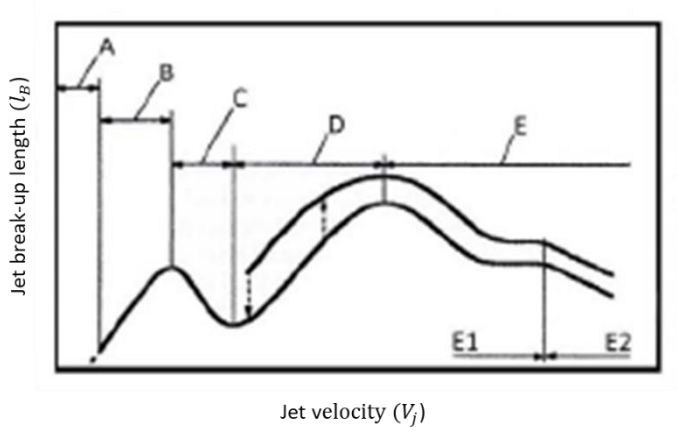


Figure 2-12: Jet stability curve illustrating break-up regimes. (A) dripping region; (B) laminar region; (C) transition region; (D) Turbulent region; (E) spray region with (E1) subsonic spray region and (E2) supersonic spray region [80]

In the dripping and laminar flow regime, jet disintegration is governed by inertial and surface tension forces. Very little work has been done on the dripping region as the liquid beam drips out of the nozzle at very low flow rates, failing to form a continuous jet with definable length. The flow transition from the dripping flow regime to the laminar region is indicative of the jet break-up length increasing proportionally with the jet velocity [62]. In the transition region of the stability curve, aerodynamic forces start becoming more significant and the breakup mode changes from dilational to sinuous. While the aerodynamic effects play a secondary role in this region, jet disintegration is primarily attributed to liquid turbulence. As seen in Figure 2-12, the flow transitions from laminar to turbulent, with the break-up length decreasing as jet

velocity increases. In the fully turbulent region, the aerodynamic effects become more prominent with the liquid turbulence and break-up length increasing with jet velocity as confirmed in several studies [79, 82, 88]. There are some disagreements about the flow behaviour in the atomisation region of the stability curve. Earlier studies stated that as jet velocity increases, the breakup length decreases and eventually becomes zero. However, McCarthy and Molloy [93] observed that a small coherent portion of the jet exists downstream of the nozzle, irrespective of the jet velocity. Subsequent research by Hiroyasu et al. [79, 80] and Arai et al. [81, 82, 88] confirm the findings by McCarthy and Molloy [93] with evidence that indicate a finite region of the jet does remain before fully atomizing into drops across the velocity range.

As discussed previously Weber's [68] original theory describes laminar jet flow very well. It states that for a given liquid and nozzle, the breakup length varies linearly with jet velocity, with irregularities caused solely due to the surface tension of liquid which is also known as the capillary phenomenon. Weber's theory integrates nozzle exit diameter, liquid surface tension, viscosity, and density. However, this theory does not take important factors such as turbulence levels, velocity profile, and cavitation into account. It ceases to function at the peak of the stability curve, where the flow transitions from laminar to semi-turbulent flow since additional factors that contribute to jet disintegration such as the effects of the ambient fluid are significant in the transition region.

In light of the shortcomings of this theory, Weber and various other researchers have attempted to incorporate the atmospheric effects appropriately. However, the improved

versions have not been successful in predicting the local maximum and the boundaries of laminar to-semi-turbulent transition region of the stability curve [62, 94, 95].

There is no consensus on the jet velocity or Reynolds number value corresponding to the onset of turbulence as the transition region has not been precisely quantified by the experimental work. McCarthy and Molloy [93] developed an empirical correlation to estimate the transitional Reynolds number and is presented by Equation (2-11) below. However, a limitation of this correlation is that it is only valid for jets flowing out of long tubes into quiescent atmosphere where the exit velocity profile is fully-developed and parabolic.

$$Re = 3.25Oh^{-0.28} \tag{2-11}$$

It is important to note that many numerical investigations on jet breakup and disintegration have been carried out. This is mainly due to the lack of a solid theoretical framework to develop computational models upon. Yeh [96] developed a numerical model for flow in plain-orifice atomisers which examined the effect of nozzle geometry on discharge coefficient, C_D, considering parameters like Reynolds number, turbulence intensity at the inlet, nozzle aspect ratio, and contraction angle. Tafreshi et al. [97] and Anantharamaiah et al. [98] developed computational models to simulate the flow in nozzles used for hydro-entangling applications to determine the influence of the contraction angle and aspect ratio on the emerging jet flow. In their numerical

investigation, Yoon and Heister [99] established that the boundary layer formed at the nozzle exit orifice can greatly impact jet atomisation.

Richards et al [100, 101] studied the disintegration mechanism of a jet exiting a nozzle both experimentally and numerically. In this study a full transient model was simulated to represent behaviour from jet start-up to break-up into drops. The authors reported that the numerically obtained results for interface, drop shapes and average jet lengths were in satisfactory agreement with the experimental data of Meister and Scheele [102]. Their numerical study which integrated VoF and continuous-surface-force (CSF) methods showed that the jet break-up length has a greater sensitivity to the Reynolds number.

Modelling the injection of a liquid jet into high-speed gas flow requires predicting the gas/liquid interface under turbulent conditions with high Reynolds numbers. Interface capturing formulations incorporate VoF and/or level set (LS) techniques solving the complete Navier-Stokes equations for both the liquid jet and gas, along with an interface equation. Numerical studies applying the VoF method have aimed to track free boundaries or fluid-fluid interfaces effectively and to predict the flow instabilities and cusp formation [103, 104]. Similarly, studies with level set (LS) approaches also capture the interface implicitly with a level set function which transitions smoothly across the interface, compared to the sharp volume fraction jump in VoF [105]. Brinckman et al. [106] developed a CFD methodology to model the liquid jet discharge and break-up in high velocity fluid flows utilizing a RANS framework. This study used a unified, multiphase, thermodynamic model that is valid for both gas and liquid phases

replacing the traditional VoF approach employed in studies investigating applications involving incompressible flows.

2.2.4.1 Droplet distribution

As a jet undergoes primary breakup, the generated droplets form a distribution of diameters. A convenient representation of this droplet size distribution can be done by employing the Rosin-Rammler distribution given by Equation (2-12). The Rosin-Rammler formulation describes the exponential relationship that exists between the cumulative mass fraction, Y_{d_0}, of droplets with a diameter less than d_0. Here, $\overline{d_0}$ reflects an average diameter which corresponds to the value of computed diameter where the cumulative mass fraction is approximately ≈ 0.368. n_s, refers to the spread parameter is calculated using the equation expression displayed in Equation (2-13).

$$Y_{d_0} = 1 - e^{\left(d_0/\overline{d_0}\right)^{n_s}} \tag{2-12}$$

$$n_s = \frac{\ln(-\ln(Y_{d_0}))}{\ln\left(d_0/\overline{d_0}\right)} \tag{2-13}$$

In instances where Rosin-Rammler is inadequate or the formulation does not accurately model the measured droplet distribution, alternative distributions such as the log-normal can be implemented. The log-normal provides a useful model for droplet distributions when the diameters defined in the log format follows a normal distribution.

The probability density function based on the mean deviation, $\bar{x}$, and standard deviation, σ, for the log-normal distribution is presented by Equation (2-14) below:

$$f(d_0|\bar{x},\sigma) = \frac{1}{d_0\sigma\sqrt{2\pi}} exp\left(-\frac{(\log(i-\bar{x}))^2}{2\sigma^2}\right) \quad (2\text{-}14)$$

Here i refers to each value from the population.

2.2.4.2 Jet break-up length

The subject of jet break-up length behaviour beyond the first wind-induced breakup regime has caused some dispute due to the discrepancies in the observations reported in literature. Haenlein [69] pointed out that the breakup length increases with increasing jet velocity before abruptly tending to zero, while McCarthy and Molloy [93] reported a continual increase in the break-up length. Hiroyasu et al. [79] claimed that the jet behaved sporadically with elongating and contracting lengths as the jet velocity was varied. The authors linked these inconsistencies to variations in internal nozzle flow patterns stemming from separation and cavitation effects, which also showed hysteresis.

In an attempt to parametrize the jet break-up phenomenon, Kazuya et al. [107] performed a two-dimensional numerical investigation using the Moving Particle Semi-implicit (MPS) approach considering the surface tension. The influence of the Weber number and Froude number (Fr) on the jet breakup length was explored in this study

and the authors confirmed that the numerical results from this analysis are in good agreement with the experimental measurements of Tanasawa and Toyoda [73]. The authors found that the breakup lengths computed numerically were approximately 70-80% of the experimentally measured lengths when computed taking gravitational effects into consideration. However, the numerical analysis for jet break-up without gravitational effects, resulted in breakup lengths about 25% of experimental lengths. The researchers explained this was likely due to the acceleration of the break-up process caused by the particle fluctuations. They also found that the computed droplet size distribution after disintegration agreed well with the experimentally correlated Nukiyama-Tanasawa [108] distribution. Additionally, they found that a smaller We results in larger droplets due to relatively stronger surface tension and that larger Fr leads to longer jet breakup length. This relationship can be attributed to the diminishing influence of gravitational forces at higher Froude numbers. Kazuya et al. [107] defined the relationship between the jet break-up length and the effect of We and Fr as follows:

$$\frac{l_B}{d_j} = 2.2We^{0.28}Fr^{0.78} \tag{2-15}$$

where d is the jet width or the diameter.

2.2.5 Secondary break-up

Secondary break-up or atomisation refers to the physical process where liquid elements formed during primary atomisation break-up further generating additional smaller

droplets. When a droplet is exposed to a disruptive air flow field, it creates an uneven pressure distribution around the droplet surface. This is the deformation phase of the secondary break-up mechanism. The pressure imbalance distorts the original spherical shape of the droplet caused by the acceleration of the ambient fluid around the droplet. Although the interfacial tension and viscous forces act attempting to hinder the deformation of the droplet, if the aerodynamic forces from the flow are sufficiently large, it will disrupt the spherical symmetry as it transitions to the fragmentation phase [109]. Thus, the Weber number, which represents the ratio of disruptive aerodynamic to restorative surface tension forces, is the key factor when characterizing secondary break-up. Viscosity of the droplet resists deformation and diffuses the energy of the aerodynamic effects, suppressing the tendency of fragmentation. This effect is accounted for with the use of Ohnesorge number, which is defined as the ratio of viscous to surface tension forces. Higher Weber numbers increase the droplet break-up tendency, while higher Ohnesorge numbers suppress the likelihood of the break-up of droplets. Dimensionless parameters such the Reynolds number, density ratio between the droplet phase and the ambient phase, viscosity ratio between the droplet phase and the ambient phase and the relative Mach number that can be related to the compressibility effects are also used to characterize the secondary break-up. Although, it is not within the scope of this thesis to study the droplets formed in secondary atomisation in detail, the discussion in this section aims to provide insights into the flow conditions, behaviour and patterns of the ejected secondary droplets so that this knowledge would be useful for the qualitative analysis carried out in Chapter 6.

Numerous comprehensive reviews exist in literature secondary breakup with reviews by Pilch and Erdman [110] and Faeth et al [111] being among the some of the early notable work. Experimental investigations by Mayers [112]; Gokalp et al. [113, 114]; Zheng and Jasuja [115]; Mansour and Chigier [116, 117]; Krzeczkowski [118] ; Krauss [119]; Ranger and Nicholls [120]; Engel [121]; Lane [122]; Hinze [123] have identified different regimes of secondary break-up. Four experimental methods reported in literature are commonly used to investigate the secondary drop break-up. These are shock tubes, continuous jets, drop towers and hybrid methods. Each experimental technique differs due to the type of aerodynamic forces exerted on droplets. Shock tubes furnish a spatially uniform step change in velocity. Drop towers provide a continuous acceleration and continuous jets cause a step acceleration in droplets by imposing shear loading. These different loadings impact the drop response and fragmentation mode and can produce variations in droplet breakup behaviour.

As secondary break-up arises from interactions between the droplet and surrounding flow, the breakup mode depends on the flow conditions. Different conditions lead to different breakup modes, as illustrated in Figure 2-13 for Newtonian droplets observed in shock tube experiments. There are five secondary breakup modes based on the Weber and Ohnesorge numbers: vibrational, bag, multi-mode (this is sometimes referred to as bag-and-stamen), sheet-thinning and catastrophic.

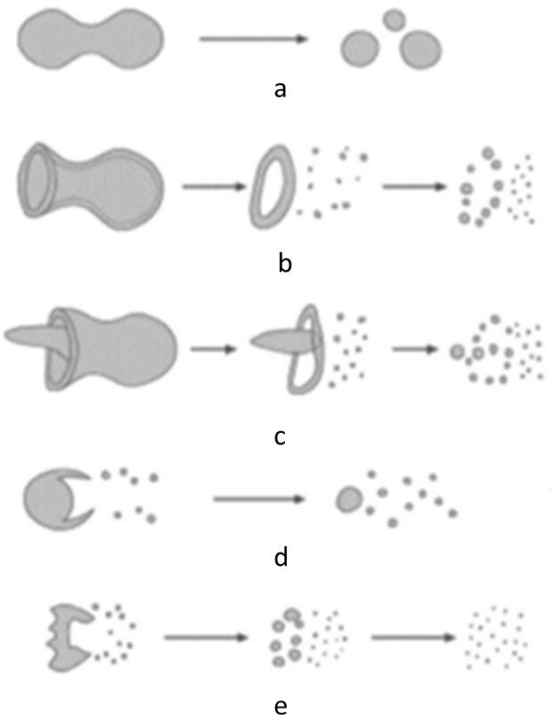


Figure 2-13: The secondary break-up morphology illustrating the regimes (a) vibrational; (b) bag; (c) multi-mode; (d) sheet-thinning; and (e) catastrophic [109]

Each secondary breakup mode has distinct drop shape dynamics and fragmentation characteristics and can be summarized as follows:

- Vibrational break-up causes oscillations at the drop's natural frequency, producing just a few fragments similar in size to the parent drop. This break-up mode is not observed frequently.

- Bag break-up forms a thin hollow bag attached to a thicker toroidal rim (also referred to as basal ring). The bag breaks-up first into many small fragments, then the rim into fewer larger fragments.

- Multi-mode break-up is comparable to bag break-up and is composed of a stamen added to the bag shape against the course of motion of the drop. Similar to the bag break-up mode, the bag disintegrates initially with the rim, and stamen breaking-up sequentially, producing a multi-sized fragment distribution.

- A thin sheet of fluid is continuously stripped from the top surface of the drop in the sheet-thinning regime which rapidly disintegrates into many minute droplets, sometimes resulting in a core similar to that of the drop.

- Catastrophic break-up corrugates the surface into large waves that form a few large fragments, which further break into smaller elements. This break-up mode is sometimes sub-categorized into wave-crest stripping and catastrophic by some researchers based on wave features.

Significant research has aimed to elucidate the physics of each secondary break-up mode. Most studies have found the droplet deformation, break-up mechanism and the transition between secondary break-up regimes are dominated by Weber number and Ohnesorge number, and are independent of other parameters like density ratio or Reynolds number. However, it is worth noting that this may be due to the limited range of such parameters achievable in experiments.

In any case, several experimental investigations have pointed out that the transitional Weber numbers between two successive break-up modes remain approximately constant for $Oh < 0.1$. These approximate values recorded by Hsiang and Faeth [111] for the transition between bag and multi-mode and multi-mode and sheet-thinning

regimes; and Pilch and Erdman [110] for the transition between vibrational and bag are listed in Table 2-2.

Table 2-2: Modes of secondary break-up varying with transitional We for Newtonian drops when Oh < 0.1

Vibrational	$0 < We \leq 11$
Bag	$11 \leq We \leq 35$
Multi-mode	$35 \leq We \leq 80$
Sheet-thinning	$80 \leq We \leq 350$
Catastrophic	$We \geq 350$

2.2.5.1 Break-up times of drops

Break-up times are an important and a commonly reported characteristic of break-up of drops. In reviewing spray structures, Faeth et al. [111] observed that during break-up, drops may travel distances as long as 30-40 times their initial diameter. The impact of the aerodynamic drag is such that the largest and smallest fragments are separated by over 100 initial diameters. Therefore, knowledge of temporal phenomena and associated timescales in secondary atomisation is essential to develop any model that resembles this process. Contradicting interpretations and results relating to break-up exist in the literature as evidenced by many definitions of break-up time reported, but

three characteristic times are of interest: initiation of breakup, primary breakup and total breakup.

- Initiation time (T_0)

The definition of break-up initiation time is arbitrary and is dependent on the mechanism. Pilch and Erdman [110] defined it as the time needed for a drop to distort beyond the oblate spheroid shape. For bag and multi-mode breakup modes, the formation of the bag signifies the initiation of break-up. Break-up of sheet stripping mode is initiated when a ligament being stripped downstream from the periphery of the drop. Initiation time is important as this denotes the point where the models developed for deformation of a spheroid no longer apply. The correlation presented by Pilch and Erdman [110] is given in Equation (2-16) below.

$$T_0 = 1.9(We - We_c)^{-0.25}(1 + 22Oh^{1.6}) \quad (2\text{-}16)$$

Here, the critical Weber number is represented by We_c. This relationship was developed for the range of $We < 10^4$; $Oh < 1.5$

Another correlation was proposed for initiation time by Hsiang and Faeth [124] as given in Equation (2-17):

$$T_0 = 1.6/(1 - \frac{Oh}{7}) \quad (2\text{-}17)$$

This expression considers $We < 10^4$; $Oh < 1.5$.

Guildenbecher et al. [109] noted that when plotted together, the two expressions show reasonable agreement at low Oh where $T_0 \approx 1.5$. But at $Oh > 2$ the correlations diverge significantly. There is no conclusive evidence on which correlation is more accurate which shows more work is required.

- Total break-up time (T_{tot})

The total break-up time is defined by Pilch and Erdman [110] as the time when a drop and its fragments no longer experience further break-up. The authors proposed an expression for the low viscous drops as presented in Equation (2-18).

$$\begin{aligned} T_{tot} &= 6(We-12)^{-0.25} && 12 < We < 18 \\ T_{tot} &= 2.45(We-12)^{0.25} && 18 < We < 45 \\ T_{tot} &= 14.1(We-12)^{-0.25} && 45 < We < 351 \\ T_{tot} &= 0.766(We-12)^{0.25} && 351 < We < 2670 \\ T_{tot} &= 5.5 && 2670 < We < 10^5 \end{aligned} \quad (2\text{-}18)$$

Pilch and Erdman [110] cited a correlation for viscous drops originally developed by Gel'fand et al. [125] as given in Equation (2-19).

$$T_{tot} = 4.5(1 + 1.2Oh^{0.74}) \qquad We \approx We_c; Oh < 0.3 \tag{2-19}$$

The transitional We numbers in given in Equation (2-18) are in a similar range as the transitional We presented in Table 2-2 which define the break-up morphologies of each regime. This implies that the flow physics responsible for break-up times differs for each break-up mode, further validating the principle of categorizing secondary atomisation into distinct structures.

Dai and Faeth [126] evaluated the total break-up time for secondary atomisation in the multimode regime and observed a local maximum around We = 40, similar to that noticed by Pilch and Erdman [110], as denoted in Equation (2-18). This process reaches a local maximum at the transition between bag/plume and plume/sheet-thinning multimode sub-regimes.

Likewise, Hsiang and Faeth [124] established the following relationship given in Equation (2-20) for total breakup time.

$$T_{tot} = \frac{5}{1 - \frac{Oh}{7}} \qquad We < 10^3; Oh < 3.5 \tag{2-20}$$

In their review, Guildenbecher et al. [109] compared the correlations of Gel'fand et al. [125] and Hsiang and Faeth [124]. The authors noted a reasonable consistency at low Oh where $T_{tot} \approx 5.0$. However, when $Oh > 0.5$, a significant deviation was seen.

2.3 Oil film break-up and the impact of droplets generated

The oil volume in a hydraulic seal either splashes back from the seal during the jet fill process or is ejected from the seal on the non-fill side. To quantify the oil droplets leaving the seal in either scenario, it is important to identify the phenomena governing droplet motion. A few important features of droplet generation dynamics that are relevant in a hydraulic seal application are droplet gas-phase interactions, droplet distortion due to high shearing forces, effects of different parameters on droplet deformation. Therefore, it is vital to understand the underlying physics involving the break-up of oil film and subsequent droplet generation to approximate the complex shape and behaviour of droplets generated, to develop accurate models which are capable of capturing this phenomenon.

2.3.1 Splashing

The study of droplet splashing has a long history dating back to the work by Worthington [127]. Splashing is a possible outcome of droplet impact which occurs under high inertia conditions. A droplet may either adhere to the surface of the film or splash as it hits the surface depending on its Weber number. Splashing has been observed to occur at high Reynolds and Weber number conditions [128, 129].

Interactions between the droplet and oil film are complex, and are influenced by a number of factors such as inertia, surface tension, liquid thermal properties, and properties of the impacting surface. The general outcomes of droplet impact on dry or wet surfaces were categorized in a study by Yarin [130] where the potential impact scenarios have been recognized as stick, spread, rebound, or splash. Yarin [130] explains that the secondary droplets formed through the splashing phenomenon schematically illustrated in Figure 2-14 is a sequential rearrangement of a two-dimensional continuum into a one-dimensional one.

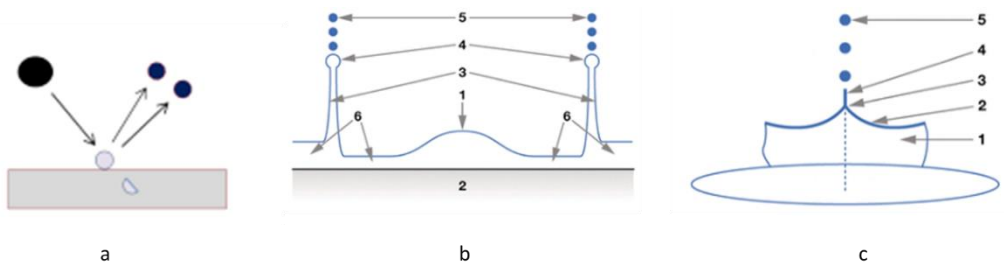


Figure 2-14: (a) Illustration of the splashing mechanism (b) where 1 - residual on top of impacting drop, 2 - wall, 3 - outwards propagating sheet, 4 - section view of the free rim, 5 - droplets emerging from cusps of free rim; (c) Magnified view of the free rim and the droplets formed where 1 - crown-like sheet, 2 - top edge of the free rim, 3 – cusp, 4 - slender jet, 5 – secondary droplets formed at jet breakup [131]

In the Figure 2-14a, the original incoming droplet is called the primary droplet. The impact of impingement on the surface in the form of a splash yields smaller droplets referred to as child or secondary droplets. There is extensive research on droplet-film interactions performed at different flow conditions. Splashing is of interest to this work as this phenomenon is observed during seal fill and a qualitative representation of this

phenomenon is presented in Chapter 6. Numerous studies have attempted to investigate the droplet impact phenomenon through DNS or VoF approaches by examining the initial time steps following impact [103, 104, 132].

Most experimental research on droplet-film impact has focused on normal incidence, with limited work on oblique impact. In normal impact, the droplet hits the surface perpendicular along the surface normal vector. Oblique impact occurs when the droplet hits the surface at a shallow angle. The surface can also be wet or dry when the droplet impacts. Films are typically characterized as thin or thick. Relative film thickness is usually used in studies related to droplet film impact to characterize the effects of film and impact. The relative film thickness, H^*, which is the ratio of film thickness, h_{of}, to droplet diameter, d_0, is described in Equation (2-21). The classifications of film thickness by various authors is summarised in Table 2-3.

$$H^* = h_{of}/d_0 \tag{2-21}$$

Table 2-3: Depiction of droplet impact surface classified by relative film thickness

Film type	Wall type	Relationship
Dry wall	Dry wall	$H^* = 0$
Thin film	Pre-wetted wall	$H^* << 1$
Intermediate film	Pre-wetted wall	$H^* = 1$
Thick film/ deep pool	Deep pool/ pre wetted wall	$H^* >> 1$

The type of film relevant to this work is thick film and the oil film flow in hydraulic seals is explored in Chapters 5 and 6. This work does not aim to finely resolve the detailed physics of splashing and secondary droplets as the primary focus is on the oil in the trough as discussed in Chapter 6. Instead, this review aims to account for the details such as splashed droplets, through published correlations that can be used to estimate the secondary droplets in the relevant or closest flow regimes. Therefore, rather than directly modelling the individual splashed droplets, their properties are determined from correlations in the literature corresponding to the conditions. This avoids resolving the complex physics but still incorporates the overall effect of splashing through the correlations.

A splashing criterion was defined by Bai et al. [133] to determine if splashing occurs when impacting on the surface film. The surface roughness coefficients are used to calculate the critical Weber number for splashing for the type of surface. If the droplet's Weber number exceeds the critical value, splashing occurs. Otherwise, the parcel sticks to the surface or film.

2.3.2 Edge separation

When a film flows past obstacles or sharp edges, it could result in a phenomenon where a portion of the liquid film either separates from the surface leading to break-up or remains attached following the edge. This may occur in fluid flows such as in scavenge offtake, regions in the bearing chamber with sudden changes in geometry and at the spill-over edge in a hydraulic seal as the oil leaves the seal. Typical film separation

phenomenon as a film encounters a sharp edge is presented in Figure 2-15. Several studies on the flow around sharp edges can be found in literature; Owen & Ryley [134] in their experimental and numerical investigation of radial stress distribution of a thin film flow around a sharp bend with a fixed radius, demonstrated that thick films ($H^* > 1.06$) [7] are more prone to separate than thin films typically at boundary walls. The non-dimensional film thickness, H^*, here is defined as the ratio of the film thickness, h_f, to the curvature, R_c; $H^* = h_f/R_c$.

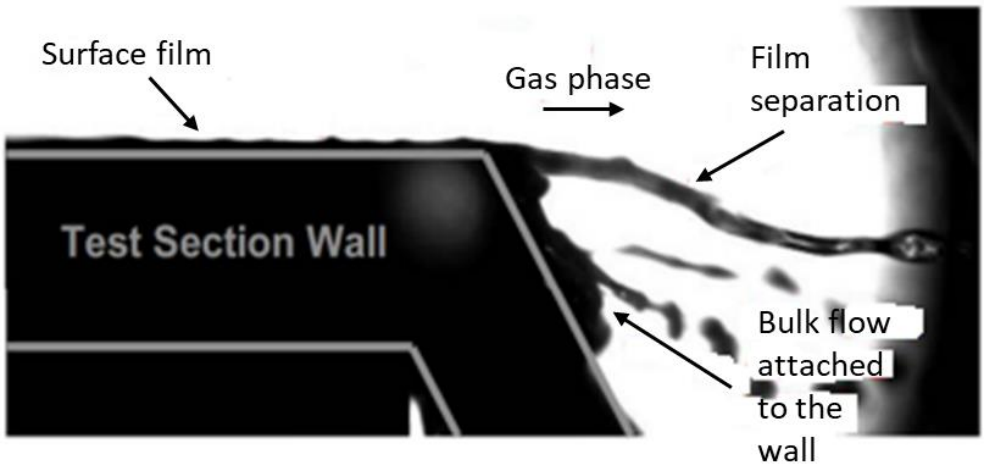


Figure 2-15: Film separation phenomenon following a sharp edge. Image from [135]

Numerous studies have examined the conditions that should be satisfied for film separation around edges to occur. Maroteaux et al. [136] highlighted that separation occurs after reaching a critical angle dependent on film perturbation amplitude and frequency. Friedrich et al. [135] observed about 90% of the liquid film separation

[7] The notation and classification of film thickness in given in Table 2-3.

occurs around corners; with films attached to thin walls beginning to separate at a force ratio of 1, separating approximately 5% of the film. The force ratio defined in this study compares inertia to restoring forces via local Weber, Froude and Reynolds numbers and corner angle. Based on these parameters, Friedrich et al. [135], proposed a model for edge separation. However, the behaviour of the droplet sizes stripped from the film analysed in this study was restricted to rectangular ducts.

2.3.3 The impact of droplets on liquid films

The impact of liquid droplets on moving liquid films is of great interest in many engineering applications and is encountered in cooling flows for power generation, flow within the cylinders in the car engine fuel systems and lubrication system in aero-engines. Understanding of the droplet impact on a liquid surface is relevant to this work as this flow phenomenon emerges as the jet impinges on the oil pool. It can be seen in literature that there is some research that has focused on droplet impact on static films and some on droplets in shear-driven flows. However, detailed analysis of the flow dynamics of the interactions between droplets and shear-driven films is limited in prior work.

Alghoul et al. [137] investigated the impact of deforming droplets on films in shear-driven flows as illustrated in Figure 2-16. They observed both 2D and 3D wave patterns on the film surface. Although there was no distinct transition between 2D rolling and 3D waves, the low film loading caused 2D wave structures and high loading produced 3D surface waves, which resulted in secondary droplets. Their experiments were

conducted at low Weber numbers with large droplets with diameters exceeding 2400μm. The authors reported that the impact mechanism on a static film is different to the process on a shear-driven film, but the impact caused by spherical droplets on shear-driven flows is comparable to that on static films.

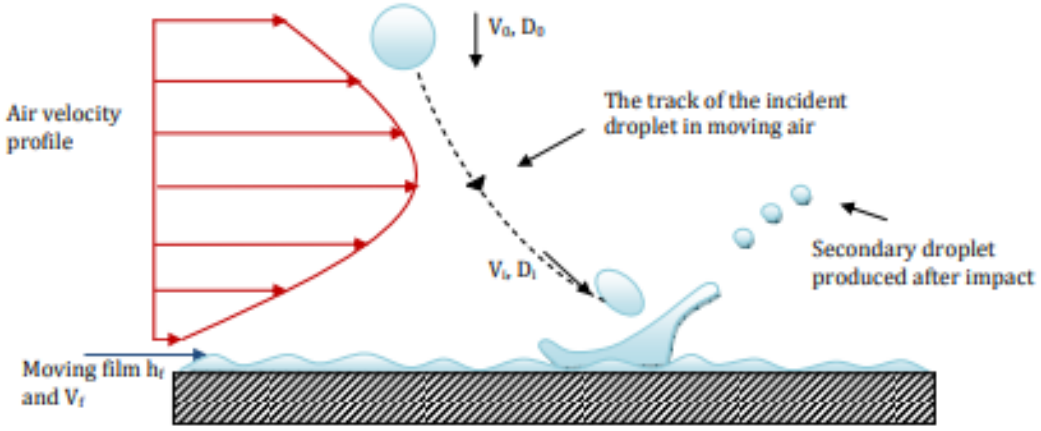


Figure 2-16: Deformation of droplets in a shear-driven flow [137]

2.4 Interface dynamics and behaviour

When multiple fluids come into contact, their molecules can interact in different ways. They may mix together or remain separated by what is referred to as a fluid interface. In CFD, it is crucial to understand how these interfaces function so that appropriate boundary conditions in the models can be established. To accurately represent fluid interfaces in the continuum descriptions, the various physical phenomena that occur at these boundaries must be accounted for. Free-surface modelling entails the numerical representation of hydrodynamic field variables across three domains: the gaseous phase, the liquid phase, and the liquid-gas interface. This interface, characterized by a

discontinuity in fluid properties, is known as a free surface. The discontinuous nature of physical properties at the free surface and the interfacial effects, demand accurate and comprehensive models of fluid behaviour. Various numerical methods have been developed to address flows with sharp interfaces, each employing different simplifications. The selection of an appropriate simplification method is often application-specific, considering factors such as the Reynolds number, Weber number, and Froude number of the flow regime in question.

One common simplification approach is that both gas and liquid phases are incompressible; the other is treating only the gas phase as compressible. Many modelling techniques address the momentum balance by breaking down the flow into distinct bulk phases and implementing a numerical jump condition at the free surface [138].

For instance, researchers like Navti et al. [139] and Caboussat [140] have developed models where the gas phase is considered compressible. In these models, the gas pressure is assumed constant and can be determined using the ideal gas law. The liquid phase, on the other hand, is governed by the Navier-Stokes equations. This approach has proven effective for flows with low Reynolds numbers and high viscosity, such as those involving molten metals [139]. In both of the simplification methods discussed above, the surface tension force at the free surface is balanced against the pressure difference, ΔP across the interface. This balance is described using the Laplace formulation: $\Delta P = \sigma_L \kappa_{if}$, where σ_L represents the surface tension and κ_{if} denotes the interface curvature [141].

Rotating flows featuring a free surface play a crucial role across diverse fields, from geophysical sciences to various industrial applications; such flows are particularly of interest in this work due to their relevance in the applications investigated and have been explored in detail in Chapters 4 and 5. These flows exhibit complex dynamics, and this has been demonstrated by a simple experiment: a cylindrical container partially filled with liquid, where the fluid motion is induced by a rotating disk while the side wall remains stationary. It has been found that a fascinating phenomenon occurs at sufficiently high rotation rates; the system undergoes a symmetry-breaking transition, resulting in the emergence of polygonal patterns on the free surface, rotating at a constant angular velocity. This intriguing effect, initially documented in [142], has been further investigated in subsequent studies [143, 144].

The behaviour and development of flow patterns in two-phase systems, as well as the properties of the gas-liquid interface, are significantly affected by interfacial shear stress. This stress plays a vital role in determining the dynamics of gas-liquid two-phase flows. While gas-liquid two-phase stratified flow exhibits a relatively simple flow pattern, accurately predicting the interfacial shear in this configuration remains a complex research challenge. This complexity arises from the intricate nature of momentum transfer occurring at the gas-liquid interface, despite the apparent simplicity of stratified flow. Understanding interfacial shear stress in two-phase flow systems is not only crucial for accurately calculating pressure drop but it also plays a fundamental role in modelling various two-phase flow phenomena. In gas-liquid two-phase flow in a pipe, the flow regime significantly influences the mechanisms contributing to the

frictional pressure drop. In such flows, frictional pressure drop arises primarily from two sources: friction between the fluids and the pipe wall, and friction at the gas-liquid interface [145]. In flow regimes with significant phase separation, such as stratified and annular flows, interfacial friction contributes substantially to the overall frictional pressure drop. This is due to considerable velocity differences (slippage) between the gas and liquid phases. Conversely, in flow patterns where one phase is dispersed within the other, like bubbly flow, interfacial friction becomes negligible. This is because there's minimal slippage between the phases, as they move at similar velocities.

In a gas-liquid annular flow that is characterized by high interfacial shear stress, the interfacial structure plays a crucial role in determining the flow behaviour. Due to its importance, the interfacial shear stress in annular flow has been the focus of numerous research studies over the years. Wallis [146] proposed a widely adopted model for interfacial shear stress using a friction factor, where the liquid film is treated as a form of wall roughness. This model introduces an interfacial friction factor and is derived from an analogy to a simplified friction correlation for fully rough pipes, though it's only valid for a limited range of roughness. This correlation has since been modified to extend its applicability to a broader range of film thicknesses by including minor adjustments to the form and constants of the original Wallis correlation and incorporating a Reynolds number dependency.

Kumar and Edwards [147] identified limitations in existing models for interfacial shear stress, noting the need for a physically-based model applicable to multidimensional predictions capable of incorporating wave characteristics. The researchers developed

the ‘law of the interface’ model, inspired by the law of the wall approach in turbulent flows. However, their model's void fraction predictions were less accurate due to inadequate mechanistic modelling of entrainment. Wang et al. [148] studied the impact of wave height on interfacial friction in annular gas-liquid flow. They discovered that as relative interfacial roughness decreases, the friction factor in annular two-phase flow reduces less considerably compared to single-phase flow. This phenomenon was attributed to the flatter wave shape characteristic of annular flow.

These studies highlight ongoing efforts to improve interfacial shear stress modelling in two-phase flows, addressing complexities such as wave characteristics and entrainment effects. A universal analytical solution for free-surface flow problems doesn't exist. Instead, researchers have developed various methods to solve a set of non-linear partial differential equations (PDEs) that describe these flows. These flow problems and be modelled using the Lagrangian or Eulerian frameworks [149].

The Lagrangian framework adopts a perspective that moves with the fluid, as if observing from within the flow itself. This can be thought of as imaginary points or particles embedded in the fluid, moving along with it. In contrast, the Eulerian framework takes a fixed perspective, observing the fluid as it passes through a stationary reference frame. This approach is often referred to as a grid-based method. Both these frameworks can be applied independently or in combination to solve fluid flow problems, each offering unique advantages depending on the specific scenario being analysed. These approaches can be further grouped into three categories: Lagrangian, Eulerian-Eulerian, and Eulerian-Lagrangian. The classification is based on

the mathematical treatment of each phase within the fluid system. A fundamental aspect of all these methodologies is the discretization of the fluid continuum into finite computational elements or localized reference frames. This discretization process forms the basis for numerical solution of the governing equations. In the context of flow modelling applicable to this thesis, the Eulerian-Eulerian approach is explored here.

A prominent homogeneous Eulerian-Eulerian based approach is the VoF method which is a technique used for simulating two-phase flows of incompressible and immiscible fluids with free surfaces. This method simplifies the complex interaction between two phases by focusing on their relative proportions within each cell of the computational domain. This VoF technique was pioneered by Noh & Woodward [150] and further developed by Hirt & Nichols [151]. VoF is considered a cost-effective solution for modelling segregated flows. It offers better memory efficiency compared to the marker-and-cell (MAC) method introduced by Harlow & Welch [152]. However, it's worth noting that poor choices in spatial discretization can lead to instabilities and unphysical results [151]. The VoF approach treats the fluid system as a single continuum with varying properties. These properties are defined by 'colour' functions, typically represented by the volume fractions of each phase. In a 2D context, as shown in Figure 2-17a, the volume fraction is calculated as the ratio of the liquid area, A_{liq}, to the total cell area, A_{cell}, as expressed in Equation (2-22).

$$\alpha_i = \frac{A_{liq}}{A_{cell}} \tag{2-22}$$

As shown above, the VoF technique is predicated on tracking the fractional volume of liquid within each computational grid cell. This volume fraction, typically denoted by α_i, is a scalar quantity constrained between 0 and 1. This function is defined as α_i = 1 for cells fully occupied by liquid, α_i = 0 for cells filled with gas, and 0 < α_i < 1 for cells containing the interface between phases. It's crucial to note that VoF doesn't explicitly define a free surface; rather, it quantifies the presence of bulk fluid. This characteristic allows for the seamless computational handling of fluid coalescence and breakup phenomena.

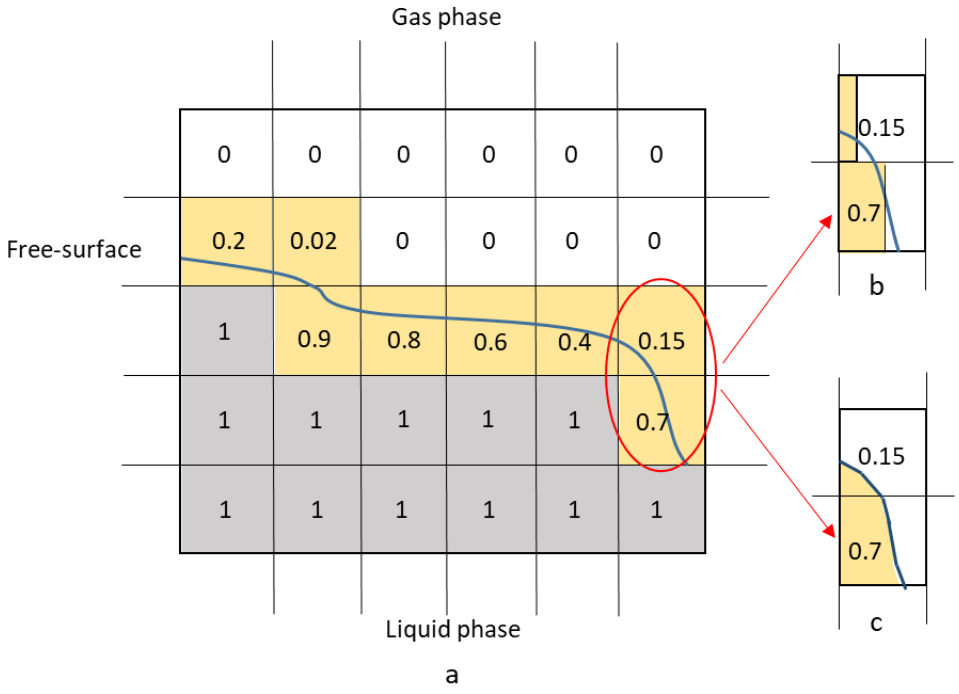


Figure 2-17: (a) Free surface construction in VoF; (b) Simple line interface construction (SLIC); (c) Piecewise linear interface construction (PLIC) (after the style of Martinez et al. [153])

Free surfaces are implicitly defined where the fluid volume fraction transitions from 1 to 0, rendering VoF highly versatile for a wide spectrum of free surface problems. A key attribute of this approach is the representation of fluid location through a single scalar value for each grid element. Early implementations of the VoF method utilized simplified approaches for interface reconstruction. These initial models employed first-order approximations or basic geometric representations to estimate the fluid interface within computational cells, specifically, the Simple Line Interface Calculation (SLIC) technique [138, 151] as illustrated in Figure 2-17b. The VoF technique has undergone continuous refinement processes over the years to improve the prediction accuracy of the free-surface. A significant advancement was the introduction of the Piecewise Linear Interface Calculation (PLIC) method, which improved interface representation by using a series of connected linear segments. This technique is shown in Figure 2-17c.

While VoF methods are renowned for their excellent mass conservation properties, challenges lie with accurately predicting interface normals and curvatures, which are crucial for phenomena such as surface tension modelling. To address these limitations, Bourlioux [154] proposed coupling the Level Set (LS) function with VoF in 1995, an approach further advanced by Sussman & Puckett [155]. The LS function, a smooth, and continuous function, is advected similarly to the volume fraction in VoF. This coupling strategy combines the interface capturing capabilities of LS with the mass conservation strengths of VoF [156]. Surface tension forces can be modelled using continuum surface force approaches, such as the Brackbill model [157], which relies on accurate interface curvature capture. The VoF technique on its own, tends to

overestimate surface tension forces without appropriate capturing of the interface curvature. This can lead to erroneous predictions of dry-out in flows where surface tension is significant [158].

Saurel & Abgrall [159] proposed a noteworthy extension of the VoF method for compressible multiphase flows. This approach utilized a comprehensive equation system that addresses partial pressures, surface tension, interface velocity relaxation, and mass transfer coupled with volume fraction evolution. While their approach showed promising results for supersonic regimes, these high-speed flows are not relevant to this work. For the application of interest in this work, particularly the flow in a hydraulic seal, the incompressible flow assumption remains adequate. Nonetheless, accurate free-surface prediction plays a crucial role in modelling these flows, highlighting the importance of interface capturing techniques in simulating the complex fluid dynamics within hydraulic seals.

2.5 Non-isothermal flows

When designing a hydraulic seal, several factors must be considered: the range of pressure differences the seal must withstand, the power required to operate the seal, and the heat transfer with surrounding walls. Therefore, an accurate estimate of the heat transfer in a hydraulic seal is extremely important. In a rotating hydraulic seal, the working fluid or oil that is supplied, is subjected to centripetal forces due to the angular velocity of the rotating shafts. The oil then fills the inter-shaft cavity within the trough to an extent that immerses the fin. The columns of oil either side of the fin form a barrier

to air creating a radial pressure gradient across the annular cavity sustaining the differential air pressure either side of the seal. The velocity gradient in the oil formed as a result of the differential rotational velocities between the trough and the fin, causes a frictional drag between both rotating surfaces and the oil. Significant amounts of heat that is generated due to this shearing of the oil is known as viscous heating and cannot usually be dissipated adequately to mating components through the natural means of heat transfer mechanisms such as conduction or radiation [1]. This could result in a rapid temperature increase of the bulk oil. To minimize the effects of this viscous heating and maintain the oil temperatures at acceptable levels so that seal functionality can be preserved, a through-flowing system with a continuous oil feed is required [59]. Failure to maintain a continuous replenishment of oil could result in increased local temperatures leading to oil coking [59]. In his patented work, a baffle is introduced by Bock [160] to define a flow path to minimize the residence time within the seal in order to eliminate the above mentioned issues. The purpose of this design was to limit the oil temperature from exceeding the maximum allowed so that the seal could be used in hotter regions of the engine. The literature has been reviewed and it is evident that the amount of prior work related to heat generation and transfer within hydraulic seals is very little. Therefore, the focus of this section is to provide insights into prior work on heat transfer in (i) rotor-stator disk systems and (ii) oil related applications due to its relevance and the possibility of extending the correlations to the case of a hydraulic seal.

2.5.1 Heat transfer within flows in rotating disk systems

Heat transfer characteristics of rotating disk systems have been an important research focus since the 1950s, motivated by applications such as turbine rotors, combustion chambers, and agitated vessels. Foundational experimental studies by Millsaps [161], on laminar heat transfer coefficients of single spinning disks in enclosed systems was based on the similarity solution study of von Kármán [29]. This was later extended to the turbulent flow through a series of experimental investigations by Cobb and Saunders [162] who concluded that the heat transfer coefficients of the rotating disk are significantly impacted by the turbulent flow leading to an increase.

Nikitenko [163] performed one of the early experiments on heat transfer of rotor-stator cavities, where he investigated different cavities across aspect ratios ranging between $0.018 < G < 0.085$ at $Re_\Omega < 1\times10^6$ with both disks maintained at isothermal conditions. They derived correlations between Nusselt number and Reynolds number, demonstrating that the heat transfer is enhanced substantially under turbulent flow. Through these investigations, the authors succeeded in deriving generalized correlations for local distributions of Nusselt number (Nu_r), defining the relationship as $Nu_r = h_T r/k_f$ where h_T and k_f are the convective heat transfer coefficient and the thermal conductivity of the fluid, for laminar and turbulent flows respectively. The correlation proposed for the Nusselt number on the rotor by the authors for laminar flow is given in Equation (2-23) while that for turbulent flow is represented by Equation (2-24). However, these correlations did not account for the effects of the aspect ratio.

$$Nu_r = 0.675 Re_\Omega{}^{0.5} \tag{2-23}$$

$$Nu_r = 0.02175 Re_\Omega{}^{0.8} \tag{2-24}$$

Owen et al. [164] combined a theoretical analysis with an experimental study to investigate the heat transfer over rotating disks. Three scenarios were considered in this study: a free spinning single disk, a rotor-stator cavity, and a rotor-stator cavity with through-flow. Different aspect ratios between G = 0.0067 – 0.18 were investigated across a range of disk rotational numbers $2\times10^5 < Re_\Omega < 4\times10^6$ for the rotor-stator cases. For the through-flow setup, coolant fluid was injected through a hole on the adiabatic stator. In the experimental arrangement, the rotor was set-up as the heat source for all the scenarios considered. The findings of this study can be summarised as below:

- For the free spinning disk case, the mean Nusselt number $\overline{Nu_r}$ was dependent on the aspect ratio of the rotor-stator cavity. As the aspect ratio G approached infinity, the mean Nusselt number of the free disk $\overline{Nu_{r,d}}$ converges to the value given by $\overline{Nu_{r,d}} = 0.017 Re_\Omega{}^{0.814}$.

- Couette type flows were observed at low aspect ratios of $G < 0.01$ where $\overline{Nu_r} > \overline{Nu_{r,d}}$. This type of flow is represented by Regions I and III in Figure 2-6.

- In the range of $0.01 \leq G \leq 0.06$, the flow was observed to be Batchelor regime (Regions III and IV in Figure 2-6) with the central core rotating. In this region,

the mean Nusselt number was found to be $\overline{Nu_r} < \overline{Nu_{r,d}}$, less than that for the free spinning disk.

- For any aspect ratio higher than $G > 0.06$, the observation was $\overline{Nu_r} = \overline{Nu_{r,d}}$, implying that the mean Nusselt number is independent of the cavity aspect ratio. The study also showed that for any aspect ratio where $G > 0.06$, the rotor heat transfer process becomes similar to that of a single disk with the convective heat transfer coefficient of the rotor becoming disassociated from that of the stator.

- Finally, the study revealed that the mean Nusselt number increases with the through-flow showing that through-flow has a high degree of influence on heat transfer rates.

The majority of the initial studies on heat transfer in rotating disks were undertaken in the years prior to 1990, as detailed in Owen & Roger [165] and Owen [166]. The main focus of these studies was to determine the bulk heat transfer properties in laminar and turbulent flow regimes and the influence of geometrical characteristics on heat transfer properties. These investigations focused on defining different local and average Nusselt number correlations to capture these effects. However, with the developments in rotating disk boundary layer models during the 1990s, much emphasis was placed on the heat transfer studies of single and two-disk systems. As a result, more recent investigations have received greater attention, shifting focus from bulk correlations to detailed boundary layer models and their implications on heat transfer.

Elkins and Eaton [167] performed an in-depth experiment on a heated single rotating disk for Reynolds numbers up to $Re_\Omega = 1 \times 10^6$. The investigations revealed that the low temperature difference in the experimental set-up led to the thermal transport being treated as a passive scalar with a minimal effect on flow velocity fields. The authors highlighted that the convective heat transfer coefficient h_T was fairly constant in the laminar region, but varied as $h_T \propto r^7$ with the onset of turbulence and $h_T \propto r^{0.6}$ in the turbulent region. They also compared the effect of momentum and thermal transport properties in these boundary layers with the corresponding two-dimensional boundary layers. In this study, with a demarcation boundary at $\frac{z}{\delta} \approx 3$, the boundary layer was separated into two regions, inner and outer. This demarcation height refers to the distance normal to the rotating disk as a function of the thickness of the boundary layer on the rotating wall. The results obtained suggested that the three-dimensional nature of the rotating disk boundary layer affects the turbulence and heat flux resulting in reduced correlation coefficients and turbulent Prandtl number, Pr_{turb} [8], compared to a 2D boundary layer.

Serre et al. [168] conducted one of the first noteworthy numerical investigations of the heat transfer in a rotor-stator disk system using a DNS approach for a cavity with an aspect ratio of $G = 0.426$ at $Re_\Omega = 1.1 \times 10^5$. The instantaneous temperature distributions within the cavity were visualised in this study showing that the hot large-scale patterns

[8] The turbulent Prandtl number, Pr_{turb}, quantifies the comparative efficacy of turbulent mixing of heat and momentum. It is defined as $Pr_{turb} = \frac{\varepsilon_M}{\varepsilon_H}$ where ε_M is the eddy diffusivity for momentum and ε_H is the eddy diffusivity for heat.

extended towards the rotor, which the authors attributed to effect of Ekman pumping. The temperature visualizations also showed a hot flow region elongating from the rotor hub to one third of the radii difference, $\Delta r = (r_o - r_i)$ where r_i and r_o are the inner and outer radius of the annular cavity respectively. The effect of buoyancy was also examined in this study at Rayleigh numbers of Ra = 0; 2 × 10^4; and 2 × 10^6. As discussed in the study of Elkins and Eaton [167], although the effects of buoyancy on the velocity fields were minimal, the mean temperature gradients were significantly affected. At higher Rayleigh numbers, when Ra = 2 × 10^4; and 2 × 10^6, a considerable temperature decrease was observed in both boundary layers, while the core temperature distribution remained fairly constant compared to when Ra = 0. This work was later built on by Poncet and Serre [169] by considering a cavity with an aspect ratio of G = 0.2 across a wider range of Reynolds numbers up to Re_Ω= 1 × 10^5, and Rayleigh numbers up to Ra = 1 × 10^8.

Tuliszka-Sznitko et al. [170] used LES to investigate heat transfer characteristics in rotor-stator cavities of two configurations. The first cavity of G = 0.2 was investigated at Re_Ω= 1 × 10^5, the second cavity of G = 0.11 was investigated at Re_Ω= 1.5 × 10^5. In their simulations, the thermal Rossby number, $B_{thermal}$, was taken as 0.01 and 0.4. The thermal Rossby number was defined as $B_{thermal} = \beta_{thermal}(T_2 - T_1)$ where T_2 and T_1 are the respective temperatures of the stator and rotor, and $\beta_{thermal}$ is the fluid thermal expansion coefficient. The local Nusselt number distributions obtained for rotor and stator showed an increase with the increasing Reynolds number, suggesting

an increase in the heat transfer rates. The study also identified that the effect of thermal Rossby on the local Nusselt numbers is comparatively negligible.

In a later study, Tuliszka-Sznitko et al. [171] attempted to validate axial distributions of Reynolds stresses, temperature fluctuations, and turbulent heat fluxes against previous experimental measurements by Elkins and Eaton [167] using both DNS and LES. This investigation considered rotor-stator cavities over a range of aspect ratios $G \approx 0.02 - 0.5$ and Reynolds numbers $Re_\Omega = 1 \times 10^5 - 2.9 \times 10^5$. The authors demonstrated that the variations in geometrical aspects, such as G and R_m, have a more pronounced effect on Reynolds stress components and turbulent heat fluxes compared to the structural parameters. The latter exhibited lower sensitivity to these geometric alterations.

2.5.2 Oil related heat transfer

As discussed in Chapter 1, the improvements in efficiency of modern aero-engines are associated with higher turbine inlet temperatures, pressures, and rotational speeds. These conditions require detailed understanding of two-phase flow physics in secondary air and oil systems to accurately predict oil heat transfer. Some of the work in this regard reports that high speeds significantly increase heat transfer in bearing chambers, negatively impacting heat-to-oil management [172]. Reaching these operating conditions results in high wall temperatures which can lead to oil coking and fires [172, 173]. Therefore, it is essential to consider the heat transfer along the housing wall, in addition to the heat sources such as bearing friction and churning, to meet the

safety and reliability needs of the modern aero-engine. However, reliable correlations related to the oil related heat transfer in engine applications is extremely limited in the open literature due to the existence of many possible flow regimes and phase interactions that cannot easily be determined under real engine conditions and the scarcity of relevant experimental data.

One of the earlier investigations in this respect was an investigation by Zimmerman et al. [173] who presented an approach to include two-phase flow correlations in computations of aero engine air/oil systems. The authors compiled an extensive review of the difficulties associated with the development of reliable correlations for the heat transfer inside the bearing chamber walls and two-phase flows in air/oil systems of aero engines. To overcome some of these uncertainties, the authors investigated the performance of a vent system at high altitude presenting pressure loss correlations for air/oil flow in different elements in the system. The authors indicated that these correlations were in agreement with the experimental results and also extended the study by carrying out a numerical computation using a two-dimensional two-fluid code.

To address the uncertainties in the design process highlighted by Zimmerman et al. [173], a bearing chamber test facility was developed at the Institute for Thermal Flow Machines (ITS) at the University of Karlsruhe. Using this facility, Wittig et al. [174] conducted an experimental investigation presenting detailed descriptions of the relevant flow phenomena and internal wall heat transfer analysis. Building upon this work, Glahn and Wittig then characterized the momentum transfer in bearing chamber oil films [175]. This study demonstrated that gravity effects cannot be neglected and must

be considered in analyzing oil film flows, even with the high shaft speeds and small chamber clearances typical of modern jet engines.

Later, Glahn and Wittig [176] presented analytical approaches to characterize oil films and related heat transfer, comparing them to experimental data obtained from the bearing chamber test rig at the University of Karlsruhe. The authors showed that heat transfer coefficients on internal bearing chamber walls can be estimated quite well with measurements of oil film thickness and velocity using correlations between momentum and heat transfer. However, this approach cannot capture the effects of droplet impingement, which can substantially increase local heat transfer. Therefore, direct heat transfer measurements were also obtained to fully characterize the heat transfer. The authors defined the temperature of the film flow, T_F, relating it to the distribution across the oil film as given in Equation (2-25).

$$\frac{\dot{q}}{\dot{q_W}} = \left(\frac{1}{Pr_F} + \frac{1}{Pr_{turb}}\frac{\upsilon_t}{\upsilon_F}\right)\frac{dT_F{}^+}{dz_F{}^+} \tag{2-25}$$

The non-dimensional temperature of the oil film, $T_F{}^+$, was defined by Equation (2-26).

$$T_F{}^+ = \frac{(T_W - T_F)\rho_F C_{p.F} U_\tau}{\dot{q}_w} \tag{2-26}$$

Here, the shear velocity, U_τ, is given as:

$$U_\tau = \sqrt{\frac{\tau_W}{\rho_F}} \tag{2-27}$$

where T is temperature, $\dot{q}$ is the heat flux, Pr is the Prandtl number, z denotes the distance from the wall. ρ, C_p and τ represent the density, specific heat at constant pressure and shear stress respectively. The subscripts W and F refer to wall and fluid respectively.

The authors highlighted that the characterization of heat and momentum transfer in oil film flows requires an appropriate estimate for the eddy viscosity term, $\frac{\upsilon_t}{\upsilon_F}$, and the turbulent Prandtl number, Pr_{turb}. This study used the empirical correlation for the eddy viscosity by Deissler [177] and a $Pr_{turb} \sim 1$. Based on these correlations, using an analytical approach, the authors presented profiles for temperature, turbulent heat transfer and Nusselt number for oil film flows for conditions typically experienced in aero-engine bearing chambers. They found some qualitative and quantitative agreement between the theoretical and experimental results and pointed out that a proper characterization of the oil film flows is crucial for accurate thermal analysis. The authors concluded that more experimental heat transfer data was needed for representative bearing chamber conditions to further validate the analytical approaches.

Expanding on the work by Glahn and Wittig [176], Glahn et al. [172] presented a discussion on local and mean heat transfer coefficients based on their systematic investigation of internal bearing chamber wall heat transfer examining the effects of

flow rate and rotational speed. This study, however, did not consider the effect of geometric parameters. The authors found that sealing air mass, lubrication oil flow rate, and rotational speed increase heat transfer, with the effects of sealing air and speed being more significant than the effects of oil flow. Circumferential distribution of heat transfer is highly speed-dependent, with large non-uniformities at high speeds. They further added that the local heat transfer near disks varies significantly with the momentum flux between the flow radially pumped outward and the flow superimposed axially at the edge of the disk.

Building upon the work of Glahn et al. [172], Busam et al. [178], performed a series of experiments to examine the geometry effects of a rear bearing chamber on internal wall heat transfer using an almost identical test rig arrangement as Glahn et al. [172]. The findings of this enabled the authors to derive an empirical correlation for the wall heat transfer for the internal bearing chamber housing wall in terms of non-dimensional parameters accounting for the impacts of geometrical characteristics, flow rates and rotational speeds. Combining the individual analogues between heat transfer and operating conditions such as sealing air mass flow, lubrication oil flow and rotational speeds, this study presented a generalized heat transfer correlation as given in Equation (2-28).

$$Nu_{D_h} = 0.35 \cdot {D_h}^{1.46} \cdot {Re'_A}^{0.48} \cdot {Re'_{OF}}^{0.32} \cdot {Re'_\Omega}^{0.35} \quad (2\text{-}28)$$

where the Nusselt number, Nu, is expressed as a function of the hydraulic diameter, D_h; rotational Reynolds number, Re_Ω, as defined previously, is based on the shaft speed and same characteristic length; air flow Reynolds number, Re_A; oil film flow Reynolds number, Re_{OF}. The prime notations have been used to define the flow Reynolds numbers based on the interpretation of the hydraulic diameter that has been calculated from $D_h = \frac{4A}{\varphi}$, with A referring to the area of the bearing chamber and φ denoting the circumference of the chamber.

2.6 Flow within hydraulic seals

A strong foundation on research into hydraulic seals has been laid at the University Technology Centre at the University of Nottingham, Karlsruhe Institute of Technology (KIT), and Rolls-Royce with their knowledge and expertise in this field. This has resulted in key analytical, numerical, and experimental investigations of hydraulic seals. The fundamental application specific works available in the open literature is discussed in this section.

One of the earlier published works in this regard is a numerical investigation by Young and Chew [26] to assess the applicability of the VoF method to model hydraulic seals. The authors reported a satisfactory 2D axisymmetric modelling strategy using ANSYS-Fluent to capture the essential flow behaviour in an engine representative hydraulic seal. This study concluded that while the VoF approach is a suitable modelling strategy for air/oil system applications, where a well-defined interface between the gas and

liquid phases exists, it is not able to provide an appropriate solution to capture some of the complex two-phase flow phenomena as that in bearing chambers.

Denecke et al. [19] investigated the effect of oil levels in a classic and advanced hydraulic seal over a range of different engine operating conditions. The authors presented a comparison between the oil level estimates evaluated using analytical approaches. To verify the validity of the assumptions made in the analytical prediction methods, the authors conducted numerical simulations in Fluent using a VoF method. The analytical and numerical results were validated against experimental results obtained from a co-rotating two-shaft test rig. In addition, they introduced an expression to account for swirl velocity, pressure and power consumption for a hydraulic seal geometry which was in close agreement with the numerically evaluated swirl velocity values. Comparing the classic and advanced hydraulic seal designs, they established that the oil angular velocity was affected significantly by the oil mass flow in the advanced seal design. The study also reported that the analytical approximations were found to be in good agreement with numerical results for the classic seal design.

Building on the previous work by Young and Chew [26], a CFD methodology to compute the maximum pressure capacity of a hydraulic seal was presented by Mathews et al. [27]. To verify the suitability of the approach, the CFD results were compared to experimental data collected from a hydraulic seal test rig. The authors developed a non-dimensional design approach to assess the performance of hydraulic seals based on a parametric study to determine the influence of different parameters on the maximum pressure capacity of the seal.

2.7 Summary

The literature has been reviewed to establish the state of the art with regard to modelling hydraulic seals. Even though there has undoubtedly been research conducted into formation, performance and breakdown of hydraulic seals, due to the proprietary nature of the research, very little data exists in the public domain. Computational modelling of these elements is challenging as it involves highly rotational multiphase flow with complex geometry and transient effects. This necessitates the capability to model the highly complex, turbulent flow accounting for numerous flow patterns and phase interactions. The difficulty lies with scarcity and relevance of experimental data due to the existence of various features of the flow making the experimental process extremely costly to conduct under real engine conditions.

Various flow phenomena encountered in the hydraulic sealing application have been reviewed in this chapter and various techniques used to predict the flow field in each of these flow mechanisms have been identified. A number of studies have estimated and measured important flow parameters such as core swirl ratio in a stator-rotor cavity, flow instabilities, droplet impact on oil films, primary and secondary break-up of jets that are also relevant in a hydraulic seal applications. However, the existing literature does not capture all likely aspects of hydraulic seal flow including viscous heating, radial velocity variation in oil, and the jet impact on a pool of oil. Some of the relevant published correlations and modelling techniques are incorporated into the numerical

model formulation to examine the performance of hydraulic seals in the latter part of this thesis.

A few studies have attempted to model the flow in a hydraulic seal. Different numerical models have been utilized to account for the multiphase, turbulent, and highly rotational air-oil flow. These include thick rimming oil film assumptions and VoF modelling to simulate the gas-liquid flow, using various numerical algorithms. However, there is still an acknowledged need to consolidate the existing numerical and analytical approaches to explore the reliability of these models which would ultimately result in improved modelling capability of hydraulic seals.

CHAPTER 3

3 Development of the Numerical Framework

3.1 Introduction

This chapter outlines the methodology used to establish a technique to model hydraulic seals using Computational Fluid Dynamics. The developed approach is used to understand the interfacial flow physics of intershaft hydraulic seals as discussed in Chapters 5 and 6.

Reasons such as the complex nature of the multiphase flow in a bearing chamber, a key location where intershaft seals are used, constraints on instruments used for testing and high costs are some of the challenges associated with experimental procedure. Also, difficulties associated with resolving individual attributes of the flow field, various undesirable flow features such as air droplet-film interaction that are unavoidable, choice of boundary conditions that governs a detailed quantitative analysis of the oil film demonstrate that the use of CFD software is a preferable alternative [179].

The CFD work reported in this thesis was carried out in three steps.

- Pre-Processing- This step involves the generation/simplification of the geometry and generating a numerical grid that will be used by the CFD solver. The geometry was generated using a CAD software – ANSYS-SpaceClaim and DesignModeler were used in this work. The numerical grids were generated within ANSYS-Mesher, Fluent-Mesher and ICEM CFD Meshing.

- Solving- Governing equations of fluid flow is solved on the numerical grid with the aid of a solver. ANSYS-Fluent was used in this work.

- Post-Processing- The data acquired from the solver has to be analysed using a suitable post-processor. Fluent, CFD-Post, MATLAB, Movie maker and MS Excel were used for post-processing of data.

This chapter also describes the fundamental concepts of numerical modelling of multiphase flows, it entails various methods and techniques that have been adopted on the physical setup which needs to be represented. The simulation results have been validated against the experimental results available in literature.

3.2 Geometry generation

The numerical simulations are based on a model representative of a hydraulic seal geometry that was investigated experimentally. The geometry of the seal was initially simplified to a 2D geometry using ANSYS-SpaceClaim. This was done with the aim

of developing a reliable methodology that can then be extended to investigate a full 3D model. The 3D model was simplified on SpaceClaim by modifying the CAD geometry of the hydraulic seal used in the experimental study conducted at the University of Nottingham. The respective geometries modelled are shown in the respective chapters. The fluid domain was then extracted with the Boolean tool. The extracted fluid domains used in different CFD studies have been presented in the respective chapters. A further investigation was done to investigate the jet impact on the trough in which an oil jet was housed in addition to the fluid domain and has been presented in Chapter 6.

3.3 Numerical Grid

The 2D geometry created for the CFD studies was discretized using ANSYS-meshing. Cell sizes up to 0.1 mm were used to create the grids. In the near wall regions cell sizing were adopted to suit the requirement of the turbulence model that was used. This was done by imposing sizing functions at the edges of the walls in the domain. Several grids were created in order to assess the dependency of the solution on the grid. A grid that was developed using a core cell sizing of 0.25 mm was used as a base mesh in all the 2D studies. The generated grids were assessed by aspect ratio and orthogonal quality to ensure that the quality requirements of a typical grid used for CFD investigations was adhered to. The quality of the grid and grid independence is discussed in depth in the respective chapters following the introduction of various concepts and variables that were used in grid independence studies.

3.4 Numerical Modelling

3.4.1 Fundamental concepts of flow equations

The foundation of CFD is the fundamental governing equations of fluid dynamics. The governing equations of fluid flow are formed upon the mathematical framework of the conservation laws of physics and can be summarised as follows:

- Conservation of mass explains that the mass of each fluid particle is conserved.
- Newton's second law states that the rate of change of momentum is equal to the net force exerted on a fluid particle.
- First law of thermodynamics conditions the rate of change of energy of a fluid particle is equal to the net heat flux and the work done on it.

The above laws represent the conservation of continuity, momentum and energy respectively and the derived mathematical expressions are accounted for in the Navier-Stokes (NS) equations that describe a compressible, unsteady viscous flow. Detailed derivations of the fluid flow equations can be found in text books and a comprehensive study of the concepts described in the following subsections is presented by Versteeg and Malalasekera [180].

As the macroscopic properties of a fluid particle are not influenced by individual molecules, a small element such as a fluid particle with sides $\delta x, \delta y, \delta z$ are considered and presented for a continuum fluid as reported in the following subsections.

3.4.1.1 Mass conservation

The continuity equation is an expression of conservation of mass within a control volume and is given by:

$$\frac{\partial \rho}{\partial t} + \nabla \cdot (\rho U) = 0 \tag{3-1}$$

where ρ the fluid density and U is is the flow velocity vector. U can be expressed in index or Cartesian vector notation. The index representation is given by, $U = (U_1, U_2, U_3)^T$ and the Cartesian vector notation is expressed as $U = U_1\hat{\imath} + U_2\hat{\jmath} + U_3\hat{k}$. The vector components are represented by U_1, U_2, U_3 and Cartesian unit vector components are denoted by $\hat{\imath}, \hat{\jmath}, \hat{k}$.

In simplified terms, Equation (3-1) states that the rate of variation of mass within the control volume, denoted by the term on the left hand side, is equal to the net rate of mass flow leaving the volume, denoted by the second term.

Equation (3-1) is reduced to (3-2) as the incompressible fluid flow condition is assumed. The flow is assumed to be incompressible if the speed of both liquid and gas in the flow is much lower than speed of sound ($Ma << 1$) throughout the domain.

$$\nabla \cdot U = 0 \tag{3-2}$$

or, using the Cartesian co-ordinate system,

$$\frac{\partial u}{\partial x} + \frac{\partial v}{\partial y} + \frac{\partial w}{\partial z} = 0 \tag{3-3}$$

where u, v, w are velocity components in x, y, z directions respectively.

3.4.1.2 Momentum conservation

The momentum equation for an incompressible fluid in an Eulerian reference frame is expressed as follows:

$$\frac{\partial}{\partial t}(\rho U) + \nabla \cdot (UU) = -\nabla p + \nabla \cdot \mu[\nabla U + (\nabla U)^T] + \rho g \tag{3-4}$$

The momentum equation is a mathematical expression stating the sum of rate of momentum change in a control volume and momentum flow over the volume equals the surface forces and volume forces. In other terms, the inertial terms which include unsteady and convective acceleration are balanced by the divergence of stress and body forces.

The momentum equation tailored to the incompressible flow takes the following form:

$$\rho\left(\frac{\partial U}{\partial t} + \nabla \cdot (UU)\right) = -\nabla p + \nabla^2 \mu U + \rho f \tag{3-5}$$

3.4.1.3 Energy conservation

The energy equation for multi-phase flows takes the following form:

$$\frac{\partial}{\partial t}(\rho E) + \nabla \cdot \left(U(\rho E + p)\right) = \nabla \cdot \left(k_f \nabla T\right) + S_h \tag{3-6}$$

where E denotes the internal energy of the fluid particle, k_f is the thermal conductivity T is temperature and S_h is source term which refers to heat generation.

In the VoF model, a pressure based solver is employed where energy and temperature is computed by mass-averaging both quantities over the control volume as shown below.

$$E = \frac{\sum_{i=1}^{n} \alpha_i \rho_i E_i}{\alpha_i \rho_i} \tag{3-7}$$

$$T = \frac{\sum_{i=1}^{n} \alpha_i \rho_i T_i}{\alpha_i \rho_i} \tag{3-8}$$

E_i, from phase i to n, depends on the specific heat and shared temperature for each phase, α is the phase volume fraction.

3.4.1.4 Equation of state

The relationship between pressure and the conserved quantities is described by the equation of state. This expression is used to close the system of equations when the energy equation is written for a stationary control volume, specifying the source terms explicitly, as there are 7 variables namely, $\rho, U_1, U_2, U_3, p, T, E$ and 5 equations which are continuity equation; momentum equations in x, y and z directions; and the energy equation.

Pressure is related to the density and temperature by the use of the ideal gas equation.

$$p = \rho R_w T \tag{3-9}$$

In Equation (3-9), R_w is the specific gas constant which is the ratio of universal gas constant to the effective molecular weight of the mixture. T can also be expressed as:

$$T = \frac{1}{c_v}(E - \frac{1}{2}|U|^2) \tag{3-10}$$

Where c_v is the specific heat at constant volume.

3.4.2 Turbulence Modelling

Turbulence is a naturally occurring phenomenon in fluid flows at high Reynolds numbers, where fluid particles deviate from the mean flow path randomly. The

turbulence characteristics are properties of the flow, not of the fluid. So each turbulent flow is unique and depends on external factors and boundary conditions, making it more complex to study than laminar flows. Instability mechanisms such as, Tollmien-Schlichting waves in 2D boundary layers and Type I, II, III instabilities in 3D boundary layers can trigger turbulence. However, the onset of turbulence does not follow an abrupt course, this evolves through a transition region. This transition region may consist large-scale coherent structures that are not fully random.

It is evident that the flow type in a hydraulic seal is turbulent with separated boundary layers as reported in the literature survey, and modelling the flow within a hydraulic seal is a major research focus within the scope of the research undertaken. Therefore, understanding the concept of turbulence and how it is modelled is essential. There is no exact definition for turbulence however, turbulent flows display distinct characteristic features. The characteristic features of turbulent flows are that they are diffusive, dissipative and chaotic. Turbulence is characterised by the non-dimensional parameter, the Reynolds number (Re) given by Equation (3-11). As the flow exceeds a critical Reynolds number the flow transitions from laminar to turbulent as shown in Figure 3-1.

$$Re = \frac{\rho U L}{\mu} \tag{3-11}$$

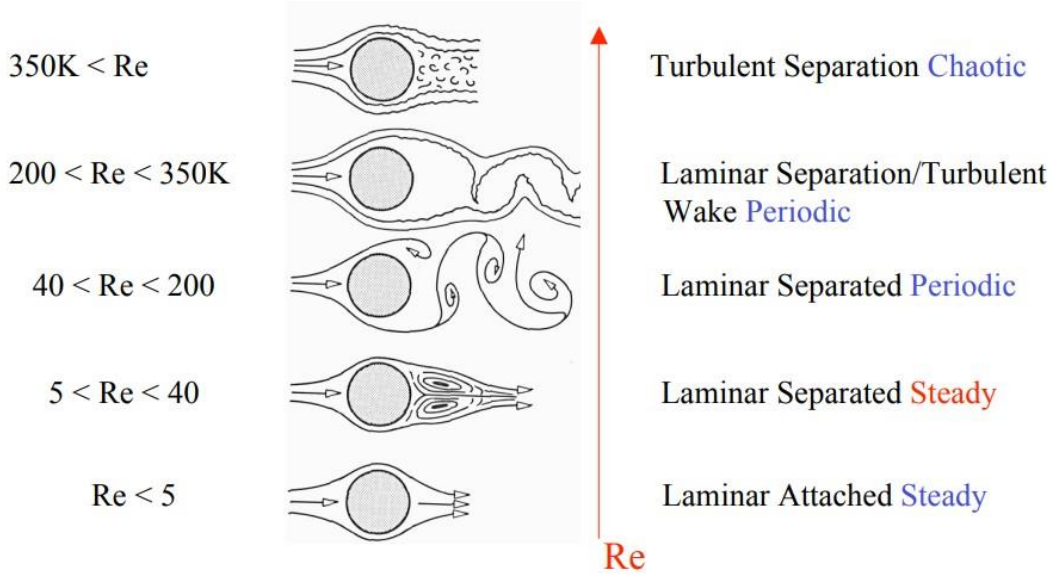


Figure 3-1: The effect of Reynolds number on the flow [181]

Some of the major challenges in modelling turbulence is the fact that turbulent flows operates over a wide range of length and time scales, the unsteady aperiodic motion, random spatial variations and strong dependence from initial conditions. The largest of the length scales are referred to as integral length scales and the smallest length scales are referred to as the Kolmogorov length scales, given by Equations (3-12) and (3-13) respectively. The largest time scales are referred to as large eddy turnover and the smallest time scales are referred to as the time scale for small eddies, given by Equations (3-14) and (3-15) respectively. The wide range of length and time scales make turbulence very computationally expensive to model, as this will require resolving the flow from the smallest scales all the way up to the largest scales [182].

$$l_0 \, \alpha \, \frac{k^{3/2}}{\varepsilon} \tag{3-12}$$

$$\eta = \left(\frac{\nu^3}{\varepsilon}\right)^{1/4} \tag{3-13}$$

$$t_L = \frac{L}{U} \tag{3-14}$$

$$t_\eta = \left(\frac{\nu}{\varepsilon}\right)^{\frac{1}{2}} \approx \frac{\nu L}{U^3} \tag{3-15}$$

In these equations, l_0 is the integral length scale; k is the kinetic energy of eddies; ε is the turbulent dissipation rate; η is the Kolmogorov length scale; ν is the kinematic viscosity; t_L is the large eddy turnover time; L is the characteristic length; t_η is the Kolmogorov time scale and U is the velocity.

Turbulence modelling can be characterised by how much of the flow is modelled and how much of the flow is resolved. As more of the flow is resolved, the accuracy of the turbulence model increases, however the computational costs also vastly increase. CFD turbulence modelling approaches can be categorised into three groups: Direct Numerical Simulation (DNS), Large Eddy Simulation (LES) and Reynolds-Averaged Navier-Stokes (RANS). Hybrid RANS-LES methods have also become available for numerical computation. A DNS approach looks to resolve the entirety of the flow. The

RANS models look to model the entirety of the flow. The LES turbulence model resolves the large-scale structures and models the small-scale structures. Figure 3-2 and Figure 3-3 illustrate the different modelling approaches that can be adopted.

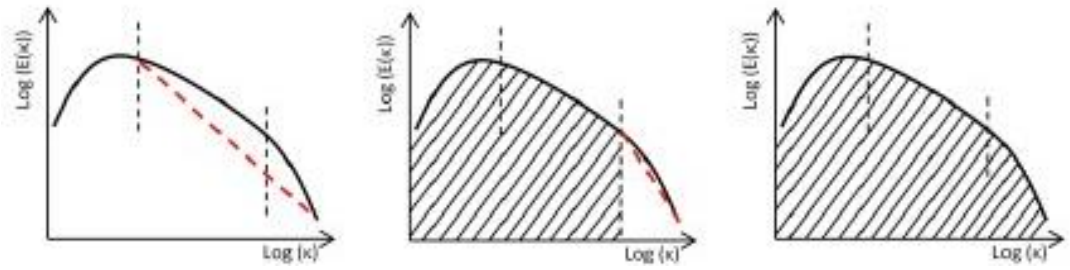


Figure 3-2: Energy cascade diagram for RANS (left); LES (centre); DNS (right) [183]

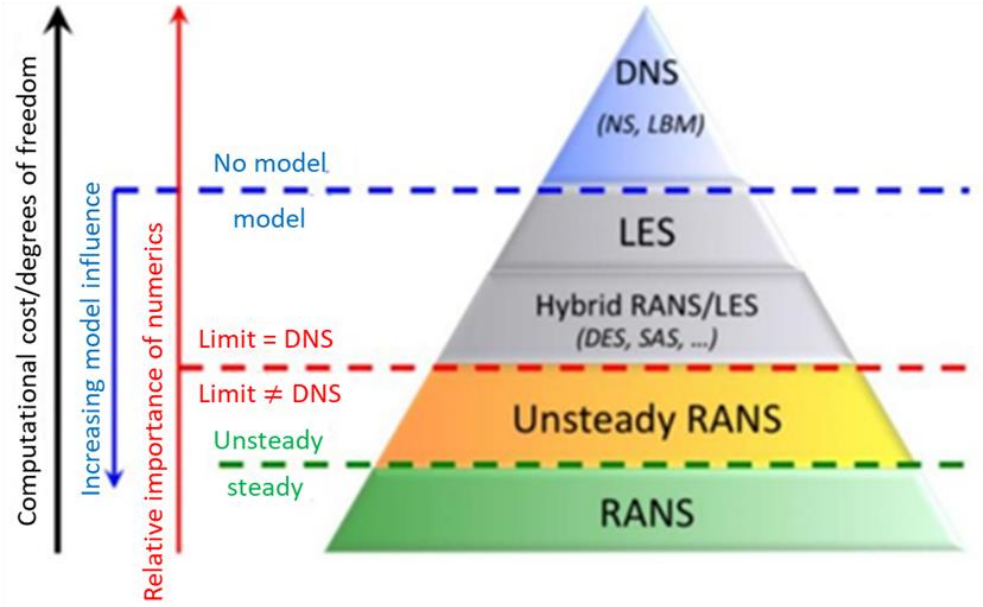


Figure 3-3: Hierarchical structure of turbulence modelling [184]

Blue dashed regions shown in Figure 3-3 represent the area where a direct solution of Navier-Stokes equations can be obtained. Red dashed lines represent the regions where a turbulence model is applied.

3.4.2.1 URANS Modelling

Turbulent flow cause flow attributes such velocity and pressure to vary with time in an irregular pattern. Alternatively, an instantaneous variable can be deconstructed into its mean and fluctuating component and is as follows [185].

$$U(t) = \bar{U} + U'(t) \tag{3-16}$$

where $\bar{U}$ is the mean flow velocity and the fluctuating, time dependent component is denoted by $U'(t)$. This deconstruction can be applied to the solution variables in the Navier-Stokes equations in Equation (3-6) to represent the turbulent characteristics. The derivation of the mean flow equations are used to simulate the turbulent attributes without representing each single fluctuation in the flow field [180]. Two unknowns, normal and tangential stresses are introduced by the Reynolds equations, this, together with the mean flow variables in the Navier-Stokes equations produce the Reynolds-Averaged Navier-Stokes (RANS) equations. A comprehensive study of the derivation of these equations can be found in the textbooks by Versteeg and Malalasekera [180] and Wilcox [186]. The RANS equations are given by:

$$\rho \frac{\partial U_i}{\partial t} + \rho U_j \frac{\partial U_i}{\partial x_j} = -\frac{\partial p_i}{\partial x_i} + \frac{\partial}{\partial x_j}(2\mu S_{ji} - \overline{\rho u'_j u'_i}) \tag{3-17}$$

where the mean strain rate tensor and Reynolds stress tensor are modelled by S_{ji} and $\overline{\rho u'_j u'_i}$ respectively. Within the RANS equations the stress tensor term must be modelled and turbulence modelling tackles the problem of how this term is modelled. The Boussinesq approximation [187] which describes the relationship between Reynolds stresses and velocity gradients, can be applied to provide closure to the RANS equations. The Reynolds stress tensor for an incompressible fluid takes the following form and the turbulent viscosity μ_t, is introduced in this equation.

$$-\overline{\rho u'_i u'_j} = \mu_t \left(\frac{\partial U_i}{\partial x_j} + \frac{\partial U_j}{\partial x_i} \right) \tag{3-18}$$

Numerous models have been put forth to determine the turbulent viscosity. They include Prandtl's mixing length model based on zero-equation models, Spalart-Allmaras model built on one-equation models and $k - \varepsilon$ and $k - \omega$ models based on two-equation models. Test cases performed in this work use two-equation models. These models are established on the basis that turbulence is composed of eddies and on the theory of energy cascade which states that large eddies are likely to break up into smaller eddies transferring its kinetic energy as the turbulence decays. This implies that the energy is transferred within a range of wavenumbers. Wavenumber κ, is defined as follows:

$$\kappa = \frac{2\pi}{\lambda} \tag{3-19}$$

$E(\kappa)$, known as the energy spectrum function, is defined as the turbulence kinetic energy per unit mass and wavenumber. The relationship between the two parameters is illustrated in Figure 3-4.

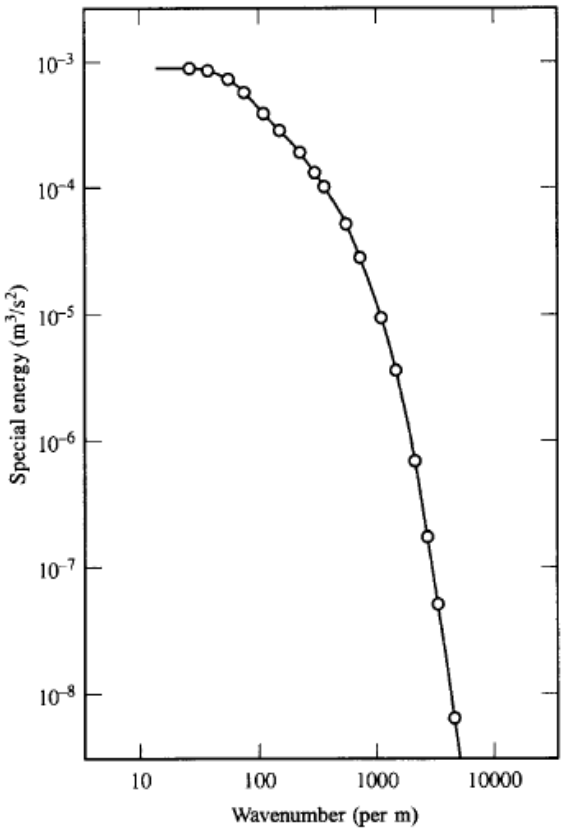


Figure 3-4: Energy spectrum of turbulence [180]

It can be seen in Figure 3-4 that the spectral energy $E(\kappa)$ rises as the wavenumber, k, decreases. Kolmogorov observed a range of wavenumbers that correspond to the region

where inertial transfer of energy dominates and has been named the inertial subrange. This hypothesis concluded that the rate of production energy production should be in equilibrium with its rate of dissipation to maintain the energy balance. In other words, $E(\kappa)$ is dependent upon the wavenumber κ and the rate at which large eddies supply energy ϵ. Kolmogorov's hypothesis formed the basis on which turbulent viscosity is described. Turbulent viscosity can be described as a function of turbulence kinetic energy k and turbulence dissipation rate ε. Following through from this work Afzal and Narasimha [188] were successful in eliminating the ambiguity of the asymptotic variation in the inertial subrange. Assuming that viscous effects are insignificant for the largest eddies and the only relevant variables are k and l, spectral energy was redefined as below:

$$E(\kappa) = klg(\kappa l) \tag{3-20}$$

Where l is length of a large eddy and $g(\kappa l)$ is an undetermined function.

Two-equation models are built on this theory. The $k-\omega$ model and its variant SST $k-\omega$ model assume turbulent viscosity is proportional to k/ω. The $k-\varepsilon$ model and its variants realizable $k-\varepsilon$ and RNG $k-\varepsilon$ models adopt the theory that the turbulent viscosity is proportional to k^2/ε.

Standard $k-\varepsilon$ model

The standard $k-\varepsilon$ model, is two-equation model operating on the assumption that flow is fully turbulent to compute the turbulent viscosity μ_t in Equation (3-18) through the

calculation of turbulence kinetic energy k and its dissipation rate ε. Transport equations for k and ε are solved by deriving k from the exact equation and ε through closure estimations approximated through physical reasoning. The transport equations for k and ε are as follows:

$$\frac{\partial}{\partial t}(\rho k) + \frac{\partial}{\partial x_i}(\rho k U_i) = \frac{\partial}{\partial x_j}\left[\left(\mu + \frac{\mu_t}{\sigma_k}\right)\frac{\partial k}{\partial x_j}\right] - \rho\epsilon - Y_M + S_k + G_k + G_b \quad (3\text{-}21)$$

$$\frac{\partial}{\partial t}(\rho \epsilon) + \frac{\partial}{\partial x_i}(\rho \epsilon U_i) = \frac{\partial}{\partial x_j}\left[\left(\mu + \frac{\mu_t}{\sigma_\varepsilon}\right)\frac{\partial \epsilon}{\partial x_j}\right] + C_{1\epsilon}\frac{\epsilon}{k}(G_k + C_{3\epsilon}G_b) - \frac{\rho C_{2\epsilon}\epsilon^2}{k} + S_\epsilon \quad (3\text{-}22)$$

In Equation (3-21), the production of turbulence kinetic energy due to mean velocity gradients and buoyancy are denoted by, $G_k = 2\mu_t S_{ji} S_{ji}$, and $G_b = -\frac{1}{\rho}\left(\frac{\partial \rho}{\partial T}\right)_p g_i \frac{\mu_t}{Pr_t}\frac{\partial T}{\partial x_i}$ respectively. Here, $\rho\epsilon$ denotes the rate of destruction of ε and S_k and S_ϵ are user defined terms. For high turbulent Mach number [9] flows, the effect of compressibility is accounted for by the term, $Y_M = 2\rho\epsilon {Ma_t}^2$. The value of Pr_t is taken as 0.85 in this model. The default model constants [189] are as follows: $C_{1\epsilon}$ = 1.44; $C_{2\epsilon}$ = 1.92; C_μ = 0.09; σ_k = 1.0; σ_ε = 1.3. The gravity component in the i^{th}direction is given by g_i.

[9] The turbulent Mach number here is expressed as $Ma_t = \sqrt{k/c^2}$; c is the speed of sound given by $c = \sqrt{\gamma RT}$

Equation (3-22) represents the turbulence dissipation equation. In this equation, the terms on the right hand side denote diffusion, the rate of production of ϵ due to mean velocity gradients and buoyancy, the rate of destruction of ϵ and a source term respectively. The model calculates turbulent viscosity from the computed values of k and ε transport equations as shown below:

$$\mu_t = \rho C_\mu \frac{k^2}{\epsilon} \tag{3-23}$$

Standard $k-\omega$ Model

This form of the two-equation turbulence model was derived by Wilcox [186]. Low Reynolds numbers, compressibility and shear flow spreading are taken into account in this model. Similar to the $k-\varepsilon$ model, the $k-\omega$ model use two transport equations to compute the turbulent viscosity. The specific dissipation rate ω is used as opposed to the dissipation rate ε in the k − ε model. Equations used are:

$$\frac{\partial}{\partial t}(\rho k) + \frac{\partial}{\partial x_i}(\rho k U_i) = \frac{\partial}{\partial x_j}\left[\left(\mu + \frac{\mu_t}{\sigma_k}\right)\frac{\partial k}{\partial x_j}\right] + G_k - Y_k + S_k \tag{3-24}$$

$$\frac{\partial}{\partial t}(\rho \omega) + \frac{\partial}{\partial x_i}(\rho \omega U_i) = \frac{\partial}{\partial x_j}\left[\left(\mu + \frac{\mu_t}{\sigma_\omega}\right)\frac{\partial \omega}{\partial x_j}\right] + G_\omega - Y_\omega + S_\omega \tag{3-25}$$

Terms G, Y, S are the rate of production, the rate of destruction and the source term respectively and Y_ω defines the dissipation of ω and is computed as follows:

$$Y_\omega = \rho\beta f_\beta \omega^2 \tag{3-26}$$

where;

$$f_\beta = \frac{1 + 70\chi_\omega}{1 + 80\chi_\omega} \tag{3-27}$$

$$\chi_\omega = \left|\frac{\Omega_{ij}\Omega_{jk}S_{ki}}{(\beta_\infty{}^* \omega)^3}\right| \tag{3-28}$$

$$\Omega_{ij} = \frac{1}{2}\left(\frac{\partial U_i}{\partial x_j} - \frac{\partial U_j}{\partial x_i}\right) \tag{3-29}$$

The effective diffusivity terms used in this model can also be defined as:

$$\Gamma_k = \left(\mu + \frac{\mu_t}{\sigma_k}\right) \tag{3-30}$$

$$\Gamma_\omega = \left(\mu + \frac{\mu_t}{\sigma_\omega}\right) \tag{3-31}$$

A thorough description of the transport equations and terms can be found in Wilcox's work [186]. The $k - \omega$ model computes the turbulent viscosity in the following way:

$$\mu_t = \alpha^* \frac{\rho k}{\omega} \tag{3-32}$$

where α^* is damping function related to the turbulence viscosity at low Reynolds numbers. The constants used in the model are given below:

$$\alpha^*{}_\infty = 1, \alpha_\infty = 0.52, \alpha_0 = \frac{1}{9}, \beta^*{}_\infty = 0.09, \beta_i = 0.072 \tag{3-33}$$

$$R_\beta = 8, R_k = 6, R_\omega = 2.95, \zeta^* = 1.5, \sigma_k = 2, \sigma_\omega = 2 \tag{3-34}$$

SST $k-\omega$ Model

The SST (Shear-stress transport) k- ω model is a two equation eddy viscosity model and is a popular variant of the k- ω model. This model was developed based on the work of Menter [190, 191]. The SST k- ω model is a blend of the k- ω formulation used for the near wall region, enabling the ability to completely resolve the boundary layer all the way through to the viscous sub layer and $k-\varepsilon$ in the fully turbulent region far from the walls, restricting the sensitivity to inlet free-stream turbulence properties. The transport equations which solve k and ω values in the SST k- ω model is given in Equations (3-35) and (3-36).

$$\frac{\partial}{\partial t}(\rho k) + \frac{\partial}{\partial x_i}(\rho k U_i) = \frac{\partial}{\partial x_j}\left(\Gamma_k \frac{\partial k}{\partial x_j}\right) + \widetilde{G_k} - Y_k + S_k \tag{3-35}$$

$$\frac{\partial}{\partial t}(\rho\omega) + \frac{\partial}{\partial x_i}(\rho\omega U_i) = \frac{\partial}{\partial x_j}\left(\Gamma_\omega \frac{\partial \omega}{\partial x_j}\right) + G_\omega - Y_\omega + D_\omega + S_k \tag{3-36}$$

It can be seen that the transport equations are formulated similar to those of the standard k- ω model, however, further modifications to these equations have been introduced in ANSYS-Fluent [192]. The model constants here are different and a damped cross-diffusion derivative term, D_ω, described in Equation (3-45), is introduced as a blending function to effectively blend the two turbulence models and allow for a smooth transitions between the two. This combined with an additional viscosity limiter which accounts for turbulent shear stress provide the basis of function for the SST k- ω model. The turbulent viscosity, μ_t, and turbulent Prandtl numbers for k and ω are presented in Equations (3-37) to (3-38).

$$\mu_t = \frac{\rho k}{\omega} \frac{1}{\max\left(\frac{1}{\alpha^*}, \frac{S_\varepsilon F_2}{\alpha_1 \omega}\right)} \tag{3-37}$$

$$\sigma_k = \frac{1}{\frac{F_1}{\sigma_{k1}} + (1 - F_1)/\sigma_{k2}} \tag{3-38}$$

$$\sigma_\omega = \frac{1}{\frac{F_1}{\sigma_{\omega 1}} + (1 - F_1)/\sigma_{\omega 2}} \tag{3-39}$$

The coefficients used in the above equations are defined below in Equations (3-40) through (3-44).

$$F_1 = \tanh\left(\phi_1{}^4\right) \tag{3-40}$$

$$F_2 = \tanh\left(\phi_2{}^2\right) \tag{3-41}$$

$$\phi_1 = \min\left[\max\left(\frac{\sqrt{k}}{0.09\omega y}, \frac{500\mu}{\rho y^2 \omega}\right), \frac{4\rho k}{\sigma\omega_2 D_\omega{}^+ y^2}\right] \tag{3-42}$$

$$\phi_2 = \max\left[2\frac{\sqrt{k}}{0.09\omega y}, \frac{500\mu}{\rho y^2 \omega}\right] \tag{3-43}$$

$$D_\omega{}^+ = \max\left[2\rho\frac{1}{\sigma_{\omega 2}\frac{1}{\omega}\frac{\partial k}{\partial x_j}\frac{\partial \omega}{\partial x_j}}, 10^{-10}\right] \tag{3-44}$$

where S_ε refers to the strain magnitude, F_1 and F_2 are blending functions, y describes the distance to the next particle and $D_\omega{}^+$ estimates the positive part of the cross diffusion term, D_ω, as given in Equation (3-45).

$$D_\omega = 2(1 - F_1)\rho\,\frac{1}{\omega\sigma_{\omega 2}}\frac{\partial k}{\partial x_j}\frac{\partial \omega}{\partial x_j} \tag{3-45}$$

The production of turbulence in terms of $\widetilde{G_k}$ and G_ω is modelled as follows:

$$\widetilde{G_k} = \ min(G_k, 10\rho\beta^* k\omega) \tag{3-46}$$

$$G_\omega \ = \ \frac{\alpha}{\upsilon_t}\widetilde{G_k} \tag{3-47}$$

The evaluation of the term α_∞ is another form of difference between the standard and SST k- ω models. In the standard k- ω model α_∞ is defined as a constant with a value of 0.52, but for the SST k- ω model, α_∞ is determined as given in Equation (3-48).

$$\alpha_\infty = \ F_1\alpha_{\infty_1} + (1 - F_1)\alpha_{\infty_2} \tag{3-48}$$

where α_{∞_1} and α_{∞_2} are as follows:

$$\alpha_{\infty_1} = \ \frac{\beta_{i1}}{\beta^*_\infty} - \frac{\varsigma^2}{\sigma_{\omega1}\sqrt{\beta^*_\infty}} \tag{3-49}$$

$$\alpha_{\infty_2} = \ \frac{\beta_{i2}}{\beta^*_\infty} - \frac{\varsigma^2}{\sigma_{\omega2}\sqrt{\beta^*_\infty}} \tag{3-50}$$

The turbulence dissipation is modelled as shown below with the dissipation of k given in Equation (3-51) with the dissipation of ω described in Equation (3-52).

$$Y_k = \rho\beta^* k\omega \tag{3-51}$$

$$Y_\omega = \rho\beta\omega^2 \tag{3-52}$$

Here β^* = 1 and is different to the way it is evaluated in the standard k- ω model where β^* is a piecewise function; $\beta = F_1\beta_{i1} + ((1 - F_1)\beta_{i2}$; and the model constants are σ_{k1} = 1.176; $\sigma_{\omega1}$ = 2.0; σ_{k2} = 1.0; $\sigma_{\omega2}$ = 1.168; α_1 = 0.31; β_{i1} = 0.075; β_{i2} = 0.0828; and ζ = 0.41.

Although the k- ω model is isotropic, the SST k- ω model predicts flow separation better than most RANS models and accounts for the behaviour of adverse pressure gradients appropriately. This model allows for the transport of the principal shear stress in boundary layers with adverse pressure gradients. The k- ω also offers high accuracy-to-computational cost ratio, which makes it an attractive choice of turbulence modelling.

One main drawback of RANS based models is that it relies on a single turbulence model to simulate the behaviour of all eddies. Application of the RANS models is therefore restricted due to the development of large eddies is dependent upon the formulation of the problem [180]. This issue has been addressed in the Large Eddy Simulation (LES) by the use of a time-dependent computation.

3.4.2.2 LES Modelling

The energy cascade within turbulent flows results in a transfer of energy from the large-scale structures to small scale structures. The large eddies carry most of the energy and the small eddies carry a smaller proportion of the energy. As large-scale structures contribute to a greater degree to the properties of the flow than the small-scale structures; it is more important to accurately model the large-scale structures than the small-scale structures.

The instantaneous properties can be decomposed into the sum of a filtered component and a fluctuating component. A filter is applied to the Navier-Stokes equations and continuity equation to separate the resolved scales from the unresolved scales. Derivation of the transports equations of this model is explained in great detail by Kassinos et al. [193].

The LES approach is able to resolve the unsteady flow structure while reproducing the turbulence to a much higher degree of accuracy than the RANS models. The LES model resolves the largest scales of turbulence and model the rest of the scales by implementing sub-grid turbulence models with accurate prediction of flow recirculation and vortex shedding. However, the unsteady nature of the flow modelled leads to higher computational and programming costs and remains the biggest limitation [180], [193].

3.4.2.3 DNS Modelling

With a DNS approach for the turbulence, the flow is resolved to the smallest spatial and temporal scales. With fully resolving the entire energy spectrum this approach provides the most accurate method for dealing with turbulence. This approach is requires a mesh fine enough to resolve the smallest structures and a time scale to match. Hence, DNS approach to modelling flow has only been employed to a handful of very simple geometric cases that operate at very low Reynolds number.

3.4.2.4 Near wall modelling

Near wall modelling is of utmost importance when modelling turbulence, as solid walls are the main source of vorticity and turbulence and the precise computation of wall quantities such as velocity gradients and pressures at the walls is required in engineering applications [181].

The ability to define the flow separation and reattachment positions depend on the accurate prediction and modelling of turbulence development in near wall regions. Figure 3-5 illustrates the typical velocity profile of a turbulent boundary layer which expands from viscous boundary layer to log layer.

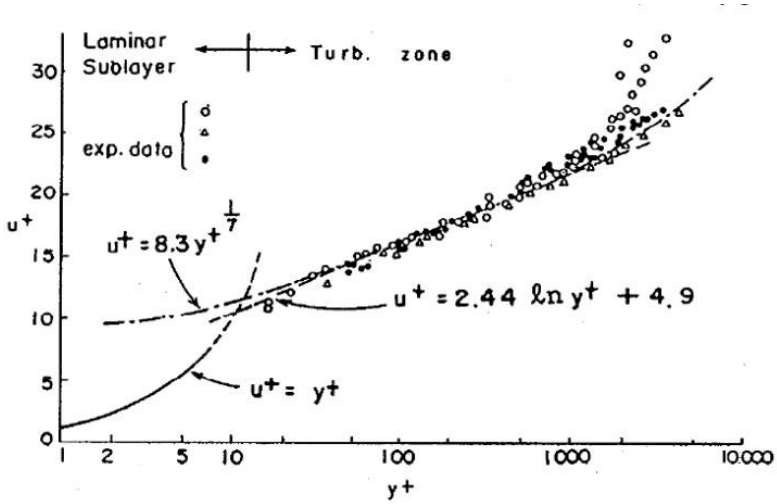


Figure 3-5: Typical velocity profile for a turbulent boundary layer [181]

The following non-dimensional quantities are typically used to describe the turbulent attributes of the wall.

$$y^+ = \frac{\rho U_\tau y}{\mu} \tag{3-53}$$

$$u^+ = \frac{U}{U_\tau} \tag{3-54}$$

where y is the distance from the wall; y^+ can be considered as a flow Reynolds number relies on the distance from the wall; $u^+$is the velocity normalised by Reynolds number; U is the velocity and U_τ is the shear velocity that is proportional to shear stress τ_w as defined below.

$$U_\tau = \sqrt{\frac{\tau_w}{\rho}} \tag{3-55}$$

A main challenge in CFD is the consideration of how the near-wall sublayer should be treated. One reliable way to address this challenge is to adopt a fine grid and a low Reynolds number model. However, this will lead to very high computational costs for 3-D problems. Therefore wall function treatments in k - ε and k - ω models are used. The k - ω model uses a fine grid to resolve the boundary layer fully extended from the viscous sub layer. Hence the first grid point should ideally be positioned in the $y^+ < 5$ region. At high Reynolds numbers the viscous sublayer is very thin making the resolving very difficult. This would require a substantial number of cells with high aspect ratio to resolve the viscous dominated layer leading to large mesh requirements [194]. Hence the preferred wall function treatment is that implemented in the k - ε model. This treatment accounts for the first grid cell placed in the logarithmic region where $y^+ \approx 30$.

The fundamental principles that dictate the near wall turbulence modelling and wall function approach that have been used in all the CFD work outlined in this thesis are based on the recommendations provided in the Fluent theory guide [189] and are summarized as follows:

- The laminar sublayer is not resolved

- If the first grid point is in the log layer where $y^+ > 11$ then the velocity is described by

$$u^+ = \frac{1}{\kappa_c}\ln(y^+) + C \tag{3-56}$$

where κ_c is the Karman constant whose value is 0.41 and C is between 5.5 and 8.5

- To represent the imposed shear stress a slip condition where $U = 0$ is specified at the wall

- k is usually specified as a zero-gradient term

- ε is computed by solving for equilibrium condition defined by $P_k = \varepsilon$

- If the first grid point is in the viscous sublayer, the velocity is

$$u^+ = y^+ \tag{3-57}$$

Versteeg and Malalasekera [180], explain the physical aspects and derivations of equations applicable to modelling near wall turbulence in extensive detail. ANSYS-Fluent offers capability to treat ω at the walls based on the mesh topology. For the flow depicted in Figure 3-6, either Mesh A or Mesh B can be used. A is finer mesh and is able to capture the wall effects by resolving the laminar sublayer to the wall, however,

B is a coarse mesh and is not sufficiently fine to resolve it. The ideal scenario would be to employ a near-wall formulation that can be applied with coarse meshes as well as fine meshes. Wall functions aim to bridge the viscous sub layer instead of resolving the flow while ensuring accuracy for coarse meshes is not reduced significantly. The low-Reynolds number approach is adequate for fine meshes where the low-Reynolds conditions apply. With coarse meshes where the near-wall region cannot be completely resolved all the way to the viscous sublayer and appropriate low-Re conditions are not applicable, an analytical function approach is used.

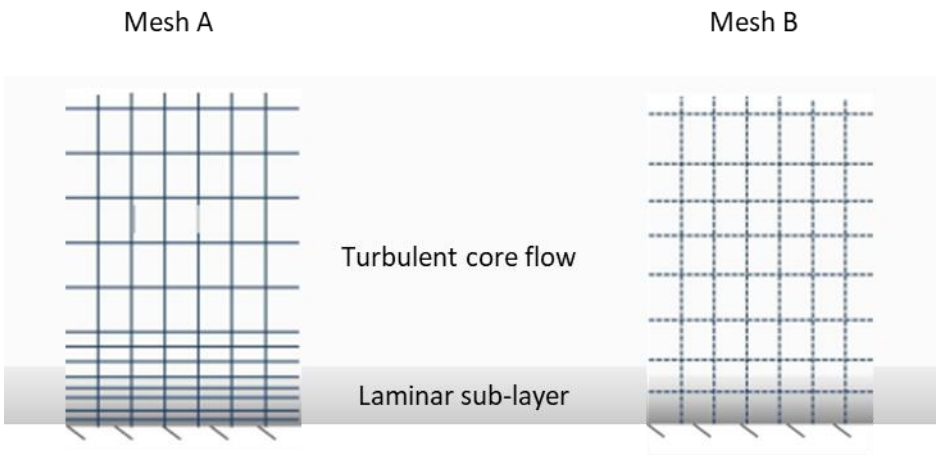


Figure 3-6: Near wall treatment depending on mesh type

ω at the wall or ω_w is presented in Equation (3-58).

$$\omega_w = \frac{\rho(u^*)^2}{\mu}\, x \begin{cases} \dfrac{6}{\beta_i (y^+)^2} & Analytical;\ y^+ < 30 \\ \dfrac{1}{\sqrt{\beta^*_\infty}} \dfrac{du^+_{turb}}{dy^+} & Logarithmic\ region;\ y^+ > 30 \end{cases} \tag{3-58}$$

Here, β^*_∞ = 0.09 and β_i = 0.072 and u^* is the non-dimensional friction velocity.

3.4.3 Multiphase Flows

The multiphase nature of a continuous fluid can be modelled in ANSYS-Fluent using several approaches; Volume-of-Fluid (VoF), Mixture, and Eulerian models. Using a continuous sequence, the phases are numerically represented in these models, which is known as the Euler-Euler approach. A generic multiphase flow model that can be used for any flow pattern has not yet been implemented and intense research is currently conducted on multiphase flow models to establish a consistent link between different flow schemes [195]. A detailed review of the derivation of governing equations for multi-phase flow can be found in the work of Scardovelli and Zaleski [138].

The suitability of the model is dependent on the nature of the fluid flow and the features of the model. The Eulerian model is considered to be the most complex multiphase model in which a set of momentum and continuity equations are solved for each phase. The phases are assumed to be inter-penetrating continuously and are coupled through pressure and interphase exchange coefficients. The types of the phases involved are accounted for in which the coupling is implemented. This model is used simulate fluid-solid and fluid-fluid flows in applications such as risers, bubble columns, and fluidized beds.

The Mixture model is comparable to the Eulerian model in the way the phases are treated; the phases are treated as interpenetrating continua. However, the Mixture model

models the phases as a single fluid and solves one combined momentum equation, unlike the Eulerian approach which solves separate momentum equations. This model specifies the relative velocities of the dispersed phases, while the Eulerian model calculates them independently. The Mixture model is used to model liquid-solid flows. Typical applications include cyclones and bubbly flows.

The VoF model works well for flows for both stratified and free surface flows. The mixture and Eulerian models are better suited for flows where the phases are mixed together or separated and/or when the dispersed phase occupies more than 10% of the volume. For flows with dispersed phases making up 10% or less of the volume, the discrete phase model can be used instead. The VoF model is appropriate for the entire range of volume fractions while the Lagrangian model is only suitable for low volume fractions [55]. The Volume-of-Fluid approach is adopted to model classic hydraulic seals as stated in literature [26, 27]. Hence, VoF is the primary choice of multiphase flow modelling approach implemented in the numerical calculations conducted in this work.

3.4.3.1 Volume-of-Fluid (VoF) model

The Volume-of-Fluid is used to investigate the flow behaviour of two or more immiscible fluids by solving the continuity equation for the volume fraction of each phase present. This method averages the fluid properties in a manner that is proportional to the volume fraction of the phases taking up their respective control volumes and assigning the same velocity to all the phases. The form of the continuity equation used

to compute the volume fraction for the ith phase is shown in Equation (3-59) followed by equations used to compute the density and viscosity values.

$$\frac{1}{\rho_i}\left[\frac{\partial}{\partial t}(\alpha_i\rho_i) + \nabla\cdot(\alpha_i\rho_i U) = S_{\alpha_i} + M_{net}\right] \tag{3-59}$$

In Equation (3-59), M_{net} denotes the net mass exchange between the phases present such as in the case of evaporation or condensation. In the present work, M_{net} term is zero, as no phase change has been modelled and there are no heat sources. $S_{\alpha_i}$is the source term. However, the volume fraction of the primary phase is computed using the following equation which accounts for mass conservation.

$$\sum_{i=1}^{n}\alpha_i = 1 \tag{3-60}$$

When the flow comprises of liquid and gas phases the following flow equations are applied to calculate the material properties:

$$\alpha_l = 1 - \alpha_g \tag{3-61}$$

$$\rho = \rho_g\alpha_g + \rho_l\alpha_l \tag{3-62}$$

$$\mu = \mu_g \alpha_g + \mu_l \alpha_l \tag{3-63}$$

Where the subscripts g and l refer to gas and liquid phase respectively. Implicit or explicit time discretization schemes can be used to solve the volume fraction equation.

Volume of Fraction parameters formulation: Implicit scheme

A numerical solution is said to be implicit when the dependent variables cannot be computed directly and coupled sets of equations and either a matrix or an iterative approach are required to compute the solution. The implicit solution can be obtained when the transport equation given in Equation (3-59) is discretised on the assumption that no phase change occurs or no mass sources are present.

$$\frac{{\alpha_i}^{n+1}{\rho_i}^{n+1} - {\alpha_i}^{n}{\rho_i}^{n}}{\Delta t} V + \sum_F ({\rho_i}^{n+1}{\dot{V}_F}^{n+1}{\alpha_{i.F}}^{n+1}) = 0 \tag{3-64}$$

In Equation (3-64), $n+1$ and n denote the current and previous time steps respectively, α_i reads the volume fraction at the given time step, V is the cell volume, $\dot{V}_F$ is the volume flow rate through the face and the face value of the volume fraction of ith phase is given by $\alpha_{i,F}$. The solution of a scalar transport equation is obtained iteratively for each of the volume fractions of the secondary phase at each time-step as the equation requires volume fractions at the current time-step. Both time dependent and steady state computations can be done using this scheme. The chosen discretisation scheme dictates how the flows through the faces are interpolated.

Volume of Fraction parameters formulation: Explicit scheme

The explicit solution does not require an iterative technique as the dependent variables are computed directly using the available known quantities. Explicit scheme, too is built on the same assumption of no mass sources and no phase change and is formulated by discretising the transport equation in Equation (3-59) and takes the following form:

$$\frac{\alpha_i{}^{n+1}\rho_i{}^{n+1} - \alpha_i{}^{n}\rho_i{}^{n}}{\Delta t} V + \sum_F (\rho_i{}^{n}\dot{V_F}{}^{n}\alpha_{i.F}{}^{n}) = 0 \quad (3\text{-}65)$$

The explicit scheme involves computing the volume fraction at the current time-step, $\alpha_i{}^{n+1}$, using the data of the previous time-step. Similar to the implicit scheme, the selected finite-difference discretization schemes are used to interpolate the face fluxes. A time dependent solution is obtained through an explicit scheme. The explicit scheme has been adopted in the present work because the existing literature reports the use of this scheme predominantly where the flow in a hydraulic seal has been modelled.

Interface computation

In ANSYS-Fluent, two methods are available for face flux interpolation in the VoF approach when the explicit time discretization is applied. The first method uses interface reconstruction techniques, while the second employs a finite volume discretization scheme, as detailed in the Fluent theory guide [189]. The two specific reconstruction-based schemes are Geometric Reconstruct and Donor-Acceptor. These options provide flexibility in how the interface between fluids is handled during simulations.

The geometric reconstruction method which is a PLIC scheme, is applied when a cell is in close proximity to the interface between two phases. The interpolation scheme employed in this approach computes the face fluxes when a cell is completely filled with one phase. The interface between fluids is represented in a piecewise approach assuming each cell within the interface has a linear gradient. This linear representation is taken into account for the calculation of advection of fluid through the cell faces. This scheme is applied for unstructured meshes and is generalized based on the work of Youngs [196]. A time dependent solution is computed through this scheme and is only available for explicit formulation of the VoF parameters in Ansys-Fluent.

The computation of face fluxes in this scheme follows a sequential form made up of 3 steps. Firstly, the information on volume fraction and its derivatives in a given cell is used to compute the position of the linear interface with respect to the centre of each partially filled cell. Fluid advection through each face is calculated next using the position of the interface and velocity distribution on the face calculated previously. Finally, the volume fraction in each cell is evaluated by balancing the fluxes computed in the previous step.

The geometric reconstruction scheme, relies on several key assumptions. Primarily, it assumes that the interface between fluids can be approximated as a planar surface within each computational cell, which simplifies the potentially complex interface geometry. This method assumes that the volume fraction data alone is sufficient to determine the orientation and position of this planar interface. It also presumes that the fluid distribution in neighbouring cells provides meaningful information for accurate

interface reconstruction, particularly in calculating the interface normal. The scheme assumes that the interface remains continuous across cell boundaries and that sharp interfaces can be maintained without excessive numerical diffusion. Additionally, it is also assumed that the linear approximation of the interface within each cell is adequate for calculating fluid fluxes across cell faces. Even though these assumptions allow for a balance between computational efficiency and maintaining a reasonable level of physical fidelity, it should be noted that this interpolation estimation is based on cell weighting. Therefore, the accuracy of the solution is impacted by the cell size.

3.4.4 Discretization

This section outlines an overview of the numerical solution strategies for the flow equations and the algorithms used. The Navier-Stokes equations are in analytical form and they need to be transformed into discretized form in order to compute the numerical solution. The available discretization schemes for the equations in CFD include Finite Difference Method (FDM), Finite Element Method (FEM), Spectral Methods, Finite Volume Methods (FVM), Discontinuous Methods (DGM), and Hybrid Methods [181]. A description of the Finite Volume Method is summarised in this section as this method has been adopted in the simulations performed for this work. A full review of all available discretization approaches is provided by Versteeg and Malalasekera [180].

3.4.4.1 Finite Volume Method

The FVM approach is the most preferred approach in solving the NS equations. The formulation is achieved by computing the conservation equations in the domain of interest that has been segregated into distinct multiple volumes. Figure 3-7 shows a vertex-centred control volume that can be accounted for an equation in two-dimensions by diving the domain Ψ into non-overlapping control volumes M, where $K_m \subset \Psi$.

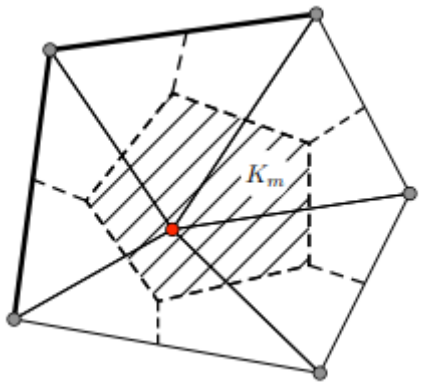


Figure 3-7: Vertex-centred control volume [181]

In the FVM method, one value of Velocity, U_m, is stored in each control volume K_m which yields the average of U in K_m and can be written as:

$$U_m = \frac{1}{|K_m|}\int_{K_m} U \, d\Psi \tag{3-66}$$

In a mathematical sense, this means that the FVM approach is based on the integral form of the governing equations and the conservation is enforced in a control volume

defined by the computational grid. The type of FVM is defined by the type of control volume and the type of evaluation of integrals [181].

The FVM formulation is done by integrating the flux integral by parts also known as the Gauss divergence theorem. The spatial derivatives of a quantity described as ϕ are converted into surface integrals by the Gauss divergence theorem as shown in the equations below.

$$\int_V \frac{\partial \rho\phi}{\partial t} dV + \int_V \nabla \cdot (\rho\phi U) dV = \int_V \nabla \cdot \left(\Gamma_\phi \nabla\phi\right) dV + \int_V S_\phi \, dV \tag{3-67}$$

where $\phi = \phi(x, y, z, t)$ is a generic quantity integrated over a control volume V. The diffusion coefficient is denoted by Γ_ϕ and S_ϕ is the source term. Applying Gauss's divergence theorem, leads to the following:

$$\int_V \frac{\partial \rho\phi}{\partial t} dV + \oint_{S_{CV}} \rho\phi U \cdot dA = \oint_{S_{CV}} \Gamma_\phi \nabla\phi \cdot dA + \int_V S_\phi dV \tag{3-68}$$

where S_{CV} represents the control volume surface and the vector area is denoted by A. The full discretized transport equation takes the following form when a geometry of a control volume with N faces are considered.

$$\frac{\partial \rho \phi}{\partial t} V + \sum_{f=1}^{N} \rho_f \phi_f U_f \cdot A_f = \sum_{f=1}^{N} \Gamma_\phi \nabla \phi_f \cdot A_f + S_\phi V \tag{3-69}$$

Where ϕ_f represents the convective value of ϕ flowing through the face f, $\nabla \phi_f$ denotes the gradient of ϕ at the face f, A_f is a vector representing the area of f, and the mass flow through f is denoted by $\rho_f \phi_f U_f$.

Discretization schemes: spatial discretization

To compute the convective terms in Equation (3-69), the stored cell values of ϕ and ϕ_f are needed. This information is obtained through a method known as upwind [181]. The second order upwind scheme has been used for the simulations performed for this work for the numerical solution of the momentum, energy equations and $k, \omega \; or \; \varepsilon$ values. The numerical computation takes the following form where the upstream cell value ϕ_U and its gradient is used to compute the face value ϕ_f, r_d is the vector displacement between the centroids of upstream cell and the face f.

$$\phi_f = \phi_U + \nabla \phi_U \cdot r_d \tag{3-70}$$

Using this scheme, a second order value of ϕ can be approximated. While it has its advantages of ease of implementation, good accuracy and efficiency, unsteady oscillatory motion could be produced in transient numerical conditions, making it unstable [197], [198], [199]. While first-order scehemes have higher numerical

stability, they are less accurate than second-order schemes. Flux limiters are a common approach to reduce the disadvantages of both first-order and second-order schemes, as it implements first-order schemes in high gradient areas and maintains accuracy of the second-order schemes [200].

Discretization schemes: Temporal Discretisation

Equation (3-69) requires the time-derivative term $\frac{\partial \rho \phi}{\partial t} V$, to be discretised over time. ANSYS-Fluent, implements this integration in a backward-differencing scheme. A generic expression for ϕ, a scalar quantity, yields the following.

$$\frac{\partial \phi}{\partial t} = F(\phi) \tag{3-71}$$

F allows for spatial discretisation. The first and second order time discretisation is performed as shown in Equations (3-72) and (3-73) respectively:

$$\frac{\phi^{n+1} - \phi^{n}}{\Delta \mathrm{t}} = F(\phi) \tag{3-72}$$

$$\frac{3\phi^{n+1} - 4\phi^{n} + \phi^{n-1}}{2\Delta t} = F(\phi^{n+1}) \tag{3-73}$$

where $n-1$, n and $n+1$, correspond to values at $(t-\Delta t)$, t and $(t+\Delta t)$ time steps respectively and the Equation (3-72) can be altered for an implicit time integration as:

$$\frac{\phi^{n+1} - \phi^{n}}{\Delta t} = F(\phi^{n+1}) \tag{3-74}$$

Equation (3-74) states that function F is evaluated at each time step. Conversely, the explicit expression computes F at the current time step, n in the following form:

$$\frac{\phi^{n+1} - \phi^{n}}{\Delta t} = F(\phi^{n}) \tag{3-75}$$

Time Step Selection

The stability of the numerical solution computed in the explicit time integration relies on satisfying the Courant-Friedrichs-Lewy (CFL) Law. The following condition should be met for a cell having a length Δx, across which the average fluid velocity is U [201].

$$CFL = \frac{U\Delta t}{\Delta x} \leq 1 \tag{3-76}$$

This is particularly important in choosing the time step size, Δt in order to approximate a somewhat smaller time step to eliminate the possibility of the divergence of the solution. However, this does not apply for implicit time integration, as the solution is independent of the time step size, thus maintaining the stability of the solution [201].

Solution Algorithms

In ANSYS-Fluent, the numerical solution methods for the governing equations are commonly known as ‘Solvers’. Computing the numerical solution is an iterative

process, and two solvers are available on ANSYS-Fluent are; the pressure-based solver and the density-based solver. The pressure-based solver is used for low-speed incompressible flows while the density-based solver is intended for high-speed compressible flows [192]. The significant difference between the two methods is that in the pressure-based solver, density is assumed constant and a pressure correction equation, derived from the continuity and momentum is used to compute the pressure. In the density-based calculation, all the flow fields such as pressure, velocity and temperature are solved using a coupled formulation in every computational cell simultaneously. The pressure is obtained from the equation of state, velocity field is determined through the momentum equations and density from continuity equation. However, the solution computation process remains the same for both methods.

The scalar variable ϕ, in the discretized full transport equation shown in Equation (3-69), is unknown at the cell centre, including those of the neighbouring cells. The count of neighbour cells are estimated by the mesh topology. This in general is a non-linear system and can be linearized to be of form as given by Equation (3-77). This produces a sparse coefficient matrix for all of the cells in the computational mesh. Gauss-Seidel method combined with an algebraic multigrid (AMG) solver is employed to solve the linear system

$$a_i \phi = \sum_j a_j \phi_j + b \tag{3-77}$$

Here the subscript j refers a neighbouring cell, a_i and a_j are linearized coefficients for ϕ and ϕ_j respectively.

The pressure-based solver uses either a segregated or coupled approach to achieve the continuity of the velocity field by solving a pressure correction equation. In both algorithms, the continuity and Navier-Stokes equations are manipulated to solve for the corrected pressure field derived from the continuity and the momentum equations. As done in the density-based solver, the pressure-based solver too discretises the solution into computational grids, linearizes the non-linear governing equations, and solves the set of equations repeatedly until the solution converges. In the segregated algorithm, variables are solved sequentially by computing the solution loop iteratively. The coupled algorithm solves a system of equations which consists of the momentum equations and the pressure-based continuity equation simultaneously. The segregated method is more memory efficient but results in slower convergence. It should be noted that both approaches are preferable depending on the nature of the CFD study carried out. The coupled algorithm is favoured to be implemented within the 2D axisymmetric studies for its higher convergence rate and the segregated approach in the 3D flow models for its memory efficiency given the typical geometries which may consist of millions of nodes. Figure 3-8 summarises the significant differences between the density-based and pressure-based algorithms [192].

Several algorithms are available in ANSYS-Fluent, specifically to couple pressure and velocity. These algorithms are SIMPLE, SIMPLEC, PISO, Coupled and FSM for unsteady flows using the non-iterative time advancement scheme (NITA). SIMPLE

represents Semi-Implicit Method for Pressure-Linked Equations. SIMPLEC is an extension of SIMPLE which refers to SIMPLE-Consistent. Although both SIMPLE and SIMPLEC are generally recommended for steady-state calculations, SIMPLEC is intended for relatively simpler flow problems where a converged solution could be obtained much faster due to the pressure-correction under-relaxation factor is generally set to 1.0, which aids in faster convergence. PISO is an extension of both SIMPLE and SIMPLEC and refers to Pressure-Implicit with Splitting of Operators. PISO is usually recommended for transient calculations and can also be used for steady-state and transient calculations on highly skewed meshes. Fractional-step method or FSM is useful for unsteady flows using the non-iterative time advancement scheme (NITA). Coupled is a pressure-based coupled algorithm as it enables the full pressure-velocity (p-v) coupling and offers robust and efficient solutions in single-phase steady-state flows.

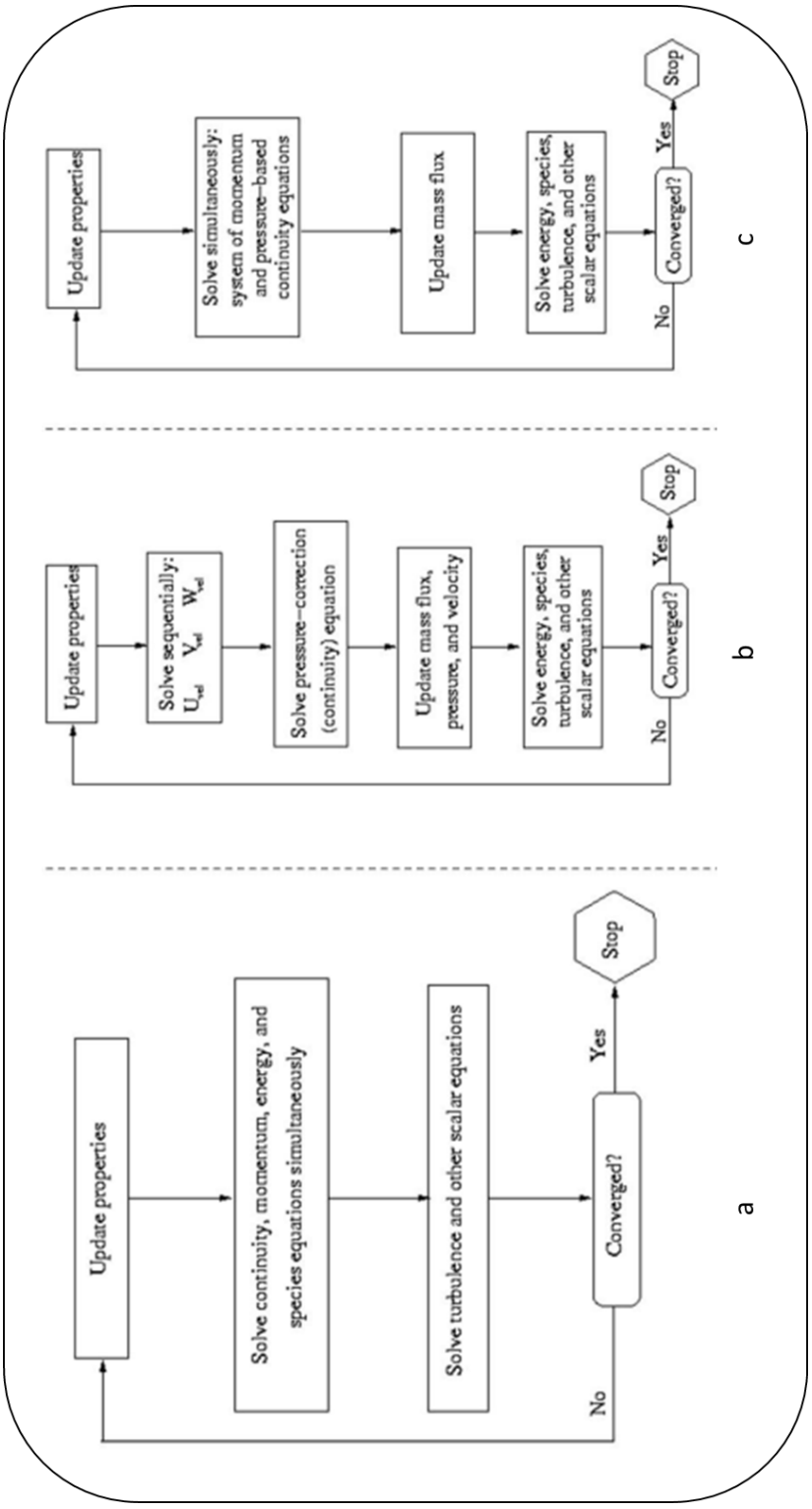


Figure 3-8: Types of CFD solvers illustrating (a) density-based; (b) pressure-based segregated solver; (c) pressure-based coupled solver [192]

For the 2D numerical simulations in this work, SIMPLE is used for the stability and faster convergence of the solution. Both Coupled and PISO schemes were also considered and investigated in the 2D numerical study of hydraulic seals. However, SIMPLE is favoured in this thesis to model the 2D flow in a hydraulic seal as the solution converged much faster. Although PISO is recommended for transient solutions, a divergent solution was induced once implemented within the 3D model. Therefore, Coupled scheme has been used for the 3D modelling as it offered a much more robust solution over the other algorithms considered.

3.4.5 Boundary conditions

The equations discussed in Section 3.4.1 govern the flow of a fluid. Flow fields differ from case to case even though the same equations govern the flow of the fluid. This is due to the effect of the boundary conditions. The governing flow equations in a flow domain are solved, conditioned to a set of constraints at the domain boundary that dictate the particular solutions to be computed [202]. These set of constraints are known as boundary conditions or initial conditions in some cases. For a viscous fluid, the boundary condition imposed on a particular wall of the domain assumes no relative velocity between the surface and the fluid immediately at the surface. This is known as the ‘no-slip’ condition [202]. If a flow is moving past a stationary surface, the following expression is applied:

$$u = v = w = 0 \text{ at the surface for a viscous flow} \tag{3-78}$$

For an inviscid flow, the flow must be normal to the surface as there is no friction between the fluid and the surface, which causes a slip of flow over the surface, and can be described as shown below.

$$U \cdot \vec{n} = 0 \tag{3-79}$$

Where u, v, w are velocity components in x, y, z directions respectively, U is the Velocity vector and $\vec{n}$ is a unit vector perpendicular to the boundary. The boundary conditions in other parts of the flow field are subject to the problem of interest. In CFD, appropriate numerical implementation of the boundary conditions is essential to simulate the real flow field that is governed by the physical boundary conditions.

The boundary conditions used in the numerical simulations carried out in this work, are discussed in the respective chapters.

3.5 Overview of the adopted modelling approach

3.5.1 Turbulence modelling

As discussed in Chapter 2, a significant amount of work has been done and valuable contributions have been made on the topic related to flow in rotating systems in the

recent years. However, the selection of a suitable turbulence model for the investigations of single phase flows in rotor-stator cavity flows remains an open issue. As pointed out by many researchers, a better prediction of the turbulence field can be achieved with second order turbulence modelling compared to the eddy viscosity based models. Nevertheless, traditional two equation turbulence models are widely and commonly used in the industry due to both their numerical stability and the favourable trade-off between accuracy and computational resources. One of the aims of the work done on the flow in a rotor-stator cavity presented in Chapter 4 is to examine if the traditional two equation turbulence models could be used as a reliable tool to model and predict the flow field within rotor-stator systems. Several turbulence models were considered in their native form for this investigation and the test cases performed in this work use RANS two-equation models, the standard $k-\varepsilon$ and SST $k-\omega$ models and the Reynolds Stress Model (RSM) implemented within ANSYS-Fluent v18.1. This section describes the fundamental concepts of numerical modelling of flows experienced in the simulations investigated in Chapters 4, 5 and 6.

The flow characteristics in the rotor-stator disk system discussed in Chapter 4, were computed on Fluent by solving the generic Navier-Stokes equations. It was assumed that the flows modelled for both test cases are incompressible and 2D axisymmetric. Flow modelled for the partially wetted disk case assumes dry air, constant temperature, constant atmospheric pressure and liquid-air interface at thermodynamic equilibrium. The standard $k-\varepsilon$ model has been implemented in the fully wetted CFD cases in Chapter 4. Virr et al. [203] demonstrated that CFD is invaluable and is capable of

predicting the flow accurately at engine operating conditions based on their validation studies on turbine disk cavity flows using the standard $k-\varepsilon$ turbulence model with wall functions and a two layer $k-\varepsilon$ / $k-l$ model. The authors indicated that satisfactory results were obtained at higher Reynolds numbers which are more representative of engine conditions. They also identified limitations associated with the wall function at low Reynolds numbers. The outcomes of this investigation were in agreement with previous studies and is confirmed by a comparison of CFD validation studies presented by Smout et al [204]. Wilson et al. [205] specified in their study on the flow in rotating systems with radial outflow, that the flow field and thermal effects within rotating disc systems can be computed with acceptable accuracy using $k-\varepsilon$ models. In addition to the numerical work carried out on rotor-stator disk systems, this model was applied in the work by Young and Chew [26], Denecke et al. [19], and Mathews et al. [27] to model the flow within a hydraulic seal.

The Shear Stress Transport (SST) variant of the $k-\omega$ model assumes μ_t is proportional to k/ω. This model was also applied in the fully wetted disk case for comparison against other turbulent models. The partially wetted disk case uses this model based on CFD results obtained for two shaft diameters in an initial study against the $k-\varepsilon$ model. The SST $k-\omega$ model was used by Jarzombek et al. [206] in a numerical study to simulate the flow within a pre-swirl chamber in which they confirmed that several commonly available eddy viscosity models can be used to model disk cavity flows. In their benchmark CFD study investigating the flow within rotor-stator cavity disk systems with contra-rotating and co-rotating disk cavity

configurations, Wu et al. [207], studied the application of a number of turbulence models. The findings of this study indicated that the experimental data were best matched by the results obtained with the SST $k-\omega$ model. Debuchy et al. [208] presented a comparison between CFD results obtained with the SST $k-\omega$ model and experimental measurements carried out with hot-wire anemometry and three-holes pressure probes in their study on the impact of external geometrical modifications on the flow behaviour of a rotor-stator system. The researchers established that the CFD results were in very close agreement with the experimental data. The CFD analysis of the flow in a shrouded rotor-stator cavity carried out by Roy et al. [209] verified that the experimental velocity profiles were well described by the numerical results attained through SST $k-\omega$ model and exhibited best overall agreement with experimental data.

Flow induced in a rotor-stator cavity system is known to be very sensitive to the swirl and turbulence levels imposed. Therefore, it is important to apply a turbulence model capable of predicting the fluid flow in the cavity accurately taking the operational characteristics of the configuration into account. Iacovides and Toumpanakis [210] concluded that the RSM provides an appropriate level of closure when modelling the flow between rotor-stator disks in an enclosed cavity. In their study using a $k-\varepsilon$ model near the walls and an Algebraic Stress Model (ASM) in the core of the flow, Schiestel et al. [211], pointed out that second-order turbulence closure terms were required to achieve a comprehensive solution which predicts rapidly rotating flows. Elena and Schiestel [212] performed numerical studies on rotating flows with and without through-flow comparing three different turbulence models. They tested a $k-$

ε low Reynolds number model, a zonal modelling approach linking RSM to the $k-\varepsilon$ model near the walls, and a Reynolds stress transport closure model derived from the study of Launder and Tselepidakis [213]. In a later study the authors modified this version accounting for the implicit effects of rotation on turbulence [214]. These authors [212, 214] deduced that the RSM model predicts the effects of turbulence in the flow field providing adequate level of closure with superior performance compared to the classic $k-\varepsilon$ model or the ASM model to simulate turbulent rotating flows with or without superimposed in- or outflow. Later, Poncet et al. [38, 215] carried out numerical simulations on a rotor-stator disk system in an enclosed cavity with an inward and outward through-flow, using an improved version of the RSM used by Elena and Schiestel [214]. These authors found that the obtained numerical results were in excellent agreement with the experimental pressure and velocity measurements. The analysis of the study on numerical calculations of turbulence modelling of a gas turbine rotor-stator system by Da Soghe et al. [216], outlines that improved predictions of the boundary layers profiles and the turbulent field have been acquired by the RSM compared to the other models. These previous investigations on the applicability of turbulence models appropriate for the modelling of rotor-stator cavity flows provide strong evidence that the standard $k-\varepsilon$, SST $k-\omega$ and the RSM model are capable of modelling the turbulent flow within the cavity. Therefore, to establish an appropriate modelling strategy, all three turbulence models were tested in the fully wetted investigations so that the developed methodology could be extended to the partially wetted flow investigations presented in Chapter 4.

Comparing the capabilities of the standard $k-\varepsilon$, SST $k-\omega$, and the RSM for predicting flow in rotating systems reveals distinct strengths and limitations. The $k-\varepsilon$ model, while computationally efficient and widely used, over predicts turbulence and fails to capture anisotropic effects induced by rotation. The SST $k-\omega$ model offers improved performance near walls and handles mildly swirling flows better, but still faces challenges with strong rotation and curvature effects. In contrast, the RSM stands out as the most comprehensive RANS model for rotating systems. By directly solving for all components of the Reynolds stress tensor, RSM accurately predicts anisotropic turbulence effects and complex flow structures in rotating systems. However, this superior performance comes at the cost of increased computational expense and complexity. The choice among these models for a rotating system typically involves balancing accuracy requirements against computational resources, with RSM generally providing the most accurate predictions for complex rotating flows, while both standard $k-\varepsilon$ and SST $k-\omega$ k-omega models offer a compromise between accuracy and efficiency.

Based on the results presented in Chapter 4, it was evident that a two-equation model such as the standard $k-\varepsilon$ or SST $k-\omega$ is capable of capturing the characteristics of the flow rotating in a cavity. Applying the methodology developed in Chapter 4 in a hydraulic seal configuration, the standard $k-\varepsilon$ was chosen to model the flow following a sensitivity study on the standard $k-\varepsilon$ and SST $k-\omega$ models. The standard $k-\varepsilon$ model has been used in both 2D and 3D models of a hydraulic seal.

3.5.2 Multiphase modelling

This section includes the key elements of the methodology used in the numerical computation of the present work, drawn from [189] and [180].

As discussed in Chapter 2, the VoF approach is used to simulate the flow behaviour of two or more immiscible fluids. The VoF method is most appropriate to simulate the multiphase nature of the flow, due to its ability to model highly rotational, complex free surfaces. The VoF approach is generally considered better than Eulerian and mixture models for simulating stratified flows, which are characterized by a well-defined interface between two immiscible fluid phases [189], such as one encountered in hydraulic seals. One of the key advantages of VoF is its ability to explicitly track the evolution of the interface between the phases, preserving the sharp definition of the boundary.

In contrast, Eulerian models do not explicitly capture the interface and instead treat the phases as interpenetrating continua. This can lead to numerical diffusion and blurring of the interface over time, which is particularly problematic in stratified flows where maintaining a clear separation between the phases is crucial. Mixture models also struggle with stratified flows, as they rely on simplified assumptions about the phase distribution that may not hold true in the presence of a distinct interface. Therefore, the VoF modelling treatment has been used in the numerical simulations carried out in this work.

As discussed in Section 3.4.3.1, the VoF method is implemented through two sequential steps: interface propagation (advection) and interface reconstruction. The first step, interface propagation, focuses on determining how the interface between fluids evolves over time by tracking the movement of volume fractions between consecutive time steps. The second step, interface reconstruction, then defines the current state of the interface at the end of each time step, specifically determining its shape, orientation, and position. Therefore, it should be noted that there are limitations associated with this method due to the interpolation treatment applied to the cells that lie near the interface between the two phases. The explicit scheme was adopted in this work to specify the volume fraction formulation to be used for the VoF, as it allows the use of geo-reconstruct interpolation scheme. The Fluent theory guide explains that the geo-reconstruct scheme, is considered the most accurate within Fluent for general unstructured meshes as this approach yields a sharp, well-defined interface, effectively eliminating numerical diffusion [189]. The explicit scheme also enables curvature calculations and is particularly beneficial in simulating flows where surface tension plays a crucial role as that in a flow rotating in a cavity.

When the rotating disk in an enclosed cavity is partially immersed in liquid, the flow within the cavity is stratified with both phases separated by an interface. Therefore, the VoF approach was applied in the partially wetted disk case in Chapter 4 to investigate the flow behaviour of water and air by solving the continuity equation for the volume fraction of each phase present [189]. For the numerical simulations in the partially wetted disk case, the transport equation is discretised on the assumption that no phase

change occurs and no mass sources are present. No multiphase model is implemented in the fully wetted disk case as it is a single phase flow. The geometric reconstruction interpolation scheme was used to compute the interface and include the effects of surface tension between water and air. The 'Implicit Body Force' treatment was applied to formulate the body forces accounting for surface tension as recommended in the Fluent User Manual [192].

The numerical formulation of the flow within a hydraulic seal which is the primary research problem of this work reported in Chapters 5 and 6, requires a combination of modelling techniques. The methodology related to modelling hydraulic seals reported in literature adopts a VoF approach [19, 26, 27]. In this present work, the geometric reconstruction scheme is combined with the interfacial anti diffusion approach to sharpen the gas-liquid interface and predict shear driven, highly turbulent rotating flows more accurately. This model offers a solution with faster convergence requiring less computational power for 2D studies with the SIMPLE solver and a highly robust solution for the 3D studies with the Coupled solver.

3.5.3 Discretisation

Numerical stability is achieved with second order spatial discretization and first order temporal discretization. In order to ensure the stability of the numerical solution, the present work relies on satisfying the Courant-Friedrichs-Lewy (CFL) criteria given by Equation (3-76). Hence, a variable time step was set-up to eliminate the possibility of the divergence of the solution. The modelling strategies tailored to each CFD study

with further enhancement techniques are described in the subsequent chapters. Simulations carried out for this work have adopted a second order spatial discretization scheme.

3.6 Summary

This chapter contains a discussion on the mathematical and computational fundamentals and framework upon which the numerical simulations have been carried out.

The nature of the multiphase flow can be represented as separate mixtures numerically based on the amount of fluid contained within identified by a colour function. The gas-liquid interface can be modelled using volume fractions of each phase. The flow field is solved with continuity and Navier-Stokes equations. The averaged Reynolds equations lays the basis to model turbulence in the fluid flow by simplifying the system but necessitates the use of turbulence models due to the complications which arise in the simplified system.

Robust numerical algorithms exist in ANSYS-Fluent, and the appropriate approaches applicable to the nature of the flow problem considered in this work have been identified. The Volume-of-Fluid method enhanced with features such as interface anti diffusion and implicit body forces combined with the use of SIMPLE and Coupled p-v coupling are identified as the potential modelling elements for further development dependent on the nature of the flow in this thesis.

CHAPTER 4

4 Investigations into fully and partially wetted disk geometries with relevance to intershaft hydraulic seals

A main research focus area of this PhD thesis is to develop an understanding of detailed operational characteristics of hydraulic seals. The available published research on intershaft seals in open literature has demonstrated promising sealing attributes and has proven to be an area of interest. It is worth noting that hydraulic seals have been used in operation for years. They meet or mostly meet existing sealing requirements within the current operational envelope and the challenge is to understand what limits that envelope and develop methods to optimize it. The research indicates that despite their reliable operation with zero leakage, the application of hydraulic seals is restricted due to temperature limitations, oil degradation and coking. Research and development of the next generation of hydraulic seals needs to focus on addressing these issues so that the seals can be utilized in hotter zones in future engines. With scant experimental data on hydraulic seals available, the ability to accurately computationally model hydraulic

seals is highly desirable and essential. To aid understanding of the performance and flow characteristics of hydraulic seals and to establish a robust numerical modelling strategy, a precursor study was carried out investigating disks rotating in stationary cavities, a configuration closer to hydraulic seals that will form the basis for the next chapter. The work reported in this chapter examines prior experimental and analytical investigations into fully and partially wetted disk configurations chosen due to the many geometric and operational similarities. These fundamental experimental investigations in the literature provide validation data that allows us to establish a robust CFD modelling methodology.

Rotating flows have gained much traction for many decades and have been studied extensively due to their relevance and significant role in a wide range of engineering applications. A rotor-stator cavity system is a typical configuration encountered in turbomachinery. The flow associated with rotating disk systems is seen in applications such as magnetic storage devices, automotive disc brakes, semi-conductor manufacturing processes and gas turbine engines. A disk rotating adjacent to a stationary disk forms what is known as a ‘rotor-stator disk cavity’ or ‘rotor-stator wheelspace’. The complexities involved with the flows in these configurations induced due to imposed through-flow, transitional zones, high rotational speeds, highly turbulent flow, 3D and wall effects present numerous challenges when developing numerical modelling approaches. The aim of this chapter is not to propose a benchmark numerical modelling strategy for disks rotating in closed stationary cavities but to investigate different rotating flow arrangements and study the operational and flow

characteristics so that a reliable CFD modelling approach could be developed for the application of intershaft hydraulic seals.

The problem addressed in this chapter is the numerically modelled flow confined between a rotating and a stationary disk. As noted in Chapter 2 , stability of the flow in rotor-stator cavities has been far less investigated than the flow stability of the single-disk family. Therefore, it is of great interest to build a deeper understanding of the flow structure of a configuration very similar to hydraulic seals and to evaluate if the developed modelling strategy is capable of capturing the most significant aspects of the flow physics. This chapter compares the published experimental data from two comprehensive studies related to enclosed disk geometries that can be used for validation of the CFD results. An overview of the CFD simulations carried out on ANSYS-Fluent is provided in this chapter together with a discussion on some of the relevant literature and groundwork for this investigation.

This chapter initially compares the flow characteristics of a fully wetted rotating disk against experimental results available in literature including the radial and tangential velocity components. The latter part of the chapter subsequently investigates the flow characteristics of a partially wetted disk by examining the effect on the angular velocity of the fluid core with varying engagement and spacing ratios for two flow regimes. It is evident from the results obtained that a great amount of understanding and insight can be gained from these test cases and can be extended for the application of hydraulic seals. This chapter develops CFD models for the fully immersed disk study of Daily

and Nece [40] and the partially wetted disk study by Ketola and McGrew [41]. The developed modelling approach is applied to a hydraulic seal in the next chapter.

4.1 Investigation into a fully wetted disk rotating in a stationary housing

The flow over a rotating disk has been studied extensively for over a period of 100 years. Much dates back to the early origins of theoretical and experimental investigations of single rotating disks, studied by Ekman [28], von Kármán [29] and Bödewadt [30]. As discussed in Chapter 2, both flow models developed by Batchelor [31] and Stewartson [32] are valid depending on the flow conditions. Later, the experimental and theoretical studies performed by Daily & Nece [40] confirmed that the flow structure in closed cavities can be categorized into four different regimes. The authors identified the four flow regimes based on the interaction of the disk, fluid and containment that can exist in closed cavities. Two regimes with laminar flow and two with turbulent flow, each regime distinguished by corresponding merged or separated boundary layers. When the boundary layers are separated, the flow is characterized by the separated three zones which resembles the Batchelor flow. They discovered that these four regimes are dependent on the Reynolds number (Re), and the non-dimensional axial clearance (s/a).

The angular velocity of the oil in the trough of a hydraulic seal is the most vital component required for the computation of key parameters of seals such as maximum

operating pressure differences, the torque/power consumption and heat transfer. An analytical solution for the angular velocity of oil can be obtained with simplified approximations and this has been discussed in detail in Chapter 5.

Another relevant approach would be to apply the flow characteristics of a rotating disk in an enclosed cavity to the analysis of internal flow of hydraulic seals. Daily and Nece [40] experimentally investigated the characteristics of the flow induced by a rotating disk fully immersed in water with no through-flow. In the experiments conducted by Daily and Nece [40], the flow is confined in the gap between a smooth bronze disk rotating at a constant speed and smooth circular cover plates serving as stators. It is enclosed at the periphery by a stationary cylindrical casing which was used to mount different combinations of bronze sleeves with appropriate spacers to vary the axial length of the chamber. A 5 hp DC motor was directly coupled to the shaft where the disks were attached interchangeably. The test apparatus used in their experiments is schematically presented in Figure 4-1.

Attempting to apply the findings of Daily and Nece [40] in a typical hydraulic seal, it was noted that the Reynolds number is of the order of 10^7 and consist of larger axial clearances where $s/a > 0.04$; placing the flow type in a hydraulic seal in Regime IV, the turbulent separated boundary layer mode.

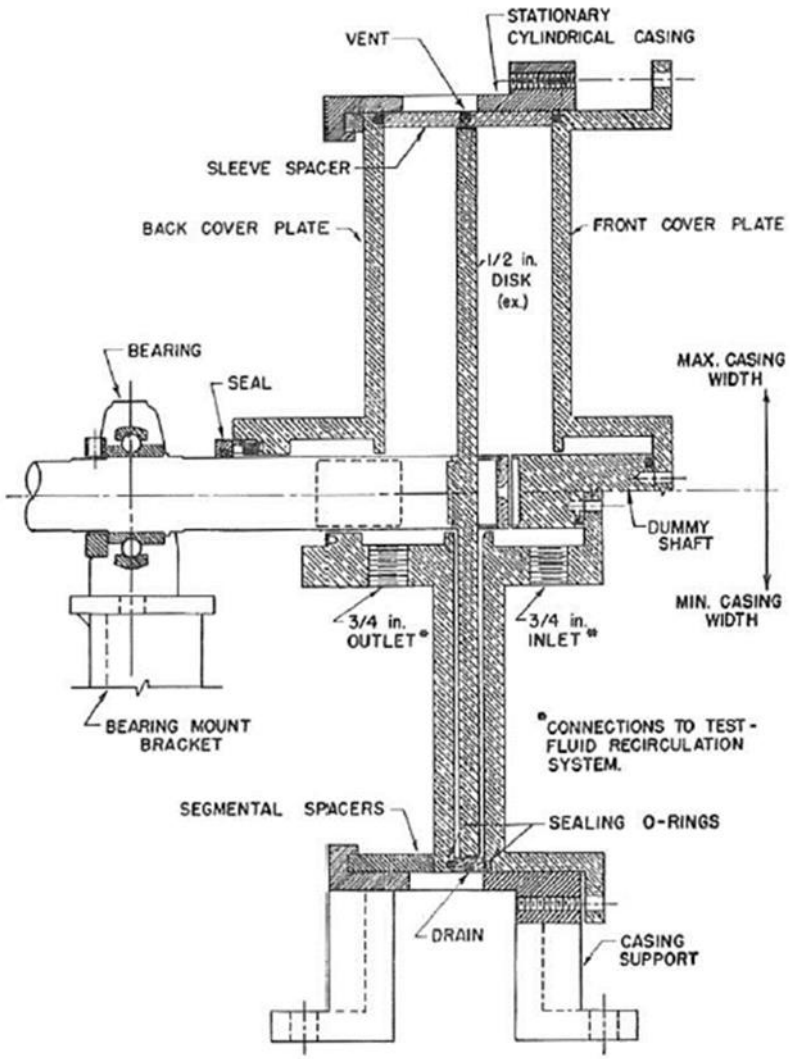


Figure 4-1: The experimental set-up used by Daily and Nece [40]

Figure 4-2 illustrates the difference in tangential velocity profiles for Regime III and Regime IV where it can be seen that with turbulent flow and separated boundary layers there is a core flow where the tangential velocity is constant for Regime IV. In this plot, the normalised tangential velocity has been plotted against the normalised distance normal to the rotating disk.

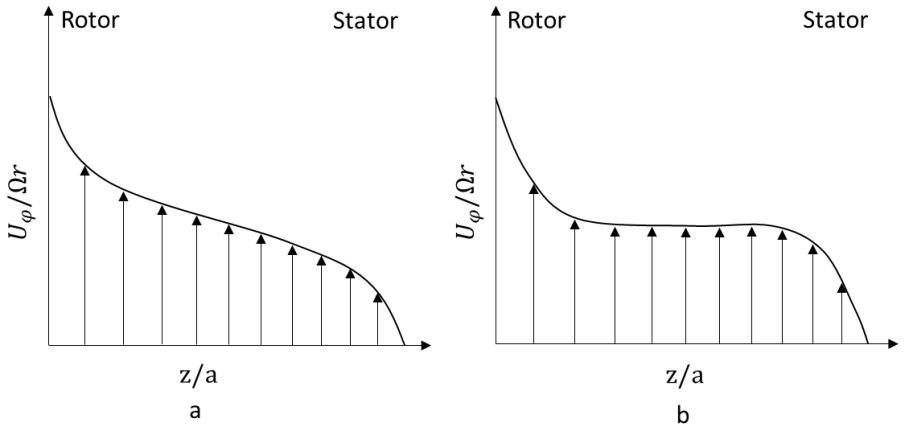


Figure 4-2: Typical tangential velocity profiles for (a) regime III and (b) regime IV

The CFD results presented in this section have been validated against the experimental mean velocity profiles for tangential and radial components obtained by Daily and Nece [40] through investigating the characteristics of the flow induced due to a rotating disk in a stationary cavity. The following sections aim to provide insights into the flow experienced in the rotor-stator cavity when the disk is fully immersed in liquid, and also to predict the existence of the flow regimes established by the authors.

4.1.1 Numerical model formulation

When addressing rotor-stator cavity flows, the induced flow is characterized by three control parameters: the aspect ratio G, disk Reynolds number Re_Ω based on the outer radius of the rotating disk and the flowrate coefficient C_W. A discussion on these parameters is presented in Chapter 2 and these parameters can be numerically presented as given in Equations (2-1) through (2-3). In this study, the main dimensionless

parameters used are G and Re_Ω, C_W is not relevant as through-flow has not been modelled ($C_W = 0$).

To simulate the flow in the cavity, numerical simulations were performed, and the flow characteristics of a fully wetted disk were investigated. The main geometric parameters of the case investigated are sketched in Figure 4-3 which shows a shaft of radius a_1 with a disk of radius a. The width of the disk is b and its clearance from the static housing is c radially and s axially. In the model, $y = 0$ at the rotational axis and $x = 0$ at the left stationary wall, where x and y denote the axial and radial co-ordinates respectively. These values are specified in Table 4-1.

Table 4-1: The Main geometric parameters of fully wetted disk CFD case (values taken from [40])

Radius of rotating disk, a (mm)	249.24
Radius of the shaft, a_1 (mm)	25.4
Thickness of rotating disk, b (mm)	12.7
Radial clearance between rotating disk and end stationary wall, c (mm)	1.59
Axial clearance between disk and end stationary wall, s (mm)	6.36

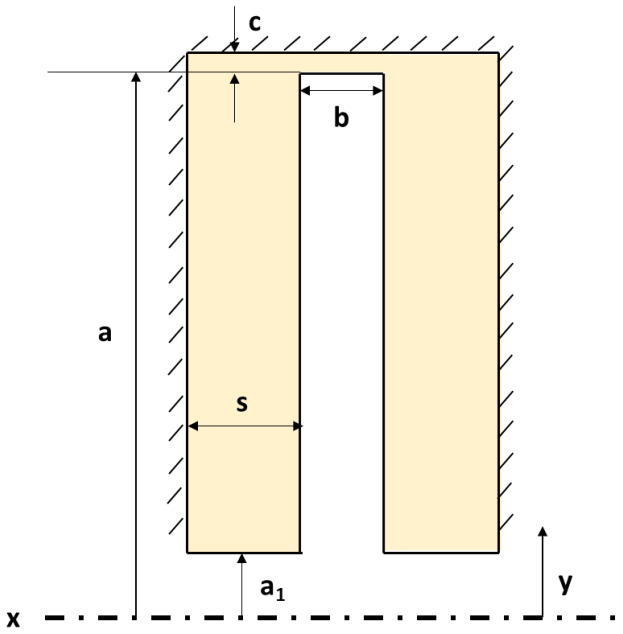


Figure 4-3: Geometry investigated in the CFD study modelling a fully wetted rotating disk

A 2D axisymmetric computational domain was considered for the simulations due to the axial symmetry of the experimental setup used in the original study. The flow within the cavity was computed using ANSYS-Fluent v18.1. The flow was modelled for a rotational Reynolds number, Re_{Ω}, of 4.4 x 10^6 and ratio of axial clearance between the rotating disk and stationary wall to rotor radius (s/a) of 0.0255. A single-phase scenario was implemented to simulate the flow field induced by the rotating disk fully immersed in water and to resemble the original flow conditions. Water was defined with constant properties of density and viscosity. For boundary conditions, the inner wall representing the rotating disk was set as a rotating adiabatic wall spinning at 48.577 rad/s, and the outer wall was representing the stationary wall was defined as a stationary adiabatic

wall. The angular velocity of the rotating wall was computed using Equation (2-2) for the disk Reynolds number specified above.

The same geometry as in the original experimental set-up is used for validation purposes. The flow was modelled for a non-flow condition as no through-flow circulation was allowed in the experiment. The flow was solved in both steady and transient modes for the $k-\varepsilon$ model and in transient mode for SST $k-\omega$ and RSM models. The 'Coupled' pressure-velocity coupling was applied together with 'PRESTO' pressure interpolation scheme. A second order upwind-biased discretization scheme was chosen for all pressure, momentum and turbulence terms. Each transient case was simulated allowing the flow to achieve pseudo steady-state using a time step, (Δt) of 10^{-4} s, each time step running for thirty iterations. This time step size was chosen to satisfy the CFL condition and maintain the Courant number below 1. Convergence at each time-step was controlled using a residual convergence criterion of 1×10^{-5} for the continuity, velocity, swirl and turbulence variables. Overall simulation convergence was monitored primarily through the reports of bulk residuals, moment coefficient of the walls and velocity magnitude at several locations. Once pseudo steady-state was achieved, the results were analysed; approximately 0.7 s was required to reach a fully developed flow solution. A total computational time of 87 core hours were required to simulate a flow time of 1 s for both $k-\varepsilon$ and SST $k-\omega$ models. In physical time, this was 21.75 hours. The fully wetted flow simulations were computed in parallel using 4 Intel Xeon Gold 6238 cores.

4.1.1.1 Mesh independence study

A mesh independence study was carried out to ensure a mesh independent solution is achieved. Three unstructured mesh sizes with quadrilateral cells were considered. Simulations were conducted on meshes with 13, 26 and 52 elements across the axial length from stator to rotor represented by Mesh 1, Mesh 2, and Mesh 3 respectively. The details of each mesh used for the mesh independence study are presented in Table 4-2.

Table 4-2: Size of meshes investigated for mesh sensitivity study

	Mesh 1	Mesh 2	Mesh 3
Number of elements across axial length	13	26	52
Number of cells	23,984	81,674	244,684

The optimal mesh was determined by comparing the axial profiles of tangential velocity in water along a line at the radial location r/a = 0.765 as illustrated in Figure 4-4. The velocity has been non-dimensionalized by the local tangential velocity at the radius, r/a = 0.765. Figure 4-5 compares the average swirl velocity at the same radial location for all three meshes where it is shown that further refinement from Mesh 2 to Mesh 3 shows no significant differences in velocity results. Based on these results, Mesh 2 shown in Figure 4-6 was chosen which illustrates the rotor-stator cavity geometry domain modelled for the configuration under investigation.

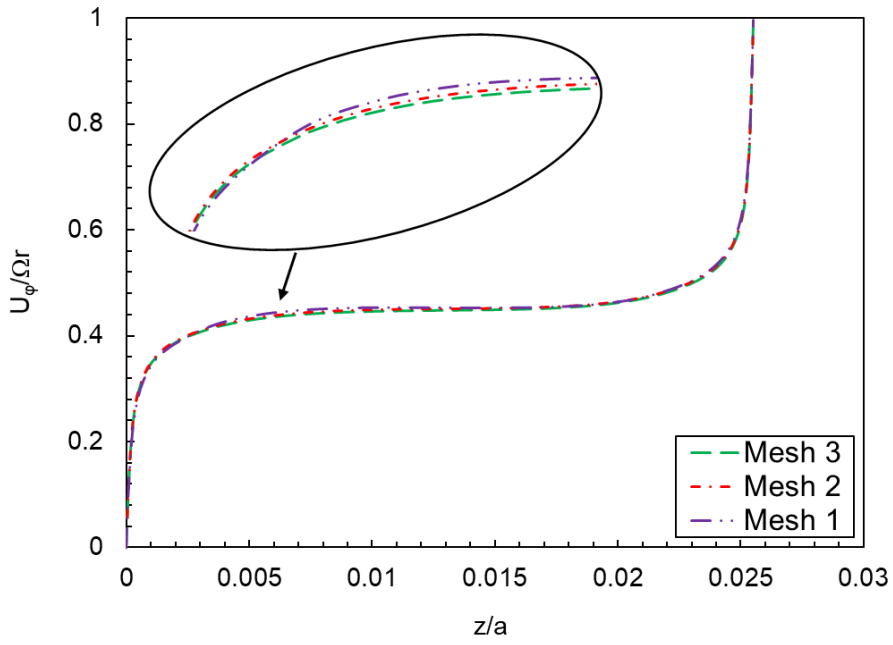


Figure 4-4: Comparison of meshes tested along a line at r/a = 0.765 in the fully wetted disk CFD investigation

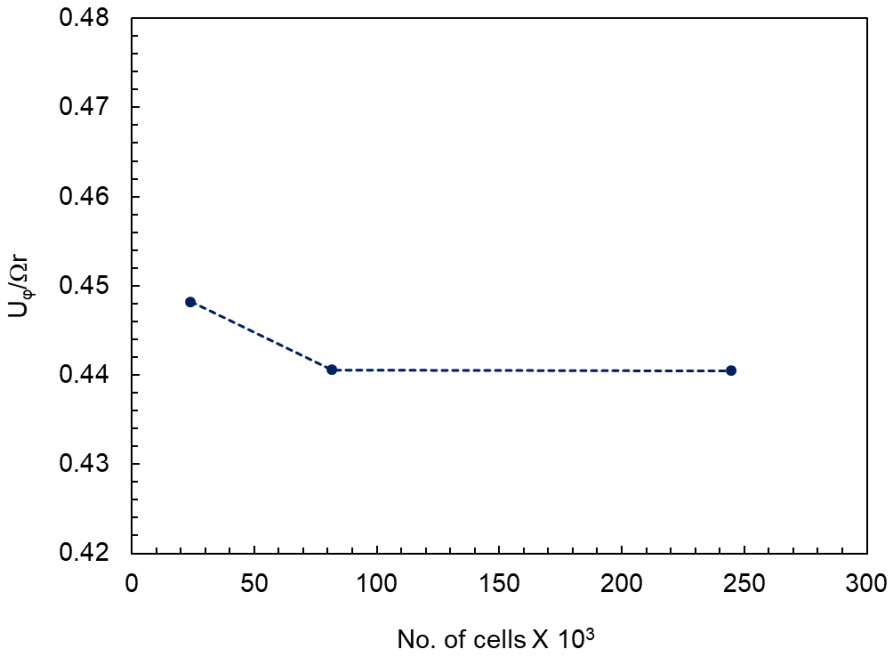


Figure 4-5: Comparison of average swirl velocity data between meshes used

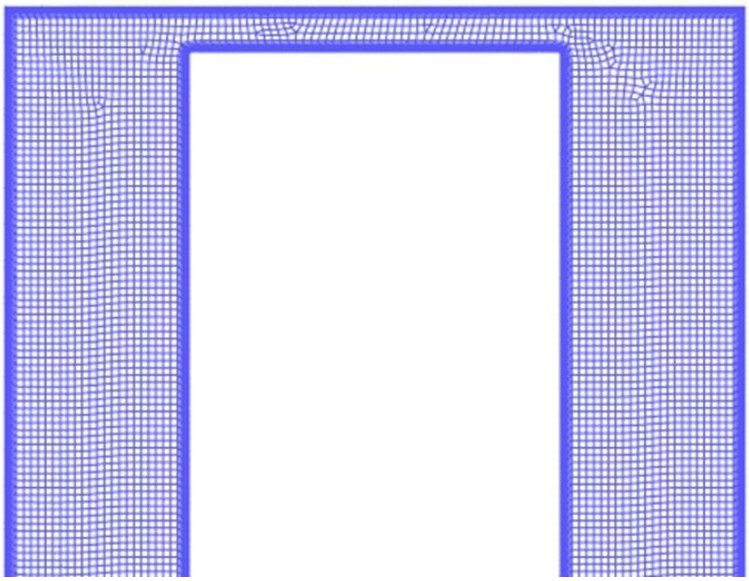


Figure 4-6: Truncated view of Mesh 2 – 0.25 mm element sized mesh

Quadrilateral mesh shown includes a base cell size of 0.25 x 10^{-3} m and was generated within ANSYS-Mesher; it includes a uniform grid spacing in the x-axis, also normal to the rotating and stationary walls. The first off-wall grid node is located at $y^+ < 1$ on the parallel edges of the stationary and rotating disks and $y^+ < 5$ on the edges making up the radial gap of the disks. The flow at the boundary layers has been resolved with the enhanced wall function available in the $k - \varepsilon$ model. To accurately model the flow at the boundary layers and capture the wall effects, 8 inflation layers with a growth rate of 1.2 were added along the rotating and stationary walls. The inflation layers were set up using the 'first layer thickness' option available within ANSYS-Mesher. This criterion is extremely useful when a specific y^+ value needs to be achieved as in the numerical investigations in this work. The first layer thickness can be set as a parameter, allowing for proportional adjustments to be made to the expected y^+ values in the solution. A first cell height of 0.025 x 10^{-3} m was selected to yield a $y^+ < 1$ on the

walls so that the boundary layer profile can be resolved all the way to the wall providing a more accurate resolution of the boundary layer. The transition ratio between the boundary layer and the uniform mesh is 2.79 and the mesh could be improved with the addition of 4 more inflation layers to ensure a smooth transition between the boundary layer and the uniform cell region in the domain. To understand the impact of this transition, a non-dimensional axial profile of tangential velocity in water along a line at the radial location r/a = 0.983 was plotted as illustrated in Figure 4-7. The inflation layer thickness spans up to a distance of z/a = 0.001 from the stationary and rotating walls. It can be seen that continuity in the velocity profile is maintained as it transitions from the boundary layer to the core flow region. Therefore, it can be said that the transition region is well resolved and has no negative impact on the results.

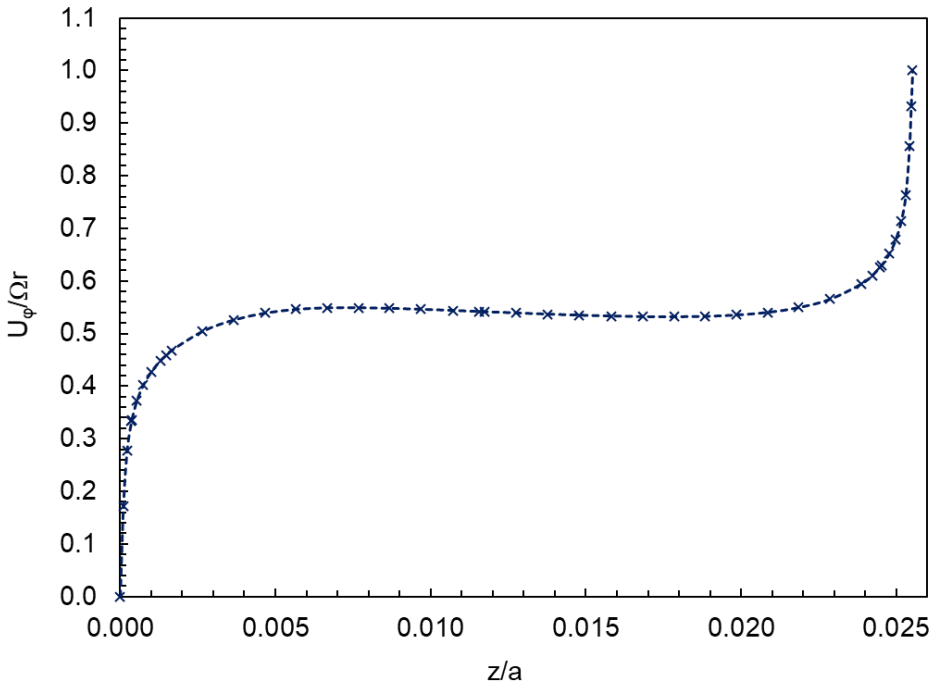


Figure 4-7: Axial profile of tangential velocity at r/a = 0.983 when Re_Ω = 4.4 x 10^6 for s/a = 0.0255

4.2 Flow characteristics of fully wetted disks

Tangential and radial velocity distributions for turbulent flow in water at Re_Ω = 4.4 x 10^6 for s/a = 0.0255 at a relative radii r/a = 0.765 were plotted in a non-dimensional form as illustrated in Figure 4-8 and Figure 4-9 respectively from the stationary wall to rotating wall with the stationary disk represented at the axial location, x = 0. The velocity has been non-dimensionalised by the local velocity, Ωr, at disk radius, r. The distance in the cavity in the direction normal to the wall has been non-dimensionalised by the disk radius, a. According to the experimental results by Daily and Nece [40], the control parameters considered, should yield a flow field characterized by Regime III. The results for steady and transient solutions using two equation models RANS $k-\varepsilon$ and SST $k-\omega$ and the RSM model were compared to the experimental data.

The experimental measurements of Daily and Nece [40] in Figure 4-8 shows a considerable variation in the tangential velocity profile in the core region suggesting the boundary layers are merged displaying the characteristics of the Stewartson flow model. The variation in the tangential velocity distinguishes Regime III from Regime IV where the core velocity is constant indicating a central core flow exists that separates the boundary layers. As the flow experiment was carried out for a small gap at a higher Reynolds number higher than $Re > 10^6$, the existence of regime III is therefore established. However, it is interesting to note that the CFD results for steady state and transient solutions for the $k-\varepsilon$ model estimate very similar tangential velocities. While the variation in tangential velocities across the same range of axial positions is

not as large as the variation displayed in the experimental data, CFD results obtained through the two $k-\varepsilon$ models and the RSM model have been able to demonstrate a tangential velocity variation in the core region.

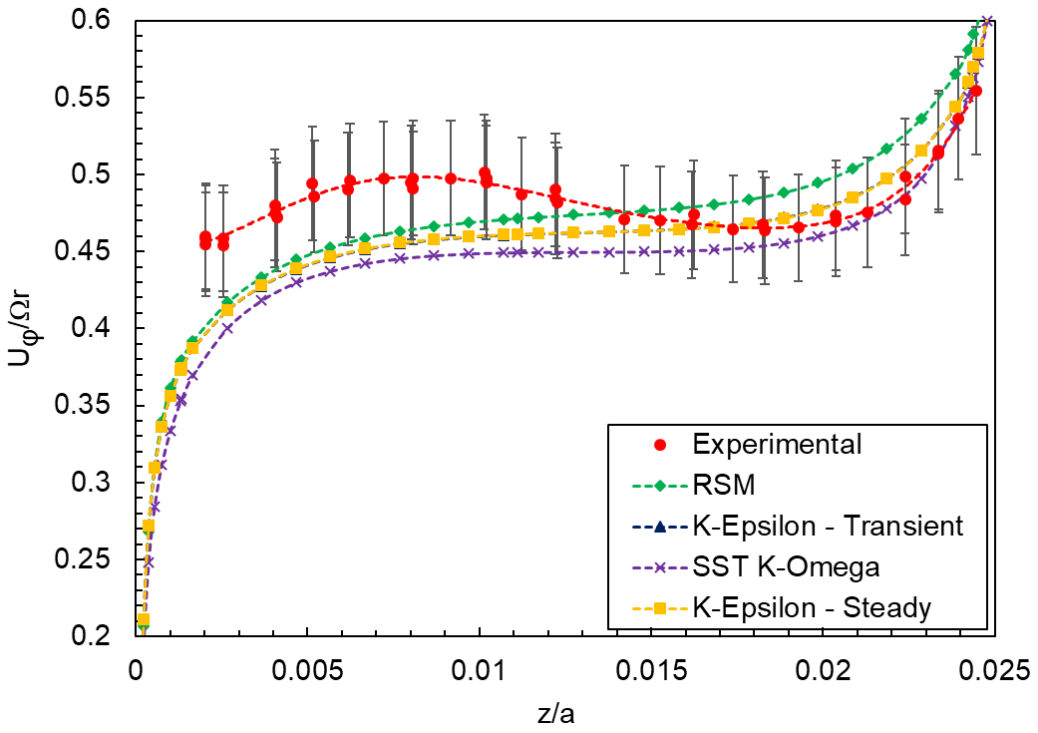


Figure 4-8: Axial profile of tangential velocity at Re_Ω = 4.4 x 10^6 for s/a = 0.0255 and r/a = 0.765

It can be seen that the tangential velocities have been over predicted by $k-\varepsilon$ model for 0.025 < z/a < 0.018 and the RSM model for 0.025 < z/a < 0.015 while the velocity profile obtained with the SST $k-\omega$ model predicts the variation in tangential velocity closer to the rotating disk quite well. All three models have under predicted the tangential velocity as it moves from the central area of the axial gap towards the stationary disk. In the region 0 < z/a < 0.013, the SST $k-\omega$ model records the lowest tangential velocity and the RSM has been able to capture the velocity closer to the

experimental data. It is noted that the velocity data obtained using the SST $k-\omega$ model does not show a significant variation in tangential velocity in the core and the variation is less than with the other models. Although the differences between the tangential velocities obtained by the RSM and $k-\varepsilon$ models in this region ($0 < z/a < 0.013$) are small, all three computational data sets are far from the experimental profile.

The velocity dip and rise exhibited in the experimental profile is questionable as the results have been obtained through pitot tube measurements; an intrusive measurement technique where any misalignment with the flow would cause an error. In this flow experiment by Daily and Nece [40], velocity profiles were measured at three different radial positions using a two-stage approach. Firstly, a 2-hole cobra probe was used as a directional probe to determine the velocity vector orientation. Subsequently, a modified pitot-static tube was employed to measure the total velocity magnitude by replicating the Reynolds numbers, probe positioning, and orientation obtained from the first phase. The total velocity was then decomposed into its tangential and radial components using the measured flow angle.

In the central portion of the flow, inaccuracies are expected in the velocity measurements due to the process of attempting to replicate the identical experimental conditions for velocity magnitude measurements. The error associated with the precise repetitive positioning of the axial location of the probe and angular alignment with the flow, as well as the instrumentation error, has not been stated in this work by Daily and Nece [40].

In boundary layer flows, pitot-tube measurements are subject to complex aerodynamic interactions arising from velocity gradients and wall proximity. The shear forces induce a non-uniform velocity distribution across the probe aperture, resulting in a spatial integration of the flow field rather than a true point measurement. Concurrently, the presence of the probe near the wall introduces blockage effects and perturbations to the local pressure field, significantly altering the flow streamlines. These phenomena are particularly pronounced in the near-wall region where viscous effects dominate. The superposition of these factors leads to a non-linear response in the measured dynamic pressure, and is often manifested as errors in velocity determination. The magnitude of these errors is attributed to the probe orientation and the non-negligible probe diameter relative to the characteristic length scale of the boundary layer. Therefore closer to walls, an adjustment to the measurements is necessary to compensate for enhanced blockage effects. Researchers often apply correction factors derived from calibration experiments or simulation, incorporating parameters such as the local velocity gradient and wall distance. This correction should ideally account for the probe induced reduction in shear-driven streamline curvature. A study by MacMillan [217] demonstrated that this effect is significant within a spatial domain extending two probe diameters from the wall.

The diameter of the probe used in this experiment is 0.343 mm and corresponds to a non-dimensional length, z/a of 0.0036. Applying MacMillan's [217] findings in Figure 4-8, it can be seen that 2 velocity data points closer to the static wall and 4 readings closer to the rotating wall are affected due to the probe effect. Therefore, to improve

the assessment of the accuracy of the CFD results, the error in the experimental data was quantified. Using the sensitivity correlations between differential pressure and galvanometer readings provided by Daily et al. [218], the error in total velocity was determined across the entire measurement scale. This error was then scaled to be applicable to the range of tangential and radial velocity readings shown in Figure 4-8 and Figure 4-9 respectively. This was done using the ranges of velocity obtained for four scales by Daily et al. [218]. The tangential component was obtained by multiplying the total velocity by $cos\,\alpha$ and the radial component by $sin\,\alpha$. To determine the sensitivity in the flow angle, α, it was assumed that the flow field within a range of ± 10° has been measured in the experiment, based on the measured range of tangential and radial velocities. The errors were then combined using standard error analysis by Bevington [219]. The error in the tangential velocity component was computed to be 7.4% and the error in the radial velocity was found to be 11.1%. The root-mean-square-error (RMSE) between the experimental data and CFD data sets obtained through the RSM, $k-\varepsilon$ and SST $k-\omega$ models is 3.1%, 2.9% and 3.5% respectively. Therefore, it can be seen that the obtained CFD results are in good agreement with the experimental data when compared with bounds of error.

It can be seen in Figure 4-9, that the CFD radial velocity profiles are divided into two zones: the flow is directed inward on the stationary disk for $0 < z/a < 0.013$ and it is ejected under the centrifugal effects of the rotating wall for $z/a > 0.013$. This suggests that a radial circulation of fluid occurs outside the boundary layers. It can be seen that the radial velocity varies closer to zero axially, and the peak normalized tangential

velocity is much greater in magnitude than that of the radial velocity. This is a typical flow feature in rotor-stator disk cavities due to the high rotational movement of the fluid particles in the central region between the disks. Therefore, the tangential velocity in such flows is far higher compared to the axial and radial components.

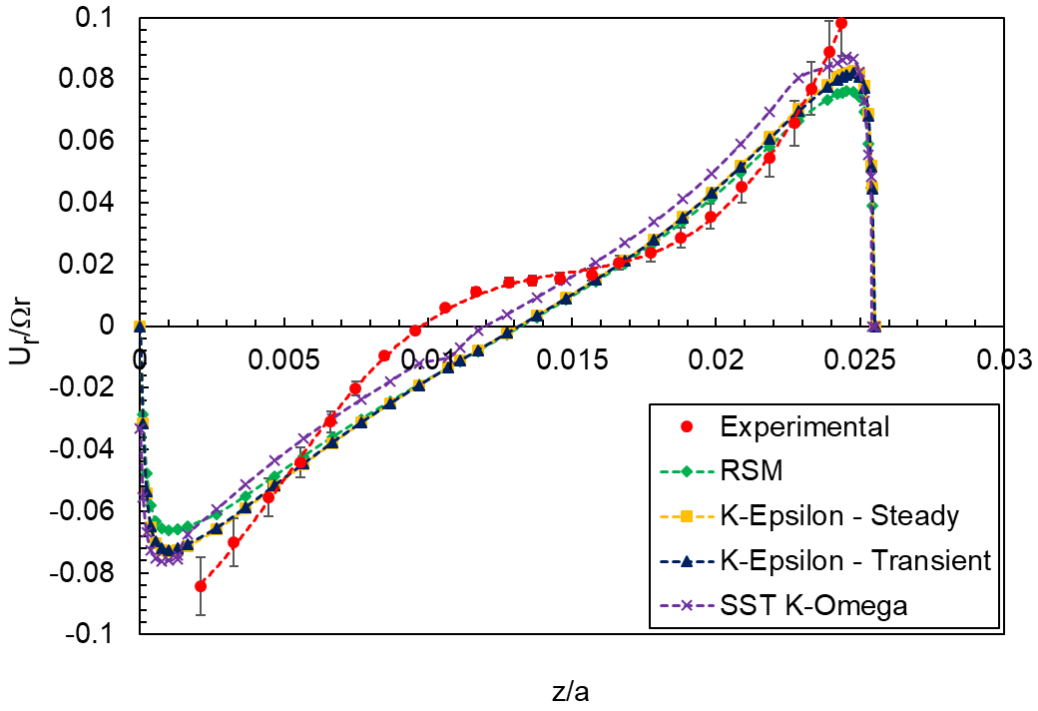


Figure 4-9: Radial velocity profile axially obtained at Re_Ω = 4.4 x 10^6 for s/a = 0.0255 and r/a = 0.765

Very similar results with negligible differences are observed in the radial velocity profiles for both transient and steady solutions obtained through $k-\varepsilon$ and the RSM models, but the SST $k-\omega$ model records slightly higher radial velocity values along the entire axial distance than the velocity values obtained through the other models. The results indicate that all the turbulence models applied in this study have been able to

predict a radial velocity profile closer to the experimental measurements compared to the tangential component. Again, the shape of the experimental data profile is different to the ones obtained with CFD. It is worth noting that this could be due to the reasons discussed previously.

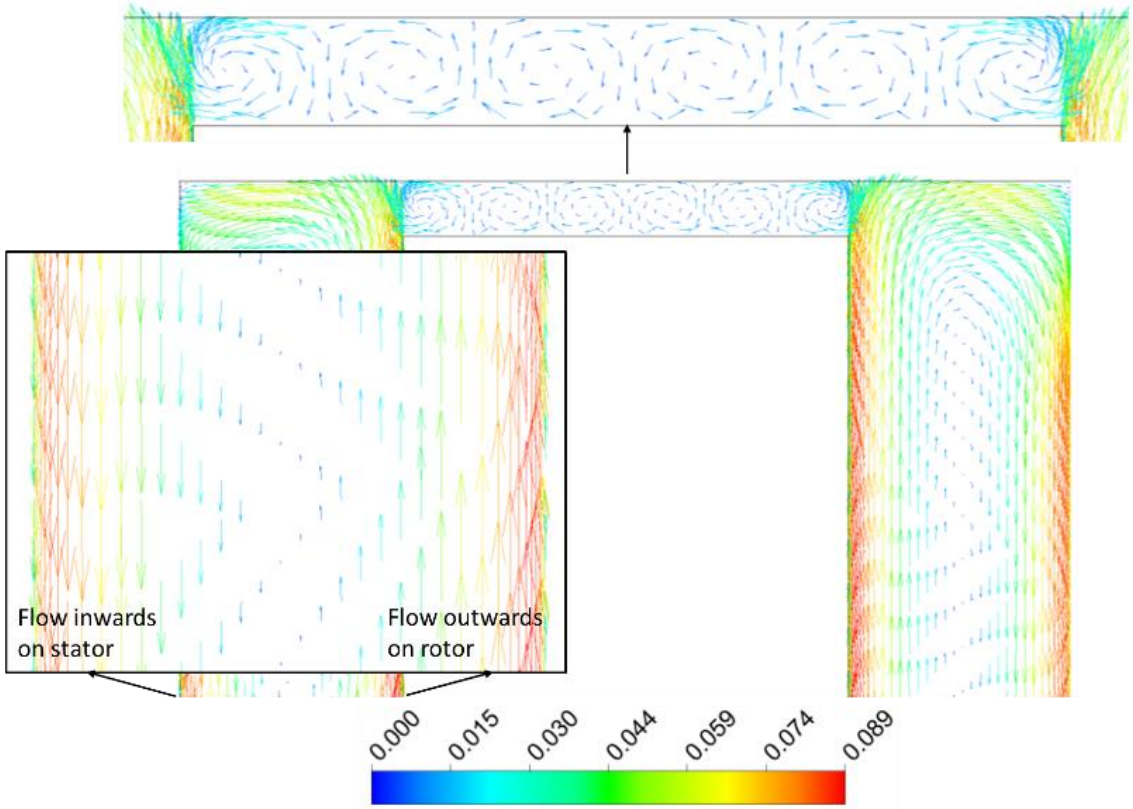


Figure 4-10: In-plane non-dimensionalised velocity vectors coloured by velocity for the secondary flow at Re_Ω = 4.4 x 10^6 and s/a = 0.0255

The in-plane velocity vectors obtained through the $k-\varepsilon$ model for the secondary flow at Re_Ω = 4.4 x 10^6 for s/a = 0.0255 at a relative radius r/a = 0.765 between the rotating and stationary wall are illustrated in Figure 4-10. It can be seen that a large recirculation zone is induced by the rotating wall as the liquid pumps up the rotating wall and moves

down the stationary wall. It also illustrates the formation of counter rotating vortices, typically referred to as Taylor vortices in the radial gap between rotating and stationary walls. The vector plot shows three pairs of Taylor vortices which begin to form at the two edges in the radial gap. These vortices appear to propagate as they develop and meet in the centre when they are fully developed.

To investigate the behaviour of the fluid flow between the rotating and stationary walls in the radial gap the Taylor Number, Ta, the radius ratio, ζ, and the wavelength of the vortices, λ, were computed using the following equations and extrapolated data from the analytical analysis by Donnelly and Schwarz [220].

$$\zeta = \frac{R_i}{R_o} \tag{4-1}$$

$$T = \frac{2\zeta^2 c^4}{1 - \zeta^2}\left(\frac{\omega}{\nu}\right)^2 \tag{4-2}$$

$$\alpha_{axial} = \frac{2\pi c}{\lambda} \tag{4-3}$$

Where R_i and R_o are the inner and outer cylinder radii respectively and α_{axial} is the axial wavenumber whose values have been read from the study of Donnelly and Schwarz [220]. In this study by Donnelly and Schwarz [220], the ion technique was utilized across several experimental investigations of Couette flow between rotating cylinders. These included identifying the critical Taylor number denoting the transition from laminar to vortex flow, characterizing both the wavenumber and shape of the

resultant vortices, and verifying predicted relationships wherein the square of vortex amplitude and amplification factor vary linearly with the difference between operating and critical Taylor values. Additionally, the study focused on quantifying vortex growth and decay rates in response to changing Taylor number.

The computed Taylor number experienced by the fluid was found to be 5.0×10^{6} and the wavelength of a pair of vortices was 3.19×10^{-3}m in the radial gap where the radius ratio was 0.99. Therefore, the number of vortices based on an ideal wavelength expected in the gap should be 8 (4 vortex pairs) as suggested by theory derived for walls at the end of the cylinders. However, as the angular velocity of the rotor increases, a greater influence on the end vortices causes the formation of a fewer number of vortices than expected as can be seen in Figure 4-10, where 3 vortex pairs are found in the radial gap.

4.3 Investigations into a partially wetted disk rotating in a stationary casing

Moving from a fully wetted disk to a partially wetted disk, it is noted that Ketola and Mcgrew [41] presented a theory of a partially wetted rotating disk and experimental data to verify the application of the theory established. The analysis of the partially wetted disk assumed the existence of all four regimes verified by Daily and Nece [40]. This study introduced an additional parameter, the engagement ratio X; which refers to the measure of the submergence of the disk in the fluid. The study confirmed that the operational characteristics of the disk are not only a function of Re_{Ω} and s/a, but also of the engagement ratio. A disk that is not wetted at all can be denoted by an

engagement ratio of zero while a fully wetted disk can be denoted by an engagement ratio of 1. Two flow regimes were considered in the study by Ketola and Mcgrew [41]; one condition with nonflow where only recirculatory flow exists in the chamber. The other condition with through-flow was considered, where a finite flow passes through the chamber. The CFD investigation which considers the no-through-flow case is reported in Section 4.3.1; through-flow cases are outlined in Section 4.3.2.

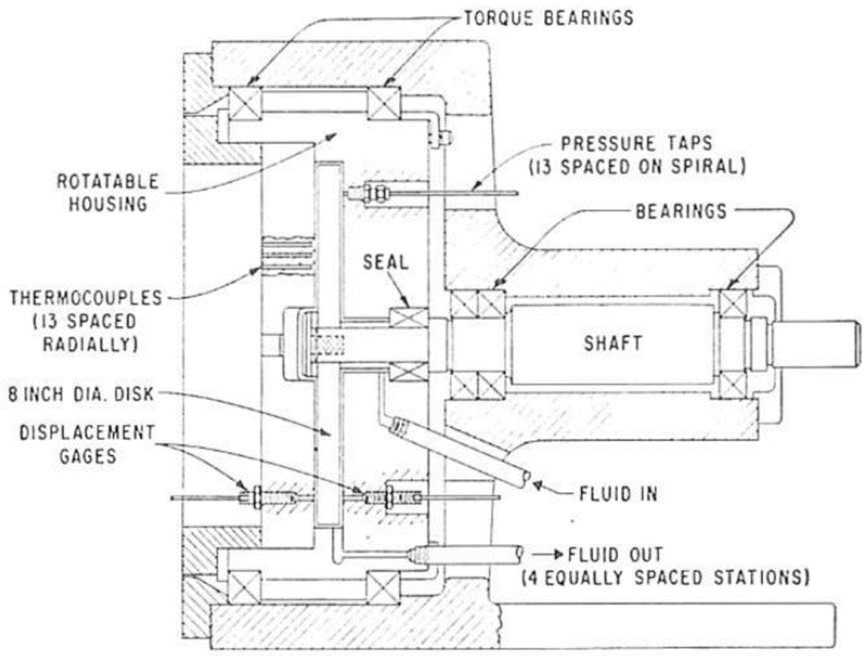


Figure 4-11: Schematic of the experimental apparatus used in the study by Ketola and McGrew (from [41])

In the original experimental set-up of Ketola and McGrew [41], one end of the shaft was coupled to a variable speed electric motor and the other end was fixed to a plain rotating disk which was placed in a stationary enclosure. This was supported by ball bearings in an aluminium housing. Spacer plates of different thicknesses were used to

vary the axial gap width between the disk and the enclosure walls. The experimental apparatus used is illustrated in Figure 4-11. The experimental conditions were simulated numerically so that the CFD results could be compared and verified. Discussed in the following subsections are the details of the numerical study and the results obtained for both non-flow and through-flow scenarios.

4.3.1 Nonflow regime

4.3.1.1 Numerical modelling approach

A CFD study of the flow characteristics of a partially wetted disk was conducted by examining the effect on the angular velocity of the fluid core with varying engagement ratios for a given spacing ratio. The validation data for the study is from Ketola and McGrew [41]. However, this publication does not explicitly include the radius of the shaft, a_1. Therefore, a shaft radius of 12.7 mm is assumed as it is consistent with the data presented in the paper. The essential elements of the geometry modelled in the CFD investigation are illustrated in Figure 4-12. Here, the axial and radial co-ordinates are denoted by x and y respectively: $y = 0$ at the rotational axis and $x = 0$ at the left stationary wall. The radial location of the interface (R) is related to the engagement ratio (X) using the following equation:

$$X = \frac{a - R}{a} \tag{4-4}$$

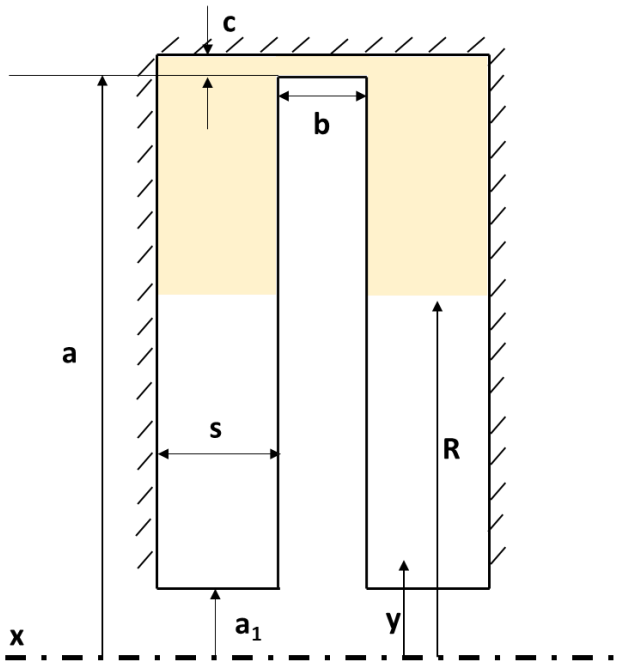


Figure 4-12: Geometry investigated in the CFD study modelling a partially wetted rotating disk

The CFD study investigates the same geometry as in the original experimental set-up of Ketola and McGrew [41] in order to replicate the experimental conditions. The main geometric parameters are summarised in Table 4-3.

Table 4-3: The principal geometric parameters used in partially wetted disk study

Radius of rotating disk, *a* (mm)	101.6
Radius of the shaft, a_1 (mm)	12.7
Thickness of rotating disk, *b* (mm)	12.7
Radial clearance between rotating disk and end stationary wall, *c* (mm)	0.635
Axial clearance between disk and end stationary wall, *s* (mm)	10.14

The 2D axisymmetric computations for both non-flow and through-flow regimes were carried out by firstly simulating an air-only single phase scenario in steady-state until the flow reached pseudo-steady state. The VoF method was then applied by patching a volume of water into the domain to model the multiphase nature of the partially wetted disk, where water was considered the primary phase. Water-air surface tension was activated with a constant surface tension value of 0.072 N/m^2. The CFD results for the non through-flow case of a spacing ratio (s/a) of 0.1 and engagement ratios (X) of 0.163, 0.275, 0.374, 0.510 and 0.75 were compared and validated against the experimental data of Ketola and McGrew [41]. In this section, the angular velocity ratio between the disk and the fluid core is defined as:

$$K = \frac{\beta_{fluid}}{\Omega} \tag{4-5}$$

where β_{fluid} is the angular velocity of the fluid core and Ω is the shaft's angular velocity.

β_{fluid} is also referred to as the swirl ratio in literature and has been a subject that has been studied extensively over the years. In one of the earliest works, Batchelor [31] suggested that the core between the stator and rotor, rotated at an angular velocity with an intermediate value between stator and the rotor rotational speeds. As discussed in Chapter 2, Picha and Eckert [33] demonstrated that the core rotates at a minimum when open to external atmosphere, but if the rotor-stator cavity contains a stationary shroud, a rotating core is formed. They also found that the angular velocity of the rotating core

reduced as the gap between the rotor and stator was increased. Based on the findings of their experimental studies, Daily et al. [218] proposed the following expression correlating the fluid core to the geometrical features of an enclosed rotor-stator cavity for the turbulent regime:

$$\beta_{fluid} = 0.49 - 0.57\frac{s}{a} \tag{4-6}$$

In the test series by Ketola and McGrew [41] examining the nonflow cases, the rotational speed was restricted to an upper limit of 3500 rpm due to internal heating as there was no fluid passing through the casing cooling the recirculatory flow within the cavity. The primary features and boundary conditions of the CFD model used to investigate the flow characteristics of the partially wetted disk case are detailed in Figure 4-13.

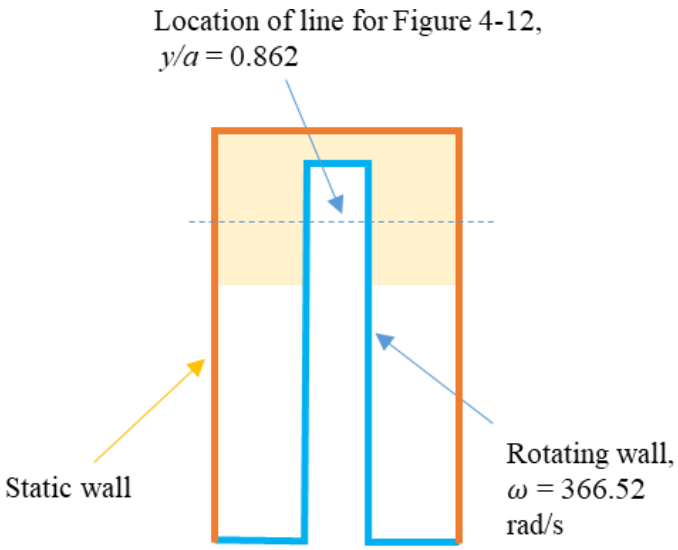


Figure 4-13: Boundary conditions modelled in the CFD model for the partially wetted disk case

The fluid was patched into the domain in the zone shaded in Figure 4-13 at the start of the transient computation. The results from the two equation models obtained in the fully wetted disk case are in good agreement with the experimental data for the mean tangential and radial velocity components. Compared to the RSM, faster converging, robust solutions were obtained with standard $k-\varepsilon$ and SST $k-\omega$ models. Taking into account this trade-off between the accuracy and computational cost, it was considered reasonable to apply a two-equation model in the rotor-stator cavity flow calculations when the disk is partially immersed in liquid. The main modelling choices used in this CFD investigation are summarised in Table 4-4.

Table 4-4: Principal modelling features of the CFD model of the partially wetted disk case

Modelling parameter	Value/ model used
Outer wall boundary condition	Stationary
Inner wall boundary condition	Rotating at 366.52 rad/s
Turbulence treatment	SST $k-\omega$
Pressure- velocity coupling	Coupled
Pressure interpolation scheme	PRESTO
Spatial discretisation algorithm	Second order upwind

The SST $k-\omega$ model was applied based on its applicability to a wide range of wall y^+ values and its ability to include interfacial turbulence treatment [221]. Previous studies show that the SST $k-\omega$ model is a suitable approach to model turbulence

particularly in cases where there is fast rotating motion in proximity to stationary walls as is the case in bearing chambers [222]. Each CFD case was simulated allowing the flow to reach pseudo steady-state using a variable time step with an initial time step time step, (Δt) of 10^{-6} s, each time step running for thirty iterations allowing the solution to converge within this pseudo time step. Convergence at each time-step was controlled using a residual convergence criterion of 1×10^{-5} for the continuity, velocity, swirl and turbulence variables. Overall convergence of the solution was primarily monitored using bulk residuals, moment coefficient of the walls and velocity magnitude at several locations. A fully developed flow was achieved with 116.7 disk revolutions in a total flow time of 2 s for which 141 core hours of computational time or 35.25 hours of physical time was required. The computations were conducted using 4 Intel Xeon Gold 6238 cores.

Mesh independence study

A mesh independence study was carried out separately for the Ketola and Mcgrew [41] geometry to ensure the solution is independent of the mesh size. Three structured mesh sizes with quadrilateral cells were considered, an element size of 0.5mm which is represented by Mesh 1, was used as a starting point for the mesh size based on the conclusions made from computation of the fully wetted disk case presented in Section 4.1. Structured meshes were investigated in this case to determine the effect of mesh quality on the solution and its ability to capture important flow detail in the cavity. The methodology developed here will be extended to the application of a hydraulic seal, therefore, it is important to examine the influence of numerical parameters. Simulations

were conducted on meshes with 20, 40 and 80 elements across the axial length from stator to rotor (s) designated Mesh 1, Mesh 2 and Mesh 3 respectively. Details of the meshes compared for this case are given in Table 4-5.

Table 4-5: Mesh sizing of the CFD case modelling partially wetted disk

	Mesh 1	Mesh 2	Mesh 3
Number of elements across axial length	20	40	80
Number of cells	15,369	40,978	148,614

Results from these three meshes were obtained for an engagement ratio of X = 0.275. A comparison of tangential velocity along an axial line midway through the liquid (at r/a = 0.862) (see Figure 4-13 for location) is shown in Figure 4-14.

The computed core velocity for Mesh 1 is somewhat lower than for Meshes 2 and 3 where results are seen to be very close as can be seen in Figure 4-14. Therefore, to select the optimal mesh, the root-mean-square-error between the experimentally obtained velocity ratio (K) and that obtained through CFD for each mesh was computed. The RMSE values for Mesh 1, Mesh 2 and Mesh 3 are 1.8%, 1% and 2.2% respectively. Results obtained with all three meshes match closely with the experimental data. However, Mesh 2 offers a compromise between computing time and interface resolution. Therefore, Mesh 2 was selected as the optimal mesh to accurately model a rotating disk partially immersed in liquid whilst ensuring minimal computational cost.

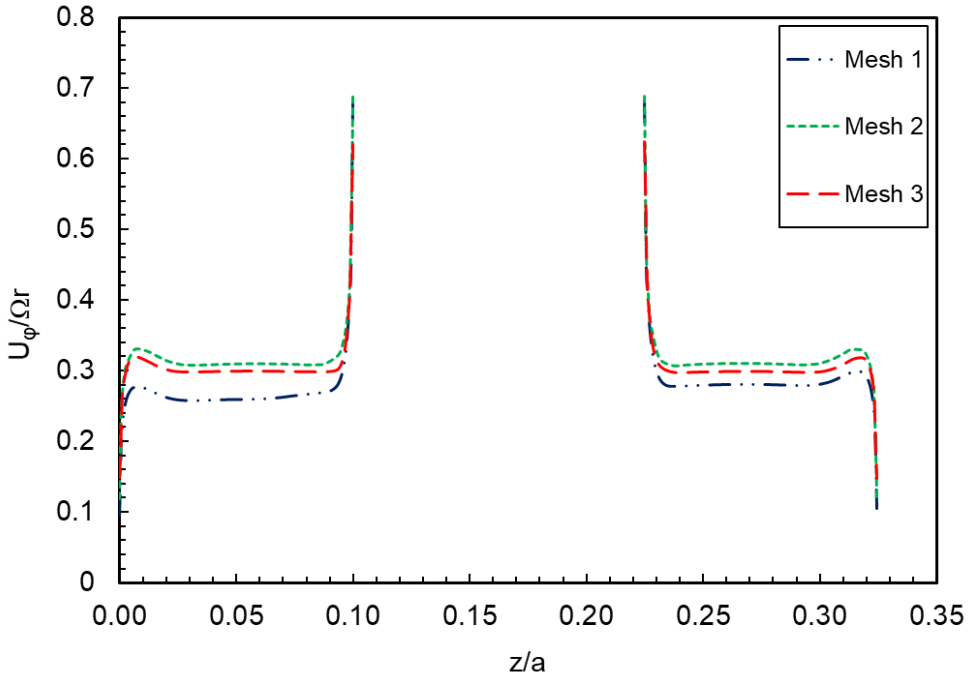


Figure 4-14: Comparison of meshes investigated monitoring the profiles of tangential velocity along a line through the liquid r/a = 0.862

4.3.1.2 Flow characteristics of partially wetted disks with no through-flow

Results were obtained for five engagement ratios, chosen to match available experimental data, X = 0.163, 0.275, 0.374, 0.511 and 0.75 at a spacing ratio s/a = 0.1. Figure 4-15 shows the volume fraction contours for an engagement ratio of 0.374 including details of the liquid/gas distribution and velocity vectors near the interface. It can be seen that the interface is not completely flat but shows a degree of slant with the liquid level being somewhat higher (when considered from the centreline of the shaft) near the rotating disk compared to the stationary surfaces.

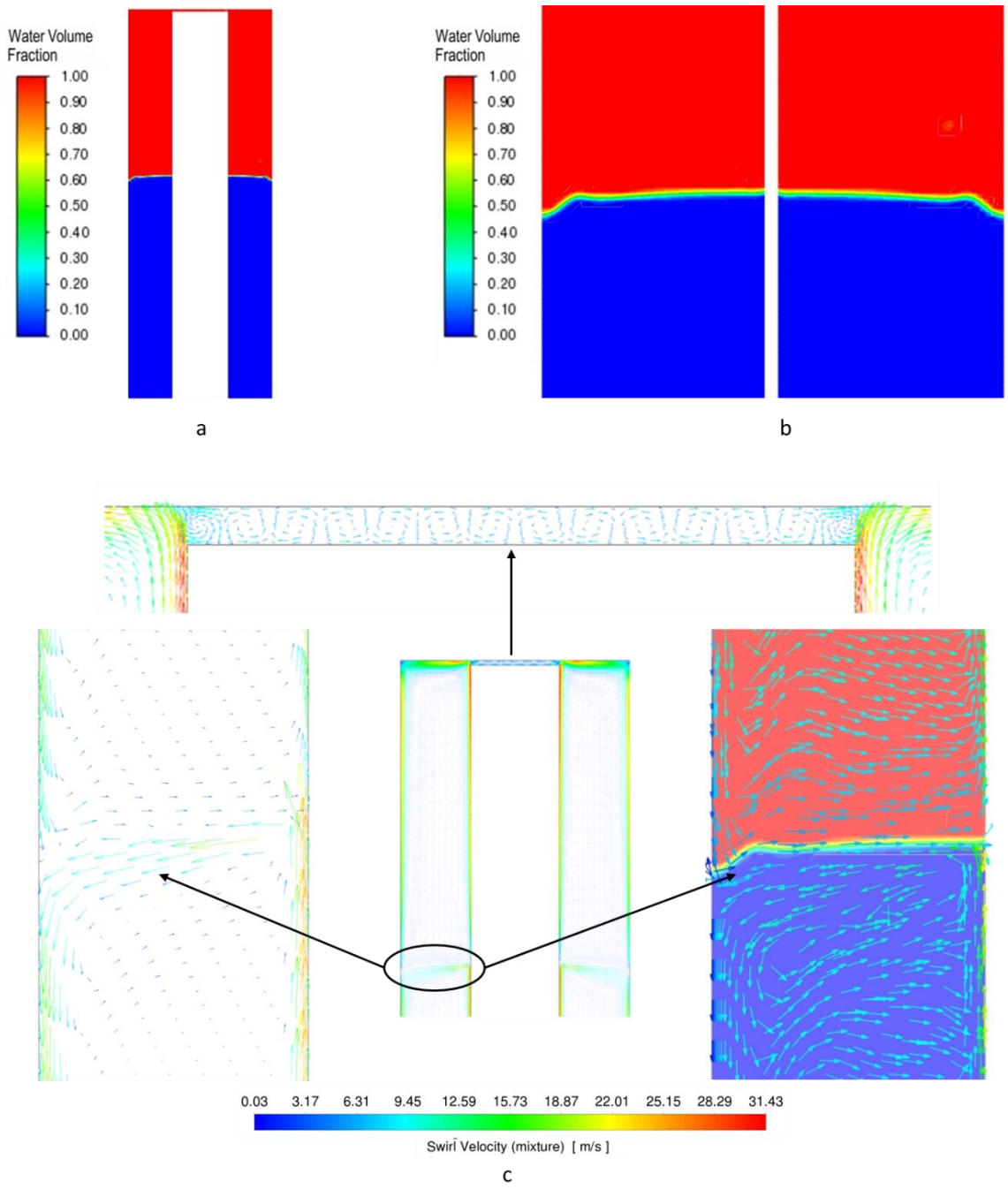


Figure 4-15: Solution for the case with X = 0.374; (a) shows overall volume fraction distribution with the detail near the interface in (b) and the in-plane velocity vectors for the secondary flow near the interface and in the radial gap in (c)

The effect of the rotating disk on the fluid near it is to pump it radially outwards and it is this that accounts for the deformation of the liquid surface as can be seen in Figure 4-15b. The significant variation in air velocity near the interface at the rotating and stationary walls forces the liquid level radially inwards closer to the stationary wall as shown in Figure 4-15a and Figure 4-15b. Instability causes the formation of counter rotating Taylor vortices, which can be seen in Figure 4-15c. It was calculated that the Taylor number experienced in the radial gap (of radial extent 6.35×10^{-3} m) was 7.41×10^{6} in the computation carried out to investigate the flow behaviour in that region. The corresponding radius ratio, ζ, and the wavelength of a pair of vortices, λ, were found to be 0.99 and 1.28×10^{-3} m. Hence, a calculation based on an ideal wavelength should yield 20 vortices. The significant effect on the end vortices has resulted in the formation of a fewer vortices in the radial gap. This is evident in Figure 4-15c; where 14 vortices can be seen. However, very similar values for the radius ratio, ζ, and kinematic viscosity, ν, have been used in fully wetted and partially wetted disk cases for the computation of Taylor number. This has resulted in a Taylor number of the order of 10^{6} for both cases with a not so large difference in the computed values due to different angular velocities of the rotating disk used in the two cases. Therefore, it was interesting to observe that the number of vortices in the fully wetted disk case has been almost halved due to the radial gap that is almost twice as that of the partially wetted disk case.

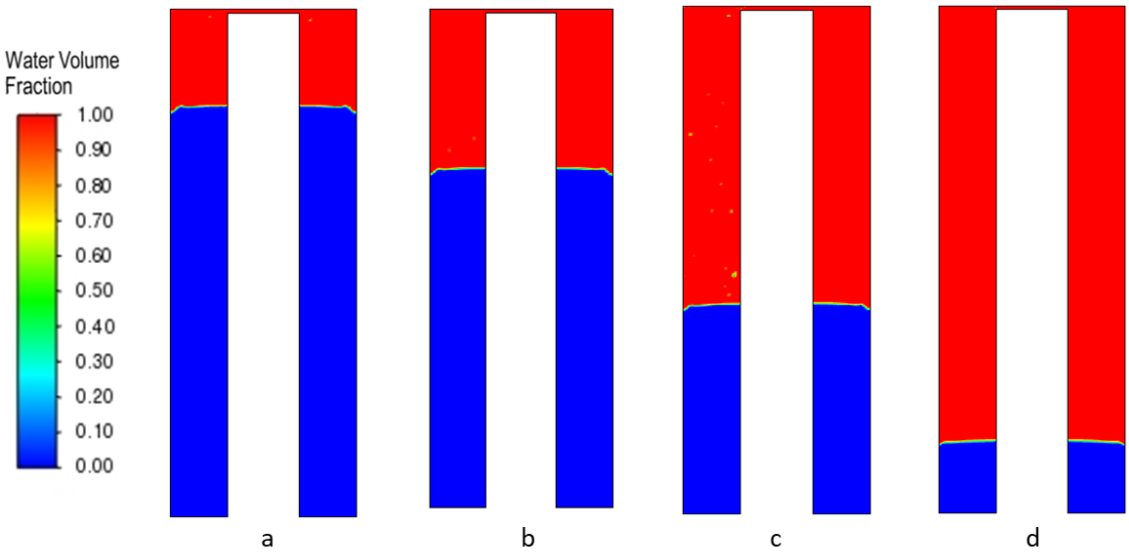


Figure 4-16: Contours of water volume fraction for the non-flow case of at (a) X = 0.163; (b) X = 0.275; (c) X = 0.511; and (d) X = 0.75

Figure 4-16 shows the volume fraction contours for the other four engagement ratios. With the exception of the case for X = 0.75, the shape of the interface is similar for the other cases. To understand the potential causes and the flow physics involved with this phenomenon, this was further investigated by plotting the in-plane velocity vector fields and stream lines of the flow field. Investigation of the vectors of normalised velocity magnitude in the air near the interface for this case is illustrated in Figure 4-17. The velocity has been non-dimensionalised by the velocity at disk radius, Ωa. Figure 4-17d shows the deformation of the interface when X = 0.75 which is not largely manifested as in the other cases. However, the interface is not completely flat as shown in Figure 4-16d.

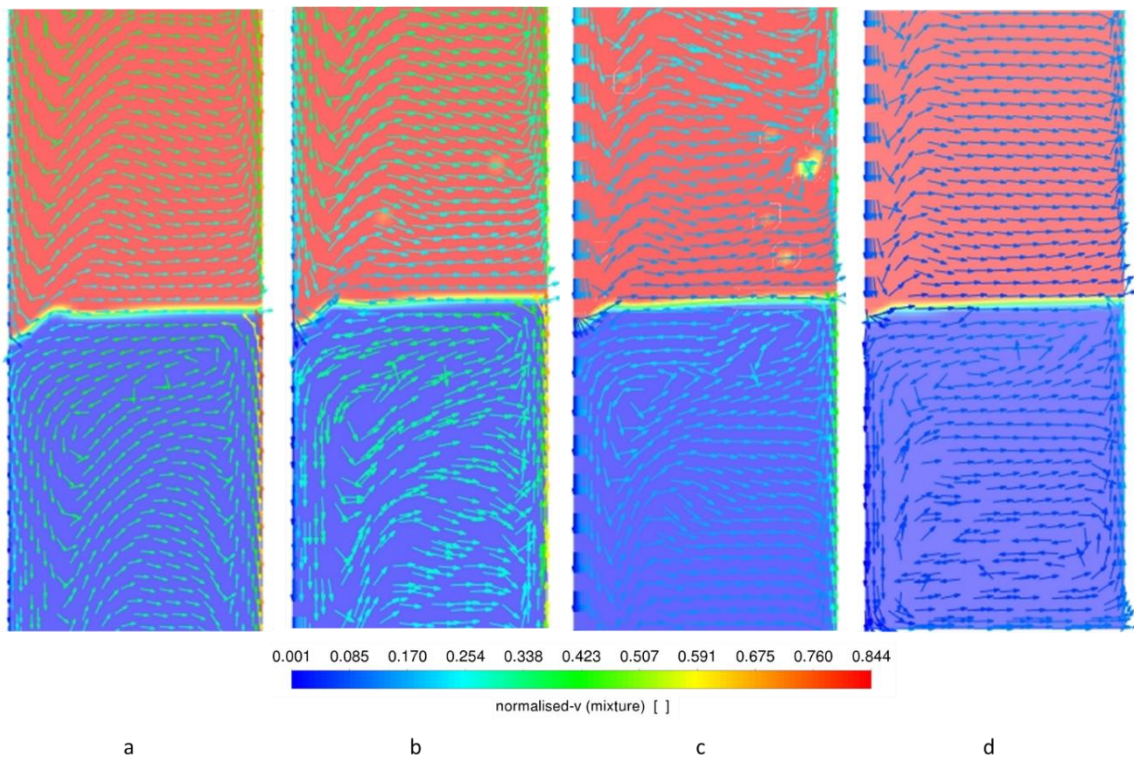


Figure 4-17: Normalised in-plane velocity vectors for the non-flow case around the interface at (a) X = 0.163, (b) X = 0.275, (c) X = 0.511, (d) X = 0.75. The in-plane velocity vectors in this region have been coloured by velocity, with the background colour indicating water volume fraction

It is apparent in the flow field displayed in Figure 4-17 that the fluid is pumped radially outward in the boundary layer on the rotating disk due to the centrifugal effects, and moves axially across to the boundary layer on the stationary disk. The fluid then returns radially inward along the stationary disk returning closer to the rotation axis. It is clearly depicted in Figure 4-17a through Figure 4-17c that in the axial cavity space where there is air, a large non-symmetric counter-clockwise recirculation zone further broken into two smaller vortices is formed at an angle to the walls. Here, the interface is far from the shaft and therefore, no interference of the secondary flow along the shaft with the

interface is experienced. At X = 0.75, as shown in Figure 4-17d, the interface is far closer to the shaft. The flow is parallel to the shaft and this modifies the size of the air secondary flow near the interface. However, there is a considerable difference in the flow field when R is the lowest or when X or the disk engagement ratio is the largest as seen in Figure 4-17d.

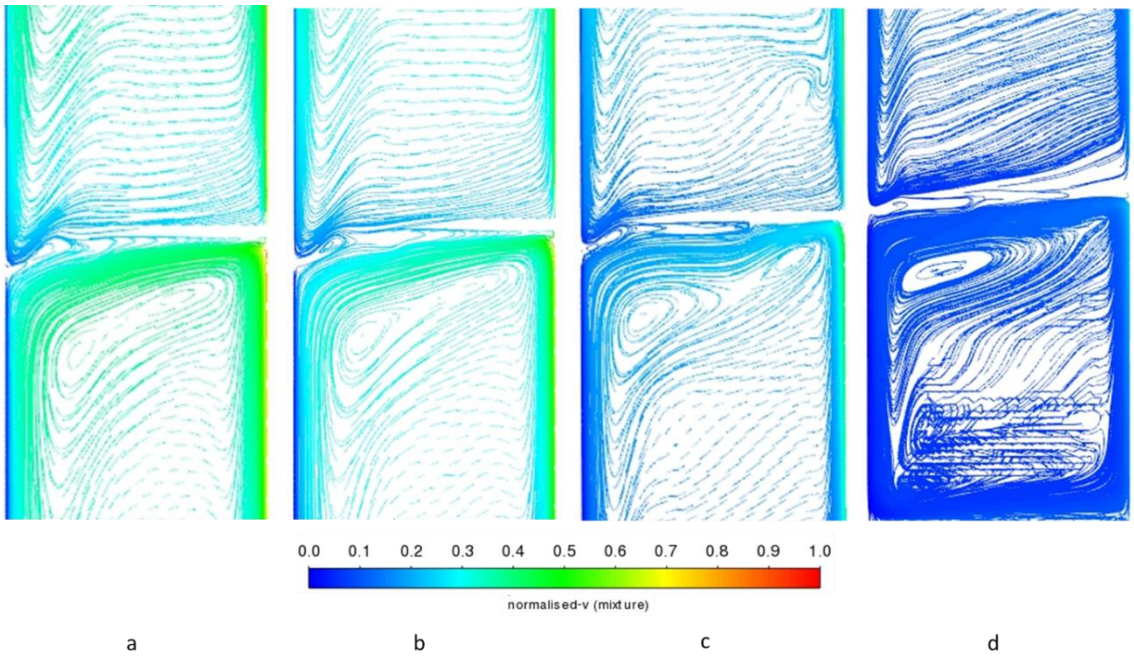


Figure 4-18: Streamlines in the axial gap between the stationary and rotating disks coloured by non-dimensionalised velocity magnitude for the non-flow case around the interface at (a) X = 0.163, (b) X = 0.275, (c) X = 0.511, (d) X = 0.75

As presented in Figure 4-18, it can be noted that the column of air rotates faster than the column of water above in each instance. It can be seen that there is a considerable velocity difference in the fluid layers just above and below the interface and this difference in velocity decreases as X is increased. This flow phenomenon explains the

deformation of the interface and why there is a dip on the interface in the boundary layer on the stationary disk.

Streamline patterns for the water column in the cavity between the stationary and rotating disks are illustrated in Figure 4-19. It can be seen that in the cavity region, the flow is centripetal along the stationary disk and centrifugal along the rotating disk exhibiting a Batchelor-like flow structure for all engagement ratios. It can also be observed that the thickness of the boundary layers on both stationary and rotating disks varies radially as X is increased. This shows that the rotating core takes up an increasing portion of the axial space as X is increased and is in agreement with the results published by Gauthier et al. [39]. This can also be confirmed by measuring mean velocity profiles at different engagement ratios. Theoretically, it is difficult to analyse the mean flow velocity as the core velocity is not uniform.

However, as suggested in literature, the flow in enclosed cavities is mainly Batchelor flow and the axial and radial velocity components of the Batchelor flow are insignificant compared to the tangential velocity [223]. In this case considered here, the main flow is tangential due to the rotation of the rotating disk and the axial gap between the disks is large enough to ensure that the secondary flow on a x, y plane can be described by the Batchelor flow model. Batchelor type flow can be characterized by three distinct zones. A centrifugal boundary layer on the rotating disk, a centripetal boundary layer on the stationary disk and a rotating core separated by the two boundary layers.

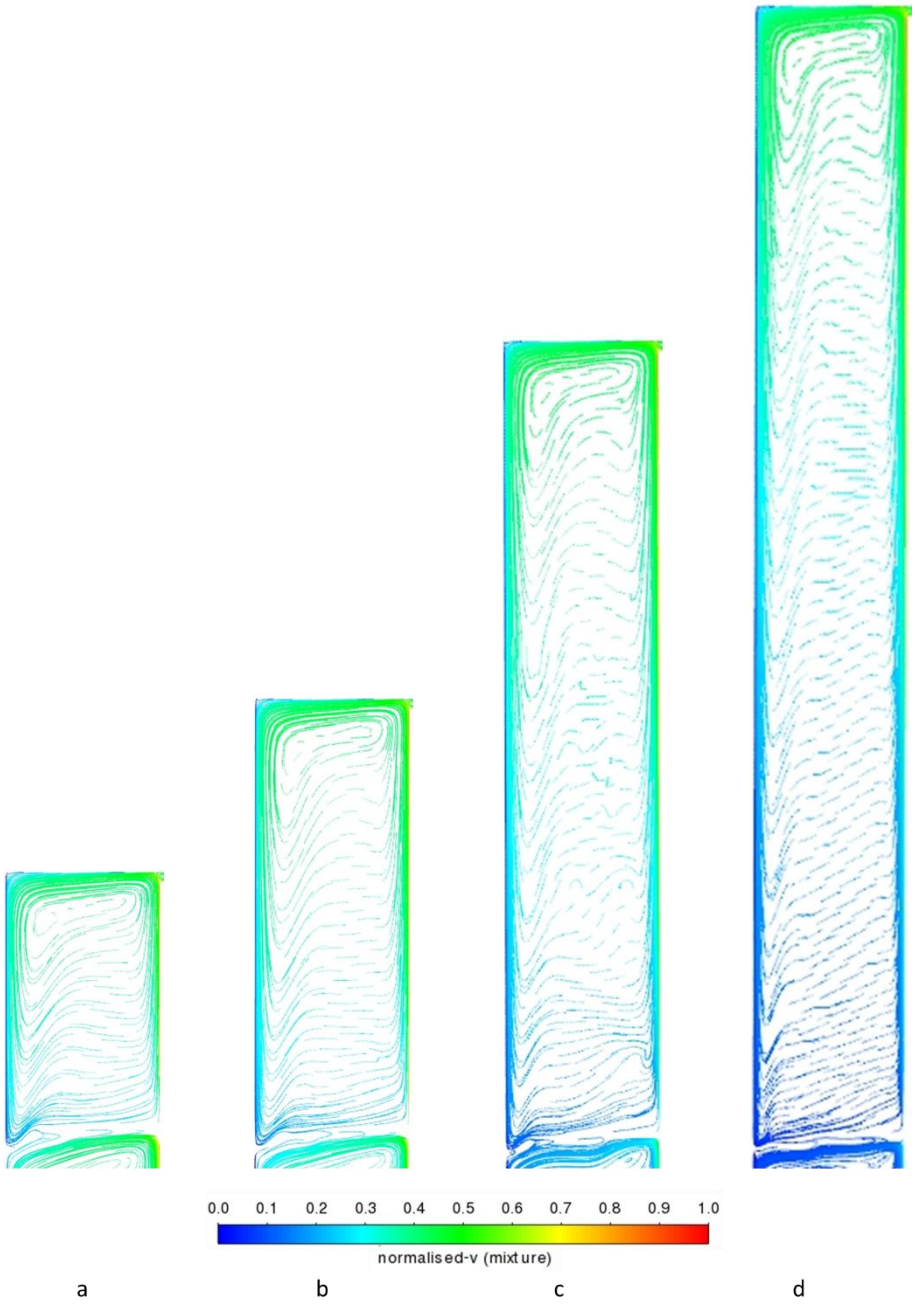


Figure 4-19 : Streamline patterns plotted for the water phase in the axial gap between the stationary and rotating disks coloured by non-dimensionalised velocity magnitude for the non-flow case at (a) X = 0.163, (b) X = 0.275, (c) X = 0.511, (d) X = 0.75

Therefore, it seems reasonable to estimate the angular velocity of the rotating core by measuring the tangential velocity at mid-height in the column of water between the bottom surface of the rotating disk and water/air interface.

The normalised tangential velocity profiles obtained axially at mid-height for different engagement ratios , X, are presented in Figure 4-20. The normalised tangential velocity profiles are plotted when $X = 0.163$, r/a = 0.919; $X = 0.275$, r/a = 0.863; $X = 0.374$, r/a = 0.813; $X = 0.511$, r/a = 0.745 and $X = 0.75$, r/a = 0.625. Based on the parameters applicable to this study, the computed Re_Ω is 4.4 x 10^6 and the spacing ratio, s/a, is 0.1 which should yield a flow structure characterized by Regime IV according to the findings of Daily and Nece [40]. These results presented below indicate that the flow structures have merged boundary layers up to a certain radius at each engagement ratio and separated beyond. The merged boundary layers are primarily seen closer to the tip of the rotating disk. It can be noticed that the tangential velocity is varying axially when $X = 0.163$ and $X = 0.275$ implying the absence of a rotating central core which suggests that the boundary layers on the two disks are joined up exhibiting characteristics of Regime III determined by Daily and Nece [40]. The transition from Regime III to Regime IV is evident in Figure 4-20c and Figure 4-20d when $X = 0.374$ and $X = 0.511$ respectively. As depicted in Figure 4-20e, when $X = 0.75$, the tangential velocity is constant along the axial distance which demonstrates that the flow is indeed Regime IV.

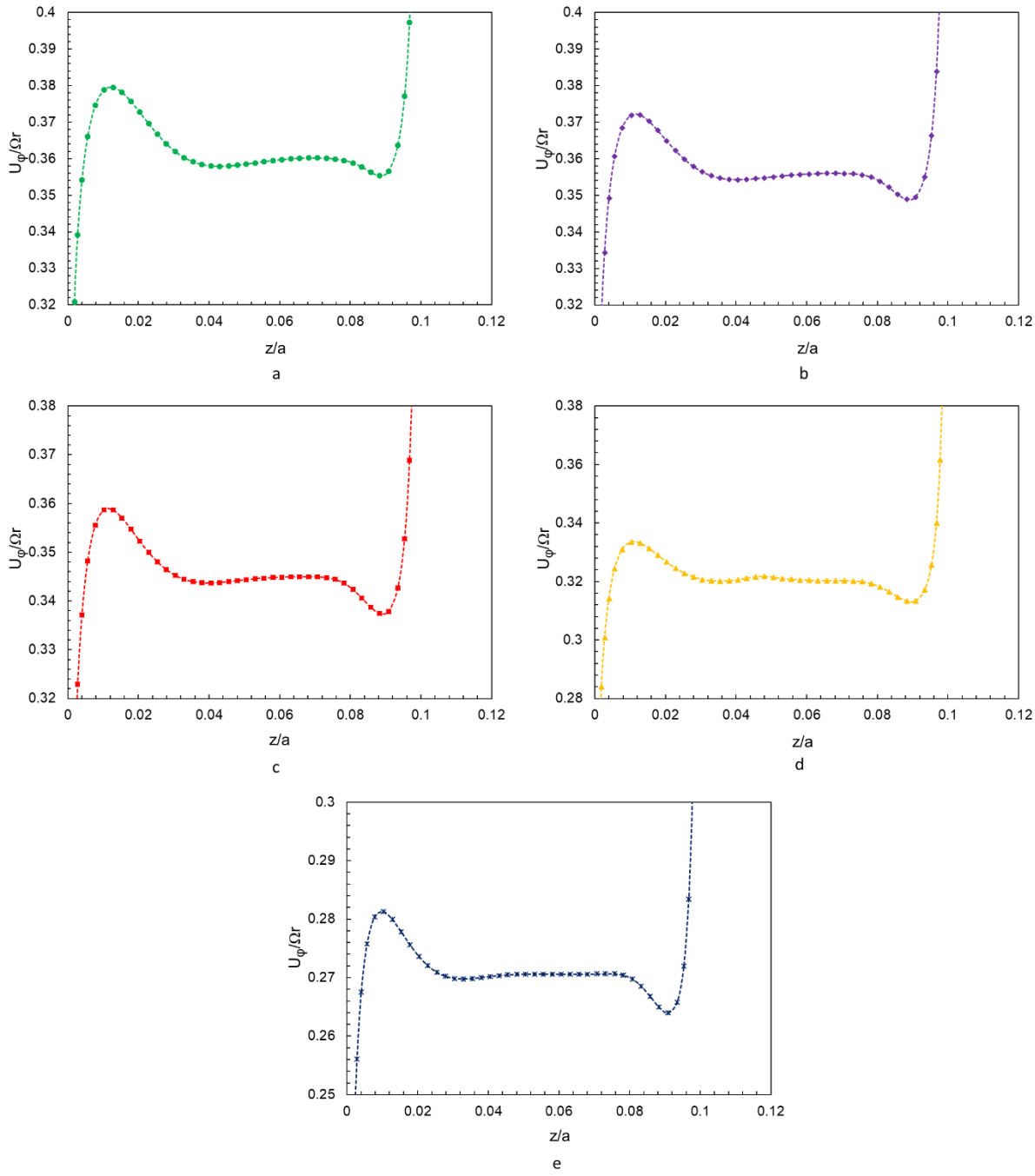


Figure 4-20: The axial profiles of non-dimensionalised tangential velocity plotted at (a) $X = 0.163$, r/a = 0.919; (b) $X = 0.275$, r/a = 0.863; (c) $X = 0.374$, r/a = 0.813; (d) $X = 0.511$, r/a = 0.745 and (e) $X = 0.75$, r/a = 0.625

When $X = 0.75$, three distinct zones are identifiable establishing that the flow is indeed of Batchelor flow type: two boundary layers adjacent to the rotating and stationary disk walls and a central core in solid body rotation where the tangential velocity is nearly independent of the location in the direction normal to the rotating disk, z. Therefore, it can be said that the Batchelor type flow is not always observed in a rotor-stator cavity system without any through-flow as it depends on the radial location. However, based on the results for this geometry, the primary flow in a rotor-stator cavity system without any through-flow can certainly be described by the Batchelor flow model.

These results confirm that the operational characteristics of the disk are not only a function of Re_Ω and s/a, but also of X as established by Ketola and McGrew in their experimental study [41]. It is also evident that the boundary layer thickness on the rotating and stationary disks varies radially as also shown in Figure 4-19. This flow feature was also observed in previous studies by Dijkstra and van Heijst [37] and Schouveiler et al. [51] who concluded that this radial variation occurs due to the increase of the angular velocity of the rotating core, $\beta_{fluid} = K\Omega$, as the radius along the rotating disk, r, increases. As shown in Figure 4-20, it can be seen that the magnitude of the tangential velocity component increases as the local radius increases and seems to be independent of the engagement ratio. It is interesting to note that the CFD model has been able to capture the overshoots and undershoots near the rotating and stationary disk surfaces and is in agreement with previous studies by Tritton [224], Young and Chew [26], and Debuchy et al. [225]. This flow feature was not captured in the velocity profiles for the fully wetted disk case presented in Section 4.2.

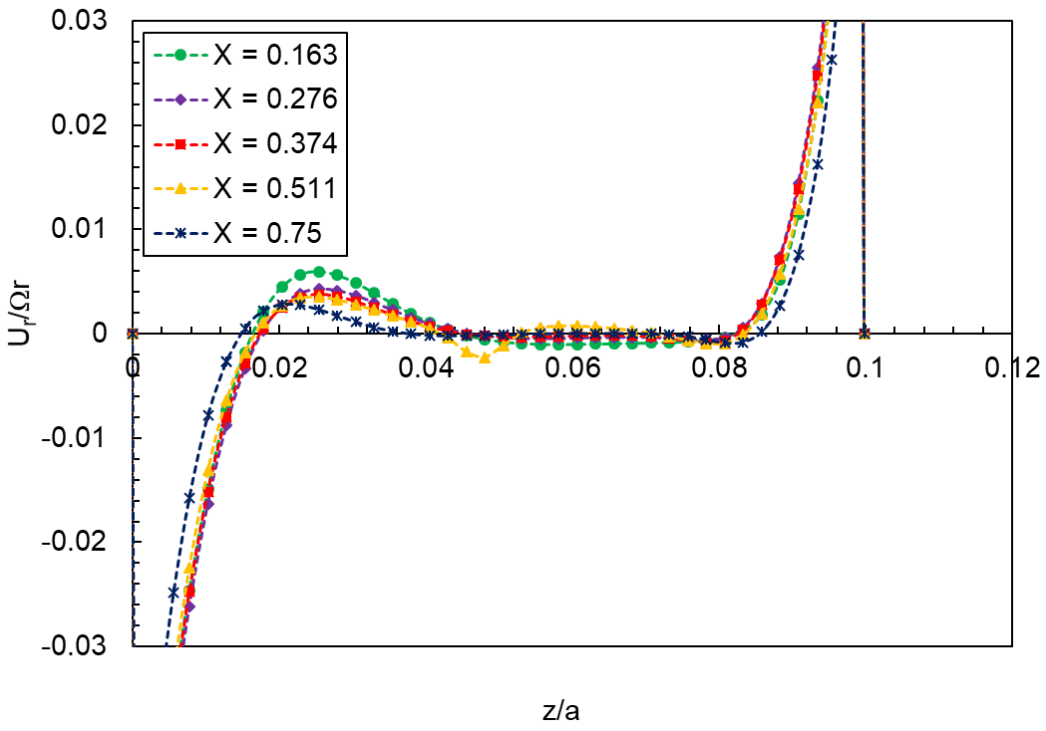


Figure 4-21: The axial profiles of non-dimensionalised radial velocity plotted at various engagement ratios $X = 0.163$ at $r/a = 0.919$; $X = 0.275$ at $r/a = 0.863$; $X = 0.374$, at $r/a = 0.813$; $X = 0.511$ at $r/a = 0.745$ and $X = 0.75$ at $r/a = 0.625$

Figure 4-21 displays the normalised radial velocity profiles obtained axially at mid-height in the column of water for different engagement ratios, X. It is very interesting to note that the radial flow circulates not only through the boundary layers but also in the core region closer to the stationary disk, where a radial exchange of fluid exists to a certain axial extent until it vanishes to an almost zero closer to boundary layer on the rotating disk. It is also worth noting that this increase in radial velocity in the rotating central core was not reproduced by both $k - \varepsilon$ and SST $k - \omega$ models when the rotating disk was fully immersed in fluid as reported in Section 4.2.

Finally, the behaviour of the tangential velocity at the three different radial locations was investigated when $X = 0.75$ to understand the characteristics of the flow field at a certain submergence ratio. The dimensionless tangential velocities were obtained at r/a = 0.315, r/a = 0.625 and r/a = 0.935 when $X = 0.75$ and the axial profiles of the obtained tangential velocity are illustrated in Figure 4-22.

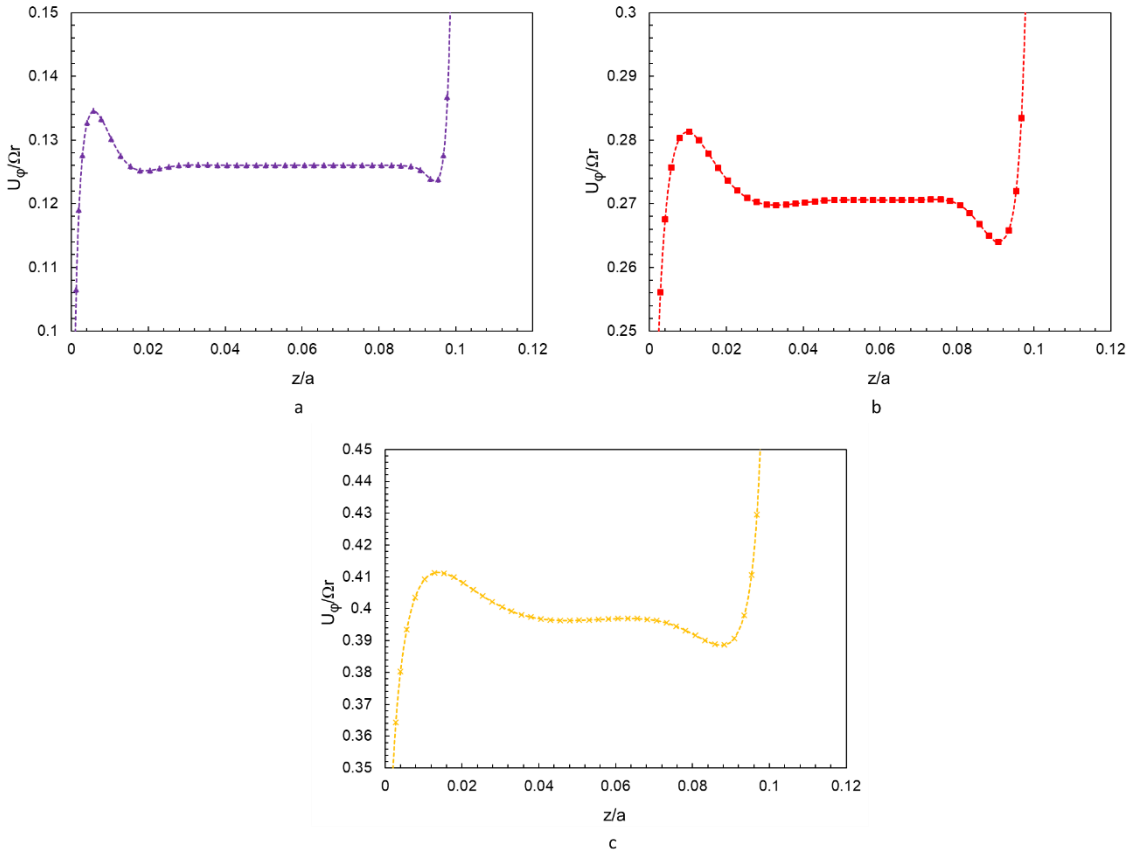


Figure 4-22: The axial profiles of non-dimensionalised tangential velocity plotted at (a) r/a = 0.315; (b) r/a = 0.625; (c) r/a = 0.935 when $X = 0.75$

Figure 4-22 shows that for a range of control parameters, the flow rotates with a central core with separated boundary layers, whereas towards the periphery of the disk there is no central core. This shows that boundary layers are merged closer to the periphery. This is in agreement with the findings of the numerical study by Randriamampianina et al. [39] and experimental results of Schouveiler et al. [36]. A possible reason for this characteristic could be the influence of a thicker Ekman layer on the rotating and stationary walls near the periphery with considerable axial gradients of velocity in the boundary layer. Another reason could be the noticeable increase in radial velocity in the core and this is confirmed by the dimensionless radial velocity profiles obtained at the same radial locations, r/a = 0.315, r/a = 0.625 and r/a = 0.935 presented in Figure 4-23.

In Figure 4-23, at locations r/a = 0.315 and r/a = 0.625, the radial velocity in the core is closer to zero, a characteristic of Batchelor flow. It can be seen that a radial circulation only occurs in the boundary layers at these locations. It can be seen that the radial velocity profile at r/a = 0.935 can be characterized by the flow directed inward on the stationary disk for z/a < 0.05 and the outward flow on the rotating disk ejected under the centrifugal effects for z/a > 0.05.

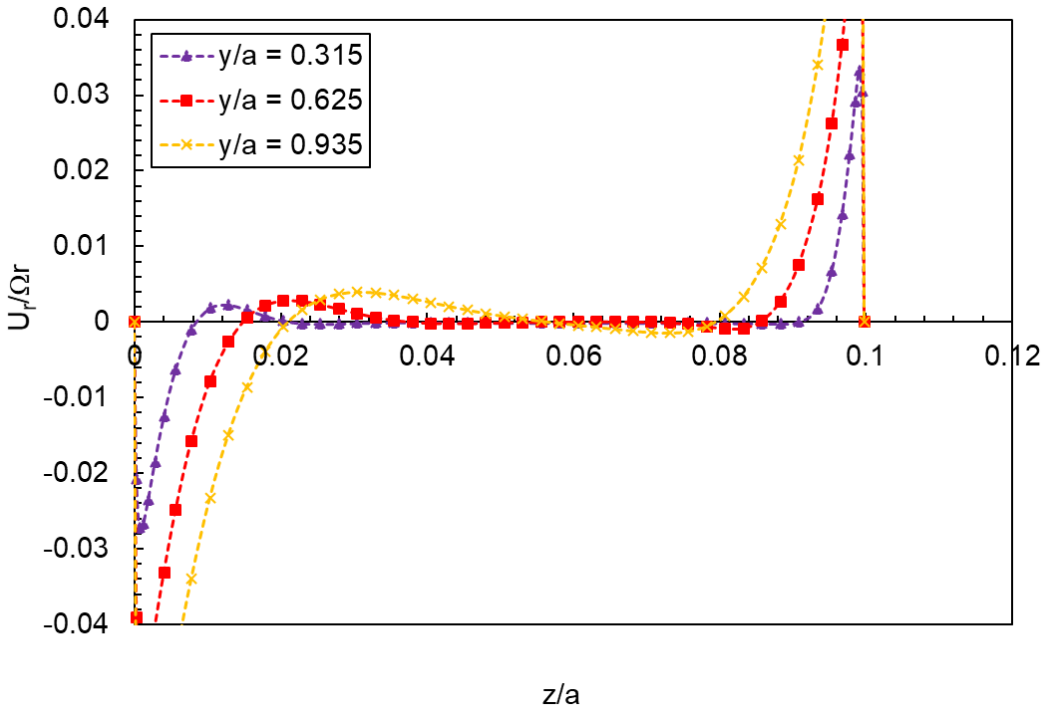


Figure 4-23: The axial profiles of non-dimensionalised radial velocity plotted at different radii r/a = 0.315, r/a = 0.625, r/a = 0.935 when $X = 0.75$

4.3.1.3 Pressure characteristics of partially wetted disks with no through-flow

When analyzing their experimental data, Ketola and McGrew [41] obtained a wall static pressure profile via a series of wall pressure tappings and presented their data in non-dimensional form baselined to the static pressure at the tip of the disk, namely: $\frac{2(p_a - p_r)}{\rho\Omega^2 a^2}$ where p_a is the wall static pressure at the disk tip radius and p_r is the wall static pressure at radius r. This can be referred to as the pressure coefficient, C_P.

An interesting quantity in flows induced in a rotor-stator cavity system is the magnitude of the mean tangential velocity in the inviscid rotating core referred to as the swirl ratio,

denoted β_{fluid}. It can be directly linked to the radial pressure gradient through the cavity. As is shown in Ketola and McGrew [41], the pressure difference is related to the radius and core velocity at that location by:

$$(p_a - p_r) = \frac{1}{2}\rho{\beta_{fluid}}^2(a^2 - r^2) = \frac{1}{2}\rho K^2\Omega^2 a^2\left(1 - \frac{r^2}{a^2}\right) \tag{4-7}$$

Alternatively,

$$\frac{dp}{dy} = 2{\beta_{fluid}}^2 r \tag{4-8}$$

Equation (4-7) is the reduced Navier-Stokes equation for the core region with the assumption that the velocity components are $U_x \sim U_y \sim 0$ and $U_\varphi \sim \beta_{fluid}$ in the core. It can therefore be seen that when the non-dimensional pressure is plotted against $\left(1 - \frac{r^2}{a^2}\right)$ the gradient is K^2 and this is presented in Figure 4-24.

The swirl ratio β_{fluid}, has been an area of interest for many years as it allows to estimate the axial thrusts applied at the walls [38, 208, 218, 226]. The CFD results from this current study are compared to experimental data of Ketola and McGrew [41]. It is evident that there is good agreement between the experimental data and the CFD model. The value of velocity ratio, K, for each engagement ratio is obtained by line-fitting the CFD data sets. The dependence of the velocity ratio on the engagement ratio can also be seen in Figure 4-24. These values of K are summarized and compared with the

experimental values in Figure 4-24 where it can be seen that the CFD values are slightly higher than the experimental ones except at high engagement ratios. These results overestimate the angular velocity of the rotating core since the axial velocity of the flow in the central core is not strictly zero. However, it can be seen that β_{fluid} is an inverse function of the local disk radius, r. The results confirm that the velocity ratio, K, correlated here by the pressure equation, is constant with radius, but is a function of the spacing ratio, s/a, and the engagement ratio, X.

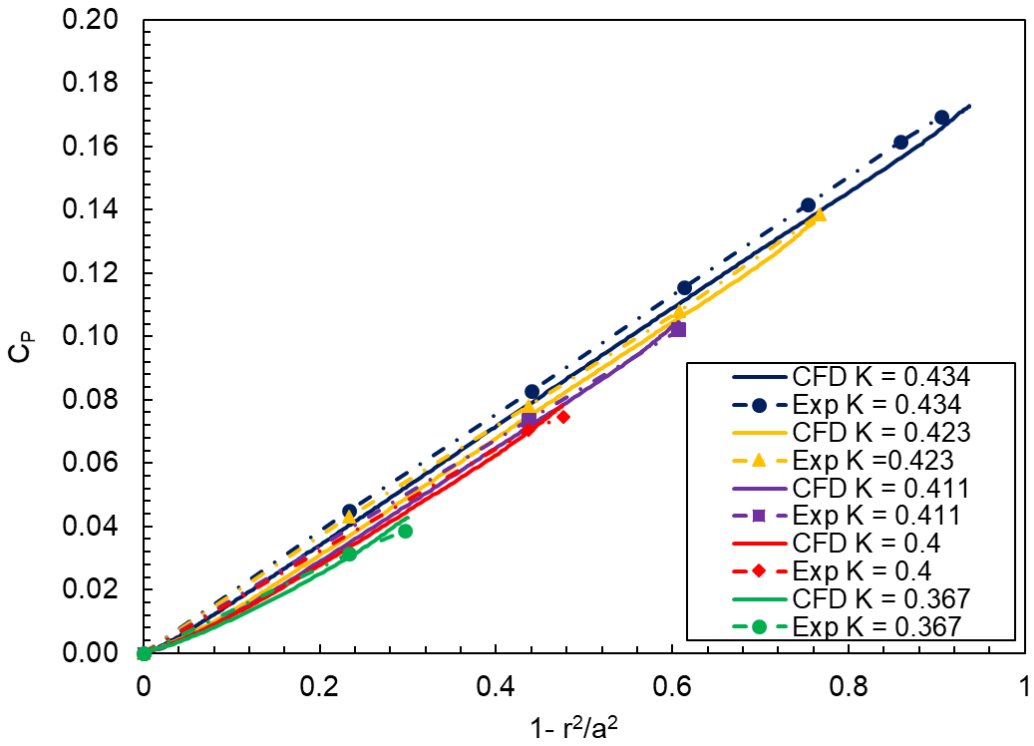


Figure 4-24: Normalized pressure data for s/a = 0.1 and engagement ratios (X) of 0.163 (green); 0.275 (red); 0.374 (purple); 0.510 (yellow); 0.75 (black) for non through-flow regime

The CFD solution also gives the option to extract the core angular velocity β_{fluid} and thus directly calculate the velocity ratio K. This has been done in Figure 4-25 where

K_1 is the value obtained using the pressure approach and K_2 is the value obtained directly using core angular velocity; Figure 4-25 is a concise representation of the data in Figure 4-24. It can be seen that the angular velocity evolves from $\Omega = 0.389\beta_{fluid}$ at $X = 0.163$, r/a = 0.919 to $\Omega = 0.413\beta_{fluid}$ at $X = 0.275$, r/a = 0.863 to $\Omega = 0.426\beta_{fluid}$ at $X = 0.374$, r/a = 0.813 to $\Omega = 0.432\beta_{fluid}$ at $X = 0.511$, r/a = 0.745 to $\Omega = 0.436\beta_{fluid}$ at $X = 0.75$, r/a = 0.625. As might be anticipated, K_1 and K_2 are essentially the same due to negligible axial and radial velocity components. It can be seen that β_{fluid} increases with the engagement ratio, X. Additionally, the RMSE between the experimental and CFD values is 1.04% which illustrates the validity of modelling approach applied.

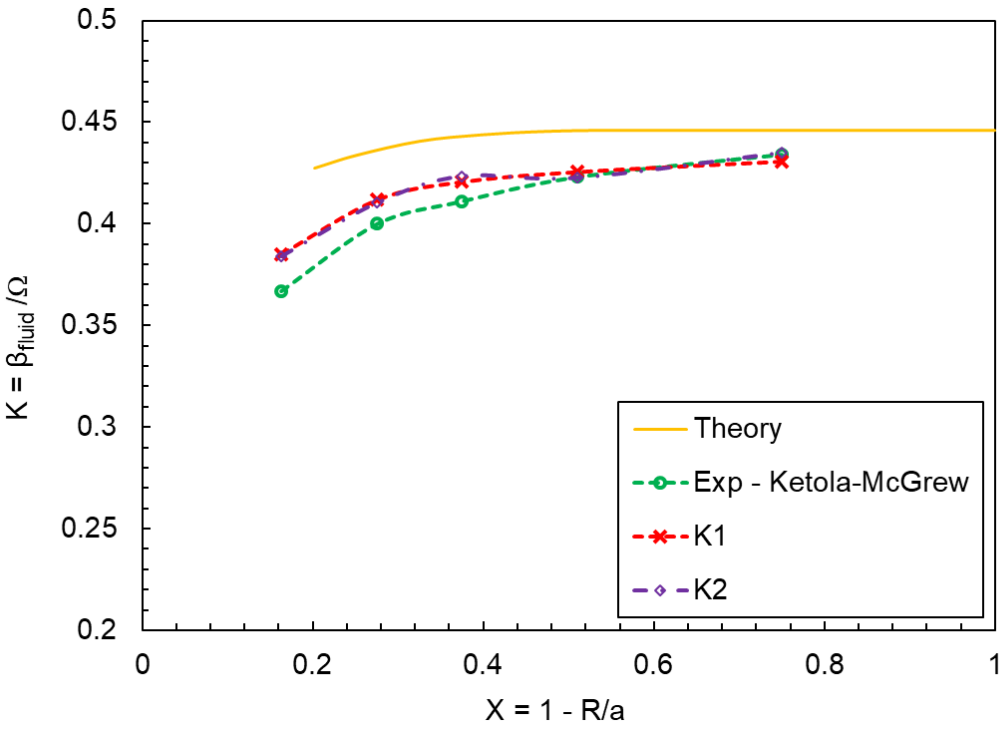


Figure 4-25: Effect of engagement ratio on velocity ratio for non-flow regime

4.3.2 Through-flow regime

A through-flowing system refers to fluid flowing through a confined space or past a surface in a directed manner. It indicates that the fluid is entering on one side of a control volume/surface, passing through the confined space, and exiting on the other side. In a through-flow system, there is a net transport of fluid from inlet to outlet. Ketola and McGrew [41] extended the investigation to distinguish the effects of flow on the pressure rise by directing the flow along one side of the disk. This allowed the authors to compare the pressure profiles on the two sides of the disk with one another as the pressures at the outer periphery are approximately equal due to very small radial gap between the rotating disk and the stationary housing and no flow from one side to the other. The authors established that the experimental no-flow data compared well with the theory developed at high engagement ratios. They also noticed that the data did not vary significantly at lower engagement ratios as it did at higher engagement ratios [41]. Based on this, they concluded that the variation in K is more compatible with the theoretical prediction estimated by the authors for through flow cases. For the flow tests reported in their study, a maximum rotational speed of 10,800 rpm was used as through-flow allows the fluid within the cavity to be cooled allowing the opportunity to test higher rotational speeds before any interference from internal heating takes place [41]. Presented in this section is the numerical model developed to replicate the experimental apparatus and procedure along with a comparison of CFD results with the experimental data obtained from the study of Ketola and McGrew [41].

4.3.2.1 Numerical modelling approach

This section outlines the geometry of the numerical model and a brief description of the CFD model set-up. The CFD methodology follows a very similar approach as described in Section 4.3.1.1 for a model with no through-flow. It can be seen in the original experimental rig schematically shown in Figure 4-11 that the flow enters the cavity axially and impinges on the rotating disk closer to the rotation axis. To simulate the liquid feed, a water inlet is introduced at a location consistent with the experimental rig geometry as a velocity inlet with constant velocities normal to the boundary to match the volumetric flow rates used in the experiments. A mass flow outlet was added to eject the liquid flow radially outward on the same side of the disk so that it resembles the location and procedure followed experimentally. As opposed to the nonflow phase reported in Section 4.3.1, a higher rotational speed was applied at the rotating wall to match the experimental conditions. A series of CFD simulations were implemented investigating several control parameters so that the results could be validated against the experimental data. In the CFD study, the following control parameters were investigated numerically: $Q = 9.73 \times 10^{-5}$ m^3/s when $X = 0.208$; $Q = 1.09 \times 10^{-4}$ m^3/s when $X = 0.751$; $Q = 1.17 \times 10^{-4}$ m^3/s $X = 0.812$; and $Q = 1.945 \times 10^{-4}$ m^3/s when $X = 0.312$ and $X = 0\ 562$. However, it was found that a uniform radial pressure gradient could not be sustained across the water columns in the two chambers either side of the rotating disk when analyzing the results from the initial CFD investigation. It can be seen that in the original experimental apparatus, approximately equal pressures on either sides of the disk have been maintained with a sealing system and suitable control

of discharge valves. Therefore, two air outlets were defined as a pressure boundary with an air volume fraction of unity in case of backflow so that the differential radial pressure of the fluid on either side of the rotating disk is balanced out by the differential air pressure either side of the cavity. The above cases were then re-simulated with the added boundary conditions. The cavity geometry domain modelled for the through-flow regime under investigation is illustrated in Figure 4-26.

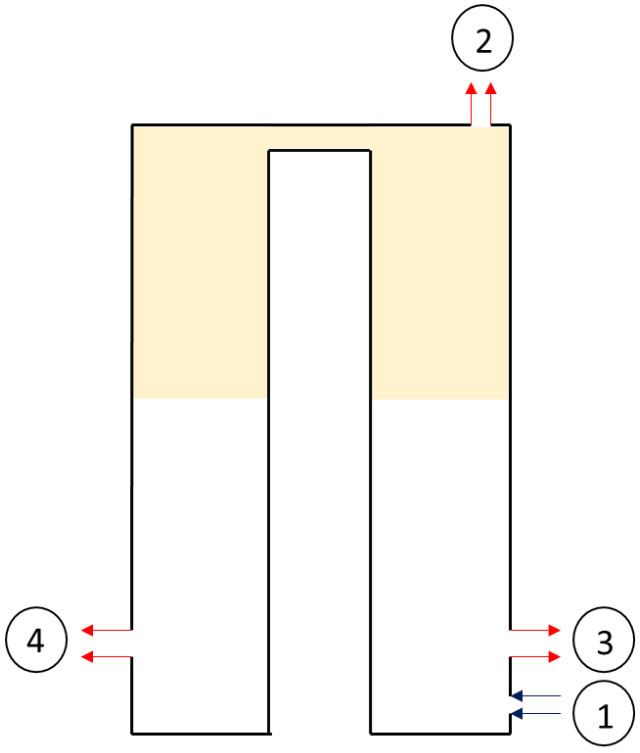


Figure 4-26: Geometry used in the CFD study with the model boundary conditions numbered (1) liquid in feed defined as a velocity inlet; (2) liquid discharge modelled as mass flow outlet; (3) and (4) air outlet defined as pressure outlet boundary

A description of the numerical model set-up highlighting the key parameters and settings applied in the series of the CFD cases investigating the through-flow regime is summarised in Table 4-6.

Table 4-6: Principal modelling features of the CFD model of the partially wetted disk case

Modelling parameter	**Value/ model used**
Outer wall boundary condition	Stationary
Inner wall boundary condition	Rotating at 1130.97 rad/s
Turbulence treatment	SST $k-\omega$
Pressure- velocity coupling	Coupled
Pressure interpolation scheme	PRESTO
Spatial discretisation algorithm	Second order upwind

Following a similar methodology as was applied in the nonflow models, a VoF modelling approach was applied in the through-flow CFD cases as well. The two-phase flow was implemented by patching a volume of water into the domain to represent the experimental engagement ratios investigated. For the primary phase, water was defined as an incompressible fluid. Air was defined as the secondary phase with constant properties. Each CFD case was simulated using a variable time step with an initial time step, (Δt) of 10^{-5} s, each time step running for thirty iterations. Convergence at each time-step was controlled using a residual convergence criterion of 1×10^{-5} for the continuity, velocity, swirl and turbulence variables. Convergence of the solution during each step change was monitored using bulk residuals, moment coefficient of the walls

and velocity magnitude at several locations. The cases were simulated allowing the flow to achieve pseudo steady-state and a flow time of 0.5 s was required to achieve a fully developed flow solution.

4.3.2.2 Flow characteristics of partially wetted disks with through-flow

Results were obtained at four volumetric flow rates, Q, each flow rate with one or more wetted ratios. Given in Figure 4-27, is a plot of radial pressure profile data for the numerical flow simulations compared against the CFD pressure data for the through-flow regime.

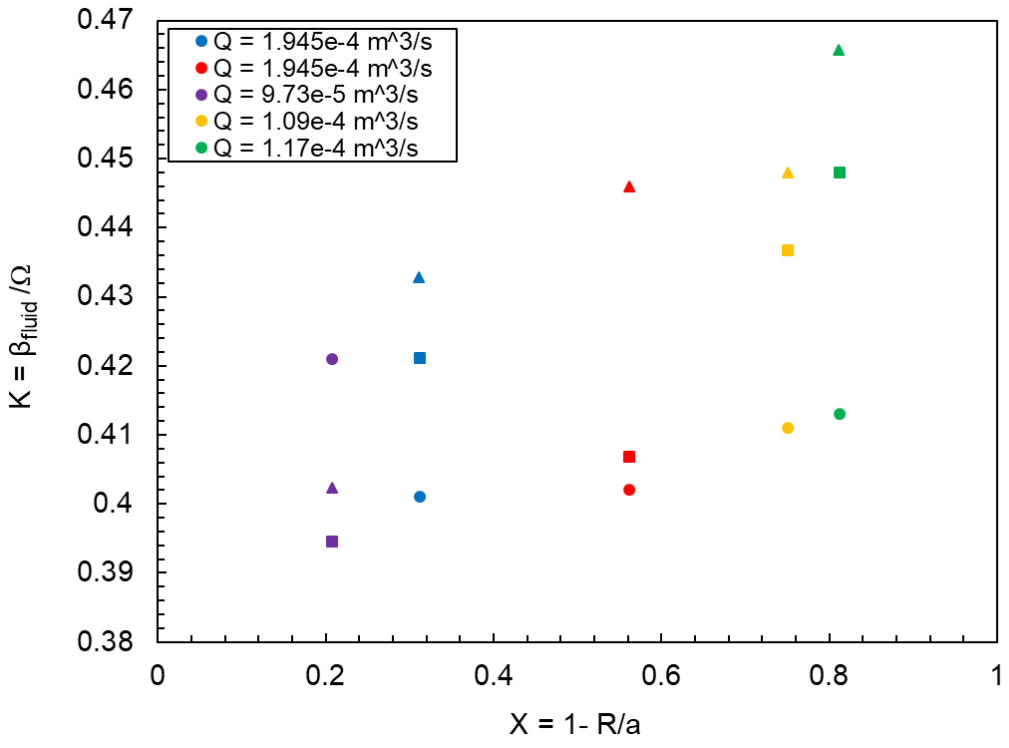


Figure 4-27: Effect of engagement ratio on velocity ratio for flow cases with circles representing experimental measurements; triangles denoting CFD K_1 and squares representing CFD K_2

It should be noted that for each case there are two velocity ratios (K); One for the chamber where there is no-flow (K_1) and the other for the chamber where the water is supplied into (K_2). Although the CFD results for the through-flow regime are in good agreement with the experimental measurements with a RMSE between the experimental and CFD values of 3%, it can be said that the CFD models for the non-flow regime were capable of predicting the flow field within the cavity quite accurately with a RMSE of 1.1% between experimental and CFD data for K.

It is observed in Figure 4-27 that the core in the chamber with no flow (K_1), rotates faster than the one in the chamber into which the fluid is injected (K_2). This is because the volume of water in the chamber with the fluid flow undergoes a net loss in angular momentum due to through-flow. It is also clear that the degree of reduction in rotation or in other words, the performance degradation of the fluid depends on the amount of through-flow and the wetted ratio.

When a supply of fluid is imposed on a rotating disk, the flow structure in the rotor-stator cavity is altered. As shown previously, this results in a reduction in the velocity field. To distinguish the effects of through-flow on the flow field, the CFD results from the case $Q = 1.945 \times 10^{-4}$ m^3/s when $X = 0.312$ were analysed. The contours of volume fraction of water is illustrated in Figure 4-28 with Figure 4-28a displaying the water volume fraction of the initial solution before any fluid was imposed into the cavity. It can be seen in Figure 4-28b which shows the contours of water volume fraction of the fully developed flow field, that the flow enters the cavity axially impinging on the rotating disk.

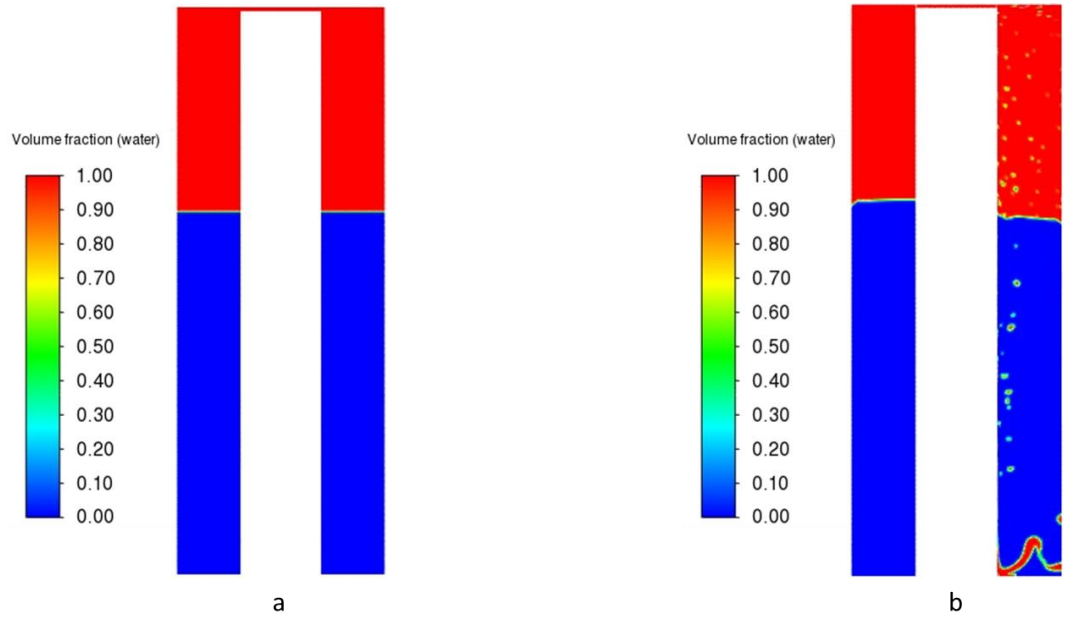


Figure 4-28: Contours of volume fraction of water of (a) the initial solution before the fluid enters the cavity (b) the final solution with a fully developed flow field for the CFD case with $Q = 1.945 \times 10^{-4}$ m^3/s and $X = 0.312$

The volume of water in the cavity will rise as a result of the incoming fluid and this can be seen in the chamber into which the through-flow was supplied. The static pressure contours for this case are presented in Figure 4-29. A slightly higher radial pressure gradient can be observed in the no-flow side and the difference in static pressure in the two chambers is due to the difference in water column heights in the chambers. It can be noted that the pressures at the periphery on either sides of the rotating disk are approximately equal as expected since there will be no flow passing from one chamber to the other when the flow field is in steady state.

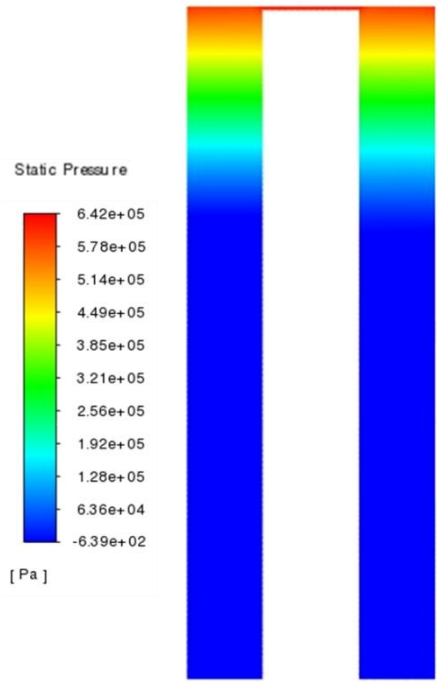


Figure 4-29: Contours of static pressure in the cavity between the stationary and rotating disks for the CFD case with Q = 1.945 x 10^{-4} m^3/s and X = 0.312

The behaviour of the flow was evaluated by plotting the tangential velocity data obtained at r/a = 0.792, r/a = 0.846, r/a = 0.896 and r/a = 0.945 for the same flow rate, Q = 1.945 x 10^{-4} m^3/s and engagement ratio, X = 0.312. The normalised axial profiles of tangential velocity obtained at these radial locations in both chambers are exhibited in Figure 4-30.

The Figures on the left with 0 < z/a < 0.12 show the velocity profiles obtained in the no-flow chamber and the Figures on the right with 0.22 < z/a < 0.32 represent the velocity profiles plotted in the chamber with through-flow.

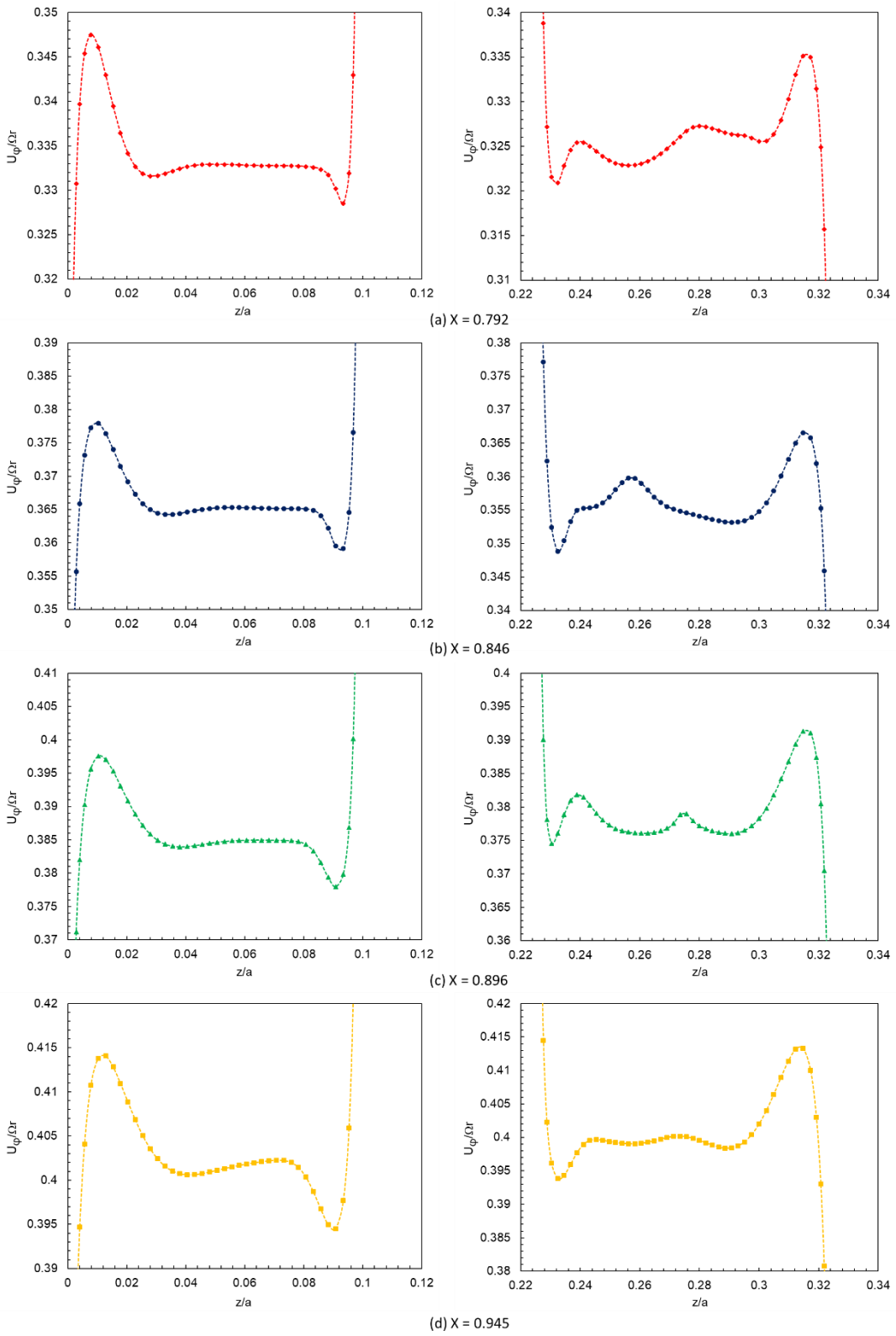


Figure 4-30: The axial profiles of non-dimensionalised tangential velocity plotted at (a) r/a = 0.792; (b) r/a = 0.846; (c) r/a = 0.896; and (d) r/a = 0.945 in both chambers for the CFD case with Q = 1.945 x 10^{-4} m^3/s and X = 0.312

When looking at the flow field in the no-flow chamber, it is clear that a central rotating core occupies the entire radial extent except closer to the disk tip indicating that the Batchelor like flow is present for most part of the cavity. As expected, the flow structure changes with through-flow and this can be seen in the figures on the right. Due to the fluid impinging on the rotating disk, the flow that is pumped radially outwards experiences a loss in angular momentum and causes a drop in the tangential velocity in the fluid closer to the rotating wall as can be seen in Figure 4-30. It is clear that the flow field at r/a = 0.945 or closer to tip of the rotating disk has not been affected as much as the central part of the cavity as there is no significant variation in the tangential velocity profile. This could be due to the water infeed not penetrating flow field at higher radii.

The non-dimensionalised axial profiles of the radial velocity component obtained at the same radial locations in both chambers are sketched in Figure 4-31. It is evident that a radial velocity component exists over the entire radial range in the main flow structure in the chamber with through-flow while in the no-flow chamber, a radial exchange only exists in the boundary layers in most part of the cavity.

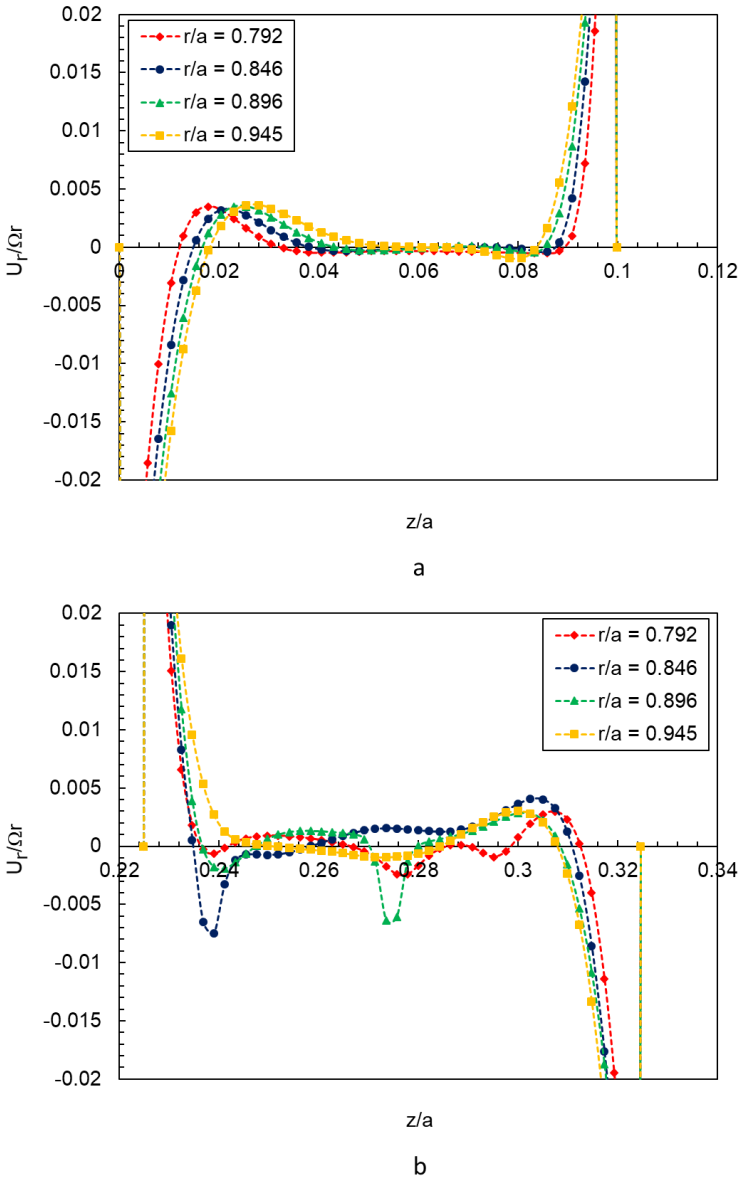


Figure 4-31: The axial profiles of non-dimensionalised radial velocity plotted at r/a = 0.792; r/a = 0.846; r/a = 0.896 and r/a = 0.945 for the CFD case with Q = 1.945 x 10^{-4} m^3/s and X = 0.312 in (a) the no-flow chamber and (b) the chamber with through-flow

4.4 Summary

This chapter presents results from a CFD study investigating an encased disk rotating both fully and partially wetted by a liquid. The study was aimed at developing modelling capability appropriate for hydraulic intershaft seals for aero-engine applications. Experimental data available in the literature was used for validation.

The initial study on a rotating enclosed disk fully immersed in a liquid established an appropriate mesh density. Results were obtained for standard $k-\varepsilon$ in both steady state and transient modes, SST $k-\omega$ and the RSM models in transient mode. Key flow features were a large recirculation driven by the flow rotating radially outwards on the rotating disk and radially inwards along the static enclosure, and Taylor vortices in the small radial gap with slightly fewer pairs than suggested by theory for closed ends. All turbulence models yielded similar results for radial and tangential velocity components when compared to data from Daily and Nece [40]. The tangential velocity in the flow closer to the rotating disk was over predicted by $k-\varepsilon$ and the RSM models and the velocity profile obtained with the SST $k-\omega$ model predicts the variation in tangential velocity closer to the rotating disk quite well. All three models have under predicted the tangential velocity as it moves from the central area of the axial gap towards the stationary disk. In this region the RSM reports the velocity values closest to the experimental data. With the lowest RMSE of 2.9%, the $k-\varepsilon$ model provides best overall prediction of the tangential velocity field. The experimental measurements of the radial velocity component were best matched by the transient $k-\varepsilon$ and RSM models with negligible differences between the point values. Overall, the results of the

two equation models are in good agreement with the experimental data for the mean velocity fields and all the operating conditions considered in this study. The two equation models also provided a faster and robust convergence of the solutions compared to RSM. With a good trade-off between the accuracy and computational cost, it is reasonable to apply a two-equation model such as the standard $k-\varepsilon$ or SST $k-\omega$ in the future calculations.

A parametric study on a partially immersed disk with no through-flow was conducted investigating five wetting ratios. The results for the nonflow demonstrated a core angular velocity ranging between 0.37 and 0.43 of shaft angular velocity, increasing with the wetting ratio. The results were very consistent with the experimental data of Ketola and McGrew [41] with velocity ratios from the CFD within 1.1% of the experimental value. A key flow feature is the deformation of the gas/liquid interface which is due to the pumping effect of the rotating disk on the liquid and the two recirculation zones, one within the gas and the other within the liquid with the consequence that the shape of the liquid/gas interface is not completely flat; the interface tends towards a flatter trend near the stationary disk with an increasing wetting ratio. The thickness of the boundary layers on both stationary and rotating disks varies radially with a thicker boundary layer closer to the disk tip and reduces as the radius is decreased. The flow within the cavity can be mainly described by the Batchelor flow model but is dependent on the radial location. The boundary layers in the liquid are merged to a certain radius and are separated beyond. At the highest engagement ratio investigated, the rotating core extends towards the centre until it occupies the entire

radial extent apart from a smaller length closer to the tip of the stationary disk. Taylor vortices were found in the narrow radial gap between the rotating and stationary disks and again, fewer pairs than for closed ends.

When a supply of fluid is imposed on a rotating disk partially immersed in fluid, the disk still pumps but the flow structure in the rotor-stator cavity is modified. Through-flow causes a reduction in the velocity field. The extent of the deterioration in the performance is dependent on the amount of through-flow and the engagement ratio. For the volumetric flow rates investigated, the fluid core rotates in the range of 0.42 to 0.47 of the shaft rotational speed. The CFD results obtained for the through-flow regime are in good agreement with the experimental results of Ketola and McGrew [41]. However, the experimental data for the non-flow tests were matched by the CFD results with just 1.1% of RMSE between the experimental and CFD velocity fields.

The work of this chapter has determined an effective modelling approach, involving an optimal mesh resolution, an appropriate turbulence model selection, and a systematic process for cavity filling. This chapter has demonstrated the key features of flows with a rotating disk and static housing. The results obtained for both nonflow and through-flow regimes of the partially wetted disk are fairly encouraging enough to move on to computing the more complex geometries where both elements rotate as in a hydraulic seal. This will form the basis of the next chapter.

CHAPTER 5

5 2D Modelling of Intershaft Hydraulic Seals: Numerical Investigation into Operation of Hydraulic Seals

The literature has been reviewed to establish the state of the art with regard to modelling hydraulic seals. Even though there has undoubtedly been research conducted into formation, performance and breakdown of hydraulic seals, due to the proprietary nature of the research, limited published research relating to hydraulic seals exists in the public domain. Also, the accuracy and reliability of the existing design approaches based on analytical derivations is not fully known. This acknowledged need to improve the ability to develop accurate computational models of hydraulic seals provides context for this chapter which involves 2D modelling of hydraulic seals. As discussed in Section 1.2.3, hydraulic seals are mostly utilized in parts of the engine that are not easily accessible and require a high integrity seal to withstand substantial pressure differences. Research and development of the next generation of hydraulic seals needs to focus on addressing these issues so that the seals can be utilized in hotter zones in future engines.

Therefore, understanding of the detailed fluid dynamic behaviour during hydraulic seal operation is crucial. This can be facilitated through the development of a CFD capability/methodology to deliver a robust modelling approach.

Design approaches established on the basis of analytical derivations can be found in the literature but a systematic numerical assessment of the maximum pressure capacity of a hydraulic seal is not offered by these methods. The uncertainty of the accuracy, reliability and consistency of these methods, requires the use of a high safety factor. However, allowing high safety margins in the oil system results in greater component weight, complexities, and therefore costs, which lead to potential reductions in the engine efficiency. Therefore, refining seal design approaches which show promise in improved robustness and reliability, presents an opportunity for advancement in engine efficiency.

Building on previously published studies, the work reported in this chapter looks at developing a CFD modelling capability for intershaft hydraulic seals for aero-engine applications. To understand the performance of a hydraulic seal, this chapter investigates the effect of axial position of the fin, and shaft rotational speeds on the maximum pressure capacity of a hydraulic seal to develop a CFD two-phase modelling strategy. The numerical simulations are based on a model representative of a hydraulic seal geometry for which some experimental data was obtained in a complementary research programme. No oil feed into the trough has been modelled in the work investigated and reported here as the objective of this chapter is to build the capability to predict the operational characteristics of the seal once it has been formed. Modelling

of an oil feed has been attempted and explored in the work presented in Chapter 6. An approach to evaluate the maximum pressure capacity of a hydraulic seal is therefore introduced in this chapter presenting the results of a 2D numerical study based on an axisymmetric VoF method.

Based on a parametric study to determine the influence of different parameters on the maximum pressure capacity of the seal and to assess the performance of hydraulic seals, results are presented for a range of shaft speeds of 2000-8000 rpm for the high speed shaft and 1000-4000 rpm for the low speed shaft with a varying fin position within the trough.

The developed approach is used to understand the interfacial flow physics of intershaft hydraulic seals and construct a reliable methodology that predicts the maximum pressure capacity of the seal. The motive of this chapter is to build a deeper understanding of the CFD prediction capabilities and to provide an analysis of the reliability of the available analytical correlation methods.

5.1 Derivation of maximum pressure capacity of hydraulic seals

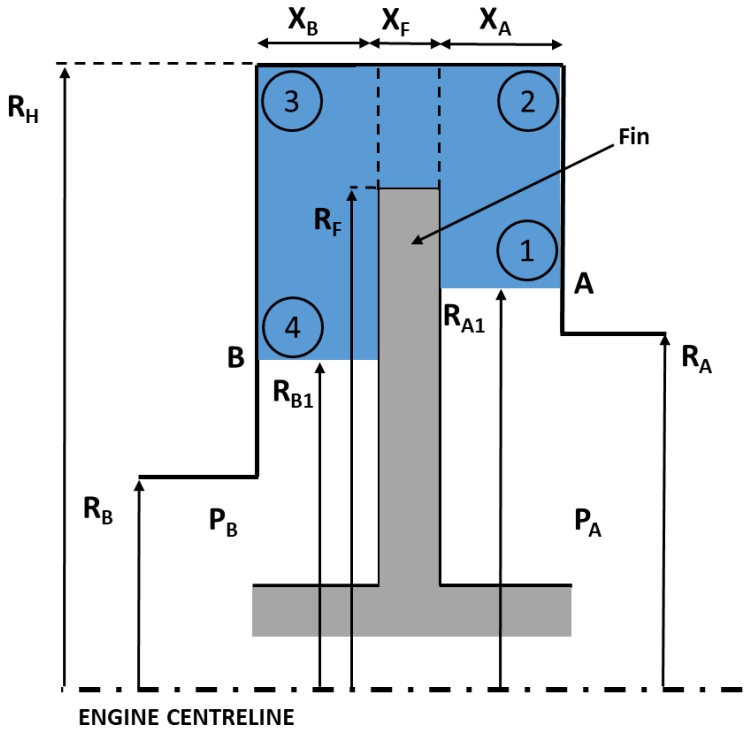


Figure 5-1: Nomenclature for maximum pressure derivation of a hydraulic seal

The equations to determine the maximum pressure capacity of a hydraulic seal can be derived from the basic equation for the steady state radial momentum balance on an infinitesimal fluid element in the trough as given in Equation (5-1).

$$\frac{dp}{dR} = \rho R \Omega^2 \tag{5-1}$$

Assuming an incompressible fluid and solid body rotation, the above equation can be integrated from positions 1 to 2 and 4 to 3 in Figure 5-1. As the pressure at the radius of the housing should be equal, it can be further simplified to:

$$\Delta P = P_A - P_B = \rho\Omega^2\left(\frac{{R_{A1}}^2 - {R_{B1}}^2}{2}\right) \tag{5-2}$$

When the seal is completely filled, $R_{A1} = R_A$ or $R_{B1} = R_B$ and liquid will spill from one side. If spilling over is maintained at the higher pressure side ($P_A > P_B$), the maximum pressure capacity of a hydraulic seal can be defined as shown in Equation (5-3) as a further increase in differential pressure will push the interface away from A and overspill will move to the low pressure side:

$$\Delta P_{max} = \rho\Omega^2\left(\frac{{R_A}^2 - {R_B}^2}{2}\right) \tag{5-3}$$

If spilling over occurs at the lower pressure side, Equation (5-3) can be modified to Equation (5-4) because once the liquid level reaches the fin, air can pass through and the seal is broken:

$$\Delta P_{max} = \rho\Omega^2\left(\frac{{R_F}^2 - {R_B}^2}{2}\right) \tag{5-4}$$

For simplification purposes gravity can be neglected at high rotational speeds of the housing and the fin, as it is far smaller than the centrifugal acceleration. Hence the equation will not be valid at all rotational speeds. However, for a rotor radius of 100mm, centripetal acceleration is $10g$ at a shaft speed of only 95 rpm, so for aeroengine applications it is valid to neglect gravity.

5.2 Overview of Analytical oil angular velocity prediction methods

It is evident from Equations (5-3) and (5-4) that the maximum pressure capacity of a hydraulic seal is governed by three elements: the density of oil (ρ_{oil}); the angular velocity of oil (Ω_{oil}); and radius (R) values. As the density and radii are known, the angular velocity of the oil column proves to be the most vital component required not just for estimating maximum operating pressure, but also in calculating key parameters of seals such as the torque/power consumption and heat transfer. However, the angular velocity of the volume of oil is not uniform.

Daily and Nece [40] experimentally investigated the flow behaviour induced by a rotating disk fully immersed in water. The authors discovered the existence of four regimes for the liquid between rotor and stator that are dependent on the tangential Reynolds number (Re_Ω) and the housing to rotor spacing ratio (s/R_F). Using the empirical torque coefficients determined by Daily and Nece [40], a bulk value for Ω_{oil} can be computed by applying a momentum balance.

Other researchers have developed a number of other methods to estimate the average angular velocity of oil that do not rely on experimental data and these are reviewed here.

In order to obtain an analytical correlation for Ω_{oil}, the following approximations reported in literature have been investigated in this chapter.

(i) Mean velocity method

This method assumes an equal influence from both the housing and fin on the oil as reflected in Equation (5-5). The mean of the housing and fin rotational speeds defines the core angular velocity and is used by Young and Chew [26] for maximum pressure predictions.

$$\Omega_{oil} = \frac{\Omega_H + \Omega_F}{2} \tag{5-5}$$

(ii) Factored methods

In these methods a weighting factor is applied to housing and fin angular velocities to yield a value between the two.

Fixed factor: The simplest approach is to assign fixed weighting factors and the most commonly used weighting factors in the literature are 0.7 and 0.8 working on the basis that the housing has a greater influence on the oil than the fin because a larger area of

it is in contact with the oil. This method is numerically represented in Equation (5-6) using a factor of 0.7.

$$\Omega_{oil} = 0.7\Omega_H + 0.3\Omega_F \tag{5-6}$$

Area based factor, total area: The fixed factor approach does not take any account of the actual geometry. A potentially better method is to use the ratio of the housing surface area to the total area to generate the weighting factor. This yields:

$$\Omega_{oil} = \frac{A_H\Omega_H + A_F\Omega_F}{A_H + A_F} \tag{5-7}$$

Analytical estimates for Ω_{oil} defined by the total area are applied in the seal pressure calculations by Denecke et al. [19].

Area based factor, wetted area: It can be argued that only the parts of the housing and fin geometry in contact with the oil contribute significantly to its core velocity and so the final approach investigated uses the wetted areas at the point of seal breakdown.

$$\Omega_{oil} = \frac{A_{H,w}\Omega_H + A_{F,w}\Omega_F}{A_{H,w} + A_{F,w}} \tag{5-8}$$

5.3 Numerical modelling approach

The flow within the hydraulic seal was computed using ANSYS-Fluent v18.1. The modelling methodology developed in Chapter 4 together with the solution strategy developed by Young and Chew [26] for modelling two-phase flows was adopted in this study with some modifications. One of the aims of the numerical investigation was to understand the limitations introduced as a consequence of the assumptions made in the various analytical approaches.

A 2D axisymmetric simulation was carried out in two stages. Firstly, an air-only single phase scenario was simulated in steady-state until the flow reached pseudo-steady state allowing the air to gain momentum from the rotors. To implement the two-phase flow, an oil volume was then patched into the domain extending from the base of the housing to half of the fin length and a VoF modelling approach was applied. Air was defined as the primary phase with constant properties. For the secondary phase, oil was defined as an incompressible fluid. Eastman 2176 is used as the sealing fluid in this investigation, the properties of which are outlined in Table 5-1.

Table 5-1: Properties of oil used in the seal

Temperature (°C)	40
Density (kg/m^3)	976.6
Dynamic Viscosity (kg/ms)	0.0273
Surface Tension (N/m^2)	0.0308

The flow modelled simulates a non-through flow regime as this model does not include an oil feed so that the performance of the seal can be assessed once it has been formed. For boundary conditions, housing and fin shafts were defined as rotating adiabatic walls rotating in the same direction. As illustrated in Figure 5-2, the housing is represented by the outer wall denoted by 1 with the extents of it marked with a red dashed line, while inner wall indicated by 2 marked with a yellow dashed line refers to the fin. An air inlet was defined as a pressure boundary as shown at 3 and an air/oil pressure outlet was defined with an air volume fraction of unity in case of backflow represented by 4 in Figure 5-2.

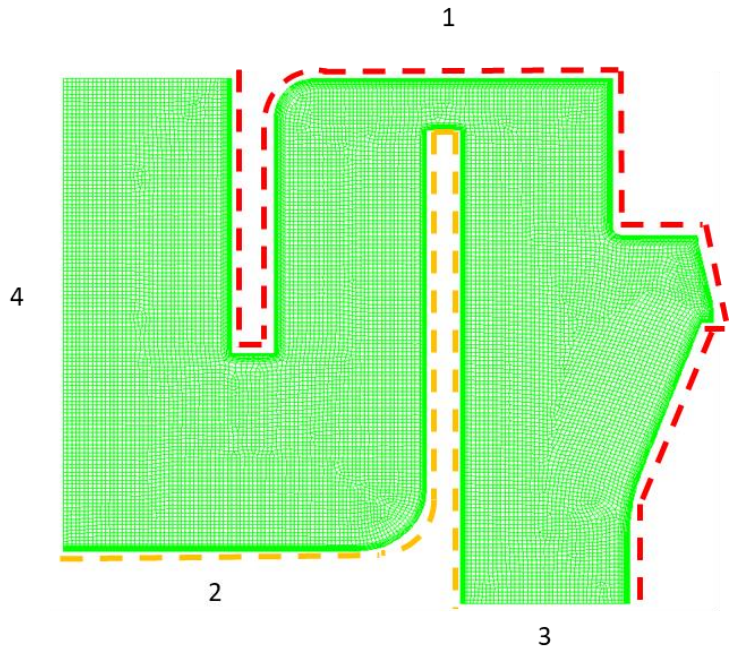


Figure 5-2: Mesh used in the CFD study with the model boundary conditions numbered: red dashed line numbered 1 represents the housing defined as a rotating wall; yellow dashed line marked 2 shows the fin modelled as a rotating wall; air pressure inlet at 3 and air/oil pressure outlet at 4.

The standard $k-\varepsilon$ turbulence model was applied in combination with the 'enhanced wall treatment' to resolve the flow at the boundary layers. Attempts were made to apply the SST $k-\omega$ model as it can be applied to a wide range of wall y^+ values and is able to include interfacial turbulence treatment [221]. However, a divergent system response was induced and thus was not included in the present work. The SIMPLE pressure-velocity coupling was applied together with 'PRESTO' pressure interpolation scheme. The chosen discretization algorithm was 'Second Order Upwind'. Interfacial anti-diffusion correction technique and interface sharpening treatment were enabled to sharpen the volume fraction distribution to capture the shape of the interface more distinctly and to reduce the numerical diffusion across the two phases.

To compute the interface and include the effects of surface tension (σ_L) between oil and air, the 'geometric reconstruction' scheme was applied as done in previous studies related to hydraulic seals. Young and Chew [26] reported the use of the geometric reconstruction approach to model typical liquid-gas flow dynamics encountered in aero-engine oil systems as this method has the capability to delineate a well-defined interface between the two fluid phases. The 'Implicit Body Force' treatment was applied to formulate the body forces accounting for surface tension as recommended in the Fluent User Manual [192].

To simulate the flow within a seal in operation, the simulations were conducted in transient mode. The pressure was increased stepwise in increments of 0.5 bar until the oil/air interface was close to the fin tip. Smaller step sizes were used subsequently as described in the numerical results in Section 5.4.1. Each step change was executed

allowing the flow to achieve pseudo steady-state using a variable time step with an initial time step, (Δt) of 10^{-5} s. A variable time step was set-up to eliminate the possibility of solution divergence by restricting the CFL number to be one. Convergence of the solution during each step change was monitored using bulk residuals, moment coefficient values and iso-clip values in the domain demonstrating the change in interface height. Computational resources required in this parametric study was specific to each case and depended on the parameters varied. The computational time required for the cases with higher rotational speeds and higher trough capacity was much higher than the ones with low rotational speeds. A flow time of 13.34 s was reached to simulate the maximum operating pressure of the seal where the fin was positioned at s/w_H = 0.75 with shaft rotational speeds of Ω_H = 8000 rpm and Ω_F = 4000 rpm. This fully developed flow simulation was achieved with 12,229 core hours, computed in parallel using 40 Intel Xeon Gold 6238 cores. The overall time lapsed for this numerical simulation was 305.725 hours.

5.3.1 Mesh

A detailed mesh sensitivity study was conducted for a case with the highest shaft speeds (8,000 rpm and 4,000 rpm for housing and fin respectively) and a pressure ratio ($p_{stat}/\Delta P_{max}$) of 0.514 to ensure a mesh independent solution was achieved. Three unstructured meshes with a combination of quadrilateral and triangular cells were investigated. Simulations were conducted varying the base cell size resulting in 40, 80 and 160 cells across the axial span of the housing base denoted by Mesh 1, Mesh 2 and

Mesh 3 respectively. The axial span of the housing at the base was determined using the fin thickness (X_F), and the distance between the housing and fin ($X_A + X_B$), as illustrated in Figure 5-3. The details of each mesh used for the mesh independence study is presented in Table 5-2.

Table 5-2: Size of meshes investigated for mesh sensitivity study

	Mesh 1	Mesh 2	Mesh 3
Number of elements across axial length	40	80	160
Number of cells	6402	20665	72301

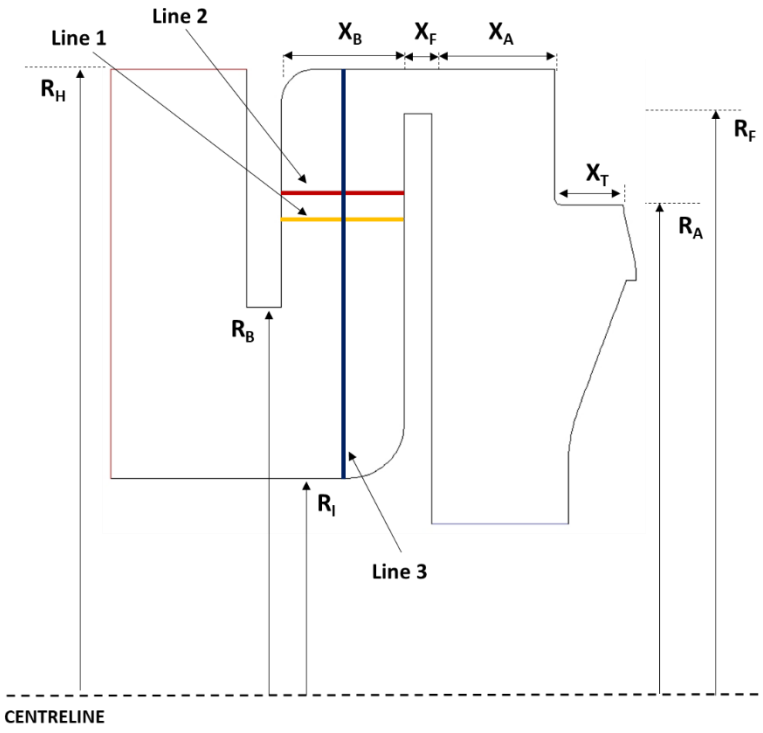


Figure 5-3: Locations of lines used to obtain tangential velocity profiles, analyze the flow domain and nomenclature used to define area

The optimal mesh was determined by comparing tangential velocity profiles of oil along Line 1 as illustrated in Figure 5-3. Figure 5-4 compares the average core tangential velocity of all three meshes where it is shown that further refinement from Mesh 2 to Mesh 3 shows no significant differences in velocity results. Based on these results Mesh 2, shown in Figure 5-2, was chosen as the optimal mesh. This mesh was generated within Ansys-Mesher and includes a uniform grid spacing in the x and y-axis, and are also parallel and normal to the rotating walls. The first off-wall grid node in the primary area of interest is located at $y^+ < 1$ at the trough wall and $y^+ < 3.3$ at the fin wall in the two-phase flow solution. To model the wall effects and represent the flow at the boundary layers accurately, 8 inflation layers with a first cell height of 0.025 x 10^{-3} m were added at the trough and fin walls.

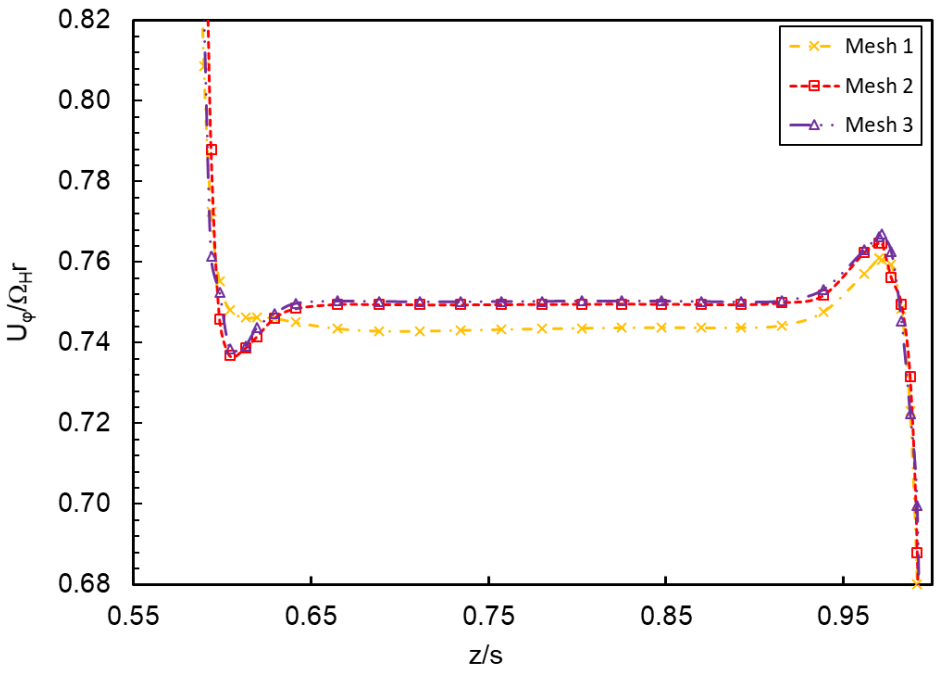


Figure 5-4: Comparison of tangential velocity profiles along line 1 (location shown in Figure 5-3)

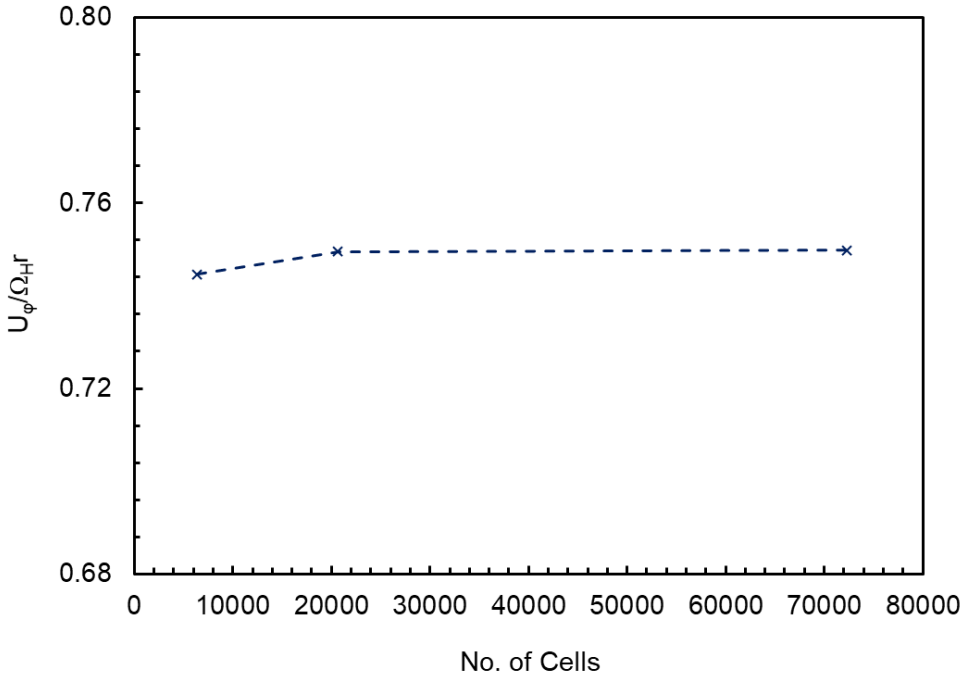


Figure 5-5: Comparison of average core tangential velocity data between meshes investigated

5.4 Numerical results of parametric study

Computations were conducted for a constant shaft speed ratio Ω_H/Ω_{oil} of 2 and housing shaft speeds of 8000, 4000, 2000 and 1000 rpm and with the fin central to the trough. At each point the maximum pressure capacity of the seal was established.

In the second stage of the study, the effect of fin position on seal capacity was evaluated with the fin positioned at trough fractions of 0.25, 0.5, and 0.75 from the LP side which is represented by chamber B in Figure 5-1. The case where the respective housing and fin speeds are 8000 and 4000 rpm with the fin positioned in the centre was chosen as the baseline case.

5.4.1 Defining Maximum Pressure

To determine the maximum operating pressure of the seal, the static pressure at the inlet on the HP side was increased gradually in steps of 0.5 bar until the height of the oil column approached the edge of the fin tip. The pressure was then increased in steps of 0.01 bar. Mathews et al. [27] followed a similar approach by adhering to a stepwise increment of 0.5 bar until the oil radius was closer to the fin. The pressure was then increased in steps of 0.05 bar until the oil level was the same as the fin height. However, they defined the last measured pressure capacity which does not lead to any bubble formation within the seal as the maximum pressure capacity.

In contrast to previous studies, this work adapts a finer resolution by using a relatively smaller step change in pressure to improve the accuracy in determining the maximum pressure capacity of the seal and capturing the flow detail. It was observed that the gradual stepwise increase in pressure led to the formation of a stream of bubbles through the seal while the oil level was almost the same as the fin height. Although the seal was no longer in equilibrium during this series of step changes in pressure, the seal was still able to sustain the differential pressure as the air leakage was not substantial. However, large leakages cause the seal to collapse. To assess the threshold leakage flow rate beyond which the seal qualifies as a failed seal, the maximum operating pressure of the seal was thus defined in terms of air leakage rate.

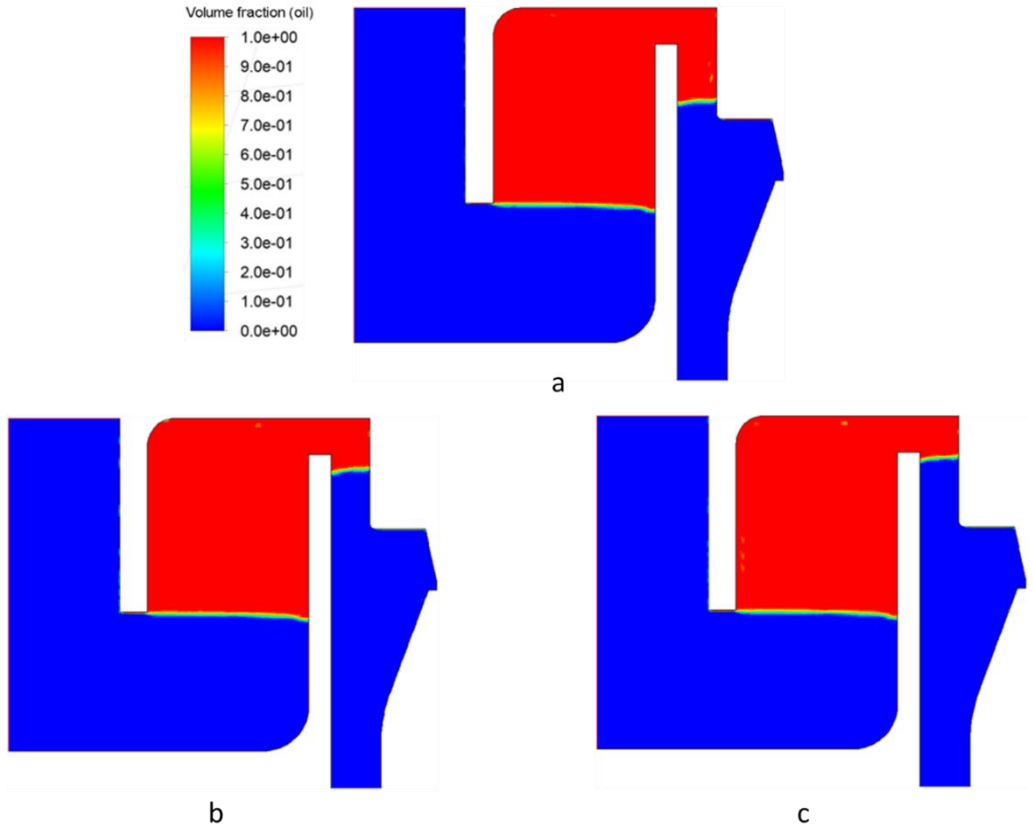


Figure 5-6: Comparison of oil volume fraction contours for numerically calculated pressures of the hydraulic seal before ΔP_{max} (a) at 1 bar; (b) at 2 bar; and (c) at 2.15 bar when Ω_H = 6000 rpm and Ω_F = 3000 rpm

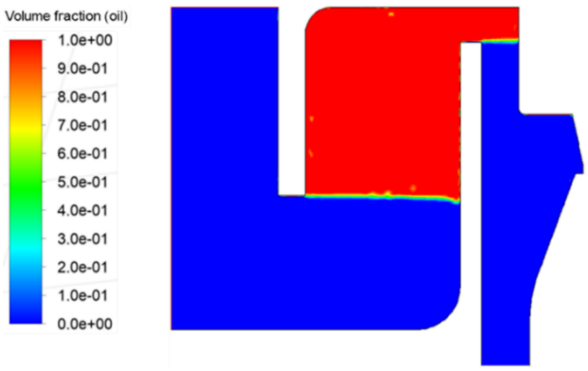


Figure 5-7: Oil volume fraction contours for numerically calculated pressures of the hydraulic seal at ΔP_{max} = 2.29 bar when Ω_H = 6000 rpm and Ω_F = 3000 rpm

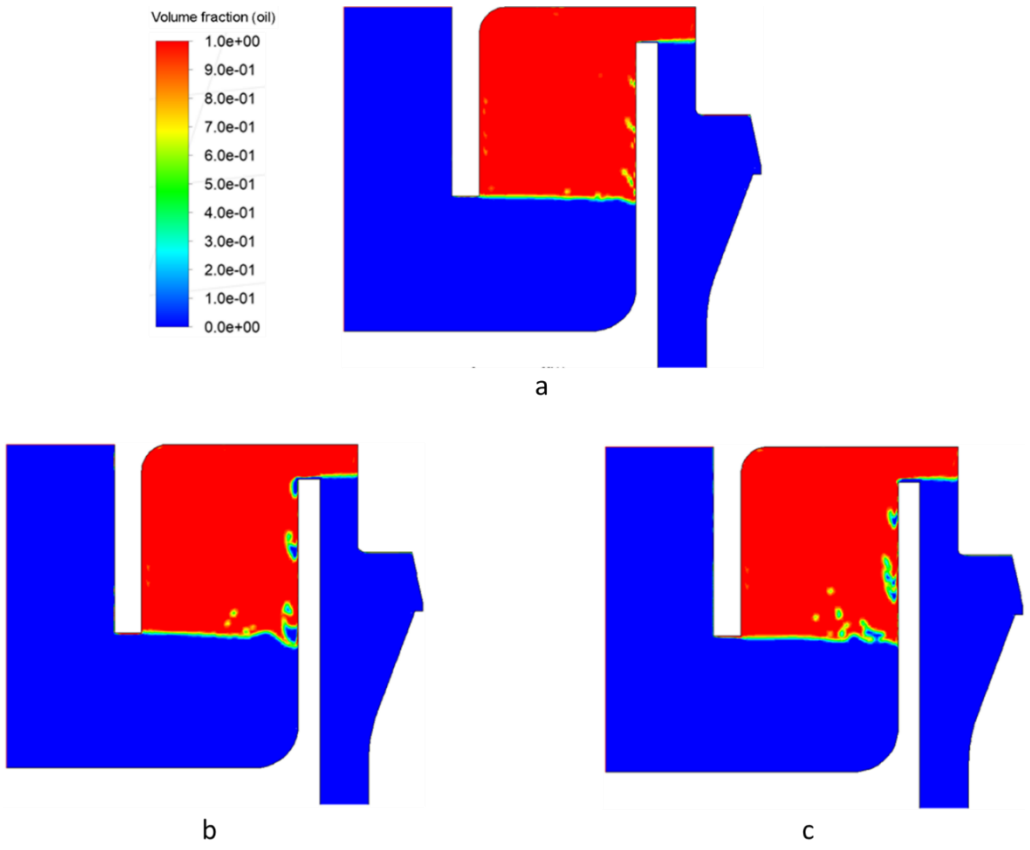


Figure 5-8: Comparison of oil volume fraction contours for numerically calculated pressures of a failed hydraulic seal (a) at 2.3 bar; (b) at 2.34 bar; and (c) at 2.36 bar when Ω_H = 6000 rpm and Ω_F = 3000 rpm

This approach was developed to determine the highest possible differential pressure the seal can withstand. This was accomplished by recording the mass-flow of air that enters through the inlet during each step change in pressure from the beginning to the end of the simulation where the air stream leaking past the fin seemed to be significant. The average of air mass-flow rate was then evaluated for each interval of pressure increment. The transitional flow times between step changes during which a momentary variation in mass-flow occurs, were disregarded in the calculation process. The last

computed step change in pressure with an air leakage rate that did not exceed 200 mg/s was considered to be the maximum pressure capacity of the seal. The value of 200 mg/s was arrived at following the investigation reported in Section 5.4.2. This methodology was applied consistently for the range of shaft speeds and axial fin positions investigated in this study.

For a case investigated when the rotational speeds of the housing and fin were 6000 rpm and 3000 rpm respectively, the fundamental stages of seal breakdown are illustrated in Figure 5-6 to Figure 5-8, illustrating oil volume fraction contours before any air leaks through, when the first small air bubbles start to leak past and finally when sufficient air is leaking past the seal for it to be defined as broken.

5.4.2 Maximum seal pressure

The maximum pressure the seal could withstand for the range of shaft speeds and fin positions was obtained during the parametric study. Figure 5-6 shows a typical sequence of seal breakdown images. The height of the oil column when the differential pressure across the seal is 2.15 bar is presented in Figure 5-6c. It can be seen that the interface is not completely flat but shows a degree of slant; a flow feature that is expected. This was also observed in the flow within a rotor-stator cavity due to the pumping effect of the rotating disk as discussed in great detail in Chapter 4. The fluid is centrifuged outwards by the rotating shafts and this effect accounts for the deformation of the oil/air surface as can be seen in Figure 5-6a, Figure 5-6b, and Figure

5-6c. The interface is somewhat higher closer to the housing due to its greater rotational speed and lower at the fin as it is the slower rotating component.

Figure 5-7 shows the oil volume fraction at a differential pressure of 2.29 bar and is considered the maximum operating pressure of the seal. The air leakage rate at this operating pressure was found to be approximately 160 mg/s. Figure 5-8c represents a failed seal at a differential pressure of 2.35 bar which reports a leakage rate of 897 mg/s. The calculated air leakage rate through the seal discussed above for a sequence of differential pressures in steps of 0.01 bar is illustrated in Figure 5-9. Here, the operating pressure of the seal, $p_{inlet} - p_{outlet}$, has been non-dimensionalised by the maximum pressure capacity of the baseline case where the housing and fin rotational speeds are 8000 and 4000 rpm respectively.

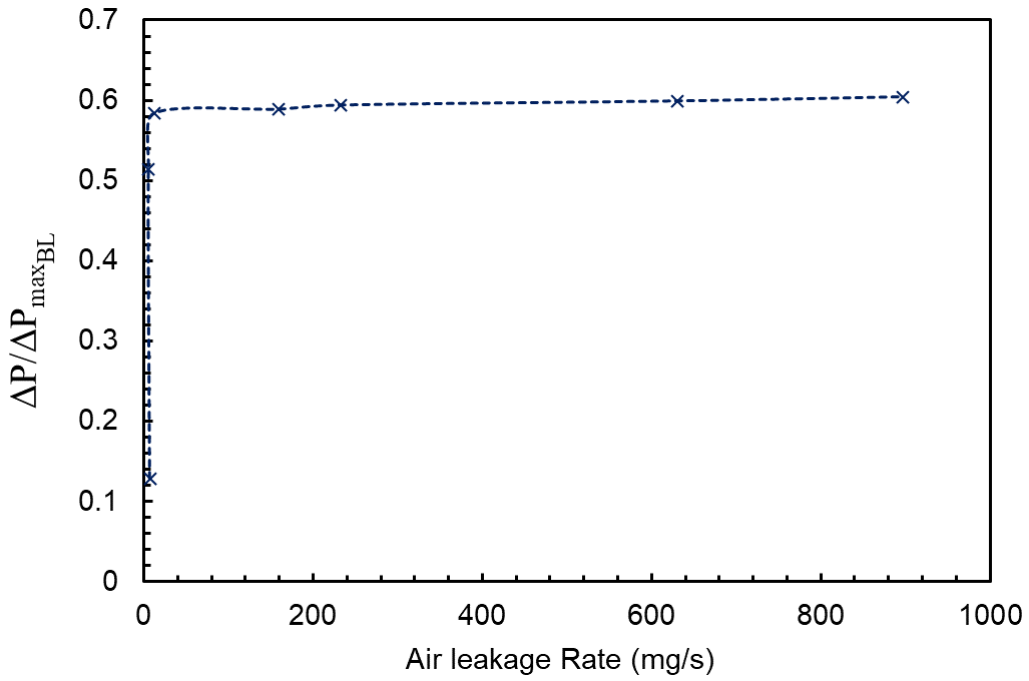


Figure 5-9: Air leakage data of the seal when Ω_H = 6000 rpm and Ω_F = 3000 rpm

This approach was applied consistently to define the maximum pressure capacity of the seal for all investigated shaft speeds and axial fin positions. The assessment of the maximum operational pressure when the respective rotational speeds of the housing and fin were 4000 rpm and 2000 rpm using this criterion is presented in Figure 5-10.

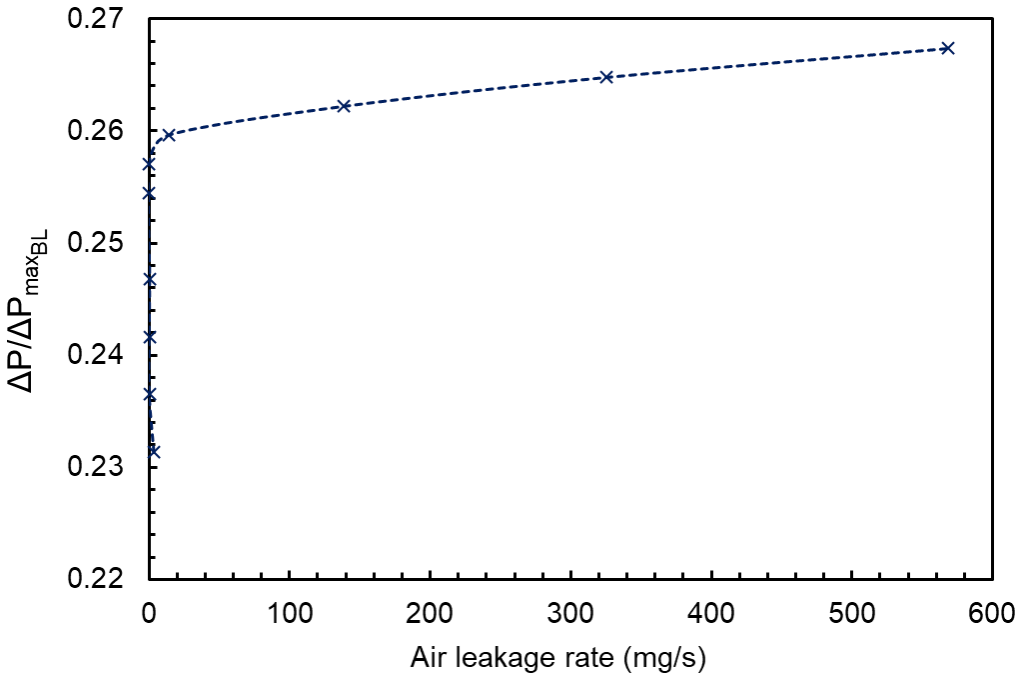


Figure 5-10: Air leakage data of the seal when Ω_H = 4000 rpm and Ω_F = 2000 rpm

In normal operation a hydraulic seal would be continually fed with oil and a question for future work is under what conditions the seal can recover from the leakage condition if the pressure is reduced after a period of leakage.

5.4.3 Determination of average angular velocity

It is obvious by looking at Equation (5-2), that a singular representative Ω_{oil} value is used to determine the maximum pressure capacity of the seal. Since the Ω_{oil} in the seal is non-uniform, it is important to establish a practise to evaluate the average Ω_{oil} in the flow domain as accurately as possible. In order to achieve this, the average tangential velocity profiles along three different lines as illustrated in Figure 5-3 were analysed. The axial line halfway between the fin tip and overspill point is represented by Line 1 at r/R_F = 0.89. The axial line midway between the base of the housing and overspill point at r/R_F = 0.92 is represented by Line 2. The radial centreline of the low pressure (LP) side of the seal is represented by Line 3. The average Ω_{oil} values evaluated by Line 1, Line 2 and Line 3 are presented in Section 5.4.4 along with other experimental results.

5.4.4 Core angular velocity

Figure 5-11 shows the mean angular velocity along each of lines 1, 2 and 3 (as defined in) for 4 housing speeds and 3 fin positions (0.25, 0.5 and 0.75). In each case the values obtained are compared to the value for Ω_{oil} obtained from Equation (5-4) denoted *Analytical*.

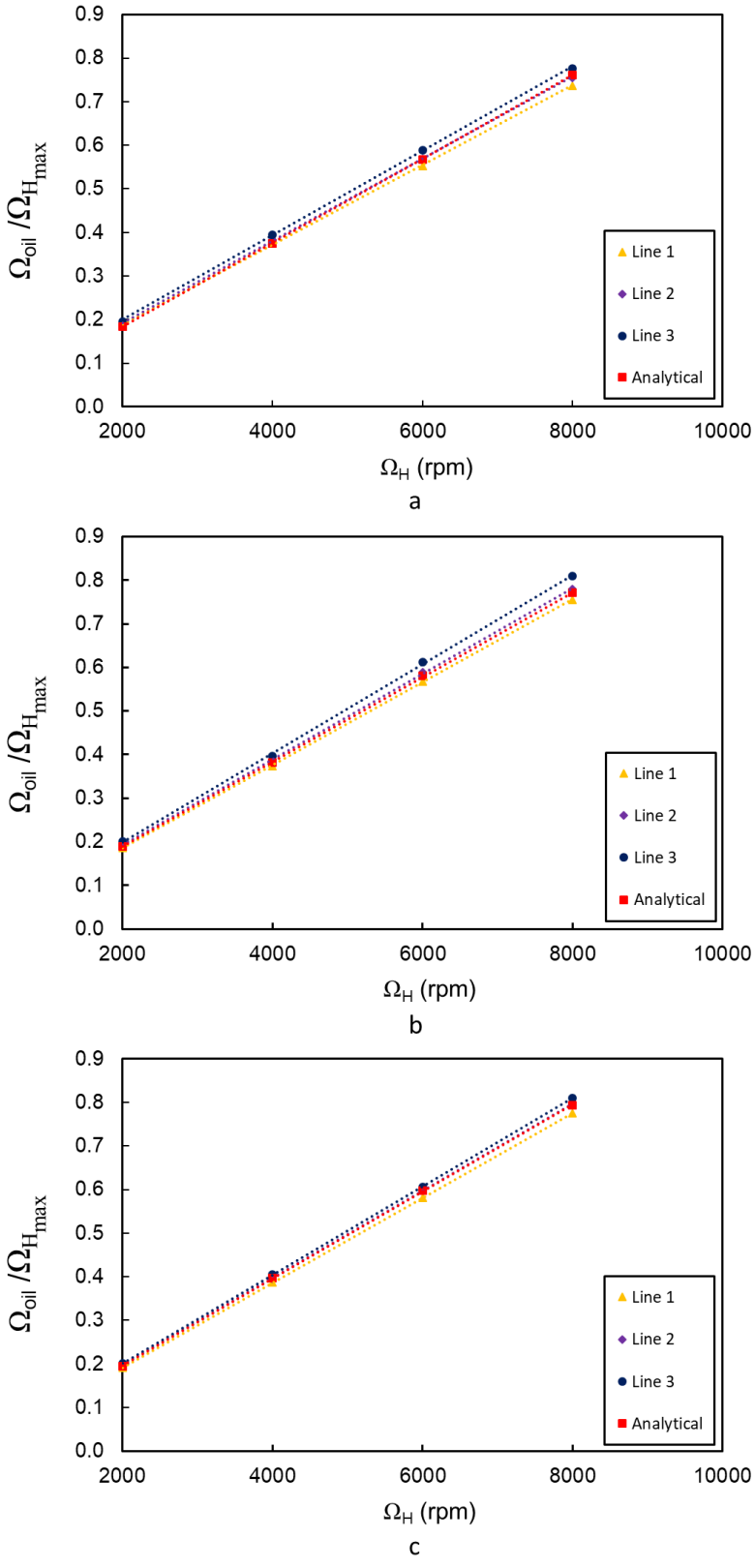


Figure 5-11: Average oil angular velocities computed along line 1, line 2 and line 3 at axial fin positions of (a) 0.25; (b) 0.5; and (c) 0.75

Although the Ω_{oil} results determined by the three lines seem reasonably close, it can be seen in Figure 5-11 that the *Analytical* results are best matched by Line 2. The percentage error between the Ω_{oil} results of Line 2 and the analytical values is 1.4% while Line 1 and Line 3 reported a percentage error of 6% and 5.7% respectively.

In this section, the maximum pressure results predicted by the CFD calculations have been used to obtain data for Ω_{oil} along three lines at locations specified in Section 5.4.3. The angular velocity values of bulk oil determined through the analytical approach have been compared against the CFD data at the specified locations. Upon examining the Ω_{oil} results, it can be said that for the geometry investigated, the best approximation for Ω_{oil} can be defined by the average velocity profile along the axial line midway between the base of the housing and overspill point:

$$h_{line2} = \frac{R_H - R_{B1}}{2} + R_{B1} \tag{5-9}$$

5.4.5 Effect of shaft speed and axial position of fin

The fin separates the two pressure chambers when the engine is in operation and is placed axially within the hydraulic seal assembly. In real engine applications, rotor expansion and relative axial movement of the shafts takes place over the engine operation envelope and thus the fin will not always be central in the trough. Hence, the axial displacement of the fin has been varied in the current study to investigate the effect of the axial position of the fin. Three instances with different fin positions were studied

and compared: s/w_H = 0.5 position where the fin was positioned in the middle equidistantly from the end wall surfaces of the housing; s/w_H = 0.25 position where a larger volume of oil was accommodated in the HP chamber and s/w_H = 0.75 position with a smaller volume of oil in the HP chamber. Here, the normalised axial fin position, s/w_H, has been obtained by non-dimenstionalising the axial distance between the housing and fin, s, by the housing width, w_H. The maximum pressure capacity of the seal, ΔP_{max}, has been non-dimensionalised by the maximum operating pressure of the baseline case, $\Delta P_{max_{BL}}$. The variation in the maximum pressure capacity of the seal with the displacement of the fin is illustrated in Figure 5-12.

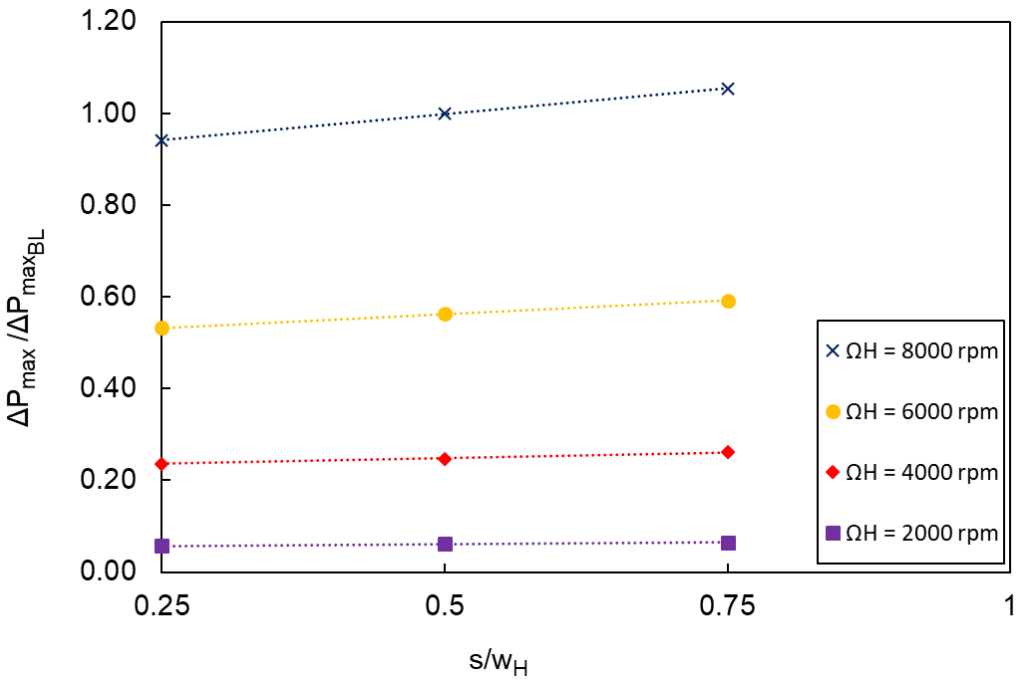


Figure 5-12: Maximum pressure capacity of the seal at three different fin positions

Looking next at the effect of shaft speed it can be seen that as shaft speed increases the pressure capacity of the seal increases. As Ω_{oil} increases linearly with shaft speed, seal pressure capacity is proportional to the square of shaft speed.

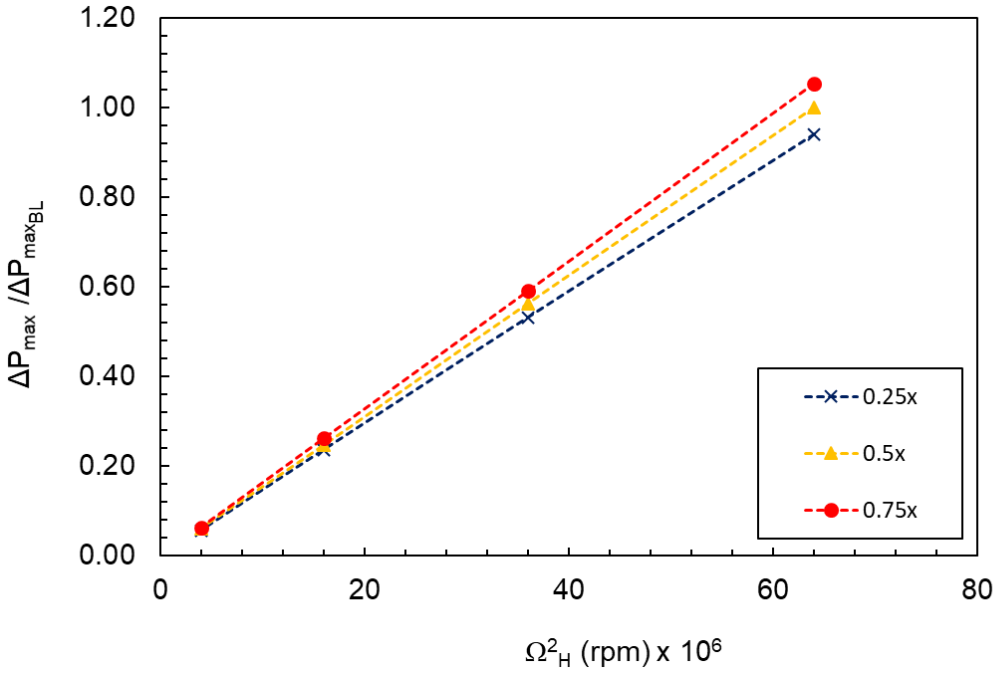


Figure 5-13: Effect of shaft rotational speeds on the maximum pressure capacity of the seal

The seal capacity results for the above shaft speeds are shown in Figure 5-13. It can be seen that the maximum pressure capacity of the seal is directly proportional to the square of the shaft speed; the maximum operating pressure varies linearly with ${\Omega_H}^2$ as illustrated in Equation (5-4). This result differs from the comparison of the seal capacity for different shaft speeds presented by Mathews et al. [27], where a linear relationship between the maximum pressure capacity and Ω_H is shown. As discussed previously, the key parameter in the maximum pressure capacity calculations is Ω_{oil}. As Ω_{oil} is

heavily dependent on both shaft speeds, it can be concluded that shaft speed has a dominant influence on the seal capacity as reflected in Equation (5-4).

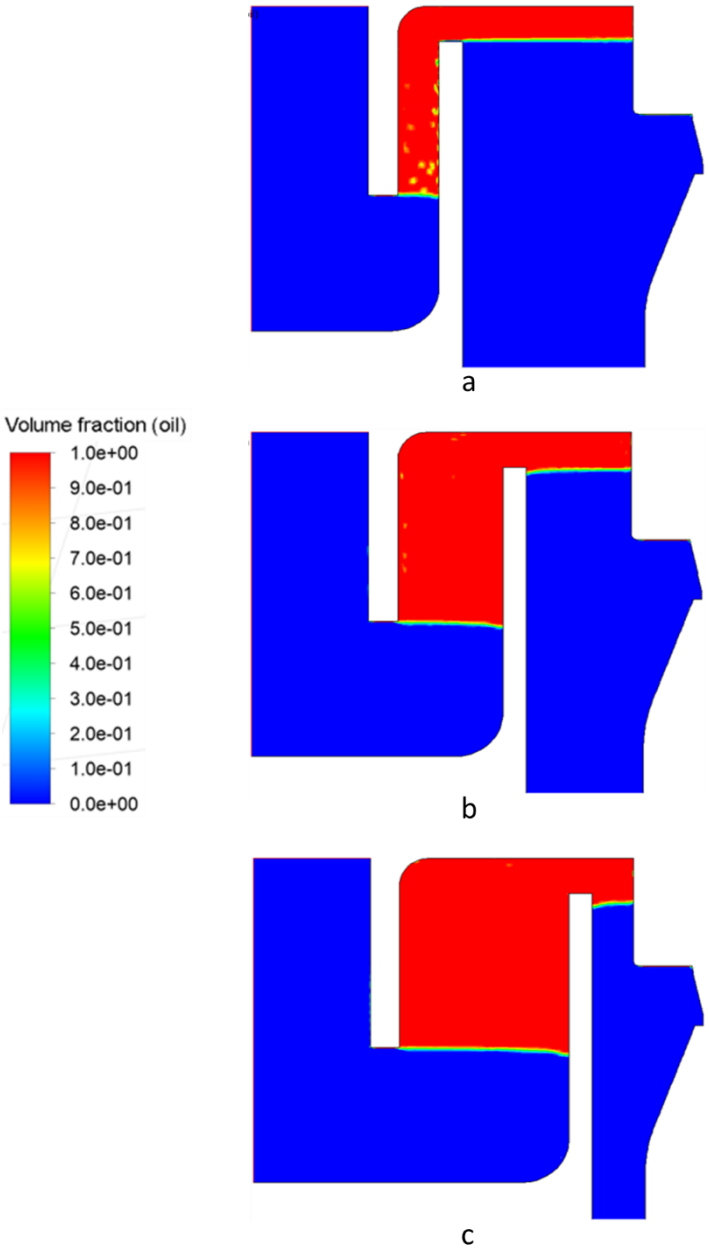


Figure 5-14: Contours of oil volume fraction at Ω_H = 6000 rpm and Ω_F = 3000 rpm for an operating seal pressure of 2.07 bar when fin is positioned at: (a) s/w_H= 0.25; (b) s/w_H= 0.5 and (c) s/w_H = 0.75

It is clear that the axial position of the fin does impact the maximum pressure capability of the seal; particularly at higher rotational speeds. With the fin closer to the HP side the pressure capacity of the seal is increased. A volume fraction contour plot when the fin is placed at axial locations s/w_H of 0.25, 0.5 and 0.75 respectively at Ω_H = 6000 rpm and Ω_F = 3000 rpm is illustrated in Figure 5-14 for a differential pressure of 2.07 bar, the pressure at which the seal is considered compromised for a fin position of 0.25. It can be seen in Figure 5-14b and Figure 5-14c that the liquid level rises up a little near the fin, driven by the secondary air flow in the cavity. With the smaller gap the secondary rotation is stronger, preventing air from leaking around the fin.

To investigate this further the in-plane velocity vector fields are presented in Figure 5-15 for fin positions of 0.25, 0.5 and 0.75. Recirculation zones are evident for s/w_H = 0.5 and 0.75 when the seal operating pressure is 2.07 bar and are highlighted in Figure 5-15. The recirculation zones create a low pressure region immediately downstream. This explains why these two fin positions can accommodate a higher pressure even though the seal has reached the maximum pressure capacity for s/w_H = 0.25.

For the same shaft speeds, the pressure capacity when the fin is positioned at s/w_H = 0.25 is approximately 6% lower than that of the baseline case. Further, it was found that the pressure capability of the seal when the fin is positioned at s/w_H = 0.75 is approximately 5% higher than the baseline case for the same shaft speeds. These findings are in contrast to the CFD results published by Mathews et al. [27] where it has been concluded that the displacement of fin is of very limited consequence due to approximately equal pressure capacities for all individual scenarios.

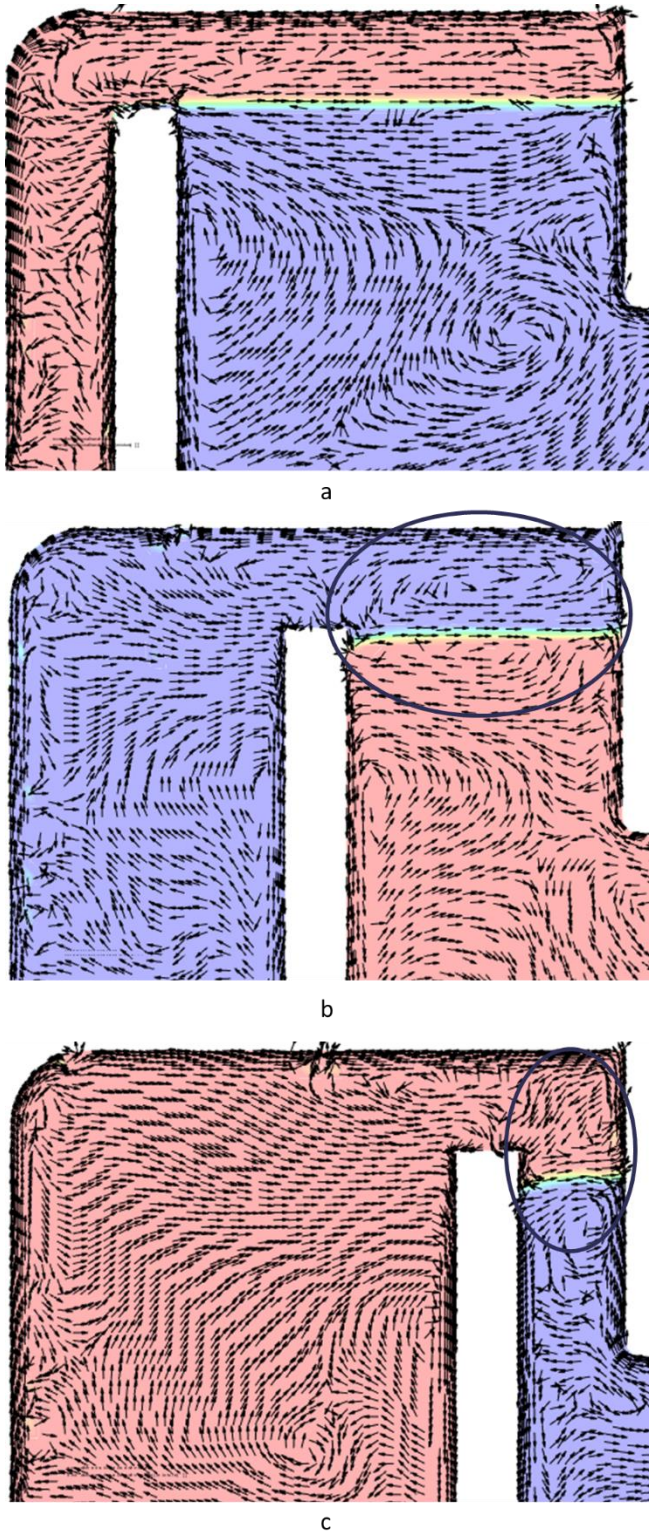


Figure 5-15: Truncated view of normalised in-plane velocity vectors at Ω_H = 6000 rpm and Ω_F = 3000 rpm for an operating seal pressure of 2.07 bar at s/w_H= (a) 0.25; (b) 0.5 and (c) 0.75 fin positions with the background colour indicating oil volume fraction

The disparity observed in the operating pressure results with varying shaft speeds and axial fin positions could be due to the different geometry used in the study by Mathews et al. [27]. Once compared with the geometry used in the work reported in this chapter, the geometry used by Mathews et al. [27] represents a much larger seal with a narrower housing. The seal investigated by these authors consists of a housing radius that is almost 1.8 times the radius of the housing of the seal in this study. It also has a radial gap between the fin and housing which is 4.2 times larger than the radial gap in the seal investigated in this thesis. The width of the housing in their study is almost half of the width of the seal investigated in this thesis. A comparison of the maximum operating pressure obtained through CFD for the two seal configurations and the maximum pressure capacity computed using analytical correlations has been presented in Section 5.4.8.

5.4.6 Analysis of Extreme Fin Positions

The investigation was extended to examine the effect of more extreme fin positions on the seal capacity. Previous experimental studies established that the flow characteristics of a rotating disk in a stationary cavity were influenced by the spacing ratio, s/R_F [40],[41]. These studies concluded that while the absolute value of s/R_F, determines the flow regime that exists within the chamber, it also affects the frictional resistance and the operational characteristics of the rotating disk. Therefore, the fin positioned at s/w_H = 0.1 and 0.9 locations where the axial distance between the fin and housing is very narrow for a housing rotational speed of 8000 rpm were investigated. The effect

of axial fin position on the maximum pressure capacity for housing rotational speed of 8000 rpm is illustrated in Figure 5-16.

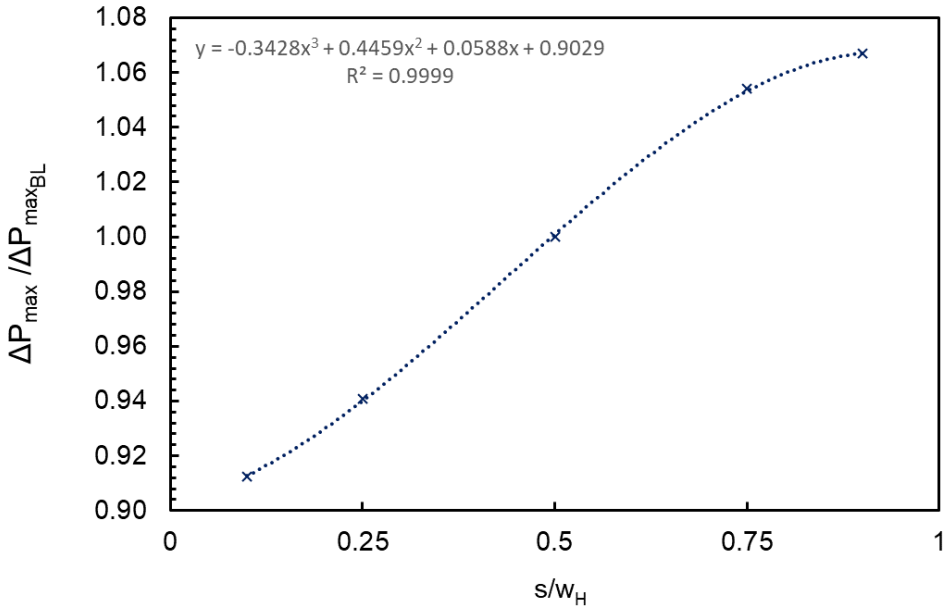


Figure 5-16: Effect of axial displacement of fin on sealing capacity when Ω_H = 8000 rpm

It can be seen that these extreme fin positions largely follow the trend in the previous section although the curve becomes somewhat "S" shaped: Highest and lowest sealing capacity is reported when the fin is positioned at s/w_H = 0.9 and 0.1 respectively. However, there is clear deviation from linear for a fin position of 0.9x.

5.4.7 Tangential velocity distribution between housing and fin

Daily and Nece [40] investigated tangential velocity distribution in their study of a disk rotating in a static housing. For a range of disk speeds non-dimensionalised as Reynolds number they identified regimes I-IV where regime IV was turbulent flow with

a core flow with a constant velocity that separates the boundary layers and regime III was turbulent flow with merged boundary layers. The spacing ratio, s/R_F, varies in each case due to the varying axial clearance between the housing and fin at each fin position.

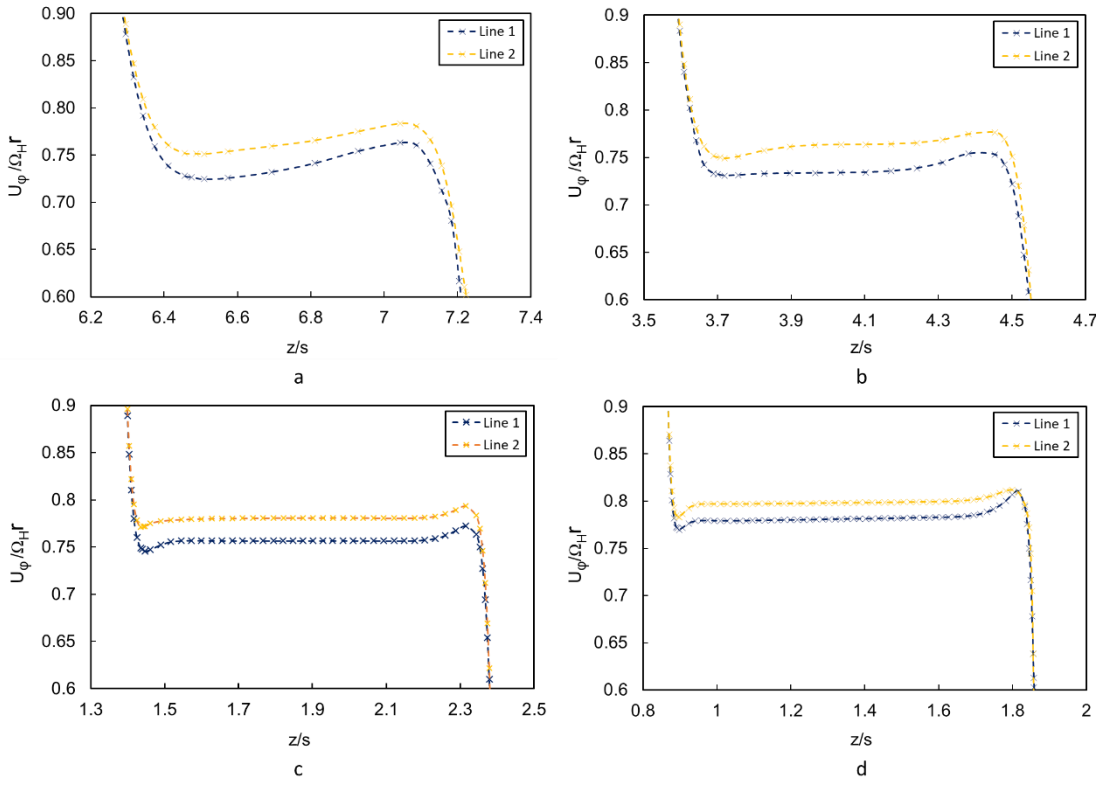


Figure 5-17: Tangential velocity profile along line 1 and line 2 (Figure 5-3) in the LP chamber at maximum pressure capacity when Ω_H = 6000 rpm and Ω_F = 3000 rpm for (a) s/w_H = 0.1, s/R_F = 0.0275; (b) s/w_H = 0.25, s/R_F = 0.0481; (c) s/w_H = 0.5, s/R_F = 0.1238; and (d) s/w_H = 0.75, s/R_F = 0.1995

Tangential velocity distributions from the housing to fin for turbulent flow in oil at a shaft speed of 6000 rpm ($Re_\Omega = \frac{\Delta\Omega {R_F}^2}{\upsilon_{oil}} = 1.3 \times 10^5$) along Line 1 and Line 2 are

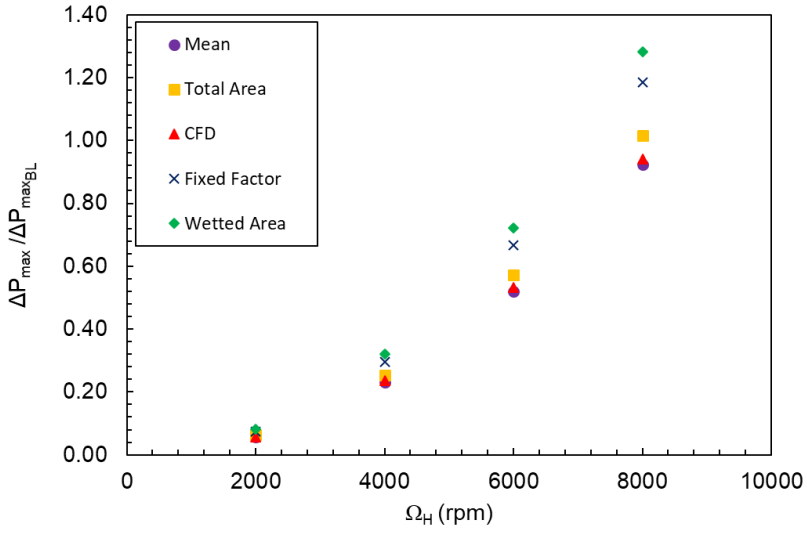
shown in Figure 5-17 for fin positions 0.1, 0.25, 0.5 and 075. In Figure 5-17a, where there is a close clearance, the tangential velocity profiles exhibit a considerable variation suggesting the boundary layers are merged. This establishes the existence of Regime III within the seal. It can be seen that the tangential velocity profiles show a constant core velocity as the clearances increase from Figure 5-17b through Figure 5-17d. Therefore it can be concluded that the flow type within a hydraulic seal at larger clearances is Regime IV.

5.4.8 Comparison of Numerical Results and Analytical Predictions

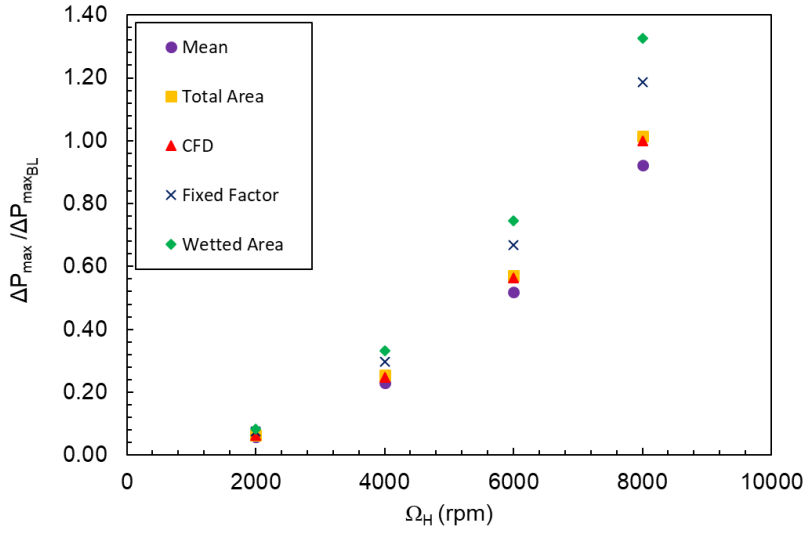
As the Ω_{oil} in a hydraulic seal is not uniform, analytical methods have been developed to estimate the average angular velocity as described previously. However, it is important to understand the restrictions associated with these oil estimate correlations. An analysis of the predicted pressures using the analytical approaches is discussed in this section. A comparison of the predicted pressure and numerically computed pressure for a range of shaft rotational speeds and non-dimensional axial position of the fin s/w_H, is also presented in this section.

The predicted maximum seal pressure estimates using the analytical approximations described in Section 5.2 are plotted together with the pressure values obtained through a series of CFD investigations carried out at s/w_H of 0.25, 0.5 and 0.75 in Figure 5-18a-c. It is clear in Figure 5-18a, that the numerically computed pressure capacity data are in very close agreement with estimates predicted using the mean velocity method explained by Equation (5-5), for all housing speeds. The RMSE between pressures

obtained through CFD and mean velocity approach is 4.4%. Of the two area averaged methods whose derivation is given by Equation (5-7) and Equation (5-8), estimates by the total area method seem reasonable. However, an over prediction of the pressure computed by the total area averaged method compared to the numerically computed pressure capacity results is noticed as the housing speed increases.



a



b

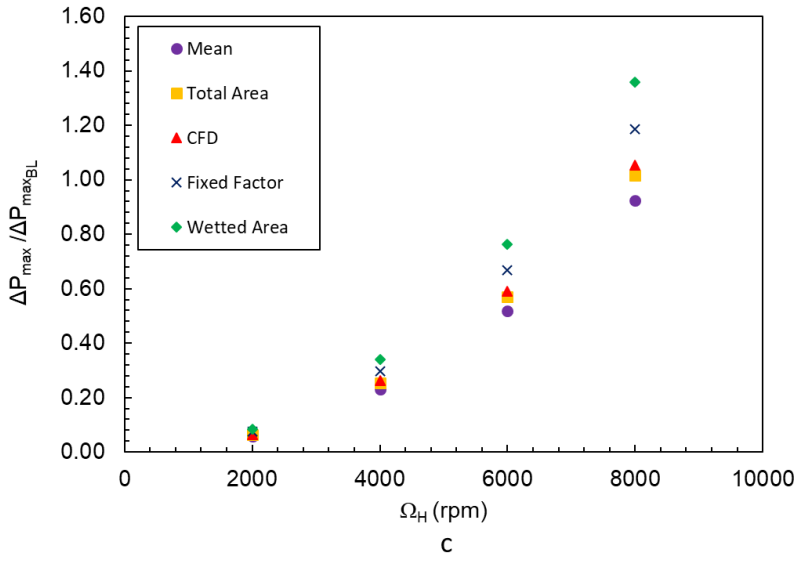


Figure 5-18: Comparison of analytically estimated seal capacity against numerically computed seal capacity at (a) s/w_H = 0.25; (b) s/w_H= 0.5; and (c) s/w_H= 0.75

The RMSE for the CFD and pressures predicted by total area approach 16.7% which is considerably higher than that of mean area method. The maximum pressure estimates obtained through the analytical approximations as well as CFD studies for s/w_H of 0.5 and 0.75 are illustrated in Figure 5-18b and Figure 5-18c respectively. It is clear that the CFD results for both fin positions are best matched by the estimates computed with the total area method. The RMSE between the data sets at s/w_H = 0.5 and 0.75 and the numerically predicted pressure are 3.6% and 8.6% respectively. Comparing the results for all three fin positions, it can be said that wetted area and fixed factored approaches tend to over-predict seal capacity whereas the mean velocity and total area methods yield results far closer to those from the CFD. While a close agreement is noticed between pressure estimates given by the mean velocity method and numerically

calculated seal capacity results at s/w_H = 0.25, this does not hold as much for s/w_H = 0.5 and 0.75 positions. This approach under predicts the pressure capacity of the seal especially at higher housing speeds which means that the mean velocity approach is less able to represent the effect of higher rotational speeds on seal capacity.

The geometrical extents considered in the two area based factor approaches are graphically presented in Figure 5-19.

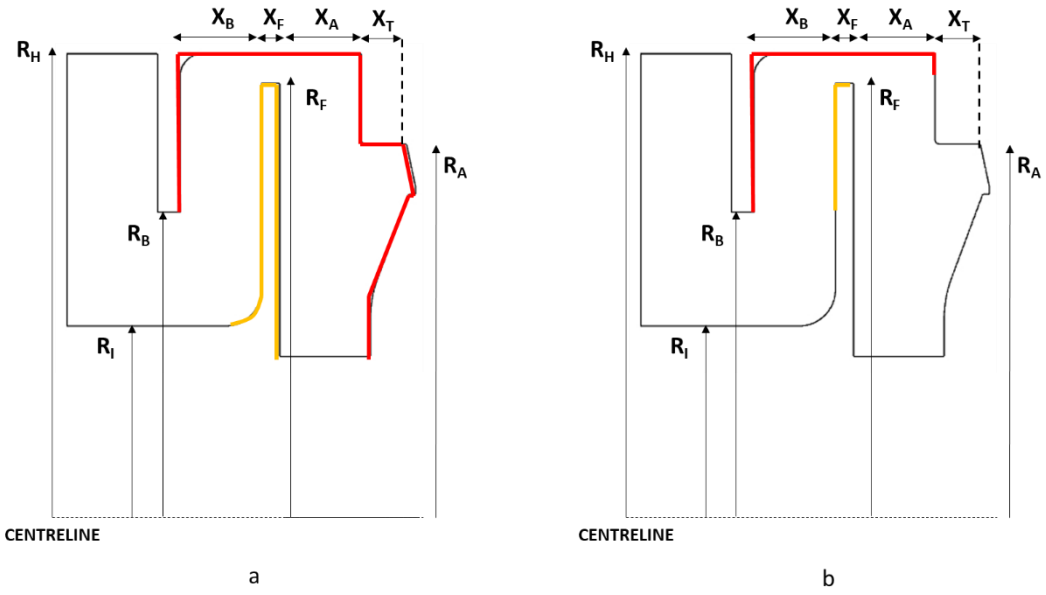


Figure 5-19: Geometrical domain considered for the approximation of bulk Ω_{oil} through area based factor methods (a) total area method; (b) wetted area approach

To define the average oil velocity, the area of the complete part as illustrated in Figure 5-19a is considered for the total area approach in this study and can be mathematically represented as follows:

$$A_H = \pi({R^2}_H - {R^2}_B) + 2\pi R_H(x_A + x_F + x_B) + \pi({R^2}_H - {R^2}_A) + 2\pi R_A x_T + \pi {R^2}_A \quad (5\text{-}10)$$

$$A_F = 2\pi {R^2}_F + 2\pi R_F x_F - \pi {R^2}_I \quad (5\text{-}11)$$

The area of the housing and fin considered for the wetted area method considers the area of both housing and fin contact with the oil as shown in Figure 5-19b and can be defined as:

$$A_H = 2\pi({R^2}_H - {R^2}_{B1}) + 2\pi(R_H - R_{B1})(x_A + x_F + x_B) - 2\pi({R^2}_F - {R^2}_{A1}) - 2\pi(R_F - R_{A1})x_A \quad (5\text{-}12)$$

$$A_F = \pi({R^2}_F - {R^2}_{B1}) + 2\pi(R_F - R_{B1})x_F \quad (5\text{-}13)$$

It can be concluded that the overall pressure estimates predicted by the total area correlation approach are closer to CFD pressure results as this method accounts somewhat for seal geometry as well as effect of housing and fin speeds. To understand as to why the total area approach can be established as an effective analytical prediction method for the seal geometry investigated, the role of the housing and fin should be taken into account. Using Equation (5-7), the total area weighting factor for the housing was computed to be 0.57 which means that the effect on the oil by the housing is only slightly greater than that by the fin. It is reasonable to make an argument that the

maximum pressure values predicted by the wetted area method would be more closely aligned with CFD predictions than the pressure estimates obtained through the total area and mean velocity methods, as it accounts for the specific housing and fin geometry in contact with the oil. However, contrary to this logical assumption, the results for the investigated geometry do not support this hypothesis. The wetted area method yields a weighting factor of 0.73 for the housing when calculated using Equation (5-8). This shows that the wetted area method predicts that the oil core is significantly influenced by the housing which leads to an over prediction of the oil bulk velocity. As pointed out by Denecke et al. [19], Ω_{oil} should be defined by the area of the total part as the velocity field is almost independent of the phase and density distribution, the results in this study justifies the validity of the total area approach for the geometry under investigation.

Although the air leakage around the fin in the 2D axisymmetric model appears as a stream of air bubbles, it is worth noting these are rather continuous annular rings of air due to the axisymmetric nature. Therefore, on this basis, it can be argued that the maximum pressure capacity of the seal is potentially over estimated with the 2D axisymmetric assumption. However, as pointed out by Mathews et al. [27] and further confirmed in the work documented in this thesis, the pressure capacity computed in the 3D simulations were in close agreement with the results obtained through the 2D axisymmetric approach. There is no evidence of 3D effects or gradients in the circumferential direction of the flow. The aim of the work reported in this section was not to verify the validity of the CFD methodology against the analytical correlations,

but it was rather an attempt to collate the approximations found in literature to obtain an analytical correlation for Ω_{oil}. An approach has been developed in this section to determine the most appropriate analytical method to compute the maximum pressure capacity of a hydraulic seal for the geometry considered. Based on the results obtained for two geometries, the total area method provides the best overall prediction of the maximum pressure capacity when compared with CFD results. A subject of future investigations should be to analyse the effect of geometry on the performance of a hydraulic seal. Upon further validation, this methodology can then be extended to other hydraulic seal geometries to understand the effect of geometry on the assumptions made in the analytical approximations.

5.4.9 Engine condition

To examine the effect of shaft speed on the maximum pressure capability of a hydraulic seal, a typical rotational speed range for HP and LP shafts with a constant shaft speed ratio was considered for the parametric study reported in this chapter. However, to appreciate the validity of the methodology established, the range of the cases was extended to investigate a more realistic engine condition where the housing shaft speed was set to 10,000 rpm and fin shaft speed was set to 1780 rpm. The investigation of the engine condition incorporates the leakage flow rate approach established in Section 5.4.1 to assess the maximum pressure capacity of the seal. This was done to assess the versatility and consistency of the introduced leakage flow rate approach. A volume fraction contour plot when the fin is placed at an axial location s/w_H of 0.5 at Ω_H =

10,000 rpm; Ω_F = 1780 rpm is illustrated in Figure 5-20 for a range of differential pressures from 4 - 4.2 bar, it can be seen that the seal is no longer in equilibrium beyond 4.14 bar and therefore is considered to be compromised.

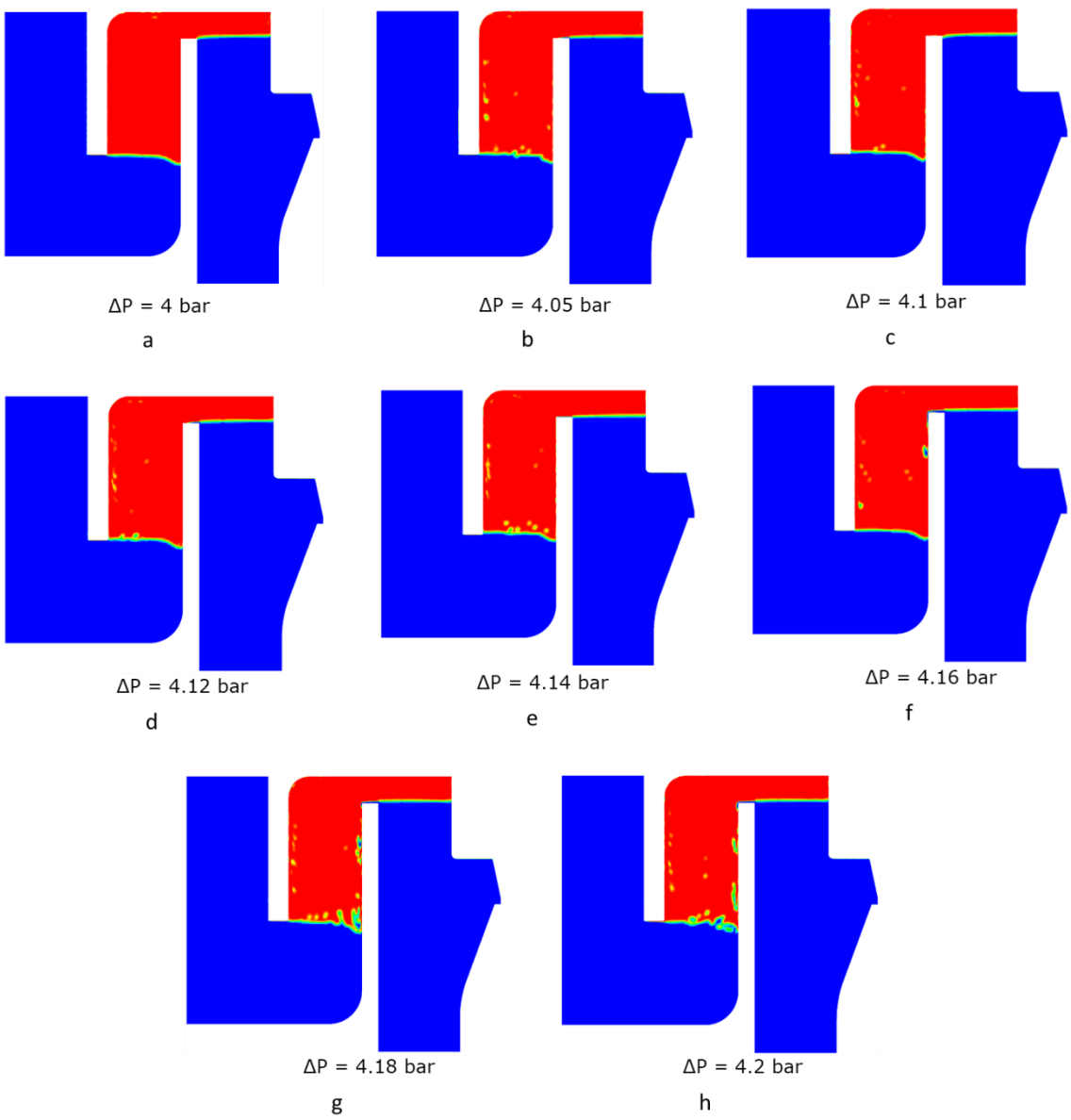


Figure 5-20: Comparison of oil volume fraction contours for numerically calculated pressures of the hydraulic seal between 4 to 4.2 bar

Figure 5-20e shows the oil volume fraction at a differential pressure of 4.14 bar and is considered the maximum operating pressure of the seal. The air leakage rate at this operating pressure was found to be approximately 123 mg/s. Figure 5-20f-h represent failed seals as the air leakage rate has exceeded 200 mg/s. The calculated air leakage rate through the seal discussed above for a sequence of differential pressures in steps of 0.02 bar is illustrated in Figure 5-21.

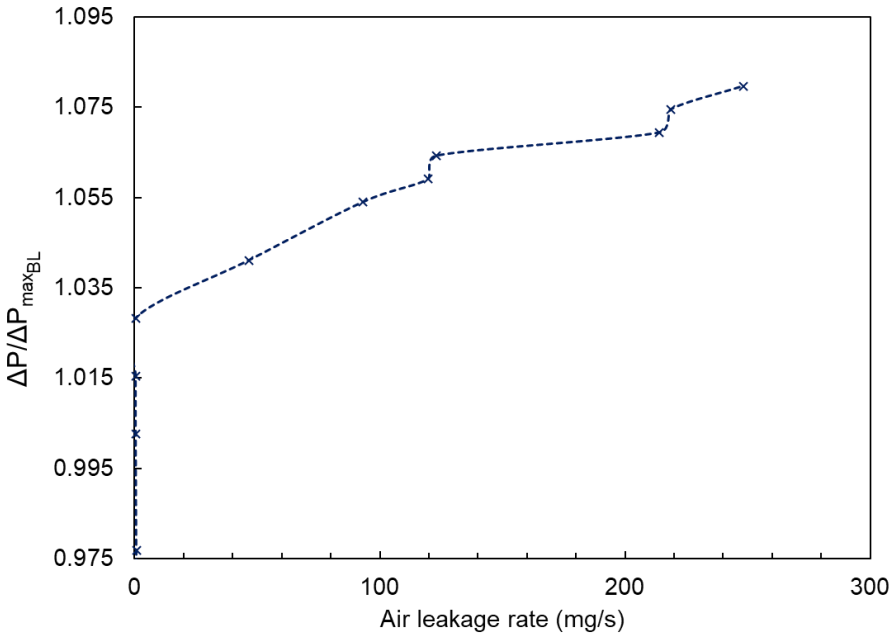


Figure 5-21: Air leakage data of the seal for the engine condition case when Ω_H = 10000 rpm and Ω_F = 1780 rpm

The seal capacity results for all the shaft speeds considered are shown in Figure 5-22. It is evident that maximum pressure capacity of the seal for this case has been best matched with the data, analytically predicted using the total area method. It can be said

that the engine condition case follows the trend observed in the key findings of this study.

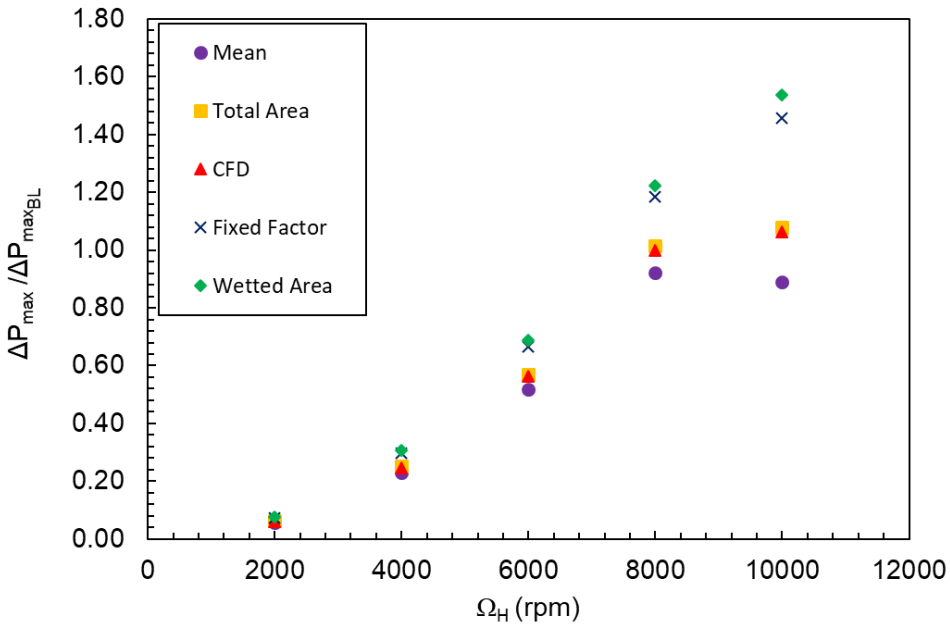


Figure 5-22: Maximum pressure capacity results of the seal for all shaft speeds considered in the main study

5.5 Validation of numerical results

Due to the lack of relevant experimental results for the geometry investigated in this chapter, a validation study of the CFD results was conducted against available experimental data for a different geometry investigating the maximum pressure capability of a hydraulic seal reported in a numerical study by Mathews et al. [27]. This validation study follows the CFD methodology explained in Section 5.3. The experimental data used in the study by Mathews et al. [27] were from experiments

conducted in a dedicated hydraulic seal rig that was published in an internal Rolls-Royce report. The CFD approach shadows the experimental procedure where the shaft speeds have been fixed first for a fin position of s/w_H = 0.5, followed by increasing the static pressure on the HP side until the breakdown of the seal occurs. The numerical study performed by Mathews et al. [27] does not include an oil supply while the reported experiments were carried out with an oil feed. Figure 5-23 depicts the maximum pressure capacity for three operating points compared against experimental and CFD results by Mathews et al. [27].

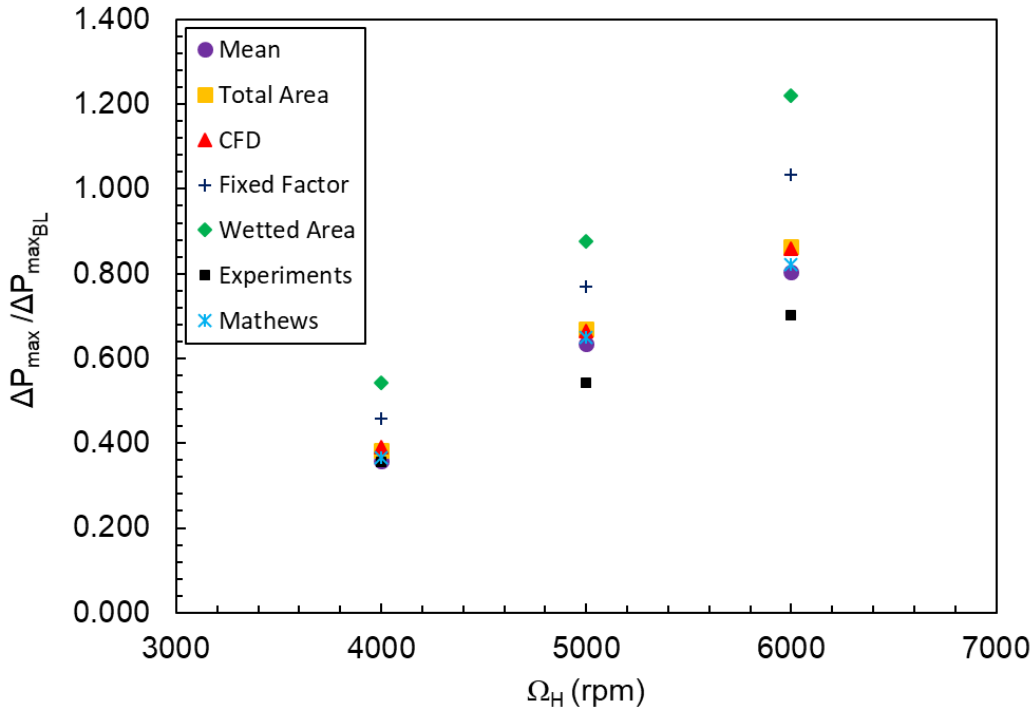


Figure 5-23: Comparison of numerically computed seal capacity against experimental data, literature and analytically computed seal capacity at s/w_H = 0.5. CFD refers to the results obtained through the methodology developed in this thesis using the geometry shown in Figure 5-24

The results show that the CFD results are in good agreement with the recorded operating pressure values by Mathews et al. [27]. However, the experimental results seem to be lower than the CFD results at all shaft speeds. This could be due to utilizing a geometry with a straight fin with parallel edges for simplification purposes. Another reason could be that an oil feed has not been modelled in the CFD simulations.

The geometry investigated is presented in Figure 5-24 where the housing depicted by 1, has a radius which is almost 1.8 times the housing radius in the primary geometry analysed in the main study of this work. However, the geometry in the study by Mathews et al. [27] consists of a much narrower housing with a width almost half of that in the primary geometry used in the work reported in this chapter. The fin is portrayed by 2 and the pressure inlet and pressure out are represented by 3 and 4 respectively.

The same technique described in Section 5.4.1 has been implemented in this series of numerical simulations to define the maximum pressure capacity of the seal. It can be seen that the maximum operating pressure varies proportionally to the shaft speeds and is in excellent agreement with the pressure estimated by the total area method. It is interesting to note that the rotating walls of the geometry used in the validation cases are in very close proximity to each other. This geometric feature influences the flow characteristics in the cavity of the seal and the vortex generated in the narrow gap between the fin and housing is evident in Figure 5-24.

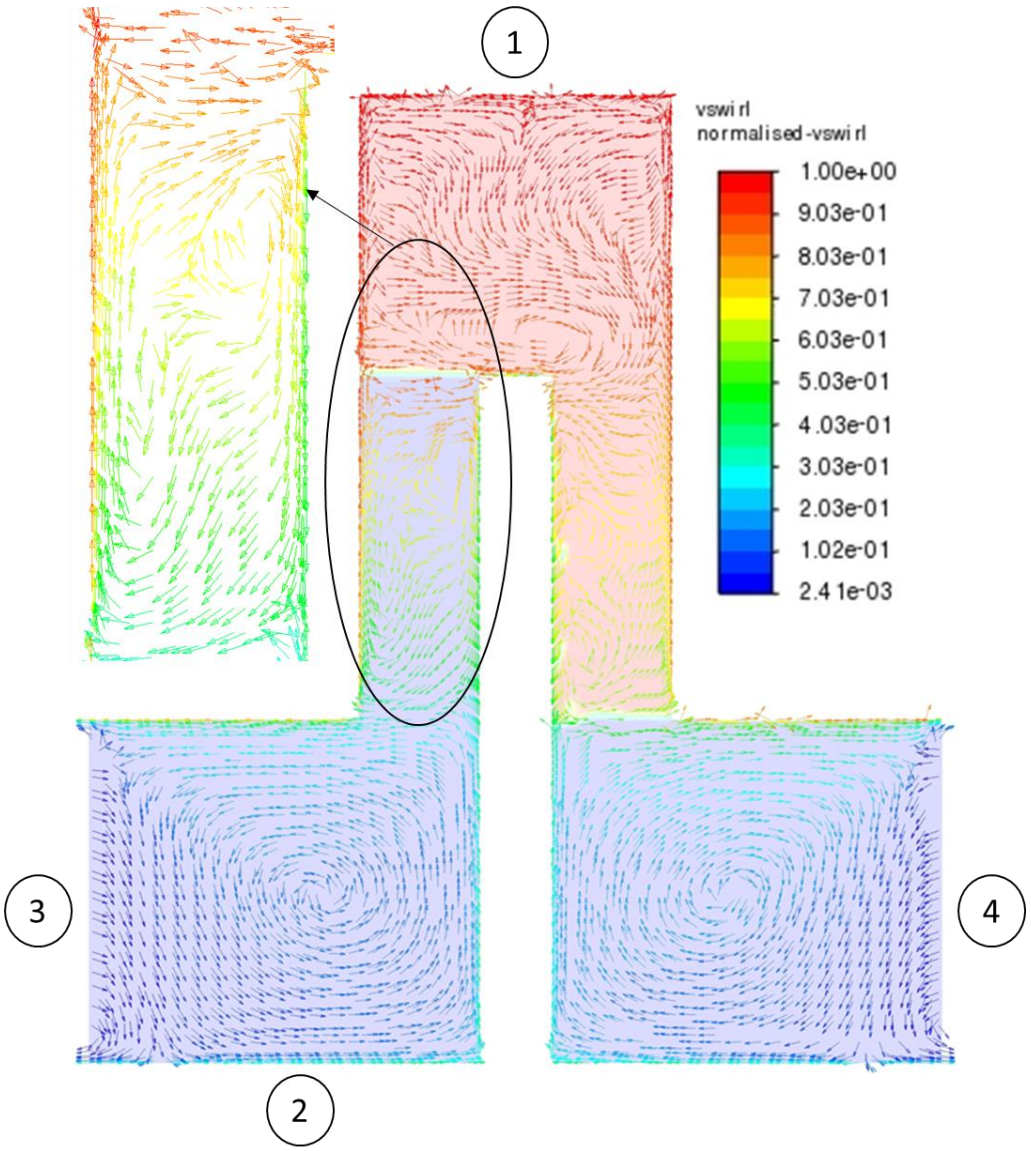


Figure 5-24: Normalised in-plane velocity vectors at Ω_H = 6000 rpm and Ω_F = 3000 rpm for an operating seal pressure of 3.34 bar at s/w_H = 0.05. The in-plane velocity vectors have been coloured by velocity, with the background colour indicating oil volume fraction

This flow feature was not seen in the original simulations reported in the main study of this chapter when the fin was placed equidistantly from the end walls. Therefore, it seems reasonable to conclude that the established CFD methodology accurately

captures the maximum operating pressure of the seal and can be extended to any geometry. It is also encouraging to note that for both geometries investigated, the numerically computed seal capacity was best matched by the pressure estimates obtained through the total area method. Therefore, based on the results obtained from both geometries, there is a strong indication that the total area method can be used to evaluate the maximum pressure capacity of a hydraulic seal accurately. However, further parametric studies should be carried out to investigate the effect of distinct geometric characteristics on the assumptions made in the analytical correlations.

Commonly used industrial hydraulic seals include a fin that has a relatively thicker base where it gets attached to the shaft with one of the edges beginning to taper down to a thinner fin tip from a mid-height. The fin is designed to have a thicker base so that the structural integrity of the part can be preserved and is typically attained with considerable fillet radii at the base. This is due to a combination of centrifugal and differential oil/gas pressure load that gives rise to a resultant bending stress at the base. The standard hydraulic seal arrangement incorporates a relatively thinner fin tip so that the circumferential profile can be adequately controlled to minimize the generation of viscous heating which occurs due to the fin rotating in a trough of oil. It should be noted that a geometry with a straight fin with parallel edges has been adopted in this work to simplify the modelling process and to allow for simplified calculations in the analytical approximations. In a hydraulic seal configuration in an engine, parallel sided edges are usually avoided to reduce the risk of seal/component failure in the event of high vibration and excitations. A tapered profile, on the other hand, has the capability to

dampen the effects of excitation due to its shape. As demonstrated in Section 5.4.5, the maximum operating pressure of a seal is largely influenced by the shaft rotational speeds and the axial position of the fin. Therefore, it can be assumed that the effect of a radiused fin with a thickness, x_F, as compared to one with parallel sided profiles with a thickness, x_F, on the maximum pressure capacity must be insignificant. A reliable methodology has been developed in this chapter to determine the maximum pressure capacity of a hydraulic seal. This developed methodology can be applied in further investigations to get an accurate understanding of the influence of different geometric configurations on the maximum pressure capacity.

5.6 Summary

Intershaft hydraulic seals act as zero flow air seals that allow a larger pressure difference across the seal when used in rotating applications subjected to centrifugal forces. Design approaches established on the basis of analytical derivations can be found in the literature but the accuracy and consistency of these methods require the use of a high safety factor. Building on previously published studies this study was aimed at developing a CFD modelling capability for intershaft hydraulic seals for aero-engine applications. To investigate the performance of a seal without an oil feed, 2D numerical simulations were conducted in ANSYS-Fluent applying a VoF method for a range of shaft speeds and axial fin positions.

Prior established analytical approximation to estimate the angular velocity of oil were collated together in this work. A comparison was made between the analytical and numerical calculations. For the geometry investigated, the numerical results were best matched by weighting factors calculated based on the areas of the housing and fin.

A consistent approach was developed to define seal capacity in terms of leakage rate. When the air leakage rate exceeded 200 mg/s the seal was deemed broken. The results presented show that the maximum pressure capacity of the seal increases linearly with the square of housing speed. This result is in contrast to the relationship established in a prior study by Mathews et al. [27] who reported a linear relationship between the maximum pressure capacity and housing rotational speed. The seal investigated in this study by Mathews et al. [27] is much narrower with a width that is half the size of seal examined in this work. Therefore, at higher shaft speeds, wider seal configurations seem to demonstrate better operational characteristics due to the square relationship with the maximum pressure capacity. At a given housing speed maximum pressure capacity increases linearly with displacement of the fin from the side of the housing on the LP side. Different flow regimes within the seal were identified as the fin was displaced axially: Regime III (turbulent flow merged boundary layers) was identified at smaller clearances where $s/R_F < 0.03$. At larger clearances when $s/R_F > 0.04$, Regime IV exists.

CHAPTER 6

6 3D Modelling of Intershaft Hydraulic Seals with an Oil Feed

The velocity gradient in the oil column of a hydraulic seal which emerges due to the differential speeds between the trough and fin, gives rise to a frictional drag between the rotating surfaces and the oil. To minimise the effects of viscous heating generated by this phenomenon and reduce the oil residence time within the seal, a continuous oil feed is usually supplied in aero-engines using a jet. Oil is distributed into a hydraulic seal using a direct or an indirect feed when the engine is in operation. Static jets are a common application of feeding oil directly into one side of the hydraulic seal (usually the lower pressure side), used mostly when it is impractical to collect oil from an external location outboard of the hydraulic seal assembly. In an application such as a hydraulic seal, a jet that does not breakup or atomise would be most desirable as the intention is to deliver all the supplied oil into the trough. In previous chapters, a successful modelling methodology to evaluate the maximum pressure capability of hydraulic seals when there was no oil feed has been established. Expanding on the existing studies, in this current chapter, a continuous through-flow oil feed at a

representative flow rate through a representatively sized jet diameter is added to the seal modelled in ANSYS-Fluent to create a model of the oil flow in the seal. This chapter investigates the oil flow breaking up into droplets/ligaments followed by the oil film formed around the circumference of the trough using a Volume-of-Fluid method when an operational differential pressure is maintained across the seal. An analysis and discussion of the numerical investigation is presented with the focus on the oil in the trough. Droplet generation through jet splashing is not sufficiently resolved for detailed analysis because of the limitations of the mesh resolution. The second part of the chapter comprises an investigation into thermal effects including oil-related heat transfer.

A complementary but truncated experimental programme at the University of Nottingham has briefly investigated a hydraulic seal with jet fill, varying jet angle and jet flowrate. This CFD study models this filling seal, employing a model representative of the experimentally investigated hydraulic seal geometry facilitating comparison to experimental data. This work investigates the fate of oil that either splashes back from the seal during the jet fill process or is ejected from the seal on the non-fill side. The developed approach is aimed to understand the interfacial flow physics of intershaft hydraulic seals and construct a reliable methodology which provides an analysis of oil behaviour in the seal.

6.1 Experimental set-up and procedure

The experimental work was conducted outside this PhD research project but as the data is not published it is necessary to provide some details here. The experiments were conducted using the 3-Shaft test rig assembly at the University of Nottingham, which has three variable speed AC motor drives coupled to gearboxes giving maximum speeds of 35,000 rpm (drives 1 and 2) and 60,000 rpm (drive 3).

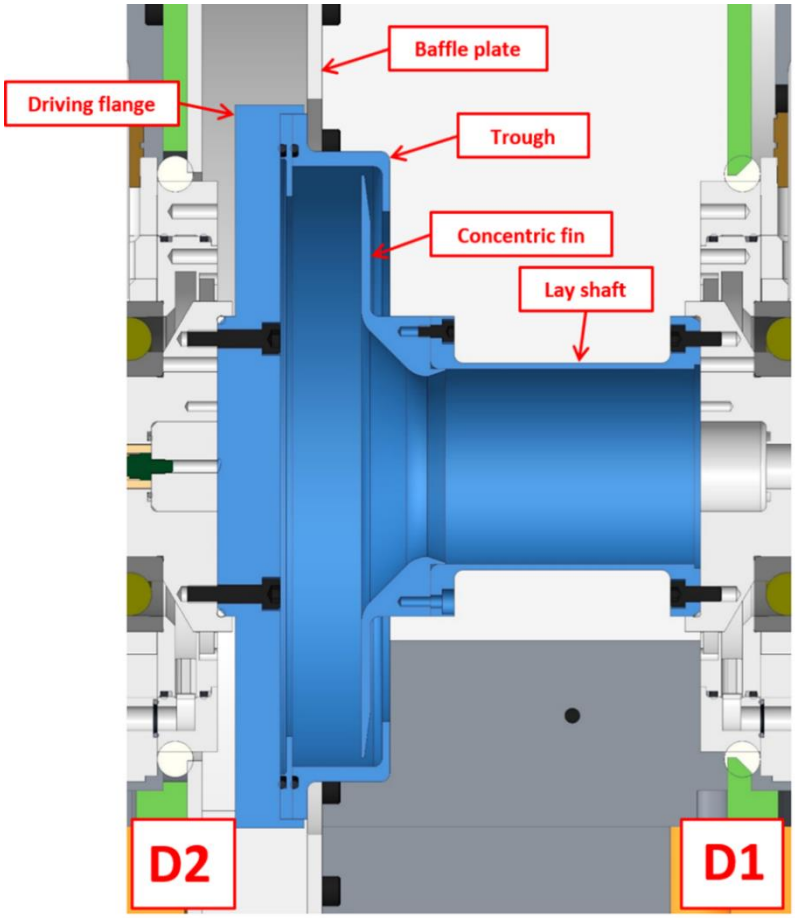


Figure 6-1: Oil-based inter-shaft seal main components [227]

Torque is measured using in-line torque flanges. The facility has data acquisition and control systems for running predefined tests and recording data. The seal test module has an independent oil supply system that can be controlled in flow or pressure mode. In these experiments, the oil system was run in flow control mode, maintaining the control valve opening to match a target flowrate. However, the oil pressure was measured upstream of the jet assembly, at the investigated flowrates of 1.1 l/min and 1.4 l/min. The corresponding pressures were recorded as 2.1 bar and 3 bar respectively. The air system used in the test module that is supplied from the central compressor is filtered and has three air supply lines that can provide air in either mass flow or pressure control modes. Oil is removed from the test module via three scavenge lines. The test seal comprises of a rotating trough and concentric fin assembled on the two drive shafts and can be viewed through the visualization chamber as illustrated in Figure 6-1. Oil is fed through a jet nozzle into the seal. Air is supplied through the bore of the high-speed output shaft linked to the gearbox. A detailed description of the test set-up and the experimental procedure followed, can be found in the study examining the impact of the jet on the pool of oil in a hydraulic seal by Warusevitane et al. [227]. Only the key details about the experimental methodology has been presented in this section.

The air feed line capable of delivering a flow rate of 1-160 g/s was used to supply air to the seal during experiments. During the tests conducted the rotation and the oil feed were implemented simultaneously based on predefined ramp times as the air flow achieved steady state. During this process, the oil that is injected into the seal, filled the trough until it spilled over on the LP side. Oil splashed on both sides of the trough. The

exiting oil was drained under gravitational effects through several drillings into separate sumps. Stationary baffle plates were used to separate the HP and LP oil sumps. The oil was then pumped back into the tank through the scavenge lines. The seal was considered to have formed once there was no longer any air flowing through it. For the series of tests performed, a range of speeds were tested with the trough and fin rotating clockwise. The investigated experimental conditions for a fin speed of 2000 rpm and trough speed of 4000 rpm are presented in Table 6-1 as this is the test condition that was numerically simulated.

Table 6-1: Recorded test conditions in the experiment used for CFD validation

Test duration (min)	30
Oil flowrate (l/min)	1.1
Oil feed temperature (°C)	40.8
Oil sump temperature (°C)	41.6
Air feed pressure (barg)	2

In this experiment, the testing profile was set to start the trough and fin rotations and oil feed simultaneously. The ramp rates for both shaft speeds and oil flow were defined in the test profile. Multiple pressure and temperature measurements were recorded, including oil feed temperature, high pressure (HP) seal pressure, and low pressure (LP) seal chamber pressure. To estimate the heat generated in the trough from friction, a thermocouple was placed in the LP oil sump to measure the temperature of oil that

splashed during the filling process as it reached the sump. Installing a thermocouple inside the trough would have added complications to the data acquisition system and hence, this approach was implemented to simplify obtaining temperature measurements. While not an accurate trough oil temperature reading, it provides a reasonable estimate, accounting for heat loss between the trough and oil pool.

6.2 Numerical modelling approach

The flow within the hydraulic seal was computed using ANSYS-Fluent v2021R1. The modelling strategy developed in Chapter 5 was extended with some modifications to represent the 3D nature of this study. The seal modelled in the present CFD study is a model representative of the hydraulic seal geometry described in Section 6.1. The fin to housing radius ratio (R_F/R_H) in this model is 0.96. For comparison, the seal geometry investigated by Mathews et al. [27] had a housing 1.8 times the diameter, almost half the width and a radial gap which is 4.2 times this one.

A 3D simulation of the full 360° geometry was carried out in two stages. Firstly, an air-only single phase scenario was simulated in steady-state, until the flow reached pseudo-steady state allowing the air to gain momentum from the rotor. The single-phase solution was used as the initial condition for the two-phase flow simulations. To implement the two-phase flow, an oil volume was then patched into the domain extending from the base of the housing to half of the fin length and a VoF modelling approach was applied. Air was defined as the primary phase with constant properties. For the secondary phase, oil was defined as an incompressible fluid. The properties of

the working fluid modelled in the CFD simulation and the oil used in the experiments are outlined in Table 6-2 . The difference in values is due to the CFD study being carried out prior to conducting the experiments using estimated properties whereas the experimental values shown are the actual measured values. To simulate a through flow regime with an oil feed, a liquid jet with a diameter of 0.0015m and flow rate of 1.62 l/min was modelled.

Table 6-2: Properties of oil used in the seal used in the CFD study and experimental investigation

	CFD	**Experiment**
Temperature (°C)	40	40
Density (kg/m^3)	976.6	972
Dynamic Viscosity (kg/ms)	0.0273	0.0325
Surface Tension (N/m^2)	0.0308	0.0282

The standard $k-\varepsilon$ turbulence model was applied in combination with the 'enhanced wall treatment' to resolve the flow at the boundary layers. The 'Coupled' pressure-velocity coupling was applied together with 'PRESTO' pressure interpolation scheme. The pressure-velocity coupling used in the 3D study is different to the one used in the 2D investigation which is SIMPLE. The 'Coupled' algorithm was applied in this study as this resulted in a robust solution as opposed to the divergent field induced by the use of SIMPLE algorithm. A second order upwind-biased discretization scheme was chosen for all pressure, momentum and turbulence terms. The 'geometric

reconstruction' scheme was used to compute the interface and include the effects of surface tension (σ_L) between oil and air. Interfacial anti-diffusion correction method and interface sharpening treatment were implemented in this investigation due to the reasons discussed in Section 5.3. As modelled in the 2D study, the 'Implicit Body Force' treatment was applied in the 3D investigation as well to formulate the body forces accounting for surface tension as recommended in the Fluent User Manual [192].

To simulate the flow within a seal in operation, the simulations were conducted in transient mode. The pressure was increased stepwise in increments of 0.05 bar until the required operational pressure of 0.2 bar was achieved. The simulation was implemented allowing the flow to achieve pseudo steady-state using a variable time step with an initial time step, (Δt) of 10^{-5} s as was done in the 2D study. A variable time step was set-up to eliminate the possibility of solution divergence by restricting the Courant-Friedrichs-Lewy number to be one. Convergence at each time-step was controlled using a residual convergence criterion of 1×10^{-6} for the pressure, velocity and turbulence variables. Overall simulation convergence was assessed primarily through monitoring the bulk residuals, moment coefficient of the walls and velocity magnitude at several locations. Mass balance between inlet and outlets was also monitored throughout. Once a steady state solution was achieved, the results were analysed; a fully developed flow solution was achieved in a flow time of 0.3 s for which a total of 52,358 core hours were required. 3D solutions were computed in parallel using 44 Intel Xeon Gold 6238 cores. The physical time spent on this 3D simulation was 1190 hours.

6.3 Mesh

A detailed mesh sensitivity study was conducted for a numerical case with shaft speeds 4,000 rpm and 2,000 rpm for housing and fin respectively and a differential pressure of 0.2 bar to ensure a mesh independent solution is achieved for the single phase model. Three unstructured poly-hexcore meshes were investigated. Although the intention is to model an oil feed delivering into the oil pool in the trough, the flow direction and the gradients cannot be pre-determined accurately. In scenarios where complex flow fields with secondary flows are expected, poly cells can be aligned to the flow much easily. Poly-hexcore cells are also capable of generating a detailed cross-section while capturing the wall effects appropriately. Poly-hexcore cells were considered in this study as it was important to create a core region with good cell quality similar to that of the 2D mesh. Simulations were conducted varying the base cell size resulting in 20, 27 and 40 cells across the axial span of the trough base denoted by Mesh 1, Mesh 2 and Mesh 3 respectively. The details of each mesh used for the mesh independence study is presented in Table 6-3.

Table 6-3: Sizes of meshes investigated for mesh sensitivity study

	Mesh 1	Mesh 2	Mesh 3
Number of elements across axial length	20	27	40
Number of cells	3,690,231	8,372,269	10,638,061

The optimal mesh was determined by comparing flow fields using contour plots and line graphs. As an example, velocity profiles of air in the z-direction along an axial line at r/R_F = 0.092 are illustrated in Figure 6-2; the velocity profiles in the HP region are included in the non-dimensional axial length ranging from 0.78-1. Comparing the average core velocity in the HP chamber of all three meshes, it can be seen that refinement from Mesh 1 to Mesh 2 and Mesh 2 to Mesh 3 shows no significant differences. Based on these results, Mesh 1 shown in Figure 6-2 was chosen as the optimal mesh as it represents a fair trade-off between accuracy and computational efficiency whilst minimizing the computational cost in comparison.

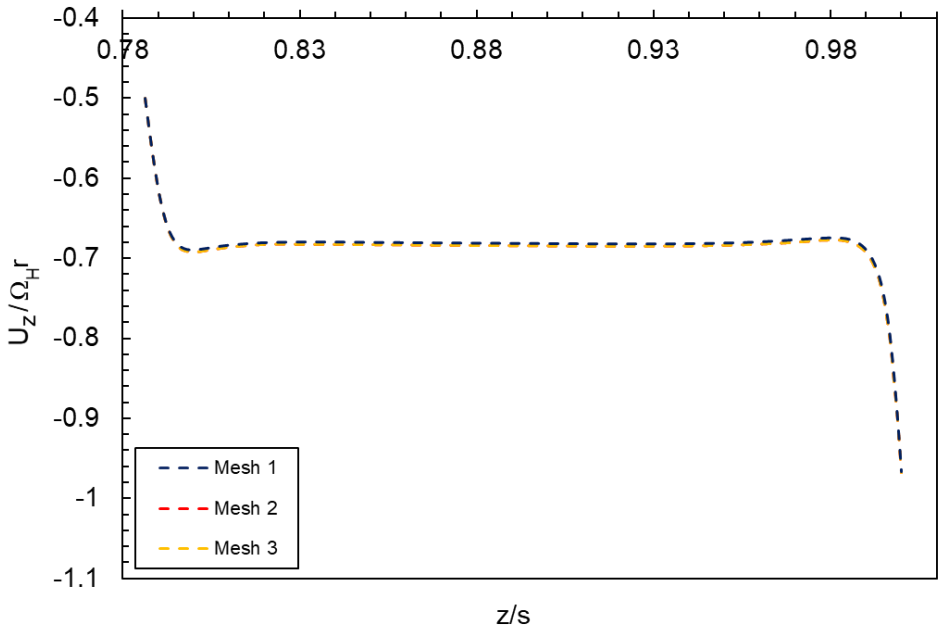


Figure 6-2: Comparison of meshes investigated for the single phase model in this study

Figure 6-3 illustrates the seal geometry domain modelled for the geometry under investigation. The poly-hexcore mesh shown has approximately 3.69 million cells and

was generated within Fluent-Mesher; it includes a uniform grid spacing in the *z*-axis, also parallel and normal to the rotating walls. For boundary conditions, housing and fin shafts were defined as rotating adiabatic walls rotating in the same direction.



Figure 6-3: Isometric view of poly-hexcore mesh used in the CFD study.

As illustrated in Figure 6-4 , the housing is represented by the outer wall denoted by 1 while the inner wall indicated by 2 refers to the fin. The air inlet was defined as a pressure boundary labelled as 3 and an air/oil pressure outlet, defined with an air volume fraction of unity in case of backflow, is labelled 4.

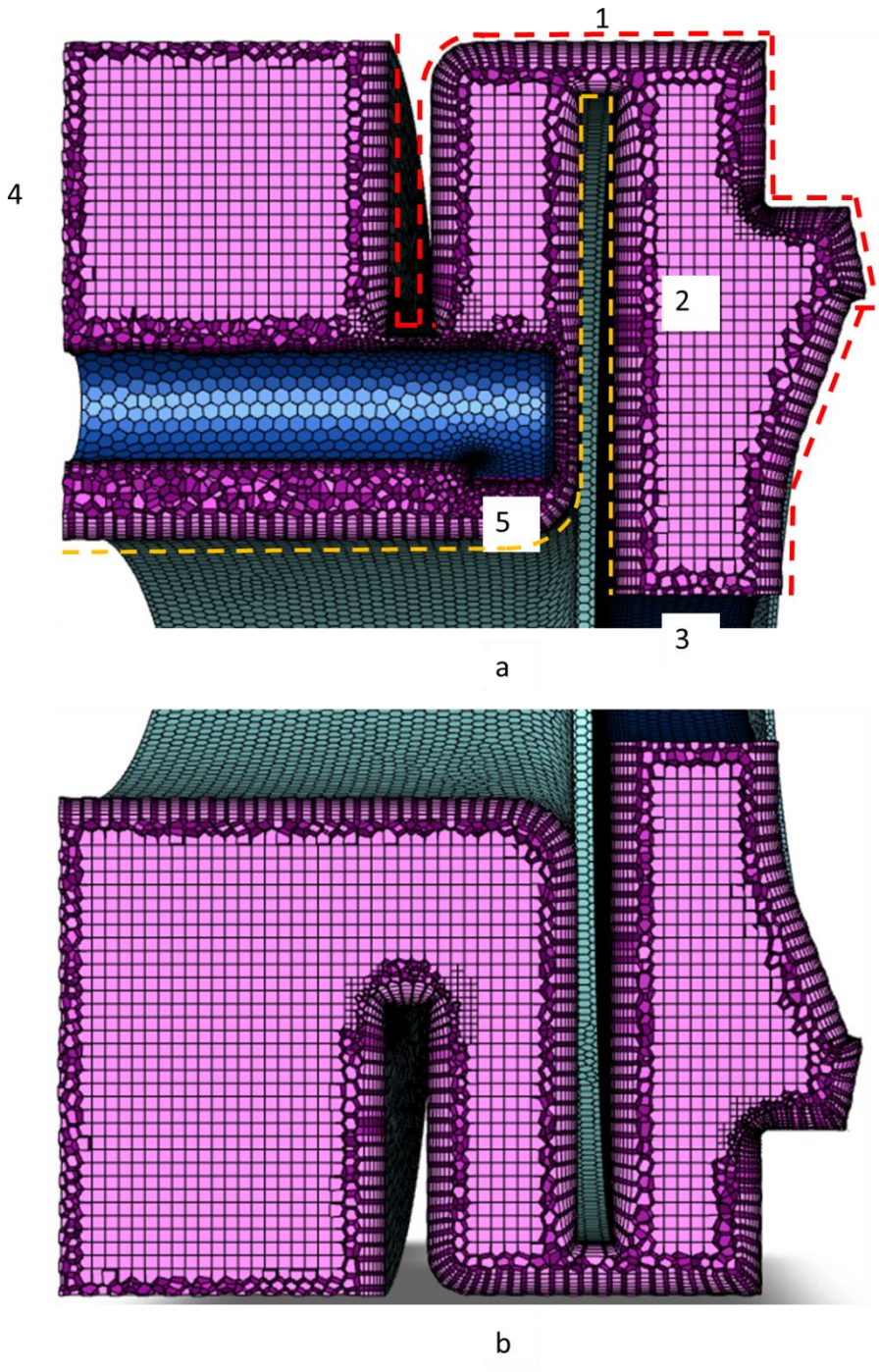


Figure 6-4: Cross-sectional xy view of the mesh used in the CFD study with the model boundary conditions numbered (a) top plane showing the nozzle (b) bottom plane

The extents of the boundaries of the outer wall is denoted by a red dashed line and the inner wall by a yellow dashed line on the top plane. To simulate the oil feed, an oil inlet denoted by 5 was introduced as a velocity inlet with a constant velocity of 15.3 m/s normal to the boundary to match the volumetric flow rate used in one of the experiments. For the two-phase study adaptive mesh refinement with two levels of refinement resulting in a final grid with 5,679,241 cells was used to achieve local refinement around the interface and ensure that the interface is solved adequately.

The first off-wall grid node in the principal area of interest is located at $y^+ < 1.2$ at the trough wall and $y^+ < 1.8$ at the fin wall. To accurately model the flow at the boundary layers and capture the wall effects, 8 inflation layers with a first cell height of 0.0001m were added at the trough and fin walls. To ensure additional accuracy around the critical parts of this seal geometry, a region of higher refinement was applied around the nozzle and the oil path as illustrated in Figure 6-5.

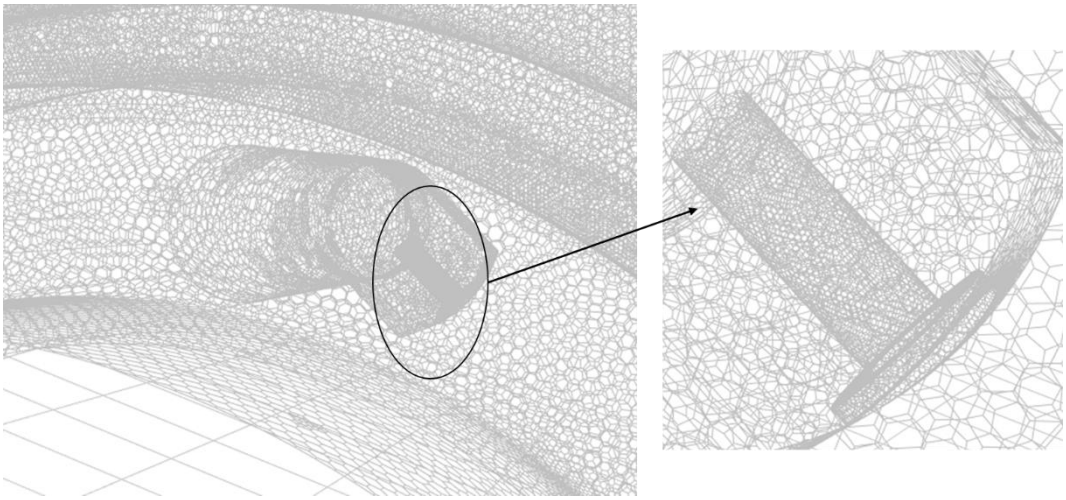


Figure 6-5: Region of local refinement around the nozzle and oil path

6.4 Investigation into the impact of jet on the pool of oil in through

To investigate the flow behaviour within a seal when an oil feed in injected, computations were conducted for housing and fin shaft speeds of 4000 and 2000 rpm respectively and with the fin central to the trough for a differential pressure of 0.2 bar across the seal. A continuous through-flow oil feed at 1.62 l/min flow rate through a 0.0015m sized jet diameter was added to the seal to replicate the oil supply into the seal. To achieve a continuous through-flow of oil, the case was run until the spill over occurred all around the trough rim. These test case conditions were simulated numerically so that the CFD results could be compared and verified against the data obtained through a series of experiments implemented as described in Section 6.1. Discussed in this section are the results obtained from the numerical study.

A volume fraction contour plot when the flow field has reached quasi steady state at a differential pressure of 0.2 bar is illustrated in Figure 6-6. Here quasi steady state refers to the state of the flow when the temporal variations of monitored flow parameters at a spatial location are much smaller than the spatial variations that it can be considered constant. As seen in Figure 6-6, a much higher differential pressure can be sustained by this seal as the oil level in the HP chamber has only risen up to half of the fin height. It is also apparent that the oil has begun to spill over from the LP side and that the interface is not completely flat but shows a degree of slant especially closer to the rotational walls (fin).

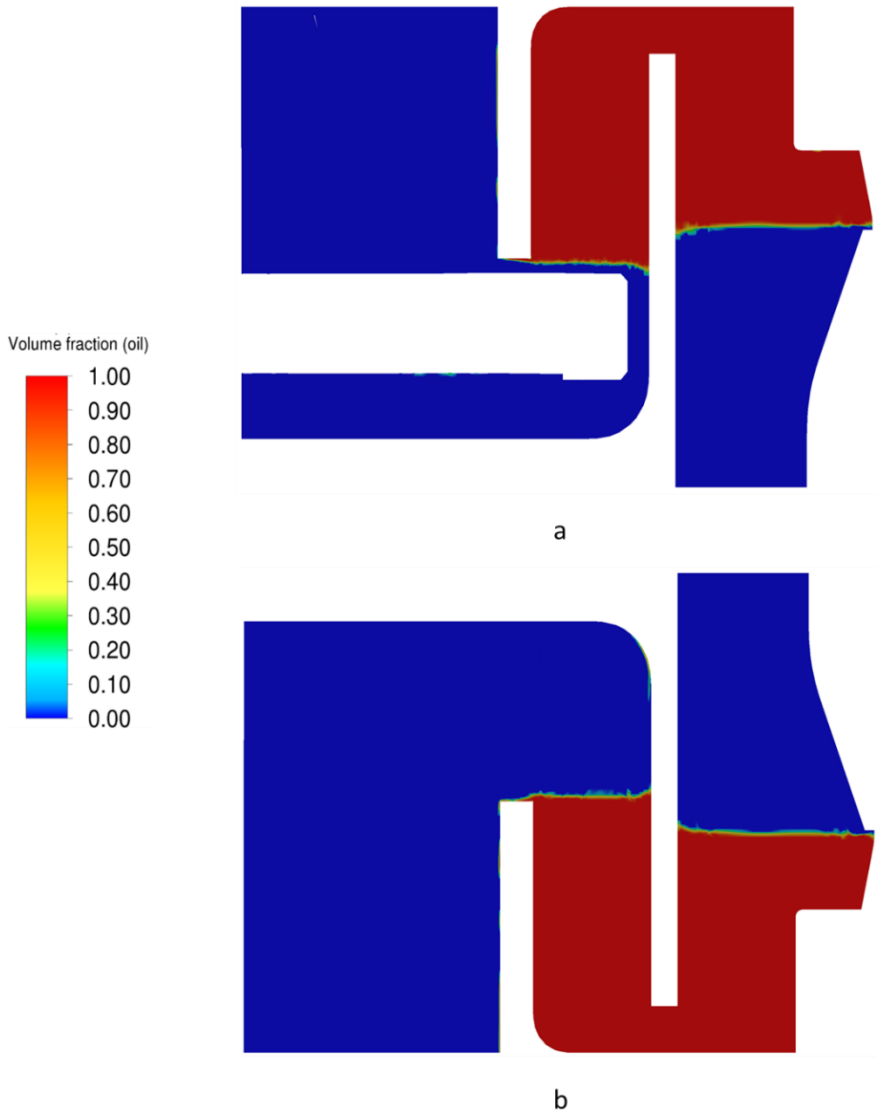


Figure 6-6: Contours of oil volume fraction at Ω_H = 4000 rpm and Ω_F = 2000 rpm for a seal with an oil feed rate of 1.62 l/min and an operating pressure of 0.2 bar when fin is positioned at s/w_H = 0.5 (a) cross-sectional view of xy top plane (b) cross-sectional view of xy bottom plane

The fluid is rotated radially outwards on the trough due to its higher rotational speed and this effect accounts for the deformation of the oil/air surface. The greater rotational speed of the trough gives a slight rise to the interface closer to the trough wall and a dip

at the fin as it is the slower rotating component. This is a flow feature that was observed in previous 2D axisymmetric work when there was no oil feed modelled. Therefore, it can be said that the oil feed does not affect the shape of the air/oil interface.

6.4.1 Jet behaviour

6.4.1.1 Jet impact on the oil in the trough

The CFD study investigating the jet impact on the oil in the trough was initially carried out in test phase modelling only the jet flow to ensure that the jet is formed appropriately. Once this was achieved, the simulation was re-run by patching in a volume of oil in the trough. The process of jet formation, impingement and its impact on the pool of oil in the trough is captured in a series of images as illustrated in Figure 6-7 and Figure 6-8. It can be seen that a long, continuous jet is formed delivering almost all of the oil into the trough.

During the experiments, the oil jet was initially characterized outside of the test chamber at different oil flow rates and temperatures. The oil jet behaviour was captured in a series of high-speed videos. The oil jet was pointed downwards in the direction of gravity without crossflow. Due to an unanticipated design flaw, a suitable jet was only maintained at an oil flow rate of 1.1 l/min and an oil temperature of 30°C. As the oil flow rate or temperature increases, a fan type jet forms as illustrated in Figure 6-9a. The objective of the jet characterization was to identify only the flow conditions that provide 100% trough capture efficiency where the jet is fully targeted inside the trough.

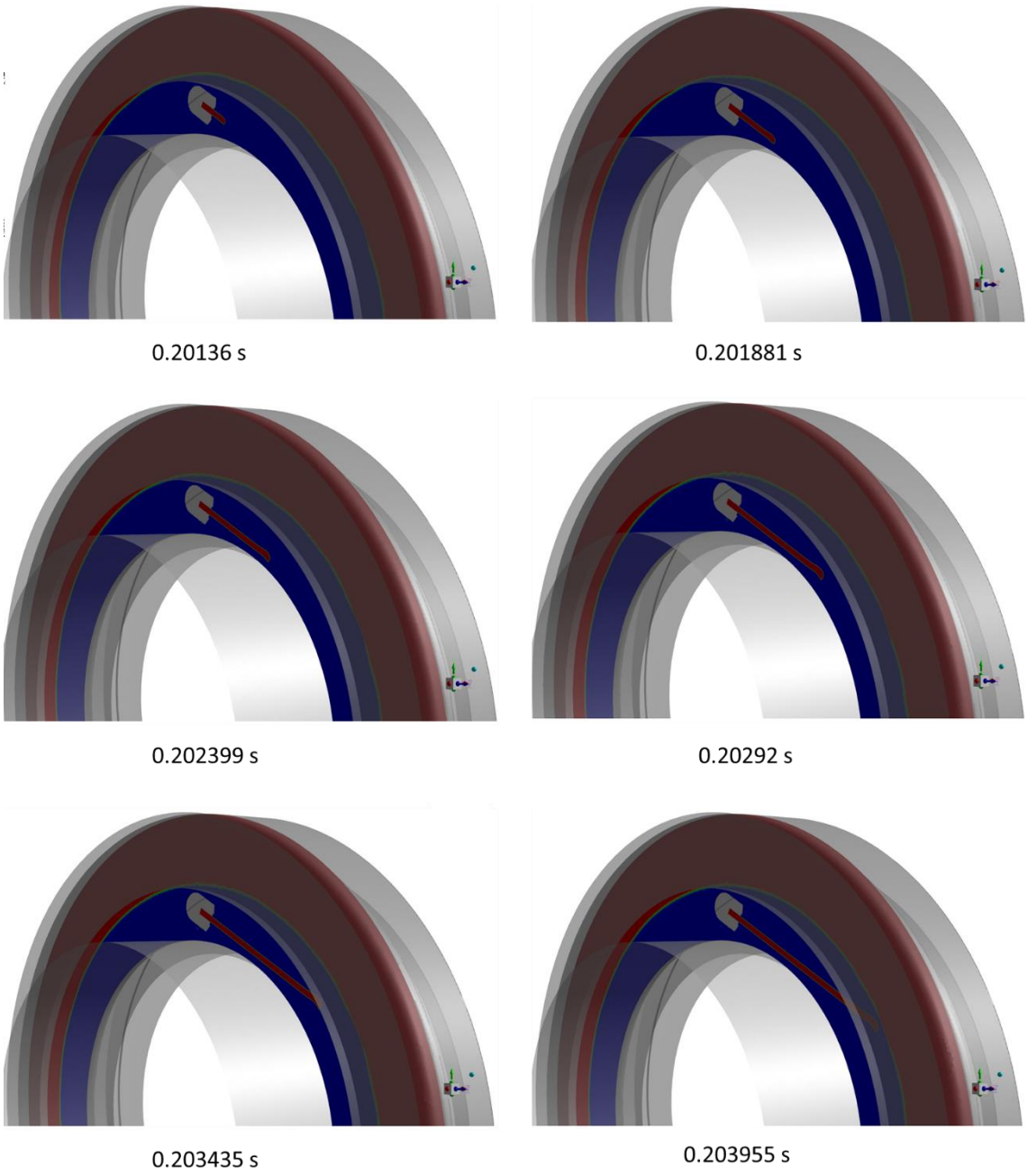


Figure 6-7: CFD images of jet behaviour before the jet impinges on the oil pool captured during the study at various time intervals. Background colour shows the oil volume fraction with oil phase represented by red.

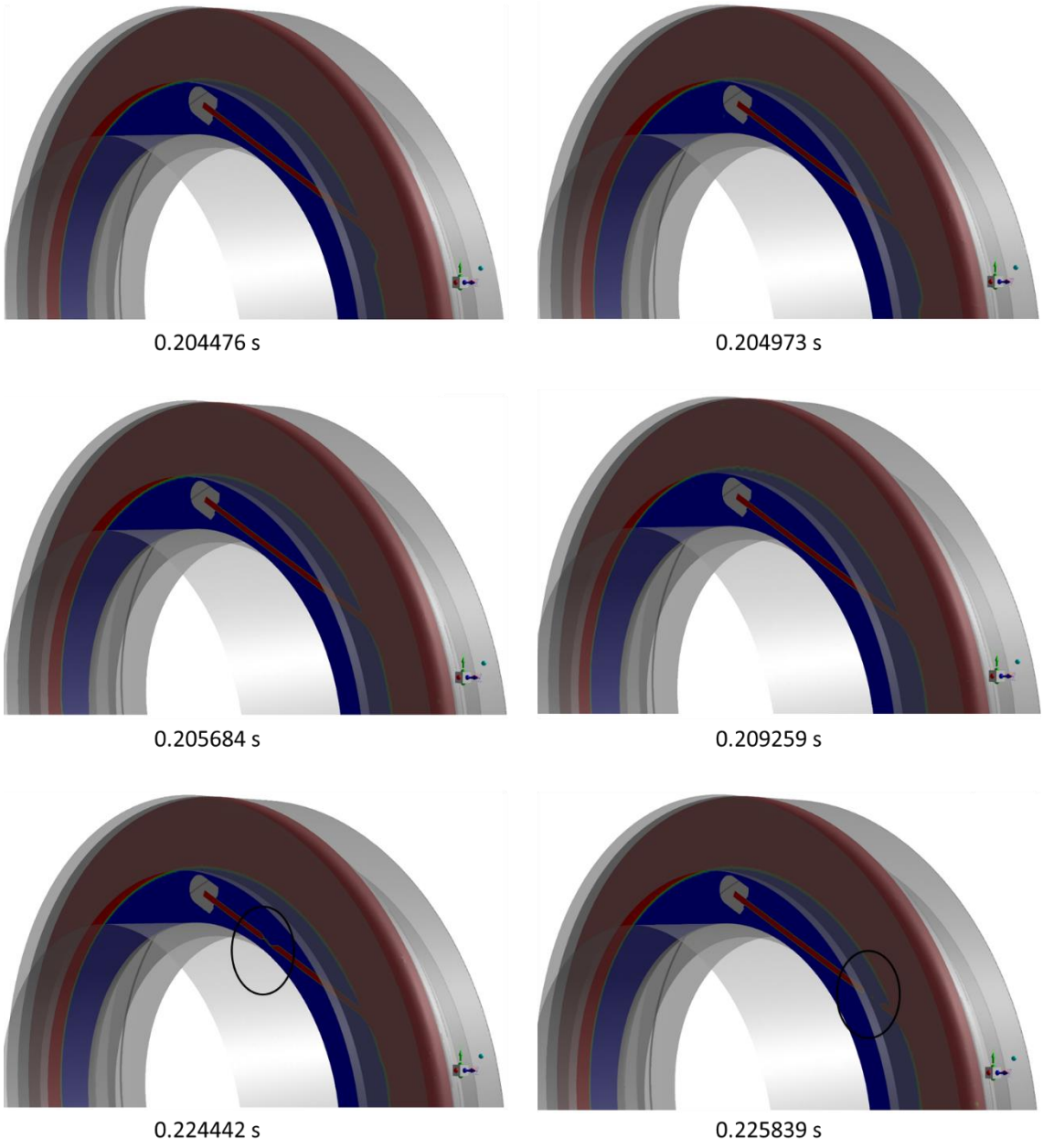


Figure 6-8: CFD images of jet behaviour after impingement illustrating the impact on the oil pool at various time intervals with instabilities highlighted

Consequently although the CFD calculations were conducted with a flow rate of 1.62 l/min, the experiments reported in this thesis, used to validate the CFD predictions were

conducted with 1.1 l/min and the jet formed is as shown in Figure 6-9b. Due to the high computational cost associated with this 3D study as stated in Section 6.2, a second CFD investigation replicating the experimental conditions could not be carried out.

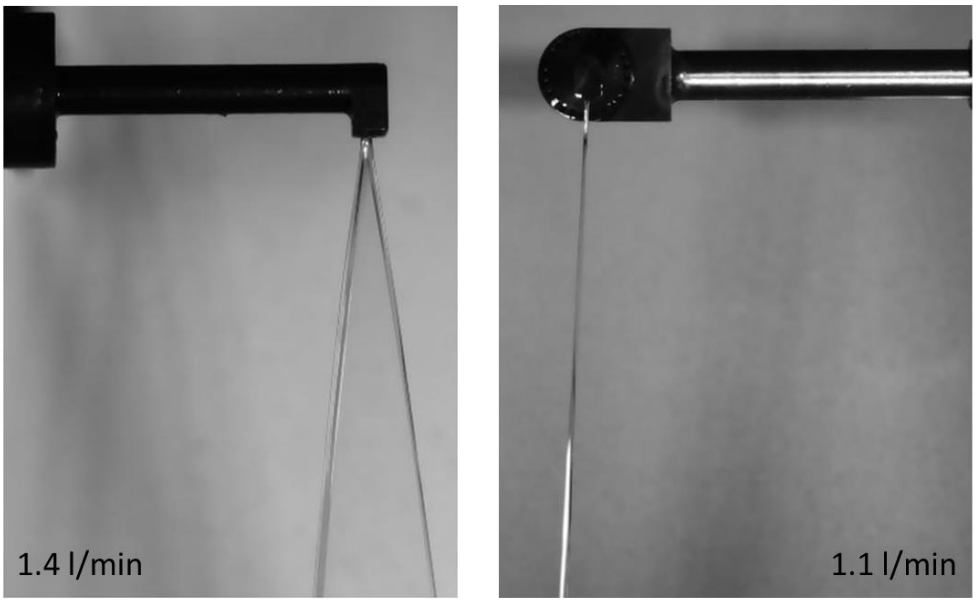


Figure 6-9: Comparison of jet behaviour illustrating two orthogonal views of the oil jet images captured during the experiment (a) at a flow rate of 1.4 l/min; (b) at a flow rate of 1.1 l/min

The jet used in experiments acts as a continuous jet for most part until the break-up of the liquid jet occurs further downstream of the nozzle. A similar breakup pattern was not observed in the CFD simulations as the jet functioned as an impinging jet. However, it can be seen in Figure 6-7 that an instability occurs towards the latter part of the simulation around 0.224 s, once the oil has been delivered into the trough. This seems to be an instability caused by a numerical artefact rather than an aerodynamic instability. Figure 6-10 obtained from the CFD study, captures an instance of this

instability at a flow-time of 0.294s which maybe a start-up feature of the jet as a fully developed flow was only achieved around 0.3s of flow-time. The modelled jet is therefore consistent with anticipated behaviour and also consistent with the requirements of a typical jet used in hydraulic seal applications.

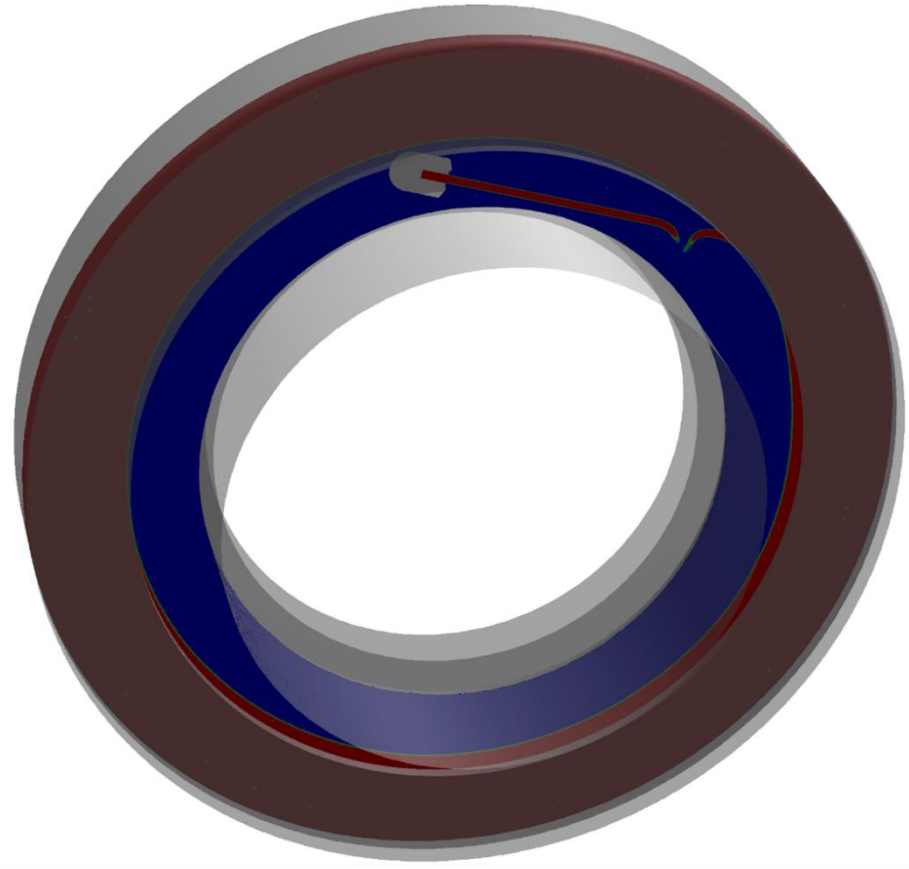


Figure 6-10: Oil jet instability likely caused by a start-up feature captured around 0.294 s illustrated on a cross- sectional view of the nozzle in *yz* plane from CFD simulation

The current work investigates the oil flow breaking up into droplets/ligaments followed by the oil film formed around the circumference of the trough using a VoF method when an operational differential pressure of 0.2 bar is maintained across the seal. When

exiting the nozzle, the liquid jet accelerates through the orifice consequently causing the ligaments to break up due to instabilities on the air-oil interface. Of particular interest in this current work is the impact of the oil jet on the oil in trough. In an attempt to present the effect of the jet on the axisymmetry of the modelled oil/air interface, the tangential velocities along iso-clips of angular co-ordinate at three circumferential locations were examined in the fully developed solution. The angular positions investigated are shown in Figure 6-11.

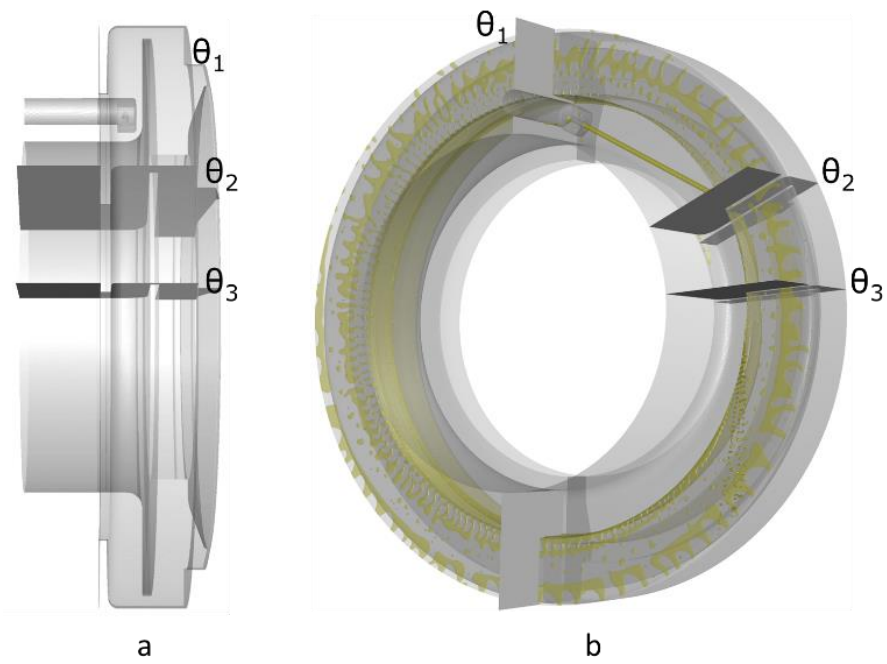


Figure 6-11: Angular locations investigated to obtain tangential velocity profiles (a) front view (b) isometric view of angular planes plotted on contours of iso-surface of oil volume fraction, $\alpha_{i,VF}$ = 0.5

Non-dimensionalised tangential velocity distribution from the housing to fin in the LP chamber plotted along the intersection between the planes shown at angular locations $\theta_1, \theta_2, \theta_3$ and the oil film is presented in Figure 6-12. θ_1 represents an angular

position upstream of the point of impact, angular location θ_2 denotes the position at which jet impingement occurs and θ_3 has been chosen to represent a downstream location but not too far from the point of impact. The surface of the housing is at z/s = 0.7 and the surface of the fin is at z/s = 1.

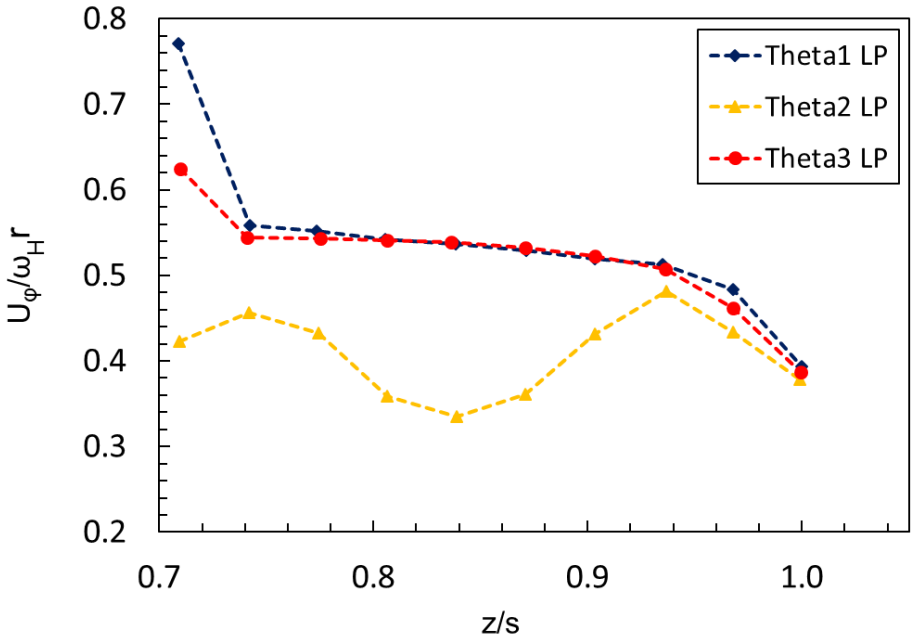


Figure 6-12: Tangential velocity profiles along angular co-ordinate iso-clips at intersection between oil column and angular locations shown in Figure 6-11.

While the tangential velocity profiles obtained at angular locations θ_1 and θ_3 exemplify identical core flow velocities, the tangential velocity profile at θ_2 records velocity values lower than those observed at θ_1 and θ_3 with the lowest velocities in the central core region. The loss of momentum on the oil film as a result of impingement causes this deceleration. Similar flow profiles and flow physics at two angular locations

upstream and downstream of the jet impact point confirm that the effect of the jet on the axial symmetry about the x-axis is negligible.

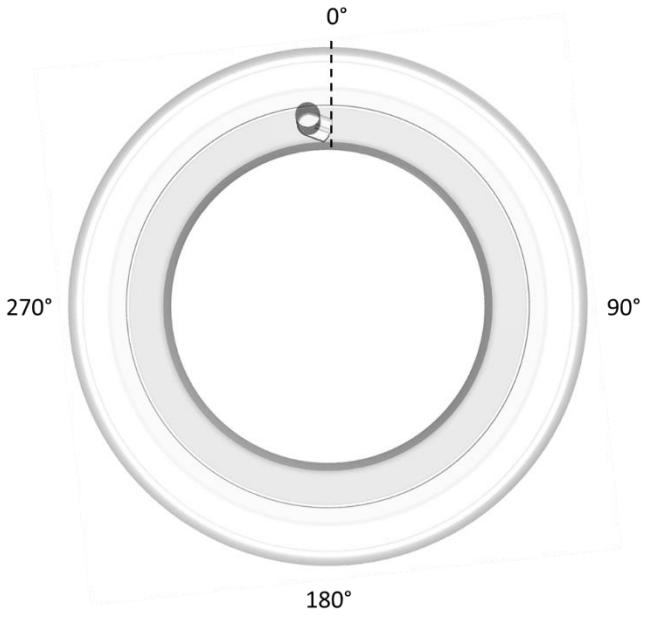


Figure 6-13: Angular locations of the trough relative to nozzle placement for measurement of oil pool thickness

As a part of the study, the effect of the oil jet on the depth of oil in the trough was also investigated. The angular orientation used to plot the film thickness measurement is illustrated in Figure 6-13. As the oil jet impinges on the oil volume in the trough, the surface of the oil pool is affected, impacting the height of the existing oil which also leads to a deformed interface between the oil and air phases. A graphical illustration of this phenomenon is presented in Figure 6-14 where a point just before impingement, soon after impingement, and surface variation after the impact is demonstrated.

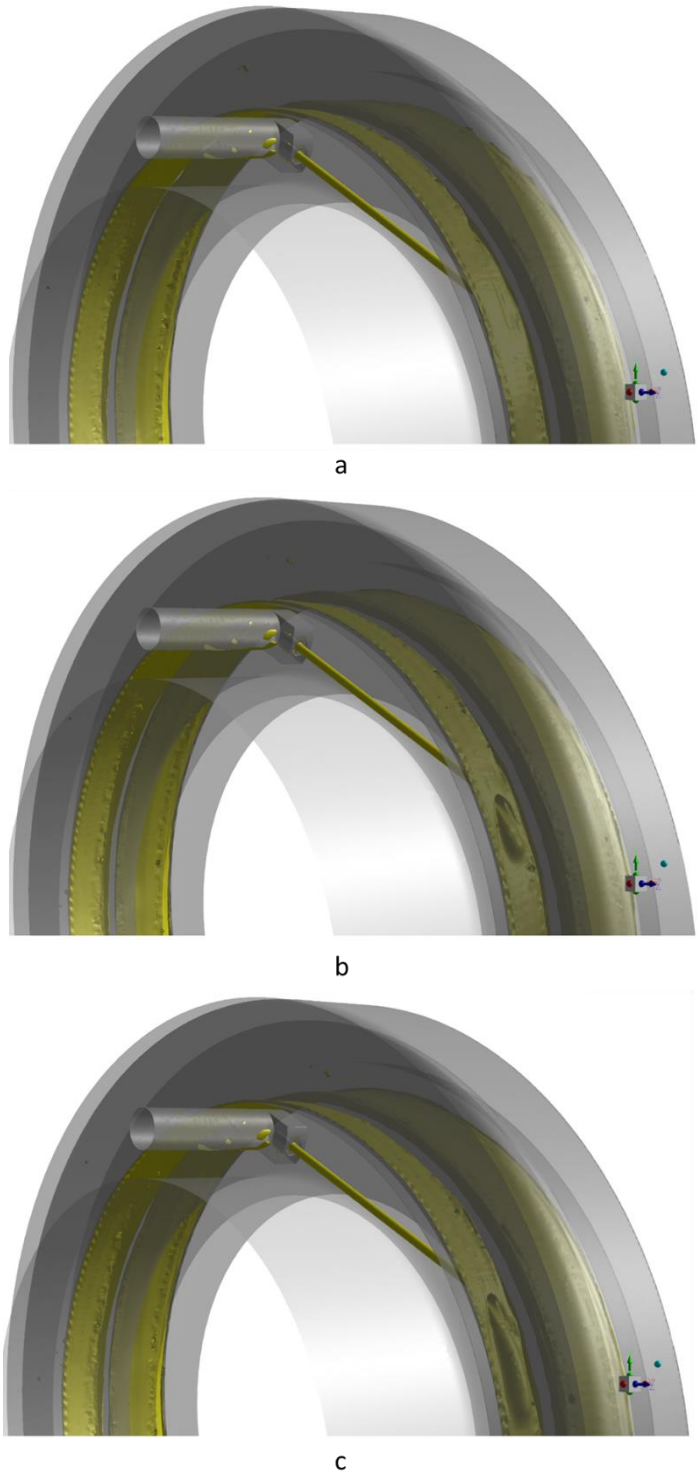


Figure 6-14: The impact of jet on surface of oil volume in the trough (a) before impingement; (b) soon after impingement around 0.204s; (c) subsequent variation in oil surface plotted on contours of iso-surface of oil volume fraction, $\alpha_{i,VF}$ = 0.5

A qualitative representation of the oil distribution around the trough wall is illustrated in Figure 6-15. This Figure presents the contours of the iso-surface of oil volume fraction, $\alpha_{i,\mathrm{VF}}$ = 0.5 along the trough wall, for the angular region 0° < θ < 360°. It can be observed that the oil film extends along the entire circumference of the trough and how the oil film thickness varies considerably immediately downstream of the impact point.

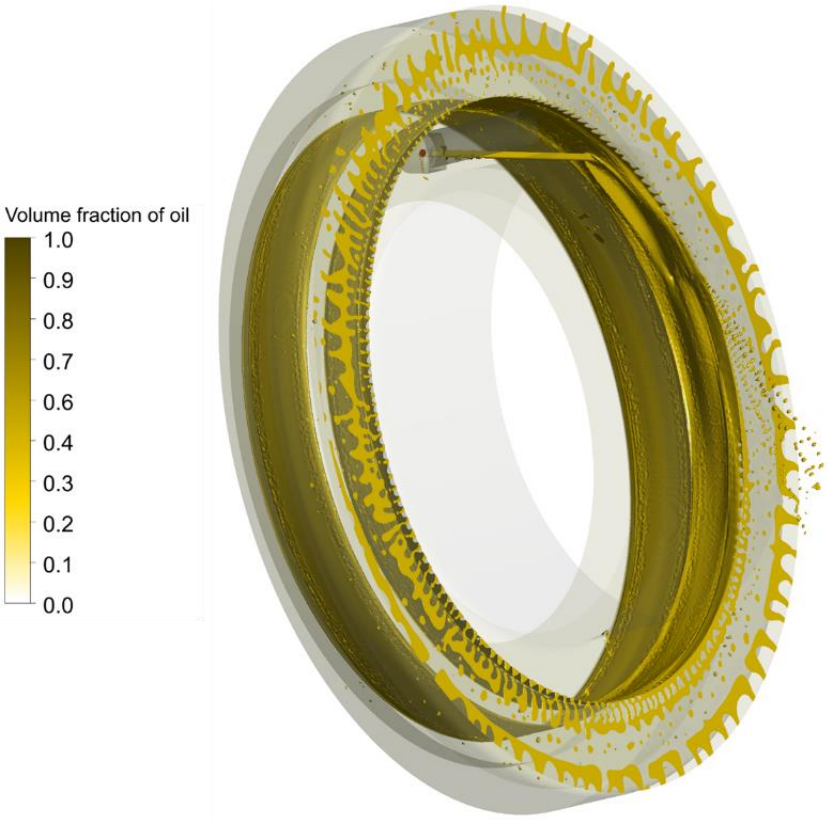


Figure 6-15: Contours of iso-surface of oil volume fraction, $\alpha_{i,VF}$ = 0.5

The variation in oil depth in the trough is shown graphically in Figure 6-16 where the y-axis plots the difference in non-dimensional oil depth, Δh^*, from the value at the overspill edge where h^*= 1 and Δh^*= 0, and the angular variable on the x-axis has zero

at the jet block location with jet impingement occurring at 75°. The non-dimensional oil depth, Δh^*, is the thickness of the oil pool along the trough calculated relative to the height of the uninterrupted surface which is the overspill edge. This can be expressed as $\Delta h^* = \frac{R_{oil\ in\ trough} - R_{overspill}}{2 * R_{jet}}$

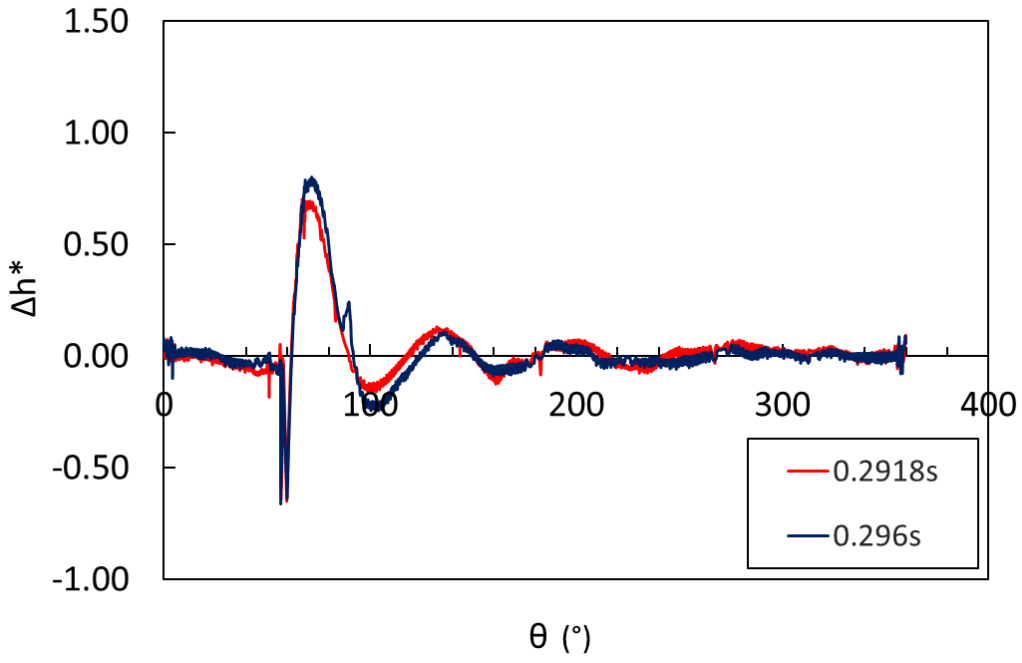


Figure 6-16: Comparison of oil distribution showing point of jet impact on the trough and variation of oil height around the trough

In the region between $0° < \theta < 75°$, upstream of the impact point, it is clear that the film thickness has not been affected. It can be seen that the greatest disturbance is caused at the point of impact at $\theta = 75°$ as a result of high momentum transfer from the jet to the oil film. A noticeable variation in the oil depth is observed in the region

between $75° < \theta < 180°$ as a result of the jet impingement. It is also evident that the oil depth does not vary significantly downstream of the second quadrant.

A fairly uniform oil depth is seen in the angular position ranges of 0° <θ < 75° and 180° <θ < 360°; the depth of the oil volume is only impacted by a negligible variation of +/- 0.1mm downstream. Therefore, it can be established that the jet impact on the depth of the oil film formed circumferentially along the trough is minimal.

6.4.1.2 Jet penetration

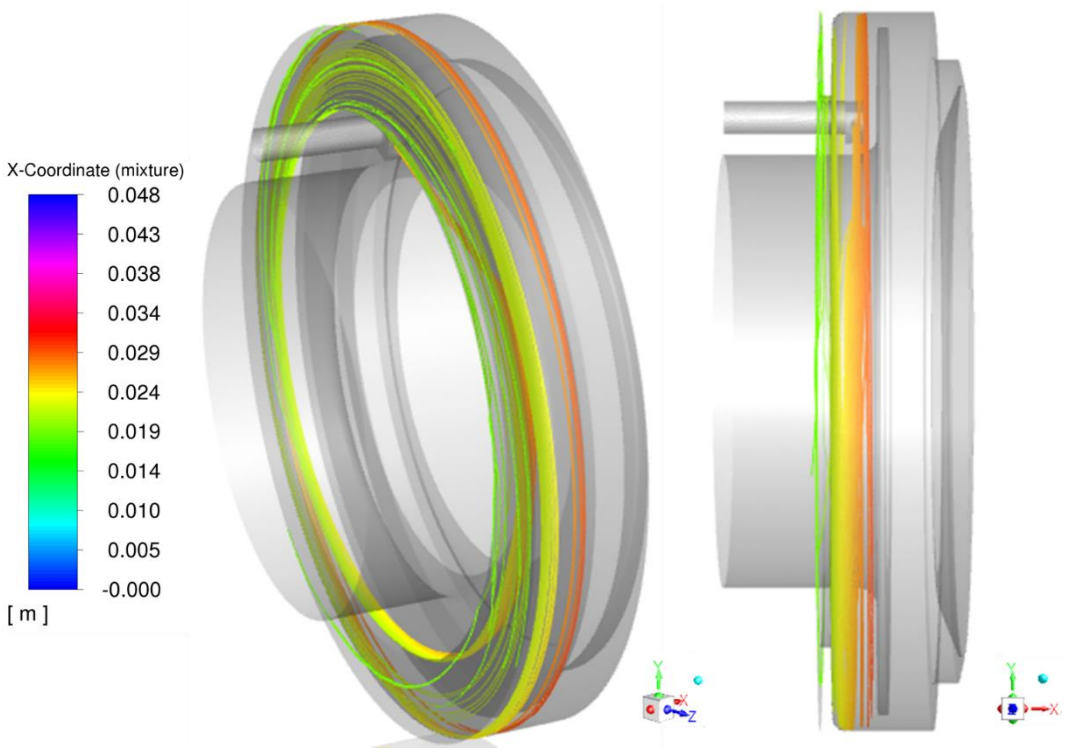


Figure 6-17: Pathlines coloured by the x-co-ordinate in the streamwise direction plotted from the oil inlet in the fully developed solution when t = 0.3 s

Figure 6-17 shows the streamwise (x-co-ordinate) penetration of the jet. It can be seen that the seal fills with the oil supplied through the jet and penetrates an axial distance of 0.03m forming a film around the trough. It is worth noting that the oil which sheds off the edge of the trough does not spray straight off the jet supply and resides in the seal before shedding. As the requirement of a continuous oil feed into the seal is to reduce the heat generation within the seal, it is essential that the oil supplied mixes with the oil existing in the trough so that the effects of the oil shearing phenomenon caused by the differential speeds between the rotating surfaces can be minimized.

6.4.2 Flow field Analysis

To investigate the influence of the secondary flow field in a hydraulic seal with a continuous oil supply, the in-plane velocity vector field plotted on a midplane slice at the angular location θ_2 in xy direction is presented in Figure 6-18. It can be seen that an outer recirculation zone is created in the LP chamber and can be characterized by the compactness and close proximity to the rotating shaft walls. The two regions are separated by the inflow of oil fed through the jet. It is interesting to note that the interchange of oil between the two chambers is minimal and the oil injected into the seal mainly resides in the LP chamber. Existence of recirculation zones is desirable as they provide long residence times of oil supplied into the seal. These low velocity regions provide stability in the flow and can assist with dissipating the heat evenly within the seal. A large recirculation zone is observed in the oil column in the HP chamber which suggests that a low pressure region is created immediately downstream

that would accommodate a higher differential pressure. This flow feature was also found in the 2D axisymmetric case without an oil feed when the fin was positioned in the centre.

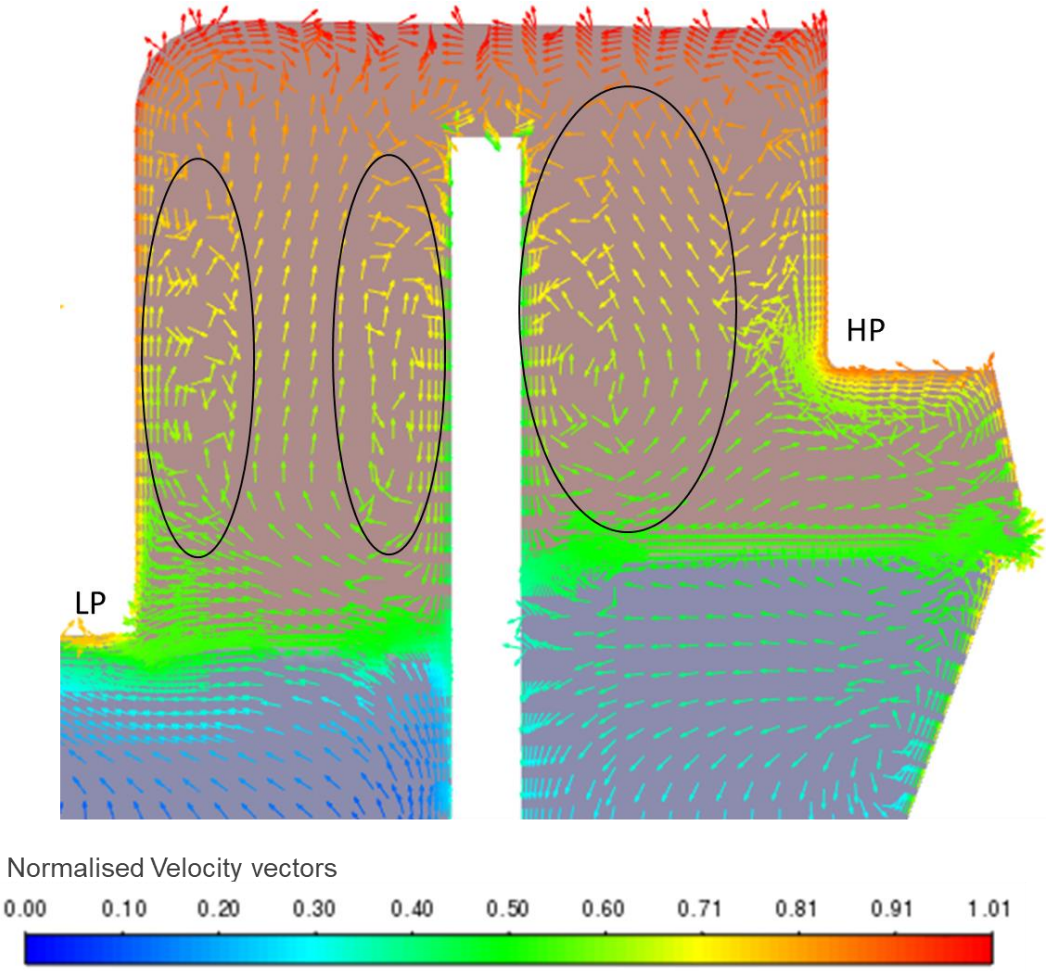


Figure 6-18: Normalised in-plane velocity vectors of the flow field highlighting regions of recirculation zones plotted in midplane slice at θ_2. The vectors on this plane have been coloured by velocity with the background colour indicating the oil volume fraction

6.4.3 Comparison against experimental results

6.4.3.1 Droplet shedding around the trough

In a hydraulic seal in operation, oil either splashes back from the seal during the jet fill process or is ejected from the seal on the LP side. This section reports a qualitative assessment of the droplet shedding behaviour around the trough obtained from the CFD study with a comparison against the images obtained experimentally. The oil flow behaviour at the bottom of the trough (approximately the 6 o'clock position) was visualised using an industrial rigid type of borescope.

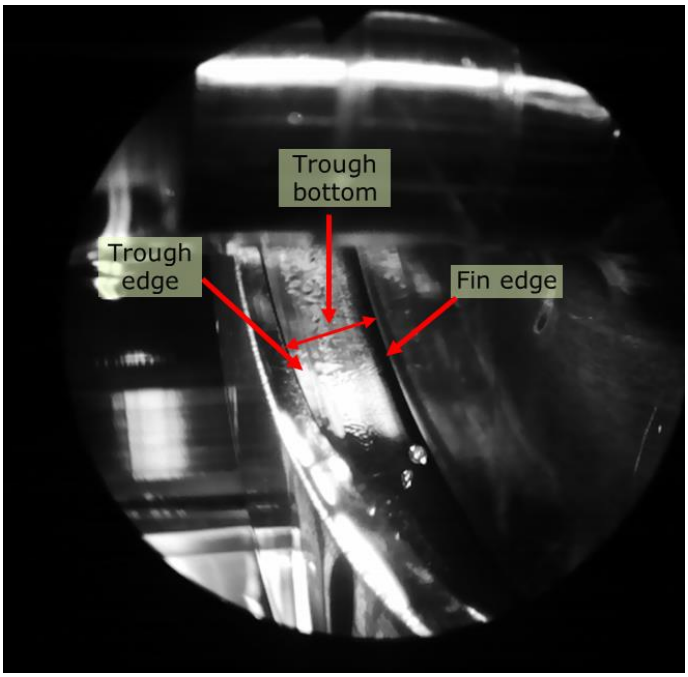
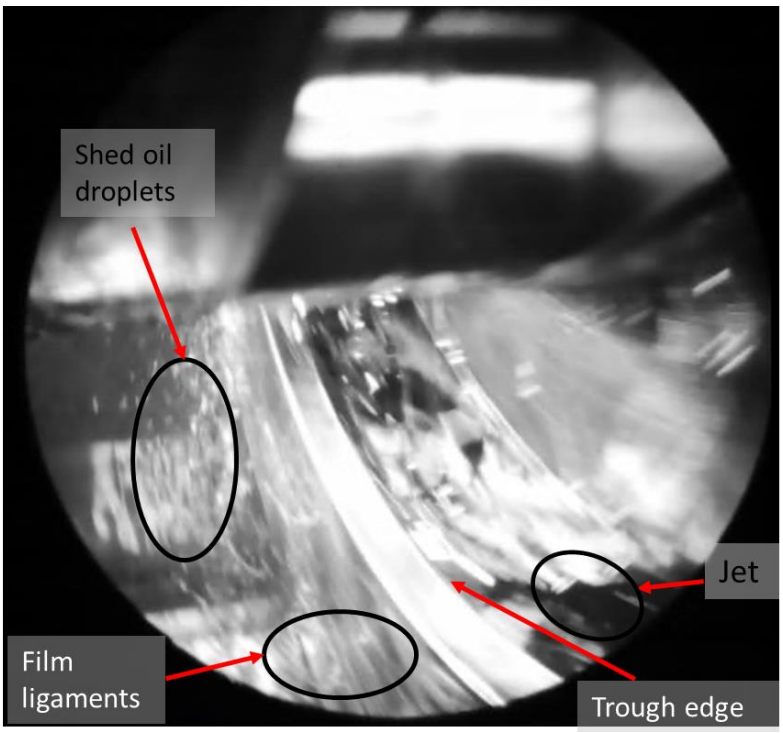


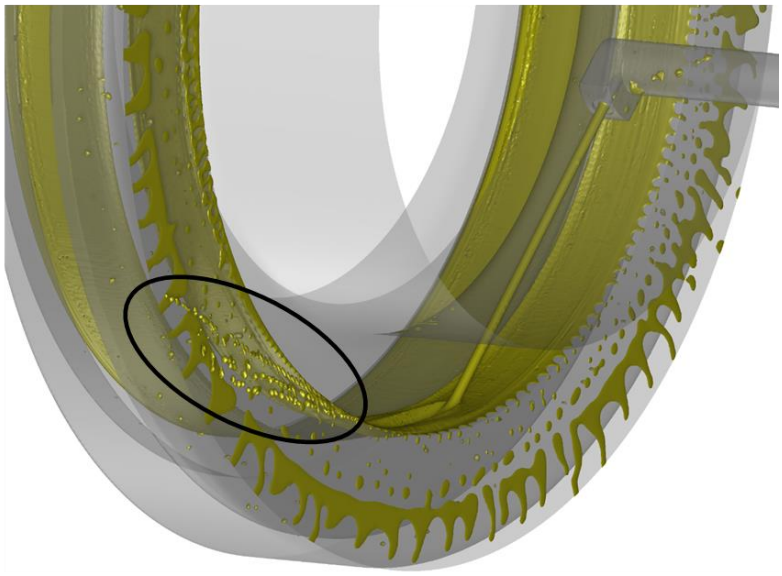
Figure 6-19: The view visible through the viewing tube in the experiments

The aim was to capture the behaviour of the oil free surface inside the trough and the oil spillage over the trough edge. The bottom side of the trough was the most suitable area for visual access where the area was illuminated from the front and back using LED lights. It was challenging to perform any optical calibration due to the restricted access, therefore all the visual data is used for qualitative description of the flow. Shown in Figure 6-19, is the view visible through the viewing tube in the experimental module. In this image the trough is not completely full.

The oil particles that do not adhere to the oil surface and are shed from the LP side are illustrated in Figure 6-20 and Figure 6-21. It is clear that ligaments form and droplets are shed from these into the chamber. Future CFD work should seek to characterize this oil shedding. Figure 6-20a shows the shedding behaviour around the edge of the trough bottom captured during the experimental investigation. Extremely similar flow behaviour is seen, creating confidence that CFD modelling can successfully capture this aspect of the flow behaviour. It is interesting to note the uneven shedding of oil to the surrounding areas in both images.



a



b

Figure 6-20: Oil Shedding from the edge of the trough (a) image of the view through the viewing tube obtained through experiment (b) contours of iso-surface of oil volume fraction, $\alpha_{i,VF}$ = 0.5 fraction plotted using CFD data

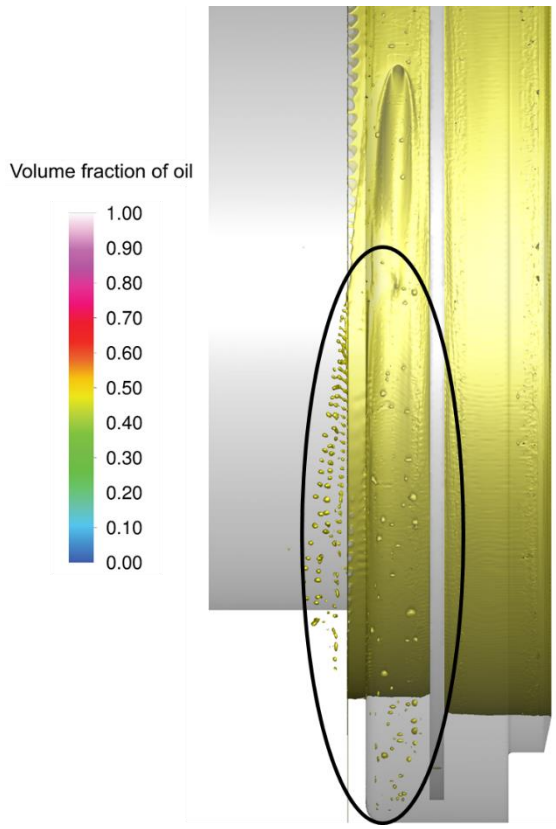


Figure 6-21: Front view of the hydraulic seal with contours of oil volume fraction displaying oil shedding behaviour

6.5 Thermal effects: oil related heat transfer

6.5.1 Numerical model formulation

As the present work aims to gain a deeper understanding of the thermal behaviour of the oil in the trough of a hydraulic seal, a parallel study investigating the oil related heat transfer was conducted. A 2D axisymmetric model of the same representative geometry

described in Section 6.2 was used in this study as the 3D investigation with an oil feed confirmed that the effect of the jet on the axisymmetry of the model is minimal.

To develop the thermal model for the hydraulic seal, an estimation of heat flux and heat transfer coefficient are required. As there is no record of heat flux or heat transfer coefficient data linked to hydraulic seals in published literature, this study used prior literature to estimate an approximate value for the heat transfer coefficient at the trough wall to compute the oil related heat transfer. To accommodate the heat loss from the trough walls to the atmosphere a convective boundary condition has been imposed at the walls in this study. As the trough wall is a thin wall with 0.005m thickness, only the 1D effect is considered.

The convective wall thermal boundary condition allows the heat flux to the wall to be computed by Fluent by using the external heat transfer coefficient and external heat sink temperature inputs as reflected in Equations (6-1) and (6-2).

$$\dot{q} = h_T(T_w - T_f) \tag{6-1}$$

$$\dot{q} = h_{ext}(T_{ext} - T_w) \tag{6-2}$$

An analytical correlation was used to compute the heat transfer coefficient for a disk rotating in air to determine an appropriate value for the external heat transfer coefficient from the trough to the surroundings. Cardone et al. [228] studied the heat transfer to a disk rotating in air for a wide range of Reynolds number values in the laminar,

transitional and turbulent flow regimes employing a heated-thin-foil technique and by gauging temperature maps with an infrared scanning radiometer to take measurements. By applying a linear regression to a sample of experimental data, they found that data fits the correlation below in the fully developed turbulent region.

$$Nu = 0.0163.Re^{0.8} \tag{6-3}$$

Looking to apply this in the case of a constant heat flux boundary condition, use is made of the fact that the temperature difference between the adiabatic wall, T_w, and ambient, T_a, conditions, $T_w - T_a$, is inversely proportional to the convective heat transfer coefficient, h_T. Relating this to the solution obtained by Northrop and Owen [229] for the boundary condition of a power law temperature difference ΔT, between disk and surrounding fluid for turbulent flow, the above relationship is modified to:

$$Nu = 0.0184.Re^{0.8} \tag{6-4}$$

This study by Northrop and Owen [229] concluded that the natural convection effects could be neglected for the rotational speeds tested as the obtained experimental results were identical for the two disks perpendicular to the direction of the gravitational force and disks facing downwards, parallel to the direction of the gravitational force. Heat transfer was modelled in the present study by applying Equation (6-4) to yield the heat transfer coefficient.

6.5.2 Numerical study and Validation

In an attempt to verify and validate the numerical results against the experimental data, numerical simulations were conducted for an experimentally investigated case in which the trough rotational speed was 10000 rpm and fin rotational speed of 1780 rpm. The CFD study looked at a steady state case with an existing oil volume at 60°C in the seal. This is an arbitrary estimate with the logic that the oil in the trough has to be hotter than the oil that is delivered into the seal as no thermal data was available at the time the numerical modelling began. The air volume in the seal was modelled at 27°C. A velocity inlet was added to replicate the oil jet that was used to supply cooler oil at 40°C to the seal at a feed rate of 1.1 l/min. Here the computed velocity is such that it matches the flow rate of the oil delivered through the jet diameter in the 3D numerical investigation. An operational seal pressure of 2 bar was maintained to be consistent with the experimental procedure. In the CFD simulation, this was implemented by increasing the seal differential pressure in increments of 0.5 bar to ensure the numerical stability of the model. The same methodology developed in Section 5.4.2 has been adopted here to increase the differential pressure across the seal systematically. A fully developed solution was achieved within a total flow time of 11.3s.

The case was set-up using the same approach described in Section 6.2. To account for the viscous heating generated within the seal due to the oil shearing, appropriate thermal boundaries should be implemented in the numerical model. An adiabatic wall condition was assigned at the fin assuming no heat was transferred by the fin to the oil due to the

smaller wetted area. To account for the heat loss from the walls to the air domain, a convective thermal boundary imposed at the trough wall. This thermal boundary condition only considers the 1D effect as this is a thin wall. The convective wall thermal boundary condition allows the heat flux to the wall to be computed by Fluent using the external heat transfer coefficient and external heat sink temperature inputs. The external heat transfer coefficient has been specified so that the heat flux from the fluid to the wall is solved implicitly by Fluent. The external heat transfer coefficient was determined using an analytical correlation reported in published literature as explained in Section 6.5 and computed to be approximately 1164 W/m^2K which has been imposed at the trough walls. This was done to simplify the modelling approach with the same accuracy as that obtained through modelling conjugate heat transfer by considering solid parts. In this case, conjugate heat transfer modelling was not required as the trough wall is very thin so that the temperature difference across the inside and outside of the trough wall can assumed to be insignificant.

The literature survey conducted during this study into establishing a thermal modelling approach to investigate the effect of the generated viscous heating suggests that the reported heat transfer coefficient value computed based on the analytical correlation given by Equation (6-4) provides a reliable base upon which the modelling could be developed. The model assumes that heat transfer occurs mainly by convection. Radiation was neglected, due to the low temperature differences between the trough wall in the rig arrangement and its surroundings. Conduction of heat was also ignored for simplification purposes as the fin is attached to one end of the inner shaft and the

heat transferred from the shaft to the fin can be assumed to be insignificant compared to that lost via convection as conduction of heat along the shaft is not constant.

6.5.2.1 Heat transfer characteristics within the seal

As discussed previously in Chapter 2, the main purpose of a continuous replenishment of oil in a hydraulic seal is to maintain the oil temperatures at acceptable levels as the shearing of the oil can lead to increased bulk oil temperatures. A continuous through-flow of oil encourages the heat to be dissipated evenly. This is largely determined by the amount of cooler oil circulation that occurs across the fin gap from one cavity to the other. To examine the effect of through-flow on heat dissipation within the seal, the flow field was analysed once the flow reached steady state conditions. The penetration of the oil feed into the trough is illustrated in Figure 6-22, where the coloured pathlines exemplify the path of the oil transferred across the seal. It can be seen that the majority of the oil feed travels along the trough wall with some mixing of oil occurring across the fin thickness although it is not a significant amount. The oil circulation within the seal observed in this study is consistent with the results obtained from the 3D study reported in Section 6.4.1.2.

Even though the injected oil is expected to mix with the bulk oil in the trough, due to the temperature differential in the oil, the denser, cooler oil is displaced to the bottom of the trough as it is the faster rotating element under the centrifugal forces as can be seen in Figure 6-22. This process could facilitate transfer of cold injected oil across the

fin clearance, forcing hotter oil from the HP chamber to the LP chamber and thereby enhancing heat dissipation from the non-feed side of the seal.

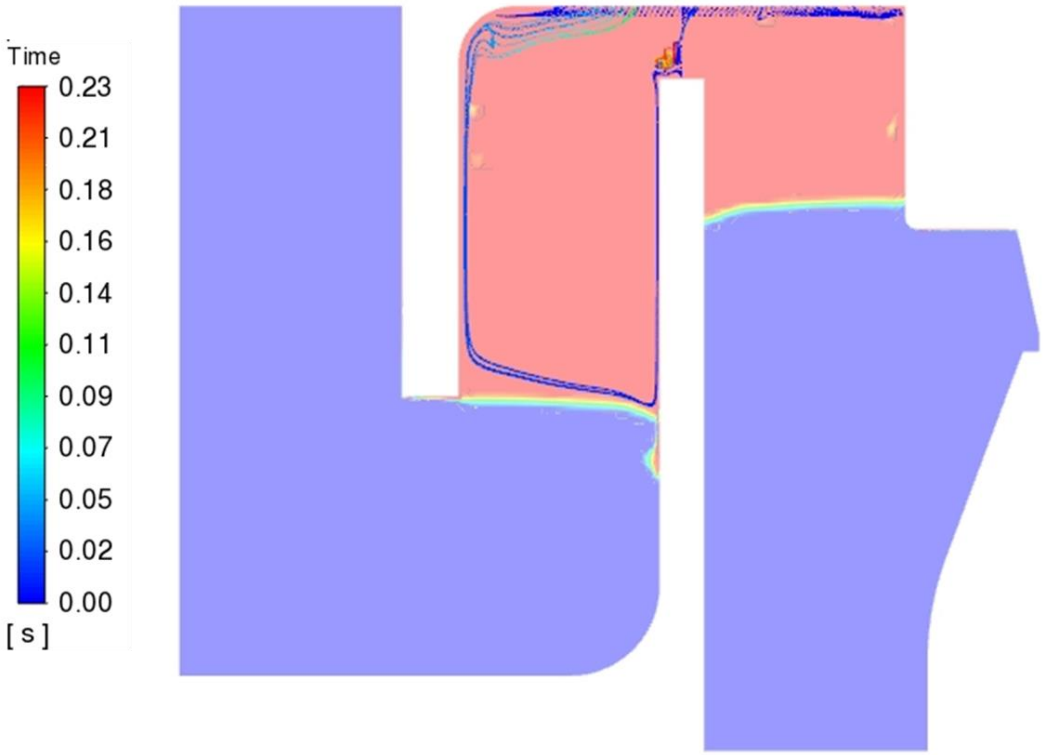


Figure 6-22: Illustration of oil feed penetration at Ω_H = 10000 rpm and Ω_F = 1780 rpm for oil feed rate of 1.1 l/min and an operating pressure of 0.2 bar with fin positioned at s/w_H = 0.5. Pathlines coloured by the particle time plotted from the oil inlet, across the fin and adjacent to the bottom of the trough with the background colour indicating oil volume fraction

The effect of oil circulation on the oil volume within the cavities either sides of the fin can be demonstrated through the temperature variation of the bulk oil reservoir. A velocity vector plot with the vectors coloured by the normalised static temperature of the oil columns is presented in Figure 6-23. The oil temperature here has been normalised by the temperature of the oil at the inlet. This Figure shows the existence of

secondary vortex flows on both sides of the fin generated as a result of the differential rotor speeds of the trough and the fin. These recirculation flows force the oil flow radially outwards along the side walls of the trough and inwards closer to the fin. Consequently extensive mixing of oil within the chambers either sides of the fin is expected.

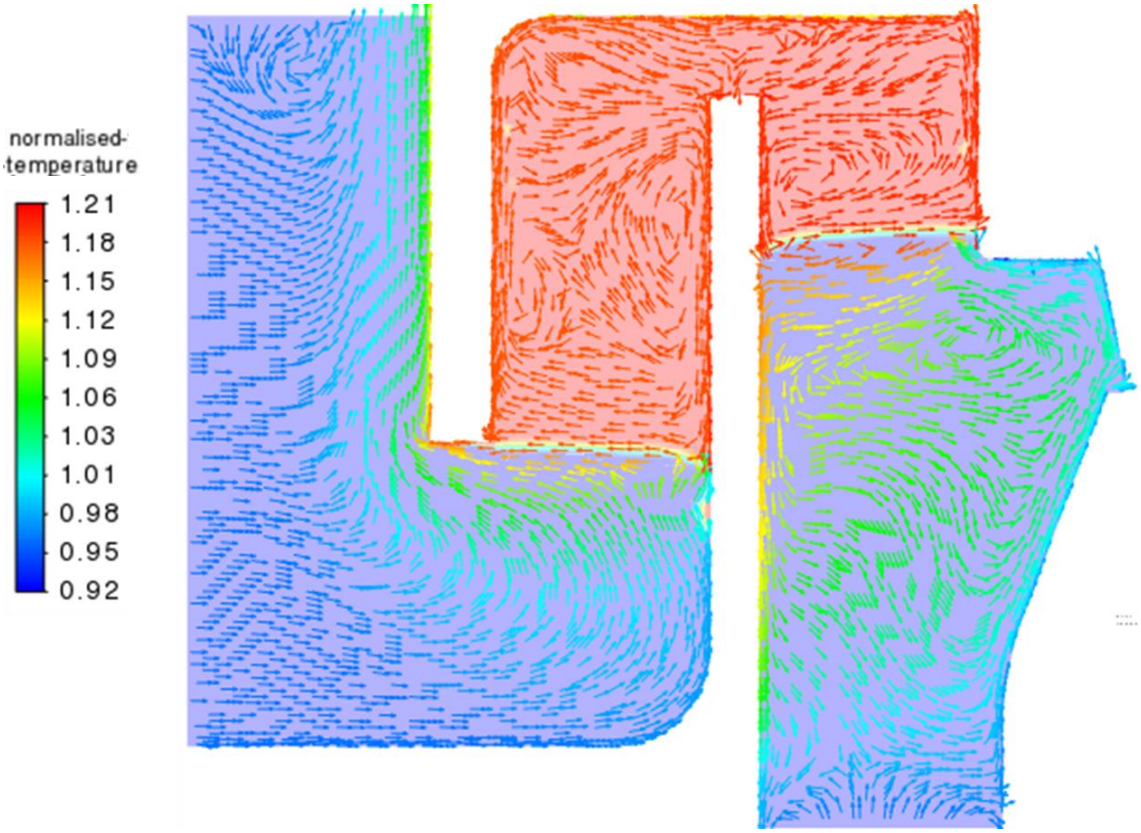


Figure 6-23: Normalised in-plane velocity vectors coloured by static temperature illustrating the temperature distribution within the oil reservoir when there is an oil feed with a rate of 1.1 l/min and an operating pressure 0.2 bar is maintained across the seal

However, in this case, it can be noticed that most of the cooler oil from the feed mixes with the oil in the low pressure chamber and that not much oil circulation across the

radial gap has occurred. A reason for this could be that the radial gap between the trough and the fin in this seal is relatively narrower compared to the configuration modelled in the study by Mathews et al. [27]. Although, a smaller gap is preferable for seal filling, it looks as though narrow gaps do not aid in heat dissipation as they can inhibit oil circulation. The difference in the bulk oil temperature in the two chambers is not substantial.

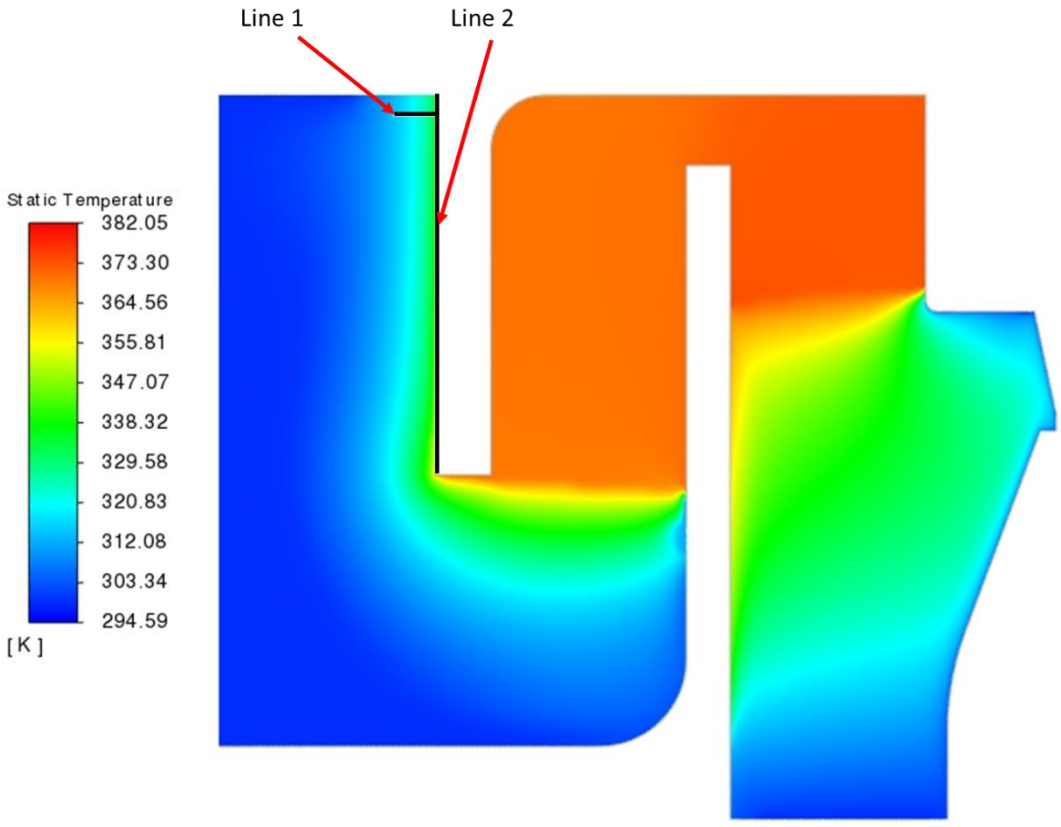


Figure 6-24: Contours of static temperature across the seal for an oil feed rate of 1.1 l/min and an operating pressure of 0.2 bar

By looking at Figure 6-22, it can be seen that most of the cooler oil from the inlet mixes with the hotter oil in the trough in the first 0.23s of the total flow time which was 11.3s.

Therefore, it can be said that most of the cooler oil delivered into the seal, sheds off the trough before entering the seal or circulating within the seal as further confirmed in Figure 6-23.

It is clear that the oil spill over which occurs at this point on the LP side leads to a reduction in the fin immersion which would aid in minimising heat generation on the other chamber where there is no oil in-feed. This explains why there is no large temperature variation across the fin gap in the oil columns in the two chambers. This is visible in the contour plot of static temperature within the seal as depicted in Figure 6-24 and the temperature profiles presented in Figure 6-25.

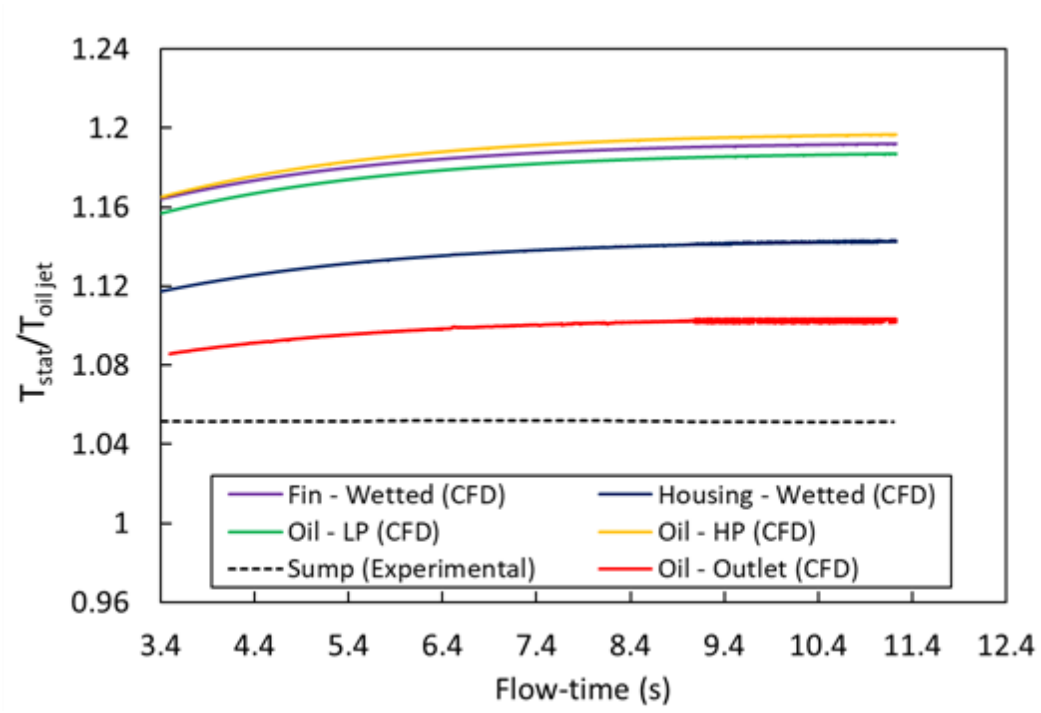


Figure 6-25: Comparison of temperature profiles for experimental/numerical tests when shaft rotational speeds = 10000rpm, 1780rpm; seal operational pressure = 2 bar; oil feed rate = 1.1 l/min

Figure 6-25 presents the static temperature results measured at the fin, trough and along the centreline in the oil columns in the LP and HP chambers once a seal operational pressure of 2 bar has been achieved. To obtain an accurate representation of the temperature profiles, only the wetted areas have been considered when measuring the average static temperature along the fin and trough walls. In the experimental set-up, a thermocouple in the sump measures the temperature of the oil entering the sump and the readings obtained are presented by the dashed line.

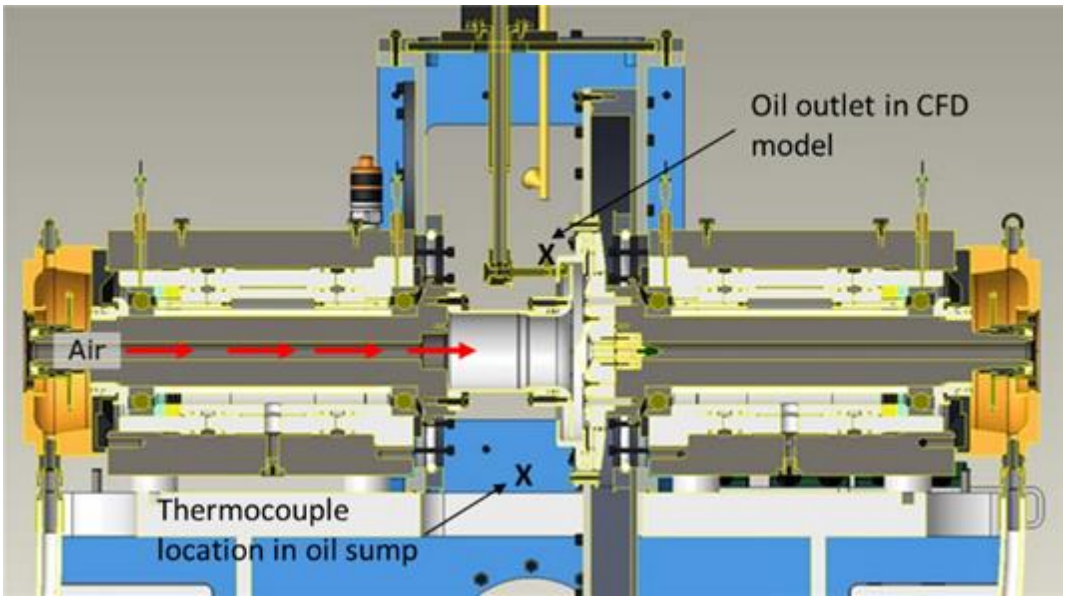


Figure 6-26: The locations of temperature measurements in experimental arrangement and CFD study

In the CFD model, the temperature of the oil closer to the model outlet was measured as the outlet was the most appropriate location being the point furthest from the seal to replicate the oil sump in the experimental arrangement. This location is indicated by the black axial line labelled as Line 1, at the radial location, r/R_H = 0.987, a little downstream of the model outlet shown in Figure 6-24; for comparison, the

measurement locations used in the both the experiment and CFD study marked by '*X*' are illustrated in Figure 6-26.

As seen in Figure 6-25, the bulk oil temperature in the LP chamber is lower than that of the oil volume in the HP chamber although the difference in temperature of oil in the two chambers is not large. This variation can be explained by the circulation of the oil feed flow as shown in Figure 6-23. It is interesting to note that a substantial amount of heat has been removed from the trough walls. This is as a result of the injected cooler oil feed being rotated radially outboard due to the faster rotational speed under centrifugal loading. The oil temperature in the sump is slightly lower than that recorded at the oil outlet in the CFD model. This is expected as the path of the oil exiting the seal is longer in the experimental arrangement and therefore would lose more heat to the surroundings through conduction.

Although a direct comparison cannot be made between the experimental and CFD results as a location equivalent to the oil sump does not exist in the CFD model, it can be seen that the oil sump temperature measured during the experiments is in the right order of magnitude as the temperature readings taken at the outlet in the numerical study. In an attempt to further ascertain the validity of the model, the effect of the radial location of the oil temperature measurement was investigated as the temperature of the oil has been measured a little downstream of the model outlet in this CFD simulation. This was achieved by measuring the static temperature of the ejected oil film along a radial line from the spill over point at the axial location, r/R_H = 0.77, to the outlet of

the CFD model. This radial line is shown as Line 2 in Figure 6-24. The computed temperature variation is presented in Figure 6-27.

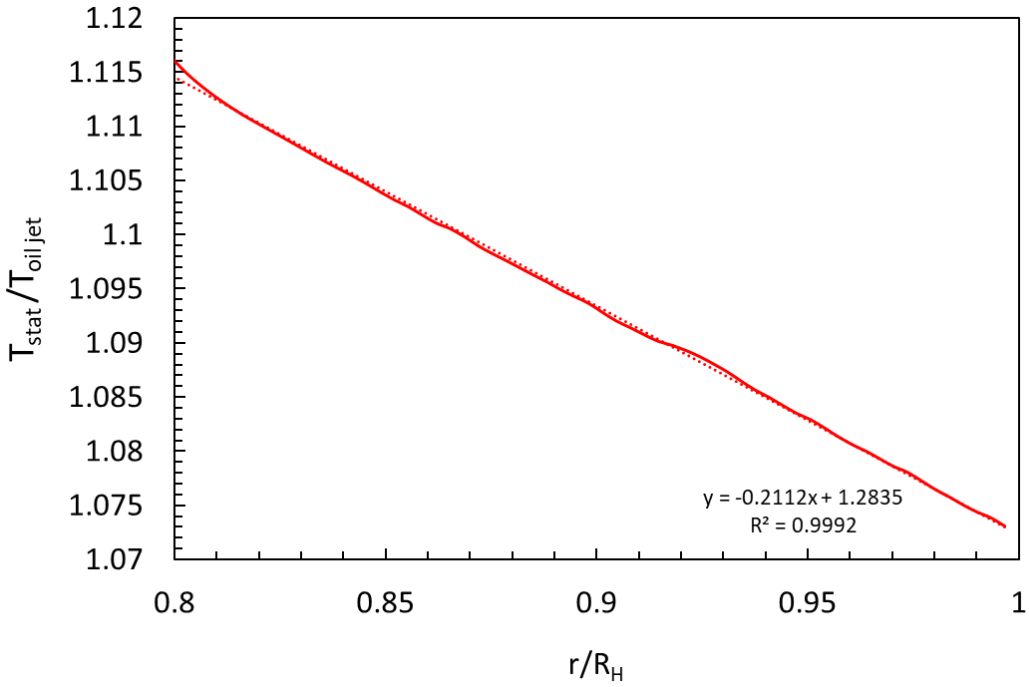


Figure 6-27: Radial temperature variation of the ejected oil film from the spill over point to the CFD outlet boundary

It can be seen that the heat loss is mainly linear as the oil that is spilled on the LP side reaches the outlet of the CFD model. The normalised temperature ratio at seal exit is approximately 1.07, recording a temperature of 336.03 K. The temperature profile has been normalised by the oil inlet temperature so that it can be compared to the experimental data. Once compared with the experimental readings of the oil in the sump, the difference between the experimental and CFD oil temperature data is 7 K, with the temperature at the seal exit in the CFD model being 7 K lower. In the

experiment it can be assumed that the oil that travels around the chamber walls lose to the atmosphere as the walls are in contact with the ambient temperature of the lab. This is fairly encouraging and gives confidence of the validity of the CFD model as an initial base for thermal modelling of hydraulic seals. However, the correlation used for the external heat transfer coefficient applied in this model was from a study which investigated the single phase flow in a cavity with rotating disk. Therefore, future models should account for heat transfer between the fin and the oil to represent a realistic condition and should include a sensitivity study to examine the influence of the heat transfer coefficient for further analysis.

6.6 Summary

Part one of the work presented in this chapter was conducted to investigate the performance of a seal with an oil feed with the aim of understanding the effect of jet on the behaviour of the oil in the trough. To accomplish this, a 3D model of a representative hydraulic seal geometry was examined in a numerical study in ANSYS-Fluent applying a VoF method for a trough shaft speed of 4000 rpm and fin shaft speed of 2000 rpm with fin positioned central to the trough.

A quantitative evaluation of the disturbance created on the surface by the jet which demonstrates that the greatest disturbance is caused at the point of impact and that the oil film thickness is only impacted by a negligible variation of +/- 0.1mm downstream. Predictions of the CFD simulation are consistent with the experimental observations. High quality CFD images providing a qualitative representation of the oil shedding

behaviour specifically the location of shedding, direction and velocity of shedding around the trough were compared with those obtained experimentally. A non-even oil shedding behaviour was observed in both the CFD simulation and experiment. The CFD results of the jet penetration indicate that the oil injected into seal does not spray straight off the jet supply but resides in the seal before shedding off the edge of the trough. The analysis into jet penetration and secondary flow field has demonstrated that the oil supplied from the jet assists in the heat management of the seal. Recirculation zones separated by the oil inflow are found in the secondary flow field which supports the hypothesis that a jet encourages even dissipation of heat within the seal. It was found that the influence of the jet on axisymmetry of the model is negligible.

Part two of the numerical study was conducted to investigate the oil related heat transfer within a hydraulic seal. The thermal model was developed using an analytical correlation in literature for the heat transfer coefficient for a disk rotating in air in order to estimate the heat transfer coefficient at the trough wall. The results show that the temperature of the oil reservoir in the HP chamber is only approximately 3 K higher than that of the oil in the LP chamber as a result of more of the supplied cooler oil mixing with the oil in the LP chamber. Thermal modelling of the seal showed satisfactory comparison to available experimental data for oil temperature rise although further experiments would have been desirable. Future numerical models should account for the wetted effect of oil within the seal when estimating the heat flux or the heat transfer coefficient at the trough walls.

CHAPTER 7

7 Conclusions and Future work

7.1 Conclusions

Intershaft seals are used in aero-engines where sealing between rotating shafts is required. Hydraulic seals act as zero flow air seals that can support a pressure difference across the seal when used in rotating applications. Due to their excellent sealing characteristics, tolerance to vibration and relative insensitivity to shaft whirl and misalignment, hydraulic seals are considered to be an attractive alternative to conventional oil-backed seals for bearing chamber sealing applications. Hydraulic seals have been used in service for many years although their design could be said to be fully optimised. They meet or mostly meet existing sealing requirements within the current operational envelope and the challenge is to identify the limitations associated with that envelope and how to enlarge it. Therefore, the development of numerical approaches to accurately represent the operation and performance of hydraulic seals is highly desirable.

In this thesis, a numerical modelling framework was developed to predict the performance of intershaft hydraulic seals. There are no comprehensive models or

evaluations of the operation of a hydraulic seal in the open literature. There are quite a few flow phenomena that exist in a hydraulic seal as identified in the thesis introduction and a survey of relevant literature is given in Chapter 2. The key modelling challenges stem from mathematically representing the behaviour of the complex flow phenomena. The flow within a hydraulic seal is highly rotational, turbulent and transient. The sealing fluid, oil, exists in three distinct forms - as a continuum of liquid in the trough; as droplets which splash back from the seal during formation and ejection and ligaments that may eject from the seal on the non-fill side. This complex multiphase interaction is further complicated by the feed jet comprising both jet impact on the oil in the trough and heat transfer effects. As explained in Chapter 3, the existing modelling approaches applicable to hydraulic seals have been combined and extended. Novel modelling methods are introduced to model the jet feed and heat transfer effects within a hydraulic seal. The CFD modelling technique based on VoF is presented and discussed.

The survey of literature confirms a paucity of data and research related to hydraulic seals. To aid understanding of the performance and flow dynamics of hydraulic seals and to establish a robust numerical modelling strategy appropriate for hydraulic intershaft seals, a precursor study was carried out investigating disks rotating in stationary cavities, a configuration similar to hydraulic seals. Chapter 4 presents the achieved outcomes across three sections. The first part presents results from a CFD study investigating an enclosed disk rotating fully immersed in a liquid. Experimental data available in the study by Daily and Nece [40] was used for validation. This initial study established an appropriate mesh density. To select a suitable turbulence model,

results were obtained for standard $k-\varepsilon$ in both steady and transient modes, SST $k-\omega$ and RSM models. The study established that, with the lowest RMSE, the standard $k-\varepsilon$ provides best overall prediction of the tangential velocity field, although the results were not significantly better than those obtained using the other models. The transient $k-\varepsilon$ and RSM models provided the closest numerical matches to the experimentally measured radial velocities, with minimal discrepancies between the point values. The dominant flow features involve substantial recirculating motion induced by radially outward flow near the rotating disk and inward flow adjacent to the stationary wall. The results from the two equation models are in good agreement with the experimental data for the mean velocity fields and other flow quantities. Compared to the RSM, faster and more robust convergence of the solutions was obtained with standard $k-\varepsilon$ and SST $k-\omega$ models. Taking into account the compromise between the accuracy and computational cost, it was considered reasonable to apply a two-equation model in the rotor-stator cavity flow calculations. Based on its applicability to a wide range of wall y^+ values and the ability to resolve the boundary layer all the way through to the viscous sub layer as discussed in Chapter 3, the SST $k-\omega$ model is used in the next stage of computations investigating the flow field with enclosed cavity when the rotating disk is partially immersed in fluid.

In the second part of Chapter 4, a parametric study on a partially wetted disk for five engagement ratios in a cavity with no through-flow is presented. The results showed that the core angular velocity increases with the engagement ratio with a velocity ranging between 0.37 and 0.43 of shaft angular velocity. The results were in excellent

agreement with the experimental data of Ketola and McGrew [41] showing that the numerically computed velocity ratios are within 1.1% of the experimental value. Key hydraulic seal applicable outcomes from the computed flow are:

- A thicker boundary layer at higher radial values that reduces with decreasing radius.
- The flow within the cavity can be mainly characterized by the Batchelor flow model but is dependent on the radial location.
- The boundary layers are joined up to a certain radius and are separated beyond
- Two secondary flow recirculation zones exist, one within the gas and the other within the liquid resulting in a liquid/gas interface that is not completely flat.
- Taylor vortices were present in the narrow radial gap between disk and the casing but with fewer pairs than for closed ends.

The final part of Chapter 4 presents a discussion on the effect of through-flow in a rotor-stator cavity and introduces a novel approach to model the through-flow by balancing the radial pressure across the cavity. When a supply of fluid is delivered into a cavity with a rotating disk partially immersed in fluid, the flow structure in the rotor-stator cavity is altered. Through-flow leads to a reduction in the velocity field. For the volumetric flow rates investigated, the fluid core rotates in the range of 0.42 to 0.47 of the shaft rotational speed and results are in good agreement with experimental data of Ketola and McGrew [41]. The computed results for the partially wetted disk model,

operating under both non-flow and through-flow conditions are sufficiently close to the experimental data to give confidence that an appropriate modelling methodology is established. In particular the work of this chapter has established an appropriate meshing and modelling approach and has shown the key features of flows with a rotating disk and static housing.

Chapter 5 investigates the pressure capacity of an aeroengine relevant hydraulic seal design. Seal pressure capacity is an important design parameter and historical design approaches established on the basis of analytical approximations can be found in the literature but the uncertainty of accuracy and consistency of these methods has led to the use of a high safety factor. Prior to this study there was limited, incomplete understanding of the effect of fin axial position within the trough, important because of the different relative axial positions of the shafts over the engine operation envelope. Building on the previously developed methodology presented in Chapter 4 with a rotating shaft and static casing, the work presented in Chapter 5 develops a CFD modelling capability for intershaft hydraulic seals for aero-engine applications where fin and trough rotate at different speeds. Investigating the performance of a seal without an oil feed, 2D numerical simulations were conducted in ANSYS-Fluent applying a VoF method for a range of shaft speeds and axial fin positions. Prior established analytical approximations to estimate the angular velocity of oil were collated together in this chapter. A comparison was made between the analytical and numerical calculations. The comparative analysis of the analytical and numerical calculations for the geometry investigated demonstrated that the numerical results were best matched

by a correlation that included weighting coefficients proportional to the relative surface areas of the housing and fin components.

A consistent approach was developed in this chapter to define seal capacity in terms of leakage rate of air through the seal. Through a parametric study investigating the air leakage rate, a criterion was derived to quantify a failed seal. The seal was deemed broken when the air leakage rate exceeded 200 mg/s. The results presented show that the maximum pressure capacity of the seal increases linearly with the square of housing speed. This result is in contrast to the relationships established between the maximum pressure capacity and geometrical parameters in a prior study by Mathews et al. [27]. This is attributed to the difference in the geometry of the seal investigated by Mathews et al. [27] , which was much narrower with a width that is half the size of seal examined in this thesis. At higher shaft speeds, the investigated seal configuration demonstrates more attractive operational characteristics compared to the one of Mathews et al. [27] due to the square relationship with the maximum pressure capacity for a given shaft speed the current seal has a far higher pressure capacity.

From the fin placement study it was found that at a given housing speed, maximum pressure capacity increases linearly with displacement of the fin from the side of the housing on the LP side. Through the established approach, different flow regimes within the seal were identified as the fin was displaced axially demonstrating the versatility of the model developed. Looking at the flow profile on the LP side of the fin, turbulent flow merged boundary layers (characterised as Regime III by Daily and Nece [40] were identified at smaller clearances where the LP axial gap to fin radius

ratio s/R_F < 0.03. At larger clearances when s/R_F > 0.04, turbulent flow, separated boundary layers are found (characterised as Regime IV by Daily and Nece [40]).

The first part of Chapter 6 extends investigation into 3D, with an oil feed modelled, a configuration far closer to realistic engine operating conditions with a specific focus on the form and behaviour of overspill oil. The aim of the study was to examine the effect of the jet on the behaviour of the oil in the trough. To accomplish this, a 3D model of a representative hydraulic seal geometry was examined in a numerical study applying a VoF method for shaft speeds of 4000 rpm and 2000 rpm for the trough and fin respectively with fin positioned central to the trough.

A quantitative evaluation of the disturbance created on the surface by the jet demonstrates that the greatest disturbance is caused at the point of impact and that the oil film thickness is only changed by a negligible variation of +/- 0.1mm downstream. Predictions of the CFD simulation are qualitatively consistent with experimental observations made available to this research. High quality CFD images providing a qualitative representation of the oil shedding behaviour at the overspill edge of the trough. The tangential range of shedding and the direction of ejected oil were compared with images obtained experimentally. A non-even oil shedding behaviour was observed in both the CFD simulation and experiment. The CFD results of the jet penetration indicate that the oil injected into seal does not spray/bounce straight off the trough oil surface but resides in the seal before shedding off the edge of the trough. The analysis into jet penetration and secondary flow field supports belief that the oil supplied from the jet assists in the heat management of the seal. Recirculation zones separated by the

oil inflow are found in the secondary flow field indicating that a jet encourages even dissipation of heat within the seal. It was found that the influence of the jet on flow axisymmetry of the model is negligible.

Part two of the numerical study reported in Chapter 6 was conducted to investigate the oil related heat transfer within a hydraulic seal. For this a 2D model was used with the jet-supplied oil of the engine seal represented in 2D by an axisymmetric feed along the LP side of the fin. The thermal model was developed using an analytical correlation in literature for the heat transfer coefficient for a disk rotating in air in order to estimate the heat transfer coefficient at the trough wall. The fin was modelled as adiabatic. The results show that the temperature of the oil reservoir in the HP chamber is higher by approximately 3 K than that of the oil in the LP chamber as a result of more of the supplied cooler oil mixing with the oil in the LP chamber. Thermal modelling of the seal showed satisfactory comparison to available experimental data for oil temperature rise although further experiments would have been desirable.

7.2 Contribution to knowledge

In this work, a reliable methodology to model the flow within a hydraulic seal is developed through a parametric study investigating the effect of fin placement and rotational shaft speeds, on seal pressure capacity. A consistent approach using the air leakage rate to predict the maximum operating pressure of hydraulic seals is introduced for the first time. A comprehensive analysis on the available analytical correlations that are used to predict the seal capacity and their validity is presented.

Also presented in this work is a CFD modelling approach for a full 3D model of a hydraulic seal. This is the first numerical investigation which considers the 3D effects of the flow as well as an oil feed into a hydraulic seal. The study includes a detailed discussion on the effect of the jet on the oil in the trough. This study provides valuable insights into flow field within the seal and presents both quantitative and qualitative evaluation of the jet impact behaviour.

Investigation on thermal effects including oil-related heat transfer in hydraulic seals presented in this thesis is also the first CFD study to characterize the performance of a hydraulic seal considering the heat generated and dissipated. A modelling framework to include effects of viscous heating generated within a seal is developed in this study which yields results of more realistic flow behaviour that have not been documented in prior investigations.

7.3 Future work

In this study, the seal formation at engine start-up has not been investigated due to unfeasible computational time and the associated cost. It was established in an experimental investigation into the performance of a hydraulic seal conducted at the University of Nottingham that the seal formation time is approximately 20 -50 s [25]. Therefore, it is currently not viable to perform detailed flow simulations of the formation and operation scenarios of a hydraulic seal simulating a minimum of physical flow time of 20 s. However, the methodology developed in this thesis can now be used

as an optimization tool. This approach can be implemented to investigate the blow-out and remake conditions of the seal.

Further CFD work can be conducted to investigate and analyse size, trajectory and thermal behaviour of ejected droplets from the seal on the LP side. A far higher mesh density would be required in the ejection region if this study is to be solely conducted using VoF. A locally refined mesh could also be used to investigate the droplet generation through jet splashing.

Although this study has been fully focussed on hydraulic intershaft seals, the methodology should be equally applicable to oil backed intershaft seals. A future investigation into oil-backed seals comparing their pressure capacity characteristics to hydraulic seals would also have value to the aeroengine industry. It would also be very valuable to systematically investigate how seal capacity is affected by trough width, and fin to trough distance.

As evidenced by the results obtained through the thermal model developed for hydraulic seals, a difference in temperature exists on the inside of the trough walls. It would be interesting to do further work to characterize this temperature difference. A parametric study should be conducted to derive estimates for the heat flux or the heat transfer coefficient at the trough walls. Thermal modelling could also investigate how the oil temperature in the seal trough varies with different chamber air temperatures.

References

[1] R. Hendricks, B. Steinetz, and M. Braun, "Turbomachine Sealing and Secondary Flows. Part 1; Review of Sealing Performance, Customer, Engine Designer, and Research Issues," 2004.

[2] A. Przekwas, M. Athavale, and R. Hendricks, "Progress in advanced modeling of turbine engine seal flows," in *30th Joint Propulsion Conference and Exhibit*, 1994, p. 2803.

[3] European Commission, *Flightpath 2050 : Europe's vision for aviation : maintaining global leadership and serving society's needs*. Publications Office, 2012.

[4] R. E. Chupp, R. C. Hendricks, S. B. Lattime, and B. M. Steinetz, "Sealing in turbomachinery," *Journal of Propulsion and Power*, vol. 22, no. 2, pp. 313-349, 2006.

[5] R. C. Hendricks, R. E. Chupp, S. B. Lattime, and B. M. Steinetz, "Turbomachine interface sealing," 2005.

[6] R. C. Bill and L. P. Ludwig, "Wear of seal materials used in aircraft propulsion systems," *Wear*, vol. 59, no. 1, pp. 165-189, 1980.

[7] R. E. Chupp, R. C. Hendricks, and B. M. Steinetz, "Gas Turbine Engines: Seals," in *Encyclopedia Of Aerospace Engineering*, 1 ed: Wiley, 2010.

[8] J. W. Chew and N. J. Hills, "Computational fluid dynamics for turbomachinery internal air systems," *Philosophical transactions of the royal society A: Mathematical, physical and engineering sciences*, vol. 365, no. 1859, pp. 2587-2611, 2007.

[9] *Introduction to jet engines*. Available: https://www.jet-x.org/aeolus.html Accessed on 10/04/2023

[10] *The Jet Engine by Rolls Royce*, 5 ed. Wiley-Blackwell, 2015.

[11] K. Willenborg, J. Au, K. Dullenkopf, and S. Wittig, "Experimental Investigation of the Two-Phase Flow Through a Leaking Bearing Chamber Labyrinth Seal," in *17th International Symposium on Air Breathing Engines (ISABE 2011), Munich, Sept*, 2005, pp. 4-9.

[12] *Trent Engine*. Available: https://www.airliners.net/ Accessed on 10/11/2022

[13] R. C. Hendricks, R. E. Chupp, S. B. Lattime, and B. M. Steinetz, "Turbomachine interface sealing," in *International Conference on Metallurgical Coatings and Thin Films*, San Diego, USA, 2005, no. NASA/TM-2005-213633.

[14] B. M. Steinetz, R. C. Hendricks, and J. Munson, "Advanced seal technology role in meeting next generation turbine engine goals," NASA Technical Memorandum 206961, 1998.

[15] *Aeroengine safety*. Available: https://aeroenginesafety.tugraz.at/ Accessed on 04/02/2023

[16] L. P. Ludwig and R. C. Bill, "Gas path sealing in turbine engines," *Asle Transactions*, vol. 23, no. 1, pp. 1-22, 1980.

[17] "Design Rules and Aids DRA 117: Hydraulic seals," 2016.

[18] M. T. Thew, "The labyrinth - hydrodynamic disk seal (LHDS)," in *8th International Conference on Fluid Sealing*, 1978, vol. v, no. 1, pp. B1. 1-B1. 12.

[19] J. Denecke *et al.*, "Advanced Hydraulic Seal Design for High Temperature Environments," in *ASME Turbo Expo 2006: Power for Land, Sea, and Air*, 2006, vol. 3: Heat Transfer, Parts A and B, pp. 1453-1462.

[20] K. Willenborg, S. Busam, H. Roßkamp, and S. Wittig, "Experimental Studies of the Boundary Conditions Leading to Oil Fire in the Bearing Chamber and in the Secondary Air System of Aeroengines," in *ASME Turbo Expo 2002: Power for Land, Sea, and Air*, 2002, pp. 739-747: American Society of Mechanical Engineers Digital Collection.

[21] K. Willenborg, S. Busam, H. Roßkamp, and S. Wittig, "Experimental Studies of the Boundary Conditions Leading to Oil Fire in the Bearing Chamber and in the Secondary Air System of Aeroengines," in *Turbo Expo: Power for Land, Sea, and Air*, 2002, vol. 36088, pp. 739-747.

[22] A. Bock, "Gas-turbine engine with a bearing chamber," ed: Google Patents, 2003.

[23] S. Michaelis and MIC., *Health and Flight Safety Implications from Exposure to Contaminated Air in Aircraft*. University of New South Wales, 2010.

[24] M. Klingsporn, "Advanced transmission and oil system concepts for modern aero-engines," in *Turbo Expo: Power for Land, Sea, and Air*, 2004, vol. 41693, pp. 391-398.

[25] R. Omar, "Oil-based inter-shaft seals performance " University of Nottingham, Internal Report 2021.

[26] C. Young and J. W. Chew, "Evaluation of the Volume of Fluid Modelling Approach for Simulation of Oil/Air System Flows," in *ASME Turbo Expo 2005: Power for Land, Sea, and Air*, 2005, vol. 3: Turbo Expo 2005, Parts A and B, pp. 1249-1257.

[27] H.-C. Mathews, H. Morvan, D. Peduto, Y. Wang, C. Young, and H.-J. Bauer, "Modelling of Hydraulic Seals Using an Axisymmetric Volume of Fluid Method (VOF)," in *ASME Turbo Expo 2013: Turbine Technical Conference and Exposition*, 2013, vol. 2: Aircraft Engine; Coal, Biomass and Alternative Fuels; Cycle Innovations, V002T01A020.

[28] V. EKMAN, "On the influence of earth's rotation on ocean currents," *Ark. Mat. Astron. Fys.*, 1905.

[29] T. V. Kármán, "Über laminare und turbulente Reibung," *ZAMM-Journal of Applied Mathematics and Mechanics/Zeitschrift für Angewandte Mathematik und Mechanik*, vol. 1, no. 4, pp. 233-252, 1921.

[30] V. U. Bödewadt, "Die drehströmung über festem grunde," *ZAMM-Journal of Applied Mathematics and Mechanics/Zeitschrift für Angewandte Mathematik und Mechanik*, vol. 20, no. 5, pp. 241-253, 1940.

[31] G. K. Batchelor, "Note on a class of solutions of the Navier-Stokes equations representing steady rotationally-symmetric flow," *The quarterly journal of mechanics and applied mathematics*, vol. 4, no. 1, pp. 29-41, 1951.

[32] K. Stewartson, "On the flow between two rotating coaxial disks," in *Mathematical Proceedings of the Cambridge Philosophical Society*, 1953, vol. 49, no. 2, pp. 333-341: Cambridge University Press.

[33] K. Picha and E. Eckert, "Study of the air flow between coaxial disks rotating with arbitrary velocities in an open or enclosed space," *proceedings of 3rd US Nat. Cong. Appl. Mech*, 1958.

[34] G. Lance and M. H. Rogers, "The axially symmetric flow of a viscous fluid between two infinite rotating disks," *Proceedings of the Royal Society of London. Series A. Mathematical and Physical Sciences*, vol. 266, no. 1324, pp. 109-121, 1962.

[35] G. Mellor, P. Chapple, and V. Stokes, "On the flow between a rotating and a stationary disk," *Journal of fluid mechanics,* vol. 31, no. 1, pp. 95-112, 1968.

[36] H. O. Kreiss and S. V. Parter, "On the swirling flow between rotating coaxial disks: Existence and nonuniqueness," *Communications on Pure and Applied Mathematics,* vol. 36, no. 1, pp. 55-84, 1983.

[37] D. Dijkstra and G. Van Heijst, "The flow between two finite rotating disks enclosed by a cylinder," *Journal of Fluid Mechanics,* vol. 128, pp. 123-154, 1983.

[38] S. Poncet, M.-P. Chauve, and R. Schiestel, "Batchelor versus Stewartson flow structures in a rotor-stator cavity with throughflow," *Physics of fluids,* vol. 17, no. 7, 2005.

[39] G. Gauthier, P. Gondret, and M. Rabaud, "Axisymmetric propagating vortices in the flow between a stationary and a rotating disk enclosed by a cylinder," *Journal of Fluid Mechanics,* vol. 386, pp. 105-126, 1999.

[40] J. W. Daily and R. E. Nece, "Chamber dimension effects on induced flow and frictional resistance of enclosed rotating disks," *Journal of basic engineering,* vol. 82, no. 1, pp. 217-230, 1960.

[41] H. Ketola and J. McGrew, "Pressure, frictional resistance, and flow characteristics of the partially wetted rotating disk," *Journal of Lubrication Technology,* vol. 90, no. 2, pp. 395-404, 1968.

[42] B. Launder, S. Poncet, and E. Serre, "Laminar, transitional, and turbulent flows in rotor-stator cavities," *Annual review of fluid mechanics,* vol. 42, pp. 229-248, 2010.

[43] A. Sirivat, "Stability experiment of flow between a stationary and a rotating disk," *Physics of Fluids A: Fluid Dynamics,* vol. 3, no. 11, pp. 2664-2671, 1991.

[44] R. J. Lingwood, "Absolute instability of the boundary layer on a rotating disk," *Journal of Fluid Mechanics,* vol. 299, pp. 17-33, 1995.

[45] R. Lingwood, "An experimental study of absolute instability of the rotating-disk boundary-layer flow," *Journal of Fluid Mechanics,* vol. 314, pp. 373-405, 1996.

[46] R. Lingwood, "On the effects of suction and injection on the absolute instability of the rotating-disk boundary layer," *Physics of Fluids,* vol. 9, no. 5, pp. 1317-1328, 1997.

[47] E. Serre, E. C. Del Arco, and P. Bontoux, "Annular and spiral patterns in flows between rotating and stationary discs," *Journal of Fluid Mechanics,* vol. 434, pp. 65-100, 2001.

[48] L. Schouveiler, P. Le Gal, M. Chauve, and Y. Takeda, "Experimental study of the stability of the flow between a rotating and a stationary disk," in *Advances in Turbulence VI: Proceedings of the Sixth European Turbulence Conference, held in Lausanne, Switzerland, 2–5 July 1996*, pp. 385-388: Springer.

[49] L. Schouveiler, P. Le Gal, M. Chauve, and Y. Takeda, "Spiral and circular waves in the flow between a rotating and a stationary disk," *Experiments in Fluids,* vol. 26, no. 3, pp. 179-187, 1999.

[50] A. J. Faller, "Instability and transition of disturbed flow over a rotating disk," *Journal of Fluid Mechanics,* vol. 230, pp. 245-269, 1991.

[51] L. Schouveiler, P. Le Gal, and M. Chauve, "Instabilities of the flow between a rotating and a stationary disk," *Journal of Fluid Mechanics,* vol. 443, pp. 329-350, 2001.

[52] M. Lygren and H. I. Andersson, "Turbulent flow between a rotating and a stationary disk," *Journal of Fluid Mechanics,* vol. 426, pp. 297-326, 2001.

[53] M. Itoh, "Experiments on the turbulent flow in the narrow clearance between a rotating and a stationary disk," *Turbulent flows- 1995,* pp. 27-32, 1995.

[54] É. Séverac, S. Poncet, É. Serre, and M.-P. Chauve, "Large eddy simulation and measurements of turbulent enclosed rotor-stator flows," *Physics of Fluids,* vol. 19, no. 8, 2007.

[55] M. Lygren and H. I. Andersson, "Large eddy simulations of the turbulent flow between a rotating and a stationary disk," *Zeitschrift für angewandte Mathematik und Physik ZAMP,* vol. 55, pp. 268-281, 2004.

[56] H. I. Andersson and M. Lygren, "LES of open rotor–stator flow," *International journal of heat and fluid flow,* vol. 27, no. 4, pp. 551-557, 2006.

[57] S. Makino, M. Inagaki, and M. Nakagawa, "Laminar-turbulence transition over the rotor disk in an enclosed rotor-stator cavity," *Flow, Turbulence and Combustion,* vol. 95, pp. 399-413, 2015.

[58] N. Itoh, "Simple cases of the streamline-curvature instability in three-dimensional boundary layers," *Journal of Fluid Mechanics,* vol. 317, pp. 129-154, 1996.

[59] K. Willenborg, S. Busam, H. Roßkamp, and S. Wittig, "Experimental Studies of the Boundary Conditions Leading to Oil Fire in the Bearing Chamber and in the Secondary Air System of Aeroengines," in *Turbo Expo: Power for Land, Sea, and Air*, 2002, pp. 739-747.

[60] M. Birouk and N. Lekic, "Liquid jet breakup in quiescent atmosphere: A review," *Atomization and Sprays,* vol. 19, no. 6, 2009.

[61] D. W. Green and R. H. Perry, *Perry's chemical engineers' handbook*. McGraw-Hill Education, 2008.

[62] R. P. Grant and S. Middleman, "Newtonian jet stability," *AIChE Journal,* vol. 12, no. 4, pp. 669-678, 1966.

[63] D. W. Lee and R. C. Spencer, "Photomicrographic Studies of Fuel Sprays," 1934.

[64] J. A. F. Plateau, *Statique expérimentale et théorique des liquides soumis aux seules forces moléculaires*. Gauthier-Villars, 1873.

[65] L. Rayleigh, "On the instability of jets," *Proceedings of the London mathematical society,* vol. 1, no. 1, pp. 4-13, 1878.

[66] L. Rayleigh, "On the capillary phenomena of jets," *Proc. R. Soc. London,* vol. 29, no. 196-199, pp. 71-97, 1879.

[67] P. Schweitzer, "Mechanism of disintegration of liquid jets," *Journal of Applied Physics,* vol. 8, no. 8, pp. 513-521, 1937.

[68] C. Weber, "Disintegration of liquid jets," *Z. Angew. Math. Mech.,* vol. 11, pp. 135-159, 1939.

[69] A. Haenlein, "Disintegration of a liquid jet," 1932.

[70] S. Tomotika, "On the instability of a cylindrical thread of a viscous liquid surrounded by another viscous fluid," *Proceedings of the Royal Society of London. Series A-Mathematical and Physical Sciences,* vol. 150, no. 870, pp. 322-337, 1935.

[71] S. Chandrasekhar, "The capillary instability of a liquid jet," *Hydrodynamic and Hydromagnetic stability,* pp. 537-42, 1961.

[72] F. P. Ricou and D. Spalding, "Measurements of entrainment by axisymmetrical turbulent jets," *Journal of fluid mechanics,* vol. 11, no. 1, pp. 21-32, 1961.

[73] Y. Tanasawa, "On the atomization of liquid jet issuing from a cylindrical nozzle," *Technol. Rep. Tohoku Univ.,* vol. 19, p. 135, 1955.

[74] H. Tabbara and S. Gu, "A study of liquid droplet disintegration for the development of nanostructured coatings," *AIChE journal*, vol. 58, no. 11, pp. 3533-3544, 2012.

[75] M. Pai, I. Bermejo-Moreno, O. Desjardins, and H. Pitsch, "Role of Weber number in primary breakup of turbulent liquid jets in crossflow," *Center for Turbulence Research Annual Research Briefs 2009*, pp. 145-158, 2009.

[76] W. v. Ohnesorge, "The formation of drops by nozzles and the breakup of liquid jets," *UT Faculty/Researcher Works*, 2019.

[77] R. D. Reitz, "Mechanism of breakup of round liquid jets," *Encyclopedia of fluid mechanics*, vol. 10, 1986.

[78] H. Hiroyasu, "The Breakup of High Speed Jets on a High Pressure Gaseous Atmosphere," *The 2^< nd> ICLASS, 1982*, pp. 69-74, 1982.

[79] H. Hiroyasu, "Break-up length of a liquid jet and internal flow in a nozzle," in *Proc. Fifth International Conference on Liquid Atomization and Spray Systems*, 1991, pp. 275-282.

[80] H. Hiroyasu, "Spray breakup mechanism from the hole-type nozzle and its applications," *Atomization and sprays*, vol. 10, no. 3-5, 2000.

[81] M. Arai, M. Shimizu, and H. Hiroyasu, "Break-up length and spray angle of high speed jet," in *Proceedings of ICLASS*, 1985, vol. 85.

[82] M. Arai, "Break-up length and spray formation mechanism of a high speed liquid jet," in *Proceedings of the 4th International Conference on Liquid Atomization and Spray Systems*, 1988.

[83] C. Shao, K. Luo, M. Chai, and J. Fan, "Sheet, ligament and droplet formation in swirling primary atomization," *AIP Advances*, vol. 8, no. 4, p. 045211, 2018.

[84] B. Hustedt, T. Hertzberg, and G. Holmstedt, "The physics behind water mist systems," in *Interflam 2004. Edinburgh, Skottland. 2004-07-05--07*, 2004.

[85] N. Chigier, "Regimes of jet breakup and breakup mechanisms (physical aspects)," *Progress in astronautics and aeronautics*, vol. 166, pp. 109-134, 1996.

[86] N. Tamaki, M. Shimizu, K. Nishida, and H. Hiroyasu, "Effects of cavitation and internal flow on atomization of a liquid jet," *Atomization and sprays*, vol. 8, no. 2, 1998.

[87] N. Tamaki, M. Shimizu, and H. Hiroyasu, "Enhancement of the atomization of a liquid jet by cavitation in a nozzle hole," *Atomization and Sprays,* vol. 11, no. 2, 2001.

[88] M. Arai, "Similarity between the break-up lengths of a high speed liquid jet in atmospheric and pressurized conditions," *Proc. ICLASS-91,* 1991.

[89] M. Arai and K. Amagai, "Surface wave transition before breakup on a laminar liquid jet," *International journal of heat and fluid flow,* vol. 20, no. 5, pp. 507-512, 1999.

[90] A. H. Lefebvre and V. G. McDonell, *Atomization and sprays*. CRC press, 2017.

[91] H. Vahedi Tafreshi and B. Pourdeyhimi, "The effects of nozzle geometry on waterjet breakup at high Reynolds numbers," *Experiments in fluids,* vol. 35, pp. 364-371, 2003.

[92] S. P. Lin and R. D. Reitz, "Drop and spray formation from a liquid jet," *Annual review of fluid mechanics,* vol. 30, no. 1, pp. 85-105, 1998.

[93] M. McCarthy and N. Molloy, "Review of stability of liquid jets and the influence of nozzle design," *The Chemical Engineering Journal,* vol. 7, no. 1, pp. 1-20, 1974.

[94] C. Miesse, "Correlation of experimental data on the disintegration of liquid jets," *Industrial & Engineering Chemistry,* vol. 47, no. 9, pp. 1690-1701, 1955.

[95] T. Mahoney and M. Sterling, "The breakup length of laminar Newtonian liquid jets in air," in *Proceedings of the 1st International Conference on Liquid Atomization and Spray Systems, Tokyo,* 1978, pp. 9-12.

[96] C.-L. Yeh, "Numerical study of inlet and geometry effects on discharge coefficients for liquid jet emanating from a plain-orifice atomizer," *Journal of Mechanics,* vol. 18, no. 3, pp. 153-161, 2002.

[97] H. V. Tafreshi and B. Pourdeyhimi, "Simulating the flow dynamics in hydroentangling nozzles: effect of cone angle and nozzle aspect ratio," *Textile research journal,* vol. 73, no. 8, pp. 700-704, 2003.

[98] N. Anantharamaiah, H. V. Tafreshi, and B. Pourdeyhimi, "Numerical simulation of the formation of constricted waterjets in hydroentangling nozzles: effects of nozzle geometry," *Chemical Engineering Research and Design,* vol. 84, no. 3, pp. 231-238, 2006.

[99] S. S. Yoon and S. D. Heister, "A nonlinear atomization model based on a boundary layer instability mechanism," *Physics of Fluids,* vol. 16, no. 1, pp. 47-61, 2004.

[100] J. R. Richards, A. M. Lenhoff, and A. N. Beris, "Dynamic breakup of liquid–liquid jets," *Physics of Fluids,* vol. 6, no. 8, pp. 2640-2655, 1994.

[101] J. R. Richards, A. N. Beris, and A. M. Lenhoff, "Drop formation in liquid–liquid systems before and after jetting," *Physics of fluids,* vol. 7, no. 11, pp. 2617-2630, 1995.

[102] B. J. Meister and G. F. Scheele, "Prediction of jet length in immiscible liquid systems," *AIChE Journal,* vol. 15, no. 5, pp. 689-699, 1969.

[103] M. Rieber and A. Frohn, "A numerical study on the mechanism of splashing," *International Journal of Heat and Fluid Flow,* vol. 20, no. 5, pp. 455-461, 1999.

[104] E. Berberović, N. P. van Hinsberg, S. Jakirlić, I. V. Roisman, and C. Tropea, "Drop impact onto a liquid layer of finite thickness: Dynamics of the cavity evolution," *Physical Review E,* vol. 79, no. 3, p. 036306, 2009.

[105] S. Osher and J. A. Sethian, "Fronts propagating with curvature-dependent speed: algorithms based on Hamilton-Jacobi formulations," *Journal of computational physics,* vol. 79, no. 1, pp. 12-49, 1988.

[106] K. Brinckman, A. Hosangadi, V. Ahuja, S. Dash, and G. Feldman, "A CFD methodology for liquid jet breakup and vaporization predictions of compressible flows," in *46th AIAA Aerospace Sciences Meeting and Exhibit*, 2008, p. 1023.

[107] K. Shibata, S. Koshizuka, and Y. Oka, "Numerical analysis of jet breakup behavior using particle method," *Journal of nuclear science and technology,* vol. 41, no. 7, pp. 715-722, 2004.

[108] S. Nukiyama, "Experiments on the atomization of liquids in an air stream, report 3, on the droplet-size distribution in a atomized jet," *Trans. Soc. Mech. Eng. Japan,* vol. 5, pp. 62-67, 1939.

[109] D. Guildenbecher, C. López-Rivera, and P. Sojka, "Secondary atomization," *Experiments in Fluids,* vol. 46, no. 3, pp. 371-402, 2009.

[110] M. Pilch and C. Erdman, "Use of breakup time data and velocity history data to predict the maximum size of stable fragments for acceleration-induced breakup of a liquid drop," *International journal of multiphase flow,* vol. 13, no. 6, pp. 741-757, 1987.

[111] G. Faeth, L.-P. Hsiang, and P.-K. Wu, "Structure and breakup properties of sprays," *International Journal of Multiphase Flow,* vol. 21, pp. 99-127, 1995.

[112] N. Mayers, "Modélisation de la combustion cryotechnique avec prise en compte de l'atomisation primaire du jet d'oxygène liquide," *Universit ,ed£ Aix-Marseille II. These de doct,* 2006.

[113] I. Gökalp, C. Chauveau, C. Morin, B. Vieille, and M. Birouk, "Improving droplet breakup and vaporization models by including high pressure and turbulence effects," *Atomization and Sprays,* vol. 10, no. 3-5, 2000.

[114] I. Gokalp *et al.*, "Modeling droplet break-up effects for high pressure cryogenic spray combustion codes," in *36th AIAA/ASME/SAE/ASEE Joint Propulsion Conference and Exhibit*, 2000, p. 3496.

[115] Q. Zheng and A. Jasuja, "Droplet size and velocity correlations for a coaxial air blast atomized jet," in *ICLASS 94 Proceedings of the Sixth International Conference on Liquid Atomization and Spray Systems*, 1994: Begell House.

[116] A. Mansour and N. Chigier, "A Phase Doppler Investigation of Co-Axial Air Blast Atomizers," *ASME-PUBLICATIONS-HTD,* vol. 270, pp. 95-95, 1993.

[117] A. Mansour and N. Chigier, "Effect of turbulence on the stability of liquid jets and the resulting droplet size distributions," *Atomization and Sprays,* vol. 4, no. 5, pp. 583-604, 1994.

[118] S. A. Krzeczkowski, "Measurement of liquid droplet disintegration mechanisms," *International Journal of multiphase flow,* vol. 6, no. 3, pp. 227-239, 1980.

[119] W. E. Krauss, "Water drop deformation and fragmentation due to shock wave impact," 1971.

[120] J. A. Nicholls and A. Ranger, "Aerodynamic shattering of liquid drops," *Aiaa Journal,* vol. 7, no. 2, pp. 285-290, 1969.

[121] O. G. Engel, "Fragmentation of Waterdrops in the Zone," *Journal of Research of the National Bureau of Standards,* vol. 60, no. 3, p. 245, 1958.

[122] W. Lane, "Shatter of drops in streams of air," *Industrial & Engineering Chemistry,* vol. 43, no. 6, pp. 1312-1317, 1951.

[123] J. Hinze, "Forced deformations of viscous liquid globules," *Flow, Turbulence and Combustion,* vol. 1, pp. 263-272, 1949.

[124] L.-P. Hsiang and G. M. Faeth, "Near-limit drop deformation and secondary breakup," *International journal of multiphase flow,* vol. 18, no. 5, pp. 635-652, 1992.

[125] B. Gel'Fand, S. Gubin, S. Kogarko, and S. Komar, "Singularities of the breakup of viscous liquid droplets in shock waves," *Journal of engineering physics,* vol. 25, pp. 1140-1142, 1973.

[126] Z. Dai and G. Faeth, "Temporal properties of secondary drop breakup in the multimode breakup regime," *International Journal of Multiphase Flow,* vol. 27, no. 2, pp. 217-236, 2001.

[127] A. M. Worthington, *A study of splashes*. Longmans, Green, and Company, 1908.

[128] G. E. Cossali, A. Coghe, and M. Marengo, "The impact of a single drop on a wetted solid surface," *Experiments in fluids,* vol. 22, no. 6, pp. 463-472, 1997.

[129] M. Marengo, C. Antonini, I. V. Roisman, and C. Tropea, "Drop collisions with simple and complex surfaces," *Current Opinion in Colloid & Interface Science,* vol. 16, no. 4, pp. 292-302, 2011.

[130] A. L. Yarin, "Drop impact dynamics: Splashing, spreading, receding, bouncing…," *Annu. Rev. Fluid Mech.,* vol. 38, pp. 159-192, 2006.

[131] A. L. Yarin and D. A. Weiss, "Impact of drops on solid surfaces: self-similar capillary waves, and splashing as a new type of kinematic discontinuity," *Journal of fluid mechanics,* vol. 283, pp. 141-173, 1995.

[132] D. Peduto, R. Koch, H. Morvan, K. Dullenkopf, and H. Bauer, "Numerical studies of single drop impact onto a plane shallow and deep liquid pool," in *24th Annual Conference on Liquid Atomization and Spray Systems*, 2011.

[133] C. Bai and A. Gosman, "Mathematical modelling of wall films formed by impinging sprays," *SAE transactions,* pp. 782-796, 1996.

[134] I. Owen and D. Ryley, "The flow of thin liquid films around corners," *International journal of multiphase flow,* vol. 11, no. 1, pp. 51-62, 1985.

[135] M. A. Friedrich, "A separation criterion and non-intrusive thickness measurement technique for shear-driven films," 2008.

[136] F. Maroteaux, D. Llory, J. Le Coz, and C. Habchi, "Liquid film atomization on wall edges—separation criterion and droplets formation model," *J. Fluids Eng.,* vol. 124, no. 3, pp. 565-575, 2002.

[137] S. Alghoul, C. Eastwick, and D. Hann, "Experimental investigation of a single droplet interaction with shear driven film," in *Proceedings of ILASS Europe 23rd annual conference on liquid atomization and spray systems*, 2010.

[138] R. Scardovelli and S. Zaleski, "Direct numerical simulation of free-surface and interfacial flow," *Annual review of fluid mechanics*, vol. 31, no. 1, pp. 567-603, 1999.

[139] S. Navti, K. Ravindran, C. Taylor, and R. Lewis, "Finite element modelling of surface tension effects using a Lagrangian-Eulerian kinematic description," *Computer methods in applied mechanics and engineering*, vol. 147, no. 1-2, pp. 41-60, 1997.

[140] A. Caboussat, "A numerical method for the simulation of free surface flows with surface tension," *Computers & fluids*, vol. 35, no. 10, pp. 1205-1216, 2006.

[141] L. Landau and E. Lifshitz, *Fluid Mechanics: Volume 6*. Elsevier, 1987.

[142] G. H. Vatistas, "A note on liquid vortex sloshing and Kelvin's equilibria," *Journal of Fluid Mechanics*, vol. 217, pp. 241-248, 1990.

[143] T. R. Jansson, M. P. Haspang, K. H. Jensen, P. Hersen, and T. Bohr, "Polygons on a rotating fluid surface," *Physical review letters*, vol. 96, no. 17, p. 174502, 2006.

[144] R. Bergmann, L. Tophøj, T. Homan, P. Hersen, A. Andersen, and T. Bohr, "Polygon formation and surface flow on a rotating fluid surface," *Journal of fluid mechanics*, vol. 679, pp. 415-431, 2011.

[145] A. J. Ghajar and S. M. Bhagwat, "Flow patterns, void fraction and pressure drop in gas-liquid two phase flow at different pipe orientations," *Frontiers and progress in multiphase flow I*, pp. 157-212, 2014.

[146] G. B. Wallis, *One-dimensional two-phase flow*. Courier Dover Publications, 2020.

[147] R. Kumar and D. P. Edwards, "Interfacial shear modelling in two-phase annular flow," in *ASME International Mechanical Engineering Congress and Exposition*, 1996, vol. 15212, pp. 381-389: American Society of Mechanical Engineers.

[148] Z. Wang, K. S. Gabriel, and D. L. Manz, "The influences of wave height on the interfacial friction in annular gas–liquid flow under normal and microgravity conditions," *International journal of multiphase flow*, vol. 30, no. 10, pp. 1193-1211, 2004.

[149] I. Malcevic and O. Ghattas, "Dynamic-mesh finite element method for Lagrangian computational fluid dynamics," *Finite Elements in Analysis and Design*, vol. 38, no. 10, pp. 965-982, 2002.

[150] W. F. Noh and P. Woodward, "SLIC (simple line interface calculation)," in *Proceedings of the fifth international conference on numerical methods in fluid dynamics June 28–July 2, 1976 Twente University, Enschede*, 1976, pp. 330-340: Springer.

[151] C. W. Hirt and B. D. Nichols, "Volume of fluid (VOF) method for the dynamics of free boundaries," *Journal of computational physics*, vol. 39, no. 1, pp. 201-225, 1981.

[152] F. H. Harlow and J. E. Welch, "Numerical calculation of time-dependent viscous incompressible flow of fluid with free surface," *Physics of fluids*, vol. 8, no. 12, p. 2182, 1965.

[153] J. Martinez, X. Chesneau, and B. Zeghmati, "A new curvature technique calculation for surface tension contribution in PLIC-VOF method," *Computational Mechanics*, vol. 37, pp. 182-193, 2006.

[154] A. Bourlioux, "A coupled level-set volume-of-fluid algorithm for tracking material interfaces," in *proceedings of the 6th international symposium on computational fluid dynamics, Lake Tahoe, CA*, 1995, vol. 15.

[155] M. Sussman and E. G. Puckett, "A coupled level set and volume-of-fluid method for computing 3D and axisymmetric incompressible two-phase flows," *Journal of computational physics*, vol. 162, no. 2, pp. 301-337, 2000.

[156] Z. Wang, J. Yang, and F. Stern, "Comparison of particle level set and CLSVOF methods for interfacial flows," in *46th AIAA Aerospace Sciences Meeting and Exhibit*, 2008, p. 530.

[157] J. U. Brackbill, D. B. Kothe, and C. Zemach, "A continuum method for modeling surface tension," *Journal of computational physics*, vol. 100, no. 2, pp. 335-354, 1992.

[158] A. Robinson, "Computational Investigations Into Offtake Flows with Application to Gas Turbine Bearing Chambers," University of Nottingham, 2010.

[159] R. Saurel and R. Abgrall, "A multiphase Godunov method for compressible multifluid and multiphase flows," *Journal of Computational Physics*, vol. 150, no. 2, pp. 425-467, 1999.

[160] A. Bock, "Gas-turbine engine with a bearing chamber," Patent US6516618B1, 2003.

[161] K. Millsaps and K. Pohlhausen, "Heat transfer by laminar flow from a rotating plate," *Journal of the Aeronautical Sciences,* vol. 19, no. 2, pp. 120-126, 1952.

[162] E. Cobb and O. Saunders, "Heat transfer from a rotating disk," *Proceedings of the Royal Society of London. Series A. Mathematical and Physical Sciences,* vol. 236, no. 1206, pp. 343-351, 1956.

[163] N. Nikitenko, "Experimental investigation of heat exchange of a disk and a screen(Convective heat exchange between gas-turbine disk and screen-generalized steady-state process study)," *Journal of Engineering Physics,* vol. 6(6), pp. 1-11, 1963.

[164] J. Owen, C. Haynes, and F. Bayley, "Heat transfer from an air-cooled rotating disk," *Proceedings of the Royal Society of London. A. Mathematical and Physical Sciences,* vol. 336, no. 1607, pp. 453-473, 1974.

[165] J. Owen and R. Roger, "Flow and heat transfer in rotating-disc systems. Volume I-Rotor-stator systems," *NASA STI/Recon Technical Report A,* vol. 90, p. 45759, 1989.

[166] J. M. Owen, "Flow and heat transfer in rotating-disc systems," in *International Symposium on Heat Transfer in Turbomachinery*, 1992: Begel House Inc.

[167] C. J. Elkins and J. K. Eaton, "Turbulent heat and momentum transport on a rotating disk," *Journal of Fluid Mechanics,* vol. 402, pp. 225-253, 2000.

[168] E. Serre, P. Bontoux, and B. Launder, "Transitional–turbulent flow with heat transfer in a closed rotor–stator cavity," *Journal of Turbulence*, vol. 5, no. 1, p. 008, 2004.

[169] S. Poncet and E. Serre, "Large eddy simulation of non-isothermal turbulent rotor-stator flows," in *The Twelfth International Symposium on Transport Phenomena and Dynamics of Rotating Machinery*, 2008.

[170] E. Tuliszka-Sznitko, A. Zielinski, and W. Majchrowski, "LES of the non-isothermal transitional flow in rotating cavity," *International Journal of Heat and Fluid Flow*, vol. 30, no. 3, pp. 534-548, 2009.

[171] E. Tuliszka-Sznitko, W. Majchrowski, and K. Kiełczewski, "Investigation of transitional and turbulent heat and momentum transport in a rotating cavity," *International Journal of Heat and Fluid Flow,* vol. 35, pp. 52-60, 2012.

[172] A. Glahn, S. Busam, and S. Wittig, *Local and mean heat transfer coefficients along the internal housing walls of aero engine bearing chambers*. American Society of Mechanical Engineers, 1997.

[173] H. Zimmermann, A. Kammerer, R. Fischer, and D. Rebhan, "Two-phase flow correlations in air/oil systems of aero engines," *ASME paper*, no. 91-GT, p. 54, 1991.

[174] S. Wittig, A. Glahn, and J. Himmelsbach, "Influence of high rotational speeds on heat transfer and oil film thickness in aero-engine bearing chambers," 1994.

[175] A. Glahn and S. Wittig, "Two-phase air/oil flow in aero engine bearing chambers: characterization of oil film flows," *ASME Journal of Engineering for Gas Turbines and Power*, vol. 119, no. 3, pp. 578-583, 1996.

[176] A. Glahn and S. Wittig, "Two-Phase Air/Oil Flow in Aero-Engine Bearing Chambers – Assessment of an Analytical Prediction Method for the Internal Wall Heat Transfer," *International Journal of Rotating Machinery*, vol. 5, no. 3, 1999.

[177] R. Deissler, "Heat transfer and fluid friction for fully developed turbulent flow of air and supercritical water with variable fluid properties," *Transactions of the American Society of Mechanical Engineers*, vol. 76, no. 1, pp. 73-83, 1954.

[178] S. Busam, A. Glahn, and S. Wittig, "Internal bearing chamber wall heat transfer as a function of operating conditions and chamber geometry," *J. Eng. Gas Turbines Power*, vol. 122, no. 2, pp. 314-320, 2000.

[179] A. A. Hashmi, *Oil Film Dynamics in Aero Engine Bearing Chambers: Fundamental Investigations and Numerical Modelling*. Logos Verlag Berlin GmbH, 2012.

[180] W. M. H K Versteeg, second, Ed. *An introduction to computational fluid dynamics: The finite volume method*. Pearson, 2007.

[181] G. Iaccarino, "Simulation of Turbulent Flows " in *Computational methods in fluid dynamics using commercial CFD codes*, Stanford University, 2004.

[182] P. A. Durbin and B. P. Reif, *Statistical theory and modeling for turbulent flows*. John Wiley & Sons, 2011.

[183] G. Staffelbach, "Simulation aux grandes echelles et analyse acoustique de turbines a gaz industrielles multi-bruleurs," Toulouse, INPT, 2006.

[184] E. Garnier, N. Adams, and P. Sagaut, *Large eddy simulation for compressible flows*. Springer Science & Business Media, 2009.

[185] L. Davidson, "An introduction to turbulence models," 2015.

[186] D. C. Wilcox, *Turbulence modeling for CFD*. DCW industries La Canada, CA, 1998.

[187] J. Boussinesq, *Théorie de l'écoulement tourbillonnant et tumultueux des liquides dans les lits rectilignes a grande section*. Gauthier-Villars, 1897.

[188] N. Afzal and R. Narasimha, "Axisymmetric turbulent boundary layer along a circular cylinder at constant pressure," *Journal of Fluid Mechanics,* vol. 74, no. 1, pp. 113-128, 1976.

[189] A. Fluent, "Theory guide," *Ansys Inc.: Canonsburg, PA, USA*, 2015.

[190] F. Menter, "Zonal two equation kw turbulence models for aerodynamic flows," in *23rd fluid dynamics, plasmadynamics, and lasers conference*, 1993, p. 2906.

[191] F. R. Menter, "Two-equation eddy-viscosity turbulence models for engineering applications," *AIAA journal,* vol. 32, no. 8, pp. 1598-1605, 1994.

[192] ANSYS, "Fluent v17 User Manual," 2016.

[193] S. Kassinos, C. Langer, G. Iaccarino, and P. Moin, *Complex effects in large eddy simulations*. Springer Science & Business Media, 2007.

[194] A. Bristot, "Application of the Volume of Fluid Method with Heat Transfer to a Two Shaft Aero Engine Bearing Chamber," PhD, Mechanical Engineering, University of Nottingham, 2017.

[195] J. E. Mindel, "Interface tracking and solid-fluid coupling techniques with coastal engineering applications," Imperial College London, 2008.

[196] D. L. Youngs, "Time-dependent multi-material flow with large fluid distortion," *Numerical methods for fluid dynamics,* 1982.

[197] S. Cant, "Direct numerical simulation of premixed turbulent flames," *Philosophical Transactions of the Royal Society of London. Series A: Mathematical, Physical and Engineering Sciences,* vol. 357, no. 1764, pp. 3583-3604, 1999.

[198] S. E. Norris, "A Parallel Navier Stokes Solver for Natural convection and Free Surface Flow," 2000.

[199] M. Schäfer, *Computational engineering: Introduction to numerical methods*. Springer, 2006.

[200] A. S. L. Valreau, "Computational Fluid Dynamics Investigation of Oscillatory Behaviour in Annular Combustors," University of Cambridge, 2019.

[201] N. Y. Gnedin, V. A. Semenov, and A. V. Kravtsov, "Enforcing the Courant–Friedrichs–Lewy condition in explicitly conservative local time stepping schemes," *Journal of Computational Physics*, vol. 359, pp. 93-105, 2018.

[202] J. D. Anderson and J. Wendt, *Computational fluid dynamics*. Springer, 1995.

[203] G. Virr, J. Chew, and J. Coupland, "Application of computational fluid dynamics to turbine disc cavities," in *Turbo Expo: Power for Land, Sea, and Air*, 1993, vol. 78880, p. V001T03A030: American Society of Mechanical Engineers.

[204] P. D. Smout, J. W. Chew, and P. R. Childs, "ICAS-GT: a European collaborative research programme on internal cooling air systems for gas turbines," in *Turbo Expo: Power for Land, Sea, and Air*, 2002, vol. 36088, pp. 907-914.

[205] M. Wilson, J. Chen, and J. Owen, "Computation of flow and heat transfer in rotating-disc systems," in *3rd International Conference on Computers in Reciprocating Engines and Gas Turbines*, 1996.

[206] K. Jarzombek, H. Dohmen, F.-K. Benra, and O. Schneider, "Flow analysis in gas turbine pre-swirl cooling air systems: variation of geometric parameters," in *Turbo Expo: Power for Land, Sea, and Air*, 2006, vol. 4238, pp. 1403-1411.

[207] C. Wu, B. Vaisman, K. McCusker, and R. Paolillo, "CFD analysis prediction of heat transfer coefficient in rotating cavities with radial outflow," in *Turbo Expo: Power for Land, Sea, and Air*, 2006, vol. 4241, pp. 1515-1525.

[208] R. Debuchy, S. D. Gatta, E. D'Haudt, G. Bois, and F. Martelli, "Influence of external geometrical modifications on the flow behaviour of a rotor-stator system: numerical and experimental investigation," *Proceedings of the Institution of Mechanical Engineers, Part A: Journal of Power and Energy*, vol. 221, no. 6, pp. 857-863, 2007.

[209] R. Roy, D. Zhou, S. Ganesan, C.-Z. Wang, R. Paolillo, and B. Johnson, "The flow field and main gas ingestion in a rotor-stator cavity," in *Turbo Expo: Power for Land, Sea, and Air*, 2007, vol. 47934, pp. 1189-1198.

[210] H. Iacovides and P. Toumpanakis, "Turbulence modelling of flow in axisymmetric rotor-stator systems," in *Presses de l'Ecole Nationale des Ponts et Chaussées, editor, 5th Int. Symp. On Refined Flow Modelling and Turbulence Measurements, Paris*, 1993, pp. 7-10.

[211] R. Schiestel, L. Elena, and T. Rezoug, "Numerical modeling of turbulent flow and heat transfer in rotating cavities," *Numerical Heat Transfer, Part A: Applications,* vol. 24, no. 1, pp. 45-65, 1993.

[212] L. Elena and R. Schiestel, "Turbulence modeling of confined flow in rotating disk systems," *AIAA journal,* vol. 33, no. 5, pp. 812-821, 1995.

[213] B. Launder and D. Tselepidakis, "Application of a new second-moment closure to turbulent channel flow rotating in orthogonal mode," *International Journal of Heat and Fluid Flow,* vol. 15, no. 1, pp. 2-10, 1994.

[214] L. Elena and R. Schiestel, "Turbulence modeling of rotating confined flows," *International Journal of Heat and Fluid Flow,* vol. 17, no. 3, pp. 283-289, 1996.

[215] S. Poncet, R. Schiestel, and M.-P. Chauve, "Centrifugal flow in a rotor-stator cavity," *Journal of Fluids Engineering,* vol. 127, pp. 787-794, 2005.

[216] R. Da Soghe, L. Innocenti, A. Andreini, and S. b. Poncet, "Numerical benchmark of turbulence modeling in gas turbine rotor-stator system," in *Turbo Expo: Power for Land, Sea, and Air,* 2010, vol. 44021, pp. 771-783.

[217] F. MacMillan, "Experiments on Pitot-Tubes in Shear Flow," Ministry of Supply, Aeronautical Research and Council 3028, 1956.

[218] J. W. Daily, W. D. Ernst, and V. V. Asbedian, "Enclosed rotating disks with superposed throughflow: mean steady and periodic unsteady characteristics of induced flow," 1964.

[219] P. R. Bevington, "Data reduction and error analysis for the physical sciences," *New York: McGraw-Hill,* 1969.

[220] R. J. Donnelly and K. Schwarz, "Experiments on the stability of viscous flow between rotating cylinders-VI. Finite-amplitude experiments," *Proceedings of the Royal Society of London. Series A. Mathematical and Physical Sciences,* vol. 283, no. 1395, pp. 531-556, 1965.

[221] F. R. Menter, M. Kuntz, and R. Langtry, "Ten years of industrial experience with the SST turbulence model," *Turbulence, heat and mass transfer,* vol. 4, no. 1, pp. 625-632, 2003.

[222] A. Bristot, H. P. Morvan, and K. A. Simmons, "Evaluation of a volume of fluid CFD methodology for the oil film thickness estimation in an aero-engine bearing chamber," in *ASME Turbo Expo 2016: Turbomachinery Technical Conference and Exposition*, 2016: American Society of Mechanical Engineers Digital Collection.

[223] P. Childs, *Rotating flow*. Elsevier, 2010.

[224] D. J. Tritton, *Physical fluid dynamics*. Springer Science & Business Media, 2012.

[225] R. Debuchy, S. Poncet, F. A. Nour, and G. Bois, "Experimental and numerical investigation of turbulent air flow behaviour in a rotor-stator cavity," in *European Turbomachinery Conference*, 2009, p. Article n° 52.

[226] S. Poncet, M.-P. Chauve, and P. Le Gal, "Turbulent rotating disk flow with inward throughflow," *Journal of Fluid Mechanics*, vol. 522, pp. 253-262, 2005.

[227] A. Warusevitane, R. Omar, K. Johnson, and S. Ambrose, "3D Modelling of a Hydraulic Seal With an Oil Feed, Focussing on the Effect of the Jet on the Behaviour of Oil in the Trough," *Turbo Expo: Power for Land, Sea, and Air*, vol. 87059, p. V11AT22A033, 2023.

[228] G. Cardone, T. Astarita, and G. M. Carlomagno, "Heat transfer measurements on a rotating disk," *International Journal of Rotating Machinery*, vol. 3, no. 1, pp. 1-9, 1997.

[229] A. Northrop, "Heat transfer measurements in rotating-disk systems. Part. 1: The free disk," *Int. J. Heat and fluid Flow*, vol. 9, p. 1, 1988.